Simultaneous Active Control of Flexural and Extensional Power Flow in Thin Beams

by

Gary P. Gibbs

Dissertation submitted to the Faculty of the Virginia Polytechnic Institute and State University in partial fulfillment of the requirements for the degree of

Doctor of Philosophy
in
Mechanical Engineering

APPROVED:

Chris R. Fuller, Chairman

Richard J. Silcox

Harry H. Robertshaw

Harley H. Cudney

Ricardo A. Burdisso

April, 1993
Blacksburg, Virginia

Simultaneous Active Control of Flexural and Extensional Power Flow in Thin Beams

by

Gary P. Gibbs

Committee Chairman: Chris R. Fuller

Abstract

The primary goal of this dissertation consisted of two related parts. The first was to develop an analytical basis for predicting the active control of flexural and extensional power flow in thin semi-infinite and finite beams using piezoelectric actuators and sensors. The second part was to experimentally demonstrate these techniques applied to actual beam systems. In order to maintain total control authority over the system, the control actuators must be able to adequately excite both flexural and extensional motion in the beam. Accurate sensing or estimation of the actual power flow (or variables that can be related to the power flow) in the finite beam in real time is also a requirement. This dictated the development of advanced, new sensing techniques. In order that these overall goals were achieved several tasks were carried out as discussed below.

A theoretical model for the excitation of a thin beam by a single piezoelectric actuator mounted on the surface was developed. The model predicts the

simultaneous excitation of flexural and extensional motion by a single actuator whose relative amplitudes are functions of beam and actuator parameters. Further, a single pair of axially co-located, symmetrically bonded, and independently driven piezoelectric actuators can excite flexural and extensional motion of variable complex amplitudes.

A method for the real time filtering of net positive and negative traveling flexural and extensional waves was developed. The theoretical actuator and sensor models were used to study the control of flexural and extensional power flow in both finite and semi-infinite beams subjected to point force excitation at the free end. These actuator and sensing techniques when combined with an multiple input/output adaptive controller can simultaneously control flexural and extensional power flow in regions of a beam system over a band of frequencies.

The control of flexural and extensional power flow in thin beams was also experimentally investigated for both finite and semi-infinite beams. Power flow attenuations of 30 dB or more downstream of the control actuator location were demonstrated using a single pair of piezoelectric actuators for both resonant and damped beam systems. The experimental and theoretical results demonstrate the effectiveness of piezoelectric actuators and piezoelectric wave vector filters in the control of flexural and extensional power flow in thin beams.

Acknowledgements

As I have now completed my dissertation, I would like to reflect on my experience, and thank those people who contributed their technical and moral support on this project. Although I cannot possibly thank everyone who deserves credit for assistance and support on this work I will attempt to mention those who come to mind. I would like to thank Chris Fuller for providing the opportunity to work in the extremely interesting and dynamic field of active control. His insight, guidance, and leadership has provided an educational experience that I will never forget.

Secondly, I would like to thank Rich Silcox for his endless support on this project. I cannot begin to count the number of times that I carried on lengthy discussions on every aspect of this dissertation with him. As we sometimes seem to have different ways of expressing our technical thoughts on the subject, I often left his office more confused than when I entered. However, through his efforts during the four year period of work at NASA Langley Research Center, I greatly enhanced my understanding of active control of structures, and digital filtering. I would also like to thank Harley Cudney, Ricardo Burdisso, and Harry Robertshaw for their support on this project. The ideas and comments provided by the committee proved to be extremely

valuable and resulted in vastly superior research accomplishments.

I would like to express my appreciation to the Structural Acoustics Branch of the NASA Langley Research Center for their sponsorship of this project. The center not only provided the financial support, but also provided incredible laboratory facilities and technical expertise. I would like to thank Don Brown for his friendship, and his support on the development and implementation of the digital control systems used in the dissertation.

I would like to thank Mari Willcockson, and my roommates Jamie Carneal and Steve Booth for their patience and support during the 6 grueling weeks of the dissertation writing period. I would like to recognize Rob Clark for his technical and moral support throughout the eight or so years that I have known him, and especially during my graduate studies.

I would like to recognize WordPerfect Corp., and 3-D Visions Corp. (makers of Stanford Graphics) for providing unending assistance in the removal of every last hair on my head (in double handfuls) during the completion of my dissertation. I am quite confident that I am the most abused "beta tester" in the country. The best advise I can give to the young "beta tester" that may read this dissertation is to "save often."

Last and most importantly I would like to thank my family. I am truly blessed with one of the greatest families on earth. My parents, Forrest and Hilda Gibbs, have done, and will do anything they possibly can to provide me with monetary and moral support. Although they have never been wealthy, they have saved all their lives so that they can give to their children. I can never possibly thank them enough or repay them for all that they have given. I hope that they are proud of my current and future accomplishments, and my strive for excellence as this is the only thing that can come close to repaying them for their love and support. My sister, Debbie Pugh, and her husband Dave have always been there when I needed them. I really appreciate all that they have done for me. My brother Ron Gibbs, and his family have always provided encouragement, and I am grateful for their support.

I remember back in September of 1982, as I packed my car to drive up to Blacksburg for the first time, my brother (a hokie engineering alumnus) told me that I was getting ready to start one of the most enjoyable times of my life. He was older than I was and already had a lovely family and successful career. He said that he would love to be in my shoes. At the time, I did not fully understand what he meant, but now I do.

The "good times" would not be good if it were not for the "bad times."

Contents

Chapter 1

Introduction xxvii

1.1 Overview of the Active Control of Power Flow in Beams 3

1.2 Overview of Piezoelectric Actuator Models as Applied to Beam Systems 6

1.3 Overview of Piezoelectric Sensor Models as Applied to Beam Systems 10

1.4 Traveling Wave and Power Flow Sensing Techniques 12

1.5 Scope and Objectives 17

1.6 Organization 19

Chapter 2

Theoretical Developments 21

2.1 Asymmetric Piezoelectric Actuator Model 22

2.1.1 Asymmetric Piezoelectric Element - Infinite Extent . . . 24

2.1.1.1 Flexural Equation of Motion 31

2.1.1.2 Extensional Equation of Motion 33
2.1.2 Application to Infinite Beam Power Flow 35
2.2 Piezoelectric Surface Strain Sensors 42
2.2.1 Piezoelectric Flexural Sensor 43
2.2.2 Piezoelectric Extensional Sensor 46
2.3 Wave Vector Filtering in One Dimensional Media 47
2.3.1 Cotangent Method 51
2.3.2 Flexural Wave Filtering Using the Cotangent Method . 53
2.3.3 Time Delay Method 59
2.3.4 Extensional Wave Filtering using the Time Delay Method 62
2.3.5 Correlation of Wave Filtering to Power Flow 66
2.4 Control of Flexural and Extensional Power Flow in Thin Beams 70
2.4.1 Flexural and Extensional Equations of Motion 71
2.4.2 Excitation and Control of Semi-infinite Beams 73
2.4.2.1 Point Force Excitation of Semi-infinite Beams 74
2.4.2.2 Piezoelectric Excitation of Semi-infinite Beams 77

2.4.2.3 Optimal Control of Flexural and Extensional Power Flow in Semi-infinite Beams 87

2.4.3 Excitation and Control of Finite Beams 95

2.4.3.1 Point Force Excitation of Finite Beams . . 97

2.4.3.2 Piezoelectric Excitation of Finite Beams . 100

2.4.3.3 Optimal Control of Flexural and Extensional Power Flow in Finite Beams 104

Chapter 3

Control Concepts 108

3.1 The Adaptive Finite Impulse Response Filter 108

3.2 The Single Input/Output LMS Algorithm 110

3.3 The Multiple Input/Output Filtered-x LMS Algorithm 113

3.4 The MIMO Filtered-x LMS Algorithm with Real Time Wave Vector Filtering 117

Chapter 4

Experimental Work 120

4.1 Out-of-Plane Velocity Measurements 122

4.1.1 Power Flow Estimation using Two Point Finite Difference Technique 123
4.1.2 LMS Flexural Wave Decomposition 126
4.1.3 Comparison of the Finite Difference and Wave Deconvolution Techniques 128
4.2 In-Plane Strain Measurements 130
4.3 Control of Flexural Power Flow using Piezoelectric Error Sensors 133
4.3.1 Experimental Arrangement 134
4.3.2 Control Implementation 137
4.3.3 Experimental Procedure 138
4.3.4 Semi-infinite Beam Results 141
4.3.5 Finite Beam Results 148
4.3.6 Discussion 157
4.4 Simultaneous Control of Flexural and Extensional Power Flow using Piezoelectric Error Sensors 158
4.4.1 Experimental Arrangements 158
4.4.2 Control Implementation 161
4.4.3 Experimental Procedure 163
4.4.4 Experimental Results 166
4.4.5 Discussion 172

4.5 Simultaneous Control of Flexural and Extensional Power Flow using Real Time Wave Vector Filtering 174

4.5.1 Experimental Arrangement 175

4.5.2 Control Implementation 182

4.5.3 Experimental Procedure 185

4.5.4 Data Analysis 187

4.5.5 Results 193

4.5.5.1 Semi-infinite Beam Flexural Response, 608 Hz 193

4.5.5.2 Semi-Infinite Beam Extensional Response, 608 Hz 201

4.5.5.3 Wave Filter Performance Studies, Semi-infinite Beam, 608 Hz 211

4.5.5.4 Semi-infinite Beam Flexural Response, 1120 Hz 215

4.5.5.5 Semi-Infinite Beam Extensional Response, 1120 Hz 223

4.5.5.6 Wave Filter Performance Studies, Semi-infinite Beam, 1120 Hz 230

4.5.5.7 Finite Beam Flexural Response, 608 Hz . 234

4.5.5.8 Simultaneous Control of a Finite Beam at 608 Hz and 1312 Hz 244

4.6 Discussion 250

Chapter 5

Conclusions and Recommendations 256

Appendix A

Beam Response Subjected to Various Loading Conditions 274

APPENDIX B

Derivation of Far Field Power Flow for Flexural and Extensional Excitation 294

List of Figures

Figure 2.1 Pure Flexural/Extensional Strain Distributions of Symmetrically bonded Piezoelectric Actuators 24

Figure 2.2 Strain Distribution of an Asymmetric Piezoelectric Actuator . . . 26

Figure 2.3 Infinite Beam Arrangement with Two Actuators 36

Figure 2.4 Infinite Beam Power Flow, 800 Hz 39

Figure 2.5 Infinite Beam Power Flow, 800 Hz, Relative Phase = 90 deg. . 41

Figure 2.6 Surface Bonded Piezoelectric Sensor 45

Figure 2.7 Block Diagram of Cotangent Method 54

Figure 2.8 Sensor Arrangement for Flexural Wave Vector Filtering 55

Figure 2.9 Flexural Wave Vector Filter Schematic 58

Figure 2.10 Frequency Response of the desired and actual IIR filter 60

Figure 2.11 Block Diagram of Time Delay Method 62

Figure 2.12 Sensor Arrangement for Extensional Wave Vector Filtering . . 64

Figure 2.13 Extensional Wave Vector Filter Schematic 67

Figure 2.14 Semi-infinite Beam Schematic 71

Figure 2.15 Flexural Loading Condition 75

Figure 2.16 Extensional Loading Condition 76

Figure 2.17 Frequency Response of Beam Downstream of the Actuator for $x >> x_a + L_a/2$ 82

Figure 2.18 Frequency Response of the Positive Traveling Flexural Wave Under Optimal Control, for $x < x_a - L_a/2$ 93

Figure 2.19 Finite Beam Schematic 96

Figure 2.20 Flexural Loading Condition 98

Figure 2.21 Extensional Loading Condition 99

Figure 3.1 SISO LMS Algorithm Block Diagram 111

Figure 3.2 MIMO Filtered-x LMS Algorithm Block Diagram 115

Figure 3.3 MIMO Filtered-x LMS Algorithm with Real Time Wave Vector Filtering 117

Figure 4.1 Scanning Laser Vibrometer Schematic 123

Figure 4.2 Experimental Schematic 135

Figure 4.3 Photograph of Experimental Arrangement 136

Figure 4.4 Control Block Diagram 138

Figure 4.5 Flexural Velocity Distribution, 302 Hz, Semi-infinite Beam 142

Figure 4.6 Power Flow Distribution, 302 Hz, Semi-infinite Beam 144

Figure 4.7 Flexural Velocity Distribution, 802 Hz, Semi-infinite Beam 147

Figure 4.8 Power Flow Distribution, 802 Hz, Semi-infinite Beam 148

Figure 4.9 Flexural Velocity Distribution, 412 Hz, Blocking Mass 150

Figure 4.10 Power Flow Distribution, 412 Hz, Blocking Mass 151

Figure 4.11 Flexural Velocity Distribution, 802 Hz, Blocking Mass 154

Figure 4.12 Power Flow Distribution, 802 Hz, Blocking Mass 155

Figure 4.13 Experimental Schematic 159
Figure 4.14 Photograph of Experimental Arrangement 160
Figure 4.15 Controller Block Diagram 162
Figure 4.16 Normalized Response of Beam to Broad Band Extensional and Flexural Excitation by Control Transducers 164
Figure 4.17 Flexural Velocity Distribution, 704 Hz 170
Figure 4.18 Flexural Velocity Distribution, 1312 Hz 173
Figure 4.19 Schematic of the Experimental Arrangement 176
Figure 4.20 Photograph of Experimental Arrangement 176
Figure 4.21 Photograph of Piezoelectric Control Actuators 178
Figure 4.22 Photograph of PVDF Sensors 180
Figure 4.23 Photograph of Semi-Conductor Strain Gage Station 181
Figure 4.24 Controller Block Diagram 184
Figure 4.25 Flexural Velocity Distribution, No Control, 608 Hz, Semi-infinite 194
Figure 4.26 Flexural Velocity Distribution, Control, 608 Hz, Semi-infinite . . 198
Figure 4.27 Extensional Strain Distribution, No Control, 608 Hz 203
Figure 4.28 Extensional Strain Distribution, Control, 608 Hz 207
Figure 4.29 Flexural Velocity Distribution, No Control, 1120 Hz, Semi-infinite Beam 217

Figure 4.30 Flexural Velocity Distribution, Control, 1120 Hz, Semi-infinite Beam 220
Figure 4.31 Extensional Strain Distribution, No Control, 1120 Hz 224
Figure 4.32 Extensional Strain Distribution, Control, 1120 Hz 227
Figure 4.33 Photograph of the Modified Termination 236
Figure 4.34 Flexural Velocity Distribution, No Control, 608 Hz, Finite Beam 237
Figure 4.35 Flexural Velocity Distribution, Control, 608 Hz, Finite Beam . . 239
Figure 4.36 Flexural Velocity Distribution, No Control, 608 and 1312 Hz, Finite Beam 247
Figure 4.37 Flexural Velocity Distribution, Control, 608 and 1312 Hz, Finite Beam 248
Figure 4.38 Extensional Strain Distribution, No Control, 608 and 1312 Hz 250
Figure 4.39 Extensional Strain Distribution, Control, 608 and 1312 Hz . . . 251
Figure 4.40 Required Sensor Configurations for Various Loading Conditions 253

List of Tables

Table 2.1 Material Properties of Sensor and Beam 59

Table 4.1 Blocking Mass Properties 140

Table 4.2 Shaker Input Impedance, Semi-infinite Beam 145

Table 4.3 Shaker Input Impedance, Blocking Mass 152

Table 4.4 Attenuation (dB re no control) at 704 Hz 167

Table 4.5 Attenuation (dB re no control) at 1312 Hz 172

Table 4.6 Material Properties of Piezoelectric Material G-1195 179

Table 4.7 Material Properties of Polyvinylidene Fluoride (PVDF) 179

Table 4.8 Flexural Traveling Wave Amplitudes, No Control, 608 Hz, Semi-infinite Beam 199

Table 4.9 Flexural Traveling Wave Amplitudes, Control, 608 Hz, Semi-infinite Beam 200

Table 4.10 Flexural Power Flow, 608 Hz, Semi-infinite 202

Table 4.11 Extensional Traveling Wave Amplitudes, No Control, 608 Hz . 208

Table 4.12 Extensional Traveling Wave Amplitudes, Control, 608 Hz 208

Table 4.13 Extensional Power Flow, 608 Hz 209

Table 4.14 Flexural Wave Vector Filtering, 608 Hz 213

Table 4.15 Extensional Wave Vector Filtering, 608 Hz 215

Table 4.16 Flexural Traveling Wave Amplitudes, No Control, 1120 Hz, Semi-infinite Beam 221

Table 4.17 Flexural Traveling Wave Amplitudes, Control, 1120 Hz, Semi-infinite Beam 221

Table 4.18 Flexural Power Flow, 1120 Hz, Semi-infinite 223

Table 4.19 Extensional Traveling Wave Amplitudes, No Control, 1120 Hz 228

Table 4.20 Extensional Traveling Wave Amplitudes, Control, 1120 Hz . . . 228

Table 4.21 Extensional Power Flow, 1120 Hz 230

Table 4.22 Flexural Wave Vector Filtering, 1120 Hz 233

Table 4.23 Extensional Wave Vector Filtering, 1120 Hz 234

Table 4.24 Flexural Traveling Wave Amplitudes, No Control, 608 Hz, Finite Beam 240

Table 4.25 Flexural Traveling Wave Amplitudes, Control, 608 Hz, Finite Beam 241

Table 4.26 Flexural Power Flow, 608 Hz, Finite 242

Nomenclature

Arabic

a beam cross sectional area (m^2)

c slope of the assumed strain distribution (m^{-1})

A complex coefficient of positive flexural traveling wave (m)

B complex coefficient of negative flexural traveling wave (m)

C complex coefficient of negative flexural decaying nearfield (m)

d_{31} strain sensitivity (166 x 10^{-12} m/volt for piezoelectric G1195 material)

d(n) desired output of the controller as seen at the error sensor at the n^{th} time step

$d_l(n)$ desired output of the controller as seen at the l^{th} error sensor at the n^{th} time step

D complex coefficient of positive flexural decaying nearfield (m)

e(n) actual error output of the error sensor at the n^{th} time step

$e_l(n)$ actual error output of the l^{th} error sensor at the n^{th} time step

E complex coefficient of positive traveling extensional wave (m)

E_b Young's modulus of the beam (Pa)

E_{pe} Young's modulus of the piezoelectric material (Pa)

F complex coefficient of negative traveling extensional wave (m)

F_w shear force (N)

F_x in-plane force (N)

h half beam thickness (m)

H(x) unit step function (dimensionless)

I area moment of inertia of the beam (m^4)

k_e extensional wavenumber (m^{-1})

k_f flexural wavenumber (m^{-1})

K^e extensional excitation constant (dimensionless)

K^f flexural excitation constant (m^{-1})

L_a actuator length (m)

L_{es} extensional sensor spacing (m)

L_{fs} flexural sensor spacing (m)

L_s sensor length (m)

L_v spacing of velocity measurement for power estimation (m)

L_y beam width, sensor width (m)

M internal flexural moment (N*m)

m,m(x) actuator induced flexural moment (N*m)

n function time step (dimensionless)

P_e extensional power flow (Watts)

P_f flexural power flow (Watts)

R_{nf} flexural nearfield reflection coefficient (dimensionless)

R_{tf} flexural traveling wave reflection coefficient (dimensionless)

R_{te} extensional traveling wave reflection coefficient (dimensionless)

T_a actuator thickness (m)

T_s sensor thickness (m)

U total in-plane displacement (m)

u spatial in-plane displacement (m)

v_w out-of-plane velocity (m/sec)

v_u in-plane velocity (m/sec)

V applied voltage (volts)

V_1 complex voltage applied to patch 1 (volts)

V_2 complex voltage applied to patch 2 (volts)

w beam displacement in z direction (m)

W total beam displacement in z direction (m)

x coordinate along beam neutral axis (m)

y coordinate parallel to the beams surface and perpendicular to the neutral axis (m)

z coordinate perpendicular to the beams surface (m)

Greek

β_i the i^{th} coefficient of the FIR filter

δ `unit impulse function ($m^{-1)}$

δ' derivative of the unit impulse function (m^{-2})

ε strain (dimensionless)

ε_O assumed strain at neutral axis (dimensionless)

ν Poissons ratio for the beam (dimensionless)

ρ mass per unit volume of the beam (kg/m^3)

ω rotational frequency (rad/sec)

σ_b stress in beam (Pa)

σ_{pe} stress in piezoelectric material (Pa)

Θ rotational velocity (rad/sec)

$\Psi(n)$ output of the FIR filter at the n^{th} time step

$\chi(n)$ reference signal at the n^{th} time step

λ_f flexural wavelength (m)

Chapter 1

Introduction

We live in an environment that most people consider to have progressed and developed over the centuries. With this "progression" has come complexity. Our cities are larger, taller, and more crowded. Our planes are faster and more comfortable, yet they are also larger and louder. We probably have more cars in junk yards now then Henry Ford would have ever dreamed possible to manufacture. The development breeds on itself. It creates useful items, but it also creates unwanted byproducts. One of these is noise.

The search for solutions to the noise pollution problem creates many new technological developments. Traditionally, most of the noise control techniques have been passive in nature. In other words, the passive technique modifies physical properties of the system such as: mass, stiffness, density, damping, etc. The passive technique tends to be an effective means of controlling noise at higher frequencies, but not at low frequencies. A new technology termed "active control" tries to modify the vibration or noise generated by a system by actually exciting the system in some way to produce the desired effect. For

example, several additional forces (active sources) can be applied to a structure such that when their coherent response is superimposed with the unwanted primary (noise) field, the vibration over some region is reduced. Active control has shown much promise in controlling the low frequency response of a system. With the advent of digital computing, and the development of advanced materials and control schemes, a new technology called "smart structures" is evolving. In this technology, the structure contains portions analogous to the human anatomy. The "nerves" of the smart structure are the sensors and related electronics. The "muscles" of the smart structure consist of the actuator system, and the "brain" of the smart structure consists of the controller and related interface schemes. The idea behind the smart structure is not to just give new terminology to existing items, but to begin the science of integrating these items into the structure just as muscles, nerves, and brain are integrated into the human body. The "smart structures" can be used to actively control unwanted vibration, for example, or to perform any number of conceivable functions.

The advanced uses of certain materials to both sense and actuate smart structures have developed in recent years. The piezoceramic (PZT (Piezo Systems, 1987)) material is especially attractive as an actuator because of its high electrical to mechanical efficiency, its high output force to weight ratio

compared to conventional shakers, and additionally due to its size and shape (usually about the size of a business card). It is typically quite thin (1.8 mm), and can be readily bonded to, or embedded in a structure. A type of piezoelectric film, polyvinylidene fluoride (PVDF (KYNAR, 1987)), although possessing little authority as an actuator, is an extremely effective sensor. It is extremely thin, can be configured to provide an output proportional to the integral of the strain it is subjected to, and is even much more sensitive then the best semi-conductor strain gages. It is these two types of materials which will be utilized in the theoretical and experimental work presented in this dissertation.

1.1 Overview of the Active Control of Power Flow in Beams

Vibrations may travel through a structure in the form of flexural, extensional, and torsional motions (Cremer et al., 1973) and often couple to a fluid to radiate sound. This vibration is often unwanted and a wide variety of techniques have been used to reduce it. However, passive techniques are difficult to apply in the low frequency region because of the typically high required mass addition (Fahy, 1985; Kinsler et al., 1982), and it is in this situation that active control approaches have shown much promise. In particular, Redmen-White et al.

(1987), von Flotow and Schafer (1986) and Gonidou and Fuller (1989) demonstrated that active forces applied to beam-like structures can attenuate flexural waves and associated flexural power flow in the media. The work by Gonidou and Fuller showed that flexural power flow leaving finite beams terminated by an impedance (representative of a structural joint) could be controlled with only one control input. This approach is in contrast to the usual modal approach of trying to reduce the total vibrational energy in the finite beam section (Meirovitch and Norris, 1984; Post and Silcox, 1990). Thus, if vibrational energy from machinery can be confined to the immediate supporting structure before dispersing through the overall system, then efficient control approaches can be implemented. The response of systems vibrating on resonance tend to be dominated by one mode, and thus lend themselves to efficient control with one modal sensor. The response of systems vibrating off resonance can be dominated by several modes. Thus, control using a modal approach will require the use of a sensor and actuator per mode of interest to achieve efficient control (Meirovitch and Norris, 1984; Post and Silcox, 1990; Morgan, 1991; Sundararajan, 1985; Linder et al., 1991). For the off resonance case the sensor, actuator, and controller complexity increases significantly. The power flow approach (Gonidou and Fuller, 1989 and Fuller et al., 1990) requires only one actuator and controller to control the total energy traveling past the control point, and is thus less complex to implement.

Complete analysis and control of marine and aerospace type structures with long beam elements is further complicated by the presence of structural discontinuities such as joints, attachments, etc. As mentioned previously, vibrational energy is carried by three main wave forms of flexural, extensional and torsional. Cremer et al. (1973) have shown in grillage like structures that significant wave conversion phenomena can occur between flexural, extensional, and torsional waves at structural joints, due to the coupling inherent in the boundary conditions. This phenomena is very important in the aforementioned application for many reasons. For example, extensional waves, although having small out-of-plane displacements (through Poisson's coupling), may carry a large amount of energy due to the structure being much stiffer for in-plane motion. However, by impinging on a discontinuity, these extensional waves may couple strongly to flexural waves with a large out-of-plane motion that subsequently radiate large sound levels. Thus, it may be deduced that all vibrational waves are important in terms of control of structure-borne sound.

Early work by Crawley and de Luis (1987) demonstrated that piezoceramic elements bonded to a beam surface have potential for the excitation of structures. More recently Pines and von Flotow (1989) and Gibbs and Fuller (1992(a)) have shown that piezoelectric elements can be used as both sensors and actuators in the control of motion and power flow in beams. As shown by

Crawley and de Luis (1987), a piezoelectric actuator, when bonded to the surface of the beam and excited by an oscillating voltage, effectively induces a surface strain due to its expansion and contraction. Previous models, and experiments have been concerned with axially collocated and oppositely mounted pairs of actuators that are hard wired in-phase to excite pure extensional motion, or out-of-phase to excite pure flexure (Crawley and Anderson, 1990, Fanson and Chen, 1986). Experimental work by Fuller et al. (1990) showed that two independent piezoelectric actuators that are axially collocated, and bonded on opposite sides of the beam are capable of simultaneously exciting both flexural and extensional waves in beams. Their work also demonstrated the simultaneous active control of both flexural and extensional power flow in thin beams using a single pair of piezoelectric actuators and sensors.

1.2 Overview of Piezoelectric Actuator Models as Applied to Beam Systems

Over the past five years, a significant amount of research has been dedicated to the use of piezoelectric actuators and sensors to control vibration in beam like structures. Early work by Crawley and de Luis (1987) demonstrated the effective use of piezoelectric actuators in controlling transient vibrations in

beams. Both Fanson and Chen (1986), and Crawley and Anderson (1990) have theoretically analyzed the forcing functions associated with two piezoelectric actuators bonded symmetrically on opposite sides of a thin beam. They assumed that the piezoelectric is thin compared to the beams thickness, and thus does not significantly contribute to the mass (or stiffness) of the beam. The actuator is also assumed to be infinitely long, and thus the model neglects the edge effects (imperfections in the model due to insufficiently modeled boundary conditions at the edges of the piezoelectric). In their work, it is shown how the actuators, when driven with the same input voltage but 180 degrees out-of-phase, effectively exert equal and opposite line moments on the beam at the ends of the actuators and subsequently generate flexural motion in the beam. Crawley and Anderson (1990) have also shown that when the actuators are driven in-phase (symmetric excitation) the effective forcing functions are in-plane line forces of opposite direction, again concentrated at the ends of the actuator. The resulting motion in the beam in this case is purely extensional.

Recently Clark et al. (1991) have experimentally and analytically studied the harmonic excitation of a simply supported beam using multiple pairs of piezoelectric actuators configured to excite pure flexure in the beam. Their work demonstrated that arrays of suitably driven actuators can be used to excite selected modes in the beam. The analytical model for the piezoelectric

actuator forcing function correlated well to confirmed experimental measurements of the response of a simply supported beam excited by such an actuator. Dimitriadis et al (1989) have also extended the 1-D analysis of Crawley and de Luis (1987) to excitation of thin plates by rectangular 2-D piezoceramic patches. Their work showed that the forcing function was equivalent to a line moment around the complete periphery of the patch. This patch forcing function is the basis of analytical studies on active control of vibration and sound radiation from vibrating panels using piezoelectric actuators and sensors (see for example the work by Clark and Fuller, 1990).

It is interesting to note that all of the previous work has been concerned with excitation and control of short finite beams and plates dictating that the system response to the piezoelectric actuators is modally based. However, many structures in applications such as Naval vessels and aerospace structures are constructed from long slender beam elements in which the vibrational response can be considered to be transmitted by wave type motion. Due to the inherent damping in these beams due to joints, attachments, etc. it is often inappropriate and unrealistic to use a modally based model. In connection with this, it has been demonstrated that long beams tend to transmit vibrational power in a wave flow type process and it is an alternative control goal to isolate or reduce the traveling energy rather than, say, the modal response (Miller and von

Flotow, 1989). Experiments by Gibbs and Fuller (1992(a)) have shown that narrow band flexural power flow in thin semi-infinite beams can be reduced significantly by using a single pair of piezoelectric actuators configured to produce pure flexure. In order to analytically study long beam systems it is convenient to derive the system response to the piezoelectric actuator from a wave rather than a modal approach. Note, however, that the two approaches are inherently related just as modes can be thought of as a superposition of identical waves of equal amplitudes traveling in opposite directions.

To analytically study such actuator configurations it is thus necessary to use a more general situation of excitation of thin beams by a single actuator bonded to the beam. As noted above all previous actuator models have been either for pure flexure or extension. Recent developments by Gibbs and Fuller (1992(b)) have provided a model for the excitation of thin beams to a single asymmetrically bonded piezoelectric actuator. The model predicts that a single surface mounted piezoelectric actuator simultaneously excites both flexural and extensional motion in beams whose relative amplitudes are functions of beam/actuator configuration and properties (as detailed in Chapter 2). Thus, two collocated actuators bonded on opposite sides of the beam can produce any desired combination of flexural and extensional motion. This is contrasted with previous actuator models (Fanson and Chen, 1986, and Crawley and

Anderson 1990) which require two sets of actuator pairs to accomplish the same task. The model can be used, for example, to optimize the placement of actuators in arrays on more complicated beam like structures without the restrictions of the previous models (i.e. actuators must be in symmetric pairs excited either in-phase, or out-of-phase). The analysis also presents the beam response in terms of a wave rather than model approach.

1.3 Overview of Piezoelectric Sensor Models as Applied to Beam Systems

In order to effectively control the vibration of a beam system, it is necessary to be able to adequately sense (or observe) the vibration. Piezoelectric films such as poly-vinylidene fluoride (PVDF, see Kynar, 1987) offer some advantages in terms of their applications in smart structures. Because of their high stress/charge sensitivity and compact size PVDF offers extremely high sensing authority with negligible added mass or stiffness. These piezoelectric films are distributed in nature, and thus can provide spatial as well as temporal filtering and information. In contrast the more traditional transducer, the accelerometer, is an effective device to measure the point acceleration of a vibrating structure in a particular direction. PVDF films can be embedded in laminate form within

a structure, and add less mass to the structure than conventional accelerometers.

Lee and Moon (1990) developed a one and two dimensional piezoelectric sensor theory for flexural motion of beams and plates. They showed that the charge output of a piezoelectric sensor when bonded to the surface of a vibrating beam is proportional to the spatial integral of the surface strain under the sensor. They used the theory to develop modal sensors, and experimentally verified the concept for one dimensional beams. Since the modal sensor theory takes advantage of the orthogonality of modes, shaped sensors can be developed to sense or filter particular modes. Their basic theory detailing the charge output of a piezoelectric sensor in terms of surface strain under the sensor can be readily extended to the measurement of extensional motion (see Chapter 2).

A technique to spatially filter flexural vibration from a wave point of view was presented by Collins et al. (1991). In this work, a sensor can be designed that will approximate a spatial ideal low pass filter. In other words, a sensor can be designed whose shape is the inverse spatial Fourier transform of the desired wavenumber response. As an example a low pass spatial filter has a desired gain of one for $-k_c < k < k_c$, and zero for $-k_c > k > k_c$. This corresponds to a

sensor in the shape of a Sinc function (the inverse Fourier transform of the ideal low pass spatial filter). The sensor shape is thus infinite in extent but can be truncated using spatial windowing techniques. This sensor will be sensitive to both positive and negative traveling waves (for frequencies up to ω_c corresponding to k_c), but can not discriminate between them.

1.4 Traveling Wave and Power Flow Sensing Techniques

It is the main purpose of this dissertation to control beam vibration from a standpoint of energy transfer (power flow) along the structure. To understand the main concept, one can think of the structural system as consisting of two major regions. The first region of the structure is the area in which the unwanted vibration originates. The second region of the structure is the area that is to be isolated from this undesirable vibration (or energy). The main concept is to limit or isolate the transmission of energy from region one to region two in all wave forms (not just say flexural). All wave forms can and do carry energy. Thus, it is important to address each wave form. The concepts presented in this technique are the basis of a U. S. Patent by Gibbs, Fuller, and Silcox (1992(a)). The power flow technique is in contrast to approaches that desire to reduce the motion at some discrete number of points, or reduce the

response of a finite number of modes (for example: Meirovitch and Norris, 1984; Post and Silcox, 1990).

Noiseux (1970) presented a technique to estimate flexural power flow in uniform beams and plates. In this case, he proposed the use of strain gages, and rotational accelerometers to approximate the rotational component of intensity (the product of the moment times the rotational velocity). Pavic (1976) and others have shown that away from discontinuities the power flow is approximately proportional to the time average of the product of the displacement times the rotational velocity. Pavic proposed the use of a finite difference technique that approximates the structural intensity using acceleration measurements (both linear and rotational) at discrete points. McGary (1988) and Downing (1988) have shown how the flexural power flow can be estimated using accelerometers in a spatial array. These techniques typically require transformation into the frequency domain (using a spectrum analyzer), and thus do not lend themselves to a time domain estimation. Moreover, these techniques inherently approximate non-measurable field quantities using the finite difference technique. These techniques tend to be accurate where the finite difference is small compared to a wavelength in the structure. These (low order) finite difference approximations tend to be inaccurate for frequencies where the sensor spacing is significant with respect to a wavelength.

Unfortunately, when field variables are differenced with small finite difference spacing, the methods are then sensitive to phase errors between the sensors, especially for closely spaced sensors.

As is discussed in Chapter 2, for beam like structures, traveling wave amplitudes and net power flow are inherently related. A harmonic traveling wave (whether flexural or extensional) can be thought of as the carrier of energy in that direction. For thin beams and plates, the magnitude of energy carried by the wave form is proportional to the square of the displacement amplitude of the wave. For instance if the amplitude of a traveling flexural wave is doubled, then the energy associated with the wave increases by a factor of four. Also, a beam responding with equal amplitude, opposite traveling waves (irrespective of their complex phase relationship) carries zero net energy. Flexural power flow in a beam is comprised of two portions. The first is the time averaged complex product of the shear force and the out-of-plane velocity, and the second is the time averaged complex product of the flexural moment and the rotational velocity. However, the shear force, flexural moment, out-of-plane velocity and rotational velocity are all directly related to the beams out-of-plane displacement. Thus, it is not necessary to measure each one of these terms if the displacement function (wave complex amplitudes for example) can be measured or estimated, and a model of the system is known. In terms of

feedforward control of power flow, only the wave amplitudes need to be observed.

Currently it is impossible to directly measure traveling wave amplitudes, as most vibrational measurement devices measure the net superposition of the wave field acting at a point (or over a distributed area). Observing these wave types thus must come from the mathematical manipulation of quantities that can be measured, and that contain sufficiently unique temporal and spatial information. Determination of traveling waves from the measurable quantities can thus be thought of as a transformation of coordinate systems. This coordinate transformation throughout this dissertation is termed "wave vector filtering" because it provides the vector direction as well as complex amplitude of the traveling waves. For example, the transformation can take place from the out-of-plane acceleration coordinate frame (measured with accelerometers) to that of traveling flexural waves.

Fahy (1985) presented the use of a spatial based Fourier integral transform known as the wavenumber transform. The integral in discretized (numerical) form would allow the use of experimentally measured structural responses to determine wavenumber components. Pines and von Flotow (1990) analyzed the observation of traveling waves in one dimensional structures. In their work,

they formulated the wave vector filtering problem for both flexural and extensional modes with spatially collocated and non-collocated measurement quantities. Also, they discussed the effects of causality on the possible solution of the problem. Pines and von Flotow (1990) presented these transformation matrices, but did not address how these transformation matrices are solved (or approximated over some frequency range) in the time domain. As it is often difficult to measure a sufficient number of different field variables (i.e. moment and slope) at a single point the non-collocated measurement portion of there work is of particular interest.

Elliott (1981) proposed a method of measuring absorption coefficients for plane waves in air. Elliott proposed using two microphones spaced a known distance apart to determine the traveling wave amplitudes using a finite difference technique. From these two microphones the average pressure was assumed to be the sum of the two microphones, and the particle velocity was proportional to the integral of the difference of the two microphones. These quantities were summed and differenced with the appropriate gain factors to estimate the traveling waves. The entire wave vector filtering can be accomplished using analog circuits (summation, difference, and integration). The basis of the method provides real time wave estimation, but is limited to only non-dispersive media. The method is limited in terms of frequency to values where the

microphone spacing is close relative to the respective wavelength (because of the finite difference approximation).

Gibbs et al. (1992(b), and 1993) have developed a method to approximately filter the traveling waves in both dispersive and non-dispersive media using a time domain technique. This method uses two non-collocated measurements in conjunction with a digital filter network to estimate the complex traveling wave amplitudes for responses with band limited spectra. This method is termed "real time" because it can be implemented using digital filters to provide an instantaneous time estimate. Utilizing modern computing technology, this time domain technique can be implemented to provide accurate instantaneous estimation of the vibrational power flow. Some previous techniques require frequency domain information and thus are hampered by the inherent averaging and fast Fourier transform (FFT) overhead. Thus in terms of the active control of flexural and extensional vibration, the wave vector filter is an extremely useful technique to observe and control the traveling waves (and power flow). This method is presented in detail in Chapter 2.

1.5 Scope and Objectives

The objective of this work is to sense and adaptively control, simultaneously,

the flexural and extensional waves, and hence power flow, in thin beams using piezoelectric actuators and sensors. In order to control the total power flow, it is necessary to have a control input(s) which effectively excite the structure in both flexure and extension. The study of the excitation of beams required the development of a new analytical model for the excitation of flexural and extensional waves in thin beams by a single actuator bonded to the surface. Controlling the flexural and extensional power flow in beam also requires accurate wave sensing. Various sensing techniques were addressed, and a new system was developed to perform real time wave vector filtering of flexural and extensional traveling waves in beams which is required to control the power flow in certain beam configurations. These real time wave estimates can then be used as error functions of an adaptive feedforward controller. The objective of this work is to determine the performance of the various actuator and sensing configurations in controlling flexural and extensional power flow in thin beams.

The actuator and sensor models form a basis for which the optimal control of flexural and extensional power flow can be studied. A theoretical study is performed in which semi-infinite and finite beams are excited by a primary point force at an angle to the neutral axis of the beam (exciting both flexural and extensional motion), and optimally controlled by a pair of axially collocated,

symmetrically mounted, and independently driven piezoelectric actuators. This beam configuration is representative of a typical beam configuration, and the results can be extended to other beam systems. The theoretical work is then compared with experimental results to validate the theoretical concepts.

The control algorithm used exclusively in the experimental portion of the work was a multi-channel version (Elliott et al., 1987) of the filtered-x LMS algorithm (Widrow and Stearns, 1985). This algorithm is a feedforward algorithm that is extremely effective for steady state narrow band control, and can slowly track both frequency and physical system changes. It does not require detailed modeling of the plant as in contrast to state space feedback control methods. Note however, that the wave vector filtering scheme provides the error signals for the filtered-x LMS algorithm, and does require a theoretical model of the flexural and extensional wavenumbers as a function of frequency in the structure. In all the experimental studies, the multi-channel filtered-x LMS algorithm was implemented on an TMS320C25 signal processing board resident in an IBM compatible personal computer.

1.6 Organization

The theoretical developments for the actuator and sensor models discussed

previously are presented in detail in Chapter 2. Chapter 2 also covers the theoretical excitation of both semi-infinite and finite beams (with a variable termination) excited by both a point force at the free end, and by one or two asymmetrically bonded piezoelectric actuators located at some arbitrary point. These excitation results are used to determine the simultaneous optimal control of both the flexural and extensional power flow where the force acts as the primary (noise) disturbance and the piezoelectric actuators are the secondary (control) input. Chapter 3 first presents the heart of the adaptive LMS algorithm: the adaptive FIR filter. Later in Chapter 3, the filter is combined into a multiple input/output network to form the multi-channel filtered-x LMS algorithm. Finally in Chapter 3, the wave vector filter scheme is merged with the adaptive controller to form an adaptive power controller. Chapter 4 first presents the techniques to determine the wave response of the beam and subsequent power flow using both the laser vibrometer and strain gage results. The remaining portion of Chapter 4 presents the results of three series of experiments showing various stages of development of adaptive power flow control. Chapter 5 summarizes the important new understanding and developments concluded from this work and provides some recommendations for future work.

Chapter 2

Theoretical Developments

In order to control flexural and extensional energy transmission in beams, it is necessary to adequately excite, and sense these modes of vibration. The first part of this chapter is dedicated to the development of an asymmetric piezoelectric actuator model. This model is used to describe how a single piezoelectric actuator when bonded to surface of a beam excites both flexural and extensional motion. In the second part, the theory for piezoelectric surface strain sensors will be presented, and as it will be shown later, these sensors form an integral part of the wave vector filtering scheme. Since it is the premise of this work to examine and control the energy transmission from a wave approach rather than a modal approach, it is necessary to be able to observe and subsequently control the traveling waves in the beam. A real time wave vector filtering scheme was developed in order to estimate the flexural and extensional traveling waves in a beam in real time. The exact details of the relation between the traveling waves in a beam and the resulting power flow will be presented later, but suffice it to say that minimization of the traveling waves in a beam will also minimize the power flow.

The remaining portion of this chapter will be devoted to demonstrating the actuator and sensor techniques, and how these techniques are used to control power flow in both finite (modally responding) and semi-infinite beams.

2.1 Asymmetric Piezoelectric Actuator Model

An approximate analytical model is developed for the excitation of a thin beam by a single piezoelectric actuator bonded to the surface of the beam. Throughout this dissertation, the term asymmetric actuator is used for a single piezoelectric actuator bonded to the surface of the beam. The premise of this work is to investigate the excitation of beams by piezoelectric actuators on a more fundamental level than previous work, and then use the asymmetric model to predict a wave response, rather than a modal response, on more complicated structure/actuator systems. It is assumed that the single surface mounted piezoelectric actuator simultaneously excites both flexural and extensional motion in beams whose relative amplitudes are functions of beam/actuator configuration and properties.

It is thus the thrust of this section to develop new analytical relations based on wave approaches for the excitation of long thin beams by a single asymmetric piezoceramic element. The approach is to consider that the single

piezoceramic actuator drives both extensional and flexural waves in the beam. The strain field under the piezoceramic element is thus, by superposition, the sum of the two wave components, and is coupled by the actuator. Once the waves leave the actuator location they are assumed to travel uncoupled in the beam. Similar approaches have been used in analysis of point force excitation of beams by forces which are not normal to the beam surface (Pan and Hansen, 1990). In this case, the normal component of the force is considered to drive the flexural waves while the in-plane component drives extensional waves.

Figure 2.1 shows the strain distribution for a pair of perfectly bonded piezoelectric actuators configured to excite either pure flexure or pure extension as analyzed by (Crawley and Anderson, 1990). In the case of pure flexure, the finite patch effectively acts as equal and opposite line moments acting at its ends, and applied to the beam. In the case of pure extension, the finite patch effectively acts as equal and opposite in-plane point forces acting at the ends of the element on the neutral axes (See Crawley and Anderson, 1990, for the derivation). In the following analysis, it will be shown how the asymmetrically bonded piezoelectric actuator simultaneously produces both extensional and flexural motion in thin beams and how their relative magnitudes are determined by the actuator/beam configuration.

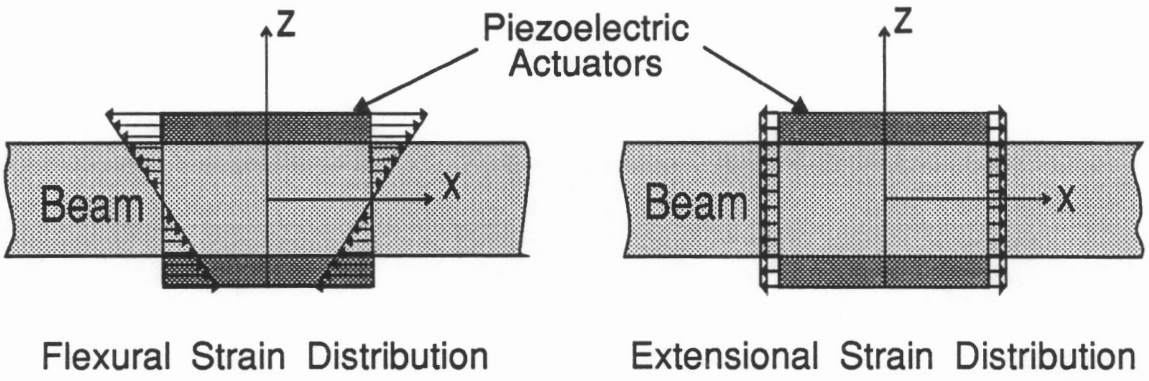

Figure 2.1 Pure Flexural/Extensional Strain Distributions of Symmetrically bonded Piezoelectric Actuators

2.1.1 Asymmetric Piezoelectric Element - Infinite Extent

When excited by an applied voltage, an unconstrained piezoelectric element will strain in all directions. Specifically, consider the piezoelectric element shown in Figure 2.2. Using the terminology of the piezoelectric (PE) material manufacturer, the piezoelectric device is oriented such that the axis number one of the PE is oriented along the x-axis of Figure 2.2 (Piezo Systems, 1987). Axis number two lies along the y direction (perpendicular to the plane of Figure 2.2), and axis three lies along the z direction of Figure 2.2. Piezoelectric elements are excited by applying an electrical voltage along their polarization direction three (the z axis of Figure 2.2). When the piezoelectric actuator is unconstrained, the actuator will strain an amount, ε_{pe}, proportional to the applied voltage as shown in the following relation (where d_{31} is the strain

sensitivity of the material, V is the excitation voltage, and T_a is the material thickness):

$$\varepsilon_{pe} = \frac{d_{31}}{T_a} V \qquad \textbf{(2.1)}$$

The subscript 31 corresponds to strain in direction one from a voltage applied in direction three. For a overview of the history and uses of piezoelectrics the reader is referred to Collins et al. (1990).

For the purpose of this analysis, the single piezoelectric actuator is taken to be a piezoceramic G1195 material (Piezo Systems, 1987) assumed to be perfectly bonded to the beam with zero glue layer thickness, as shown in Figure 2.2 (top). Material G1195 has a d_{31} of 166E-12 m/V. The actuator is also assumed to be infinite in the x direction, and have a thickness, T_a, in the z direction. The beam is infinite in the x direction and has a height of 2h in the z direction. The beam has a modulus of elasticity E_b and an area moment of inertia I.

It is assumed that a plane through the material perpendicular to the neutral axis of the beam remains planar and perpendicular to the neutral axis during deformation. This assumption is equivalent to ignoring shear strains in planes perpendicular to the middle surface of the beam, and is the basis of the

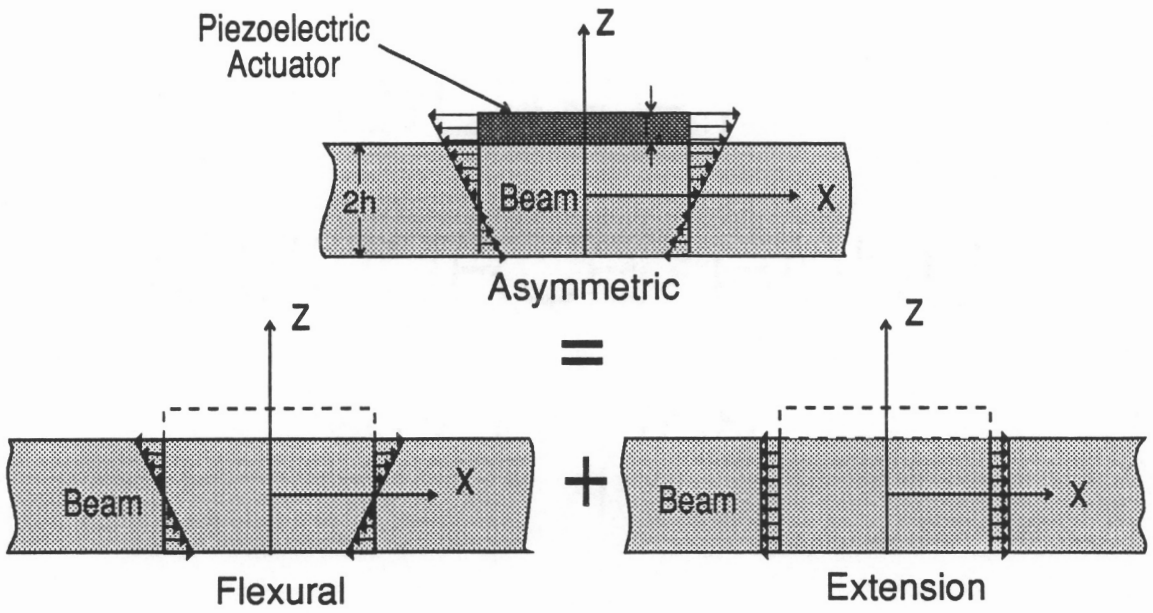

Figure 2.2 Strain Distribution of an Asymmetric Piezoelectric Actuator

Kirchhoff hypothesis of laminate plate theory (Jones, 1975). When a voltage is applied across the transducer in the z direction, the beam/piezoelectric element laminate will have an asymmetric strain distribution as shown in Figure 2.2 (top) based on the assumptions of the Kirchhoff hypothesis.

The in-plane strain distribution as a function of the z coordinate, $\varepsilon(z)$, within the cross section is shown in Figure 2.2 (top), and can be written in the form shown in Equation (2.2), where c is the slope and ε_0 is the ε intercept (the value of $\varepsilon(0)$).

$$\varepsilon(z) = cz + \varepsilon_0 \qquad \textbf{(2.2)}$$

The general linear strain distribution represented by Equation (2.2) can be decomposed into the sum of an anti-symmetric distribution, cz, (i.e. flexural component) about the center of the beam, and a uniform strain distribution, ε_o, (i.e. extensional component) as shown in Figure 2.2 (bottom). The slope, c, can be related to the out-of-plane displacement, w, as follows (Cremer et al., 1973):

$$c = \frac{\partial^2 w}{\partial x^2} \tag{2.3}$$

Using the strain distribution of Figure 2.2 (top) and Hooke's Law, the stress distribution within the beam, $\sigma_b(z)$, is given as follows:

$$\sigma_b(z) = E_b(cz + \varepsilon_o) \tag{2.4}$$

where, E_b is the Young's modulus of the beam. As stated previously, when unconstrained and excited by a voltage, V, the piezoelectric actuator will strain an amount, ε_{pe}, and have an in-plane stress equal to zero. If the actuator is then forced to return to its original state of zero strain (in other words the actuator is fully constrained from movement) while being excited by the voltage, V, a compressive stress will be induced into the actuator in an amount dictated by Hooke's Law as follows:

$$\sigma_{pe}(z) = - E_{pe}(\varepsilon_{pe}) \tag{2.5}$$

Thus when the voltage excited actuator is partially constrained by the beam it

must reach an equilibrium strain state between the fully constrained and unconstrained states. The stress distribution within the coupled piezoceramic actuator, $\sigma_{pe}(z)$, is a function of the unconstrained piezoceramic actuator strain, Young's modulus of the piezoelectric actuator, E_{pe}, and the strain distribution shown in Figure Figure 2.2 (top) as follows:

$$\sigma_{pe}(z) = E_{pe}(cz + \varepsilon_o - \varepsilon_{pe}) \tag{2.6}$$

It is seen in this relation that if the resultant strain state ($cz + \varepsilon_o$) is equal to $+\varepsilon_{pe}$ then the resultant stress would be zero (equal to the unconstrained case), and if the resultant strain state were zero then the stress would be that shown previously in Equation (2.5).

Applying moment equilibrium about the center of the beam produces the relation:

$$\int_{-h}^{h} \sigma_b(z)\, z dz + \int_{h}^{h+T_a} \sigma_{pe}(z)\, z dz = 0 \tag{2.7}$$

Next applying force equilibrium in the x direction is as follows:

$$\int_{-h}^{h} \sigma_b(z)\, dz + \int_{h}^{h+T_a} \sigma_{pe}(z)\, dz = 0 \tag{2.8}$$

After integration Equations (2.7) and (2.8) can be solved for the two unknowns, namely ε_o and c which are presented (after some manipulation) as follows:

$$\varepsilon_0 = K^e \varepsilon_{pe} \tag{2.9}$$

where:

$$K^e = \frac{\left(\frac{T_a^4}{6} + \frac{4E_b}{3E_{pe}} h^3 T_a\right)}{\left[\frac{T_a^4}{6} + \frac{8E_b^2}{3E_{pe}^2} h^4 + \frac{4E_b}{3E_{pe}}(4h^3 T_a + 3h^2 T_a^2 + hT_a^3)\right]}, \tag{2.10}$$

and

$$c = K^f \varepsilon_{pe} \tag{2.11}$$

where:

$$K^f = \frac{T_a}{(2hT_a + T_a^2)}\left[2 - \frac{\left(\frac{2}{3}E_b E_{pe} h T_a^3 + \frac{16E_b^2}{3} h^4 + \frac{1}{3}E_{pe}^2 T_a^4 + \frac{8}{3}E_b E_{pe} h^3 T_a\right)}{\left(\frac{E_{pe}^2 T_a^4}{6} + \frac{8}{3}E_b^2 h^4 + \frac{4}{3}E_b E_{pe}(4h^3 T_a + 3h^2 T_a^2 + hT_a^3)\right)}\right]. \tag{2.12}$$

The general equation of motion of a solid medium in terms of motion in all three coordinate directions is inherently coupled (Cremer et al., 1973). However, as stated in Cremer et al. (1973), if the thickness of the beam is less than a quarter wavelength in the direction of propagation, then the beam motion can be accurately separated into its out-of-plane (flexural) motion and its in-plane (extensional) motion.

The next step is to separate out the flexural and extensional components. The anti-symmetric portion of the strain distribution will induce flexural moments in the beam and will subsequently drive flexural waves. The induced moment distribution in the beam, m(x), is equal to the product of the flexural stiffness, E_bI, times the slope c.

$$m(x) = E_bIc = E_bIK^f\varepsilon_{pe} \tag{2.13}$$

This is the actuator induced moment distribution for a piezoelectric element of infinite extent. Piezoelectric elements used in practice are of finite length. For a finite length element, the piezoelectric stress distribution as shown in Equation (2.6) does not hold at the free edge at the ends of the piezoelectric where the stress must be zero. Liang and Rogers (1989) showed that the actuator stress field is unaffected by the free edge condition up to a region approximately four actuator thicknesses from the boundary. Thus for piezoelectric actuators whose length is much greater than its thickness, the edge effects are assumed negligible. The actuator induced moment distribution shown in Equation (2.13) must be modified to include the finite length. In the proximity of the element the moment distribution is given by Equation (2.13) and zero elsewhere. This is accomplished by using unit step functions, and thus for a finite length element located at $0 < x < L_a$ the induced moment distribution is presented as follows:

$$m(x) = E_b I K^f \varepsilon_{pe} [H(x) - H(x - L_a)] \quad (2.14)$$

where H( ) is the unit step function.

The uniform strain distribution portion, ε_o, will excite purely extensional waves. The uniform strain across the section, $\varepsilon(x)$, is also constant in the x direction and equal to the following:

$$\varepsilon(x) = \varepsilon_o = K^e \varepsilon_{pe} \quad (2.15)$$

Similarly, the actuator induced uniform strain distribution, $\varepsilon(x)$, can be modified to have a value equal to that shown in Equation (2.15) in the proximity of the actuator and zero elsewhere as follows:

$$\varepsilon(x) = K^e \varepsilon_{pe} [H(x) - H(x - L_a)] \quad (2.16)$$

where H( ) is the unit step function.

2.1.1.1 Flexural Equation of Motion

The Euler equation of motion for flexural vibration of the thin beam is given as follows (Cremer et al., 1973):

$$E_b I \frac{d^4 w}{dx^4} - \omega^2 \rho a w = \frac{d^2 m(x)}{dx^2} \quad (2.17)$$

where w is the out-of-plane beam displacement, ω is the circular frequency, ρ is the density of the beam, a is the cross sectional area of the beam, and m(x) is the actuator induced flexural moment distribution. This equation of motion is derived for thin beams which allows the rotary intertia, and transverse shear terms of the Timeshenko equation of motion (Timeshenko, 1955) to be considered negligible. The thin beam assumption is valid for for vibrations were the wavelength is over six times greater than the thickness of the beam (Cremer et al., 1973).

The moment distribution presented previously in Equation (2.14) is substituted into Equation (2.17) and the second partial derivative with respect to x is then taken. The result is presented as follows :

$$E_b I \frac{d^4 w}{dx^4} - \omega^2 \rho a w = E_b I K^f \varepsilon_{pe} [\delta'(x) - \delta'(x - L_a)] \qquad \textbf{(2.18)}$$

Since the above equation is proportional to force, externally applied point force would appear on the right hand side in the form of a delta function, $\delta(x)$, at the point of application. Externally applied moments appear in the equation of motion in the form of the derivative of the delta function, $\delta'(x)$. Thus, the right hand side is equivalent to equal and opposite line moments, proportional to ε_{pe} (where ε_{pe} is related to the applied voltage by Equation (2.1)), and acting at the ends of the element. Equation (2.18) is the equation of motion for flexural

excitation by a single asymmetric piezoelectric actuator. This equation can be applied to a thin beam subjected to arbitrary boundary conditions whether the solution is found using a modal or wave approach.

2.1.1.2 Extensional Equation of Motion

The equation of motion for extensional vibration is given as follows (Cremer et al., 1973):

$$\frac{d^2u}{dx^2} + \frac{\omega^2\rho}{E_b(1-\nu^2)}u = \frac{d\,\varepsilon(x)}{dx} \qquad \textbf{(2.19)}$$

where u is the in-plane beam displacement; ρ is the density; ν is the Poissons ratio; and $\varepsilon(x)$ is the actuator induced in-plane strain distribution. The induced uniform strain distribution previously shown in Equation (2.16) is then substituted into Equation (2.19) which produces the following non-homogenous equation of motion:

$$\frac{d^2u}{dx^2} + \frac{\omega^2\rho}{E_b(1-\nu^2)}u = K^e\varepsilon_{pe}[\delta(x) - \delta(x - L_a)] \qquad \textbf{(2.20)}$$

In this case the finite element can be seen to be equivalent to two equal and opposite line forces acting in the x direction at the ends of the element. Equation (2.20) is the equation of motion for extensional excitation by a single asymmetric piezoelectric actuator. This equation can also be applied to a thin

beam subjected to arbitrary boundary conditions whether the solution is found using a modal or wave approach.

An approximate analysis of excitation of a thin beam by an asymmetric piezoceramic element is presented for the first time. The model is said to be approximate because it does not include edge effects due to the finite length of the piezoelectric, or the inertia effects of the piezoelectric. The analysis shows that the single actuator is mathematically equivalent to equal and opposite moments (i.e. the δ' functions in the out-of-plane force equation), and simultaneously equal and opposite in-plane forces (δ functions in the in-plane displacement equation) located at the ends of the actuator. The relative magnitudes of these forces/moments is shown to be dependent upon the actuator and beam properties, and can be controlled by using a pair of collocated actuators with independent input voltage magnitudes and phases.

The model can then be used to study excitation of both flexural and extensional waves in beams with one or more actuators excited independently. The model can be equally applied to relatively long beam-like structures or finite structures. The work presented here represents an important step because it represents the analytical basis by which simultaneous active control of both flexural and extensional motion in flexible structures can be studied, and optimized.

2.1.2 Application to Infinite Beam Power Flow

In order to demonstrate the usefulness of the asymmetric beam excitation, an infinite beam will be analyzed which has two symmetrically bonded finite piezoceramic actuators as shown in Figure 2.3. The actuators are located with one edge at x=0 and have a length L_a. Each piezoceramic will be treated as a single independent actuator with variable relative complex amplitude in order to study how parameters such as length, relative phase and frequency effect the power flow of the subsequent flexural and extensional waves. Note in this case, since the beam is infinite, waves will be generated in contrast to the modal response of a finite structure. In the previous work the response of the beam structures to excitation by piezoelectric elements was primarily from a modal approach not a wave approach, however, the two situations are inherently related. It is believed that the wave approach allows a better understanding of the coupling between the actuator and beam as it is less restricted by boundary conditions.

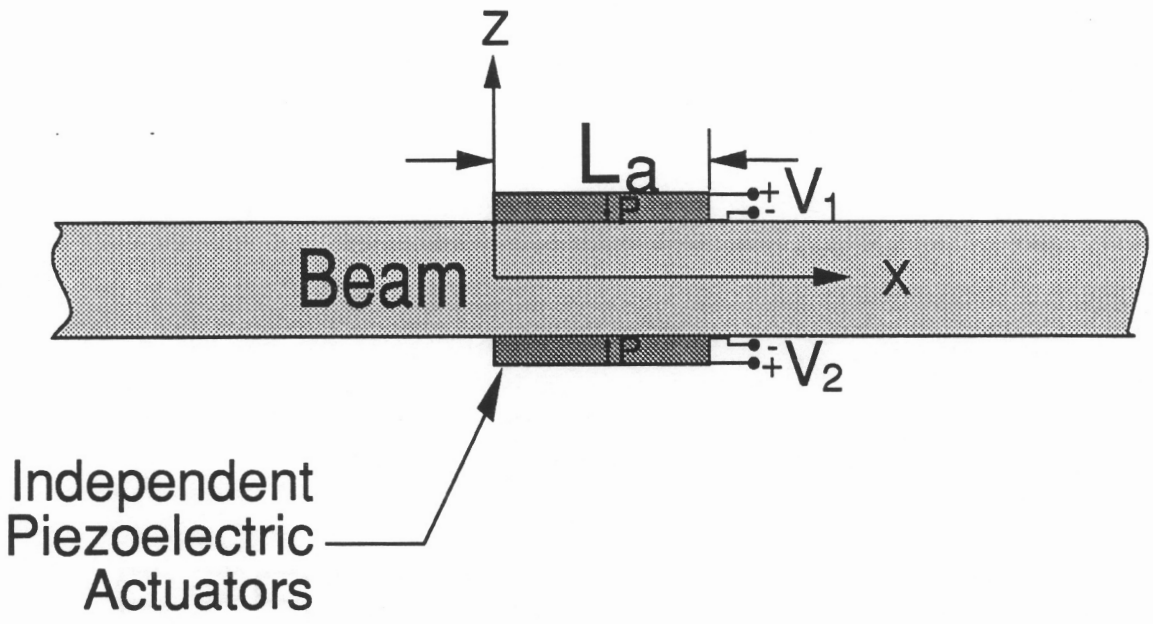

Figure 2.3 Infinite Beam Arrangement with Two Actuators

The flexural equation of motion, Equation (2.18), is solved for each individual element (with excitation voltages V_1 and V_2), and the motion, W(x,t), for the two collocated elements is found by superposition to be (as shown in Appendix A):

$$W(x,t) = \frac{d_{31}K^f(V_1 - V_2)}{4k_f^2 T_a}\left[(1 - e^{k_f L_a})e^{-k_f x} - (1 - e^{-jk_f L_a})e^{jk_f x}\right]e^{-j\omega t} \qquad \textbf{(2.21)}$$

where: ω is the rotational frequency; and k_f is the flexural wavenumber. The power flow for the flexural wave is found by taking the sum of the time averaged dot product of the shear force with the velocity, and the flexural

moment with the rotational velocity (Cremer et al., 1973). The power flow, $P_f(\omega)$, at the frequency of interest was found using the technique presented in Section 2.3.5 and is equal to:

$$P_f(\omega) = \frac{E_b I (K^f)^2 d_{31}^2 \omega}{8 T_a^2 k_f} |V_1 - V_2|^2 (1 - \cos(k_f L_a)) \qquad \textbf{(2.22)}$$

The extensional equation of motion, Equation (2.20) is solved as shown in Appendix A for one element and the displacement, U(x,t), for two collocated elements is found by superposition to be:

$$U(x,t) = -\frac{jK^e d_{31}(V_1 + V_2)}{2k_e T_a}(1 - e^{-jk_e L_a}) e^{jk_e x} e^{-j\omega t} \qquad \textbf{(2.23)}$$

where, k_e is the extensional wavenumber. The power flow for the extensional wave is found by taking the time averaged dot product of the longitudinal force with the longitudinal velocity (Cremer et al., 1973). As outlined in Section 2.3.5 the power flow, $P_e(\omega)$, for the frequency of interest is found to be:

$$P_e(\omega) = \frac{(K^e)^2 d_{31}^2 \omega E_b (1 - \nu^2) a}{4 k_e T_a^2} |V_1 + V_2|^2 (1 - \cos(k_e L_a)) \qquad \textbf{(2.24)}$$

It is interesting to note that in the previous work <u>two</u> pairs of actuators and sensors would have been necessary to excite both forms of motion; one dedicated to purely flexural, and the other dedicated to purely extensional

motion. As will be shown next, simultaneous excitation of both flexural and extensional motion of arbitrary complex amplitudes can be accomplished with a single actuator pair.

A computer algorithm was written to demonstrate asymmetric excitation of an infinite thin beam. The results derived show how both the flexural and extensional power flow in the infinite beam (Equations (2.22) and (2.24)) varies as a function of the magnitude and phase of the inputs V_1 and V_2 (i.e. the degree of asymmetry), as well as the actuator length L_a. The beam for this simulation was considered to be made of standard aluminum and had a height 2h equal to 3.175 mm and a width equal to 7.62 cm.

For the first result the excitation frequency of the piezoceramic actuators is 800 Hz. The length of the piezoceramic actuators is taken as 3.81 cm. The magnitude of V_1 and V_2 is fixed at 400 volts peak to peak. These values are representative of typical applications. The flexural and extensional power flow (dB relative to 10^{-12} Watts) is plotted as a function of the phase between V_1 and V_2 in Figure 2.4. It has been previously stated that when both of the piezoceramics are driven in-phase only an extensional wave is generated and correspondingly only extensional power flow is seen in Figure 2.4 at this phase angle. When the piezoceramics are driven 180 degrees out of phase only a

flexural wave is produced as can be seen in the Figure. For phase angles between these ranges both extensional and flexural waves can be driven simultaneously. The relative magnitude can be determined by choosing the appropriate phase from Figure 2.4.

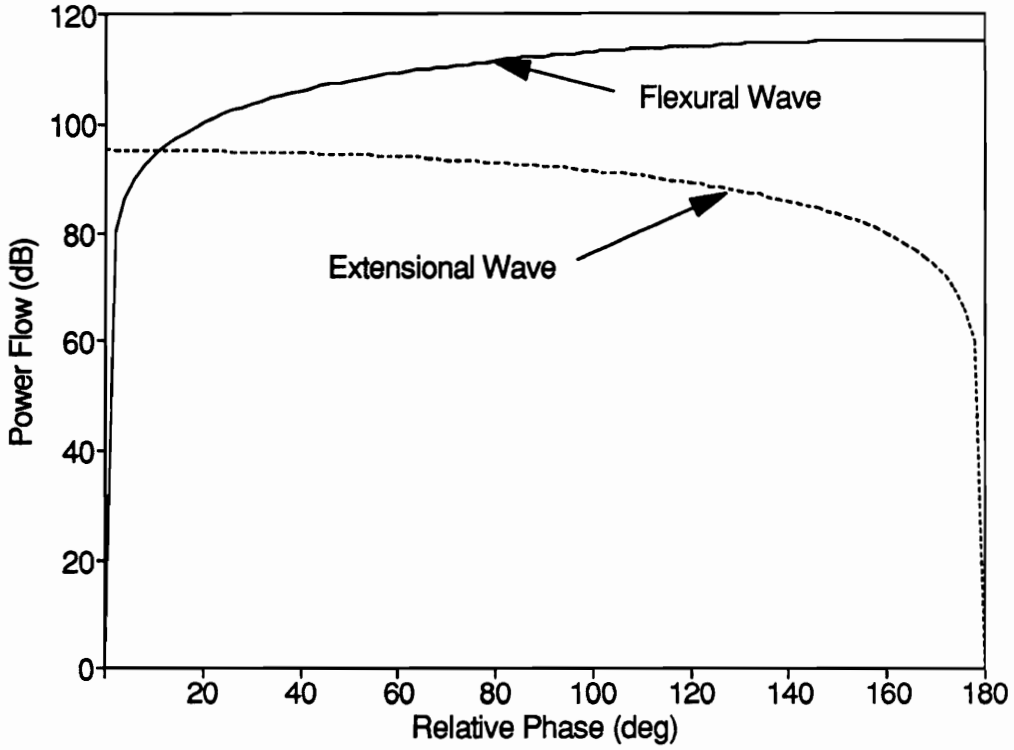

Figure 2.4 Infinite Beam Power Flow, 800 Hz

In the second illustrative result, the excitation frequency is 800 Hz and the magnitudes of the input voltages are again set equal to 400 volts peak to peak.

The phase of V_1 is chosen as 90 degrees ahead of V_2 such that both types of motion are present. The power flow for both the extensional and flexural waves as a function of non-dimensional actuator length is presented in Figure 2.5 where 1.0 is equal to the flexural wavelength, λ_f, at 800 Hz . It can be seen that as the actuator length approaches zero the power flow for both wave types approaches zero. When the actuator length corresponding to half a flexural wavelength at this frequency, the flexural wave is at a maximum because, as shown previously, an individual piezoceramic actuator effectively acts as two opposite phase moment sources externally applied to the beam at the element ends. The waves generated at each end are thus perfectly in-phase. When the actuator is equal to one wavelength, the flexural power flow is a minimum (equal to zero) because the two opposite moment inputs produce wave fields which when superimposed produce zero displacement in the far field. The results imply that there is an optimal length actuator for each frequency of excitation equal to half a wavelength.

The above conclusions can be extended to the response of a system from a modal point of view, as described in the following simple example. If an actuator pair, configured for pure flexure, completely covers the length of a simply supported beam, then the actuator length will be equal to a flexural wavelength for the second mode of vibration. The above wave point of view

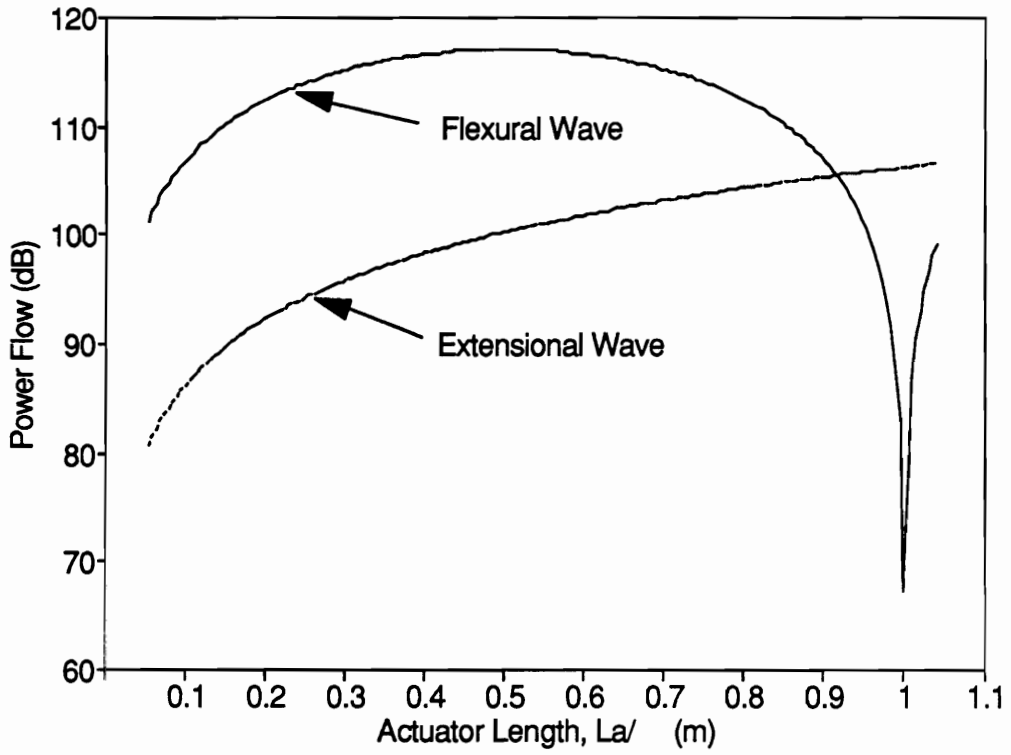

Figure 2.5 Infinite Beam Power Flow, 800 Hz, Relative Phase = 90 deg.

predicts the second mode would not be excited. The corresponding modal point of view is that while the actuator forcing function is uniform over the beam length, the second mode has equal lengths of positive and negative strain distributions and thus will not be excited. This simple example illustrates the equivalence of a wave and modal approach in terms of a finite beam response. The wave approach, however, is more fundamental in that it can be applied to

infinite structures and can be extended to include evanescent nearfields for flexural motion.

From the results it is also apparent, the extensional wave does not have a maximum power flow until the actuator length is significantly increased. This behavior is due to the much higher phase speed of the extensional wave. The far field power flow is a maximum when the actuator is a half wavelength (3.1 m), but this is impractical with the current size availability of piezoceramic actuators. It can be seen that if extensional motion is desired, then it is more efficient to make the actuator as long as possible.

The asymmetric piezoelectric actuator model was used to study excitation of both flexural and extensional waves in beams for various degrees of asymmetry and actuator length. The representative structure in the example is an infinite beam, but the analysis can be equally applied to relatively long beam like structures or finite structures.

2.2 Piezoelectric Surface Strain Sensors

Piezoelectric devices can also be effectively used as sensors on beam like structures. They are typically more sensitive then strain gages. Some

piezoelectric films, for example, are less than 0.03 mm thick, and thus are relatively light weight and can be integrated into the structure more readily then conventional accelerometers. Piezoelectric films (such as PVDF) do not offer a great deal of actuator authority because of their relatively small thickness and low strain coefficient, d_{31}, but they make extremely effective sensors. The charge produced for PVDF sensors is proportional to the integral of the surface strain field of the attached structure. Because of their high compliance they can be either permanently bonded to (using epoxy for example) or embedded into the beam, or they can be attached to the surface of the beam using double sided adhesive film. Note however that embedding PVDF film may adversely effect the structural integrity of the beam. Previously derived models for the piezoelectric output when attached to a beam subjected to both flexural and extensional motion are presented below.

2.2.1 Piezoelectric Flexural Sensor

A relation for the charge output of a single piezoelectric sensor bonded to a two dimensional flexurally responding surface was developed by Lee and Moon (1990), and is presented as follows:

$$q(t) = -\left(h + \frac{T_s}{2}\right) \int_A P_o(x,y)F(x,y)\left(e_{31}\frac{\partial^2 W}{\partial x^2} + e_{32}\frac{\partial^2 W}{\partial y^2} + 2e_{36}\frac{\partial^2 W}{\partial x \partial y}\right)dxdy\, e^{-j\omega t} \quad \textbf{(2.25)}$$

Where q is the charge produced by the piezoelectric film, h is the half beam thickness, T_s is the thickness of the piezoelectric laminae, F is a function depicting the effective surface electrode, P_o is the polarization profile,e_{31}, e_{32}, and e_{36} are the piezoelectric stress per charge constants, and W is the out-of-plane response of the two dimensional laminate.

A schematic of a piezoelectric bonded to the surface of a one dimensional beam is shown in Figure 2.6. For the purpose of the one dimensional beam analysis presented in this dissertation, Equation (2.25) can be reduced to the form of Equation (2.26).

$$q_f(t) = -\left(h + \frac{T_s}{2}\right) L_y e_{31}^o \int_0^{L_s} \frac{d^2 w}{dx^2} dx \quad \textbf{(2.26)}$$

where:

$$P_o(x,y) = F(x,y) = 1, \quad \textbf{(2.27)}$$

and

$$\frac{\partial w}{\partial y} \equiv 0. \qquad (2.28)$$

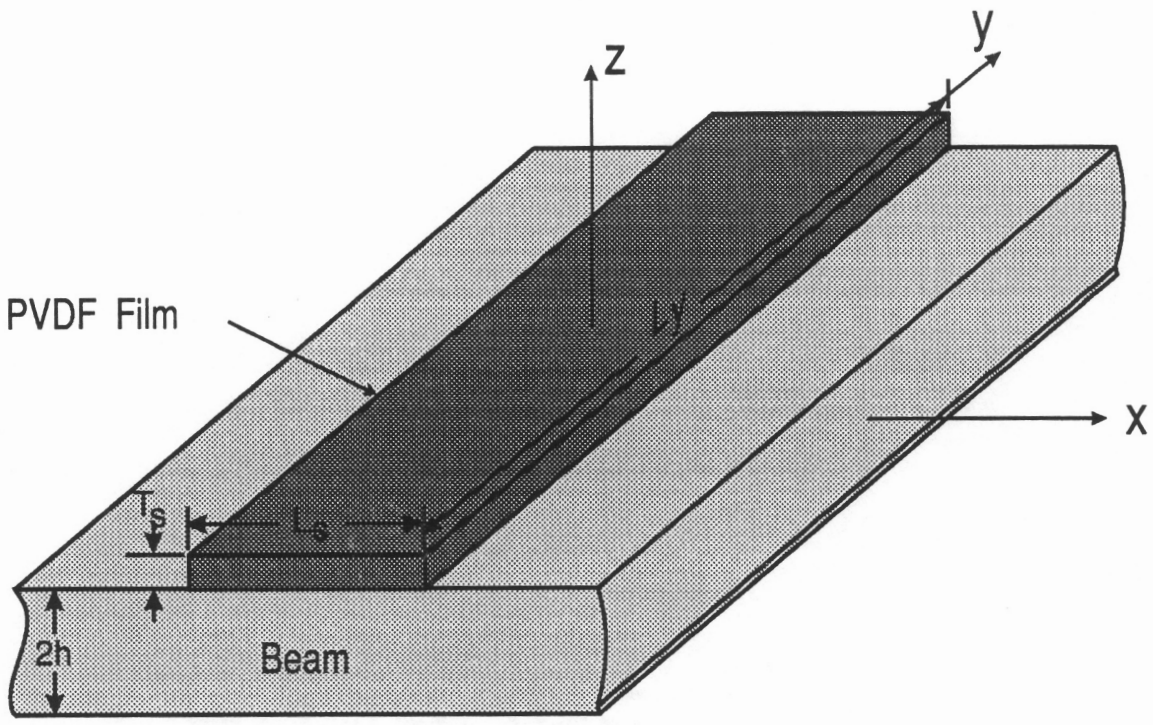

Figure 2.6 Surface Bonded Piezoelectric Sensor

The sensor output in terms of voltage is a function of the capacitance of the sensor and the attached instrumentation. Fortunately the attached instrumentation typically has a low input capacitance and high input impedance, and subsequently the voltage can be found by dividing the charge by the capacitance of the sensor. If the input resistance of the amplifier is low, then the output voltage will drop because the amplifier will significantly load the PVDF. Also, there are companies which manufacture instruments specifically

designed to amplify a charge generating device, and produce a high impedance output voltage (or pre-amp voltage level). These pre-amp voltages are used to send signals (in terms of voltage) between filters, signal conditioners, etc., but carry very little power.

2.2.2 Piezoelectric Extensional Sensor

The response of a piezoelectric sensor bonded to the surface of a one dimensional beam responding in extension as depicted in Figure 2.6, is presented as follows:.

$$q_e(t) = - L_y e_{31}^o \int_0^{L_s} \varepsilon(x)\,dx \qquad (2.29)$$

where $\varepsilon(x)$ is the extensional strain distribution of the beam. Note that we have presented the theoretical sensor charge produced by a PVDF film subjected to flexural and extensional motion in beams. The sensors are thus sensitive to both flexural and extensional motion in beams. Fortunately, two sensors can be arranged to be sensitive to only flexural motion. For instance, if two identical sensors are mounted on opposite sides of the beam, and there outputs are differenced then the resultant output will be proportional to flexural motion only. This can be seen by examining Equations (2.26) and (2.29). As seen in the flexural response of Equation (2.26), the output for one sensor mounted on the top of the beam will be proportional to the quantity $(h + T_s/2)$. However, a

sensor mounted on the bottom of the beam will produce an output proportional to $-(h + T_s/2)$. Thus if these two sensor outputs are differenced (i.e. the output of the top sensor minus the output of the bottom sensor), the resultant output is proportional to $2(h + T_s/2)$. As seen in Equation (2.29), the position of the sensor relative to the neutral axis does not effect the sensors extensional sensitivity, and thus when the two sensors are differenced the resultant extensional output will be zero.

A pair of symmetrically mounted sensors can be made sensitive to only extensional motion by summing their outputs. This result can be shown by a manner similar to the previous proof. We can now use these sensors in conjunction with a digital filter network to estimate traveling waves on a beam as will be discussed in the next section and demonstrated experimentally in Chapter 4.

2.3 Wave Vector Filtering in One Dimensional Media

In order to adaptively control traveling waves on a beam, it is advantageous to have a real time estimate of their complex amplitudes. This method is termed "real time" because it can be implemented using digital filters to provide an instantaneous time estimate. Wave vector filtering, as discussed in this

dissertation, is the real time estimation of the separate positive and negative traveling waves in a one dimensional media using vibrational response quantities of the media. The method provides the vector direction as well as complex amplitude of the traveling waves. If the traveling wave components can be estimated, then these wave estimates can be used as the basis of the cost function of a feedforward adaptive controller.

The following qualitative discussion pertains only to media which is assumed to be vibrating such that it can be described in a single dimension. Any currently available acoustic or vibration sensor can provide an estimate of the total (superposed) property of the media. For instance, a microphone approximately measures the total fluctuating pressure of the air at the microphone location. Since the total response is a superposition of the individual wave types, it is impossible to discriminate say the positive traveling wave from the negative traveling wave without some additional information or multiple microphones. In a mathematical sense, the one dimensional vibrating media spans a certain space. This space can be described using several coordinate frames (just as a three dimensional coordinate frame can be described using cartesian or polar coordinates). The response of the air, for example, can thus be described in terms of the pressure at unique microphone locations (which equals the superposition of the traveling waves at the microphone locations), or the

response can be described by the traveling waves which make up the pressure response. Both of these coordinate frames form a basis which fully describes the motion of the media (in other words, in a mathematical sense they both span the same space). The determination of the traveling waves in the air from measured physical properties (the microphone pressures) can be thought of as a coordinate transformation from the domain of the pressures measurements to the domain of the waves (i.e. from one basis to another).

For instance, if the out-of-plane displacement of a beam is measured at two independent points, then the resolution of traveling flexural waves from these measurements can be considered a coordinate transformation. To even attempt to discriminate among the wave types traveling in a one dimensional media the following minimum criteria is necessary:

1. There must exist two independent measurements of a physical property of the media (i.e. velocity, displacement, strain, etc.) that can be related to the response equation of the media.

2. The relationship between these two independent properties in terms of the response equations of the media must be known.

At frequencies where the above criteria are met, it is conceivable to filter the traveling wave components in the media. In order to develop a better understanding of the concepts, the problem will be examined for a generic media which is vibrating such that a traveling wave response equation can be used. This response equation for a general 1-D system is given as follows:

$$G(x,t) = \left(W_{+}e^{jkx} + W_{-}e^{-jkx}\right)e^{-j\omega t} \tag{2.30}$$

where G is the response of the media (say beam out-of-plane displacement, for example), W_{+} is the positive traveling wave complex amplitude, W_{-} is the negative traveling wave complex amplitude, x is the coordinate along the media, k is the wavenumber, and ω is the excitation frequency. Thus, the response, G_1 and G_2, at two discrete locations, x_1 and x_2, in matrix form is,

$$\begin{bmatrix} G_1 \\ G_2 \end{bmatrix} = \begin{bmatrix} e^{jkx_1} & e^{-jkx_1} \\ e^{jkx_2} & e^{-jkx_2} \end{bmatrix} \begin{bmatrix} W_{+} \\ W_{-} \end{bmatrix} e^{-j\omega t} \tag{2.31}$$

It is therefore desirable to solve Equation (2.31) for wave amplitudes W_{+} and W_{-} in space-time regions where the square matrix is non-singular. This approach has been performed with measured quantities using a spatial version of the Fourier transform known as the wavenumber transform (Fahy, 1985). Also Elliott has performed wave vector filtering for plane acoustic waves in ducts (non-dispersive media) in real time using an analog electrical circuit. His

method does not apply for dispersive media, and is limited to frequencies where the microphone spacing is small compared to a wavelength (because of the limitations of the finite difference approximations used in the method). The major difficulty arises when the solution to this system of equations is desired in real time as opposed to the normal method of solving the system of equations in the frequency domain. The next two sections describe two methods for the solution of Equation (2.31) in both dispersive and non-dispersive media.

2.3.1 Cotangent Method

The following time domain or "real time" solution to the wave vector filtering problem described in the previous section is called the cotangent method. It is the premise of this dissertation to adaptively control flexural and extensional waves in beams, and thus it is only necessary to obtain an estimate proportional to the traveling waves. This estimate can then be used as an error function in an adaptive controller. Since the adaptive controller minimizes the mean square error of the error function (the wave estimates) by modifying the weights of the control filter (as discussed in detail in Chapter 3) the error function does not have to be calibrated. Equation (2.31) can be manipulated using standard Guassian elimination techniques to diagonalize the square matrix of Equation (2.31). A solution to Equation (2.31) is presented in Equation (2.32). The coordinate system was centered at x_1 to simplify the

solution. The location of the origin will affect the absolute phase of the complex values of W_+ and W_-, but not their relative phase (their absolute phase is referenced to the origin which for this solution is at x_1)

$$\begin{bmatrix} (G_1 + G_2) + j\cot(\frac{kx_2}{2})(G_1 - G_2) \\ (G_1 + G_2) - j\cot(\frac{kx_2}{2})(G_1 - G_2) \end{bmatrix} = 4\cos\left(\frac{kx_2}{2}\right)\begin{bmatrix} e^{jk\left(\frac{x_2}{2}\right)} & 0 \\ 0 & e^{-jk\left(\frac{x_2}{2}\right)} \end{bmatrix}\begin{bmatrix} W_+ \\ W_- \end{bmatrix}e^{-j\omega t} \quad \textbf{(2.32)}$$

It can be seen in Equation (2.32) that W_+, and W_- are proportional to the following:

$$\begin{aligned} W_+(t) &\propto (G_1(t) + G_2(t)) + j\cot(\frac{kx_2}{2})(G_1(t) - G_2(t)) \\ W_-(t) &\propto (G_1(t) + G_2(t)) - j\cot(\frac{kx_2}{2})(G_1(t) - G_2(t)) \end{aligned} \quad \textbf{(2.33)}$$

The solution presented in Equations (2.32) and (2.33) is shown in the schematic of Figure 2.7. If measurement points one and two are time domain signals, then W_+ and W_- can be estimated in real time provided the cotangent function shown in Figure 2.7 can be approximated. If the actual wave amplitudes are desired then it would be necessary to include a model of the cosine and e^{jkx2} portions of Equation (2.32) using a digital filter (for example) which is much more difficult.

In the previous discussion, the Cotangent Method was presented for a generic media. It will now be shown how this method is applied to the sensing and control of flexural motion in thin beams.

2.3.2 Flexural Wave Filtering Using the Cotangent Method

In a region of the beam far enough away from discontinuities such that there is only a traveling wave response, the displacement response of the beam can be represented as follows:

$$W(x,t) = \left(Ae^{jk_f x} + Be^{-jk_f x}\right)e^{-j\omega t} \tag{2.34}$$

where W is the total out-of-plane beam response, k_f is the flexural wavenumber, and ω is the harmonic response frequency. In this example four PVDF strips are mounted on the beam in symmetric pairs and spaced apart by a distance L_{fs} as shown in Figure 2.8. Substituting the flexural response of Equation (2.34) into the piezoelectric charge response shown in Equation (2.26), for the given configuration, and integrating produces the following system of equations for the charge produced by the PVDF sensors due only to flexural motion:

$$
\begin{aligned}
q_3(t) &= -2\left(h + \frac{T_s}{2}\right)e^{o}_{31}L_y k_f \sin\left(\frac{k_f L_s}{2}\right)\left[A + B\right]e^{-j\omega t} \\
q_4(t) &= 2\left(h + \frac{T_s}{2}\right)e^{o}_{31}L_y k_f \sin\left(\frac{k_f L_s}{2}\right)\left[A + B\right]e^{-j\omega t} \\
q_5(t) &= -2\left(h + \frac{T_s}{2}\right)e^{o}_{31}L_y k_f \sin\left(\frac{k_f L_s}{2}\right)\left[Ae^{jk_f L_{fs}} + Be^{-jk_f L_{fs}}\right]e^{-j\omega t} \\
q_6(t) &= 2\left(h + \frac{T_s}{2}\right)e^{o}_{31}L_y k_f \sin\left(\frac{k_f L_s}{2}\right)\left[Ae^{jk_f L_{fs}} + Be^{-jk_f L_{fs}}\right]e^{-j\omega t}
\end{aligned}
\tag{2.35}
$$

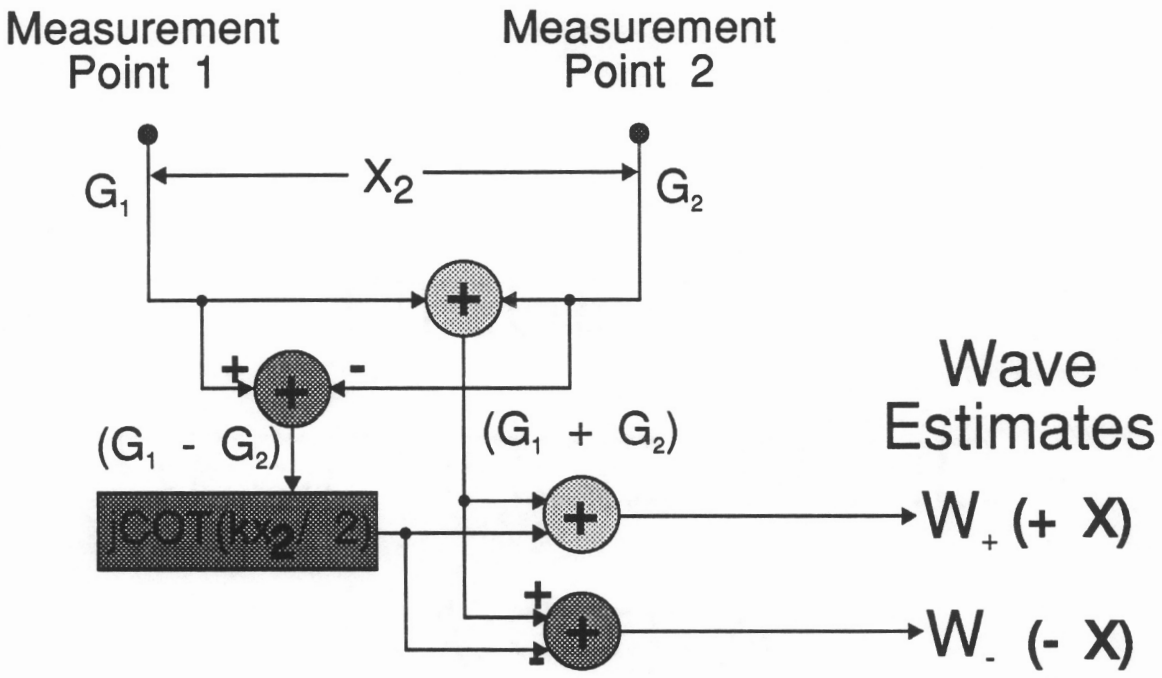

Figure 2.7 Block Diagram of Cotangent Method

In the system of Equations (2.35), q_i, is the output of the i^{th} sensor as shown in Figure 2.8. Note that the sine term of Equation (2.35) effectively acts as a

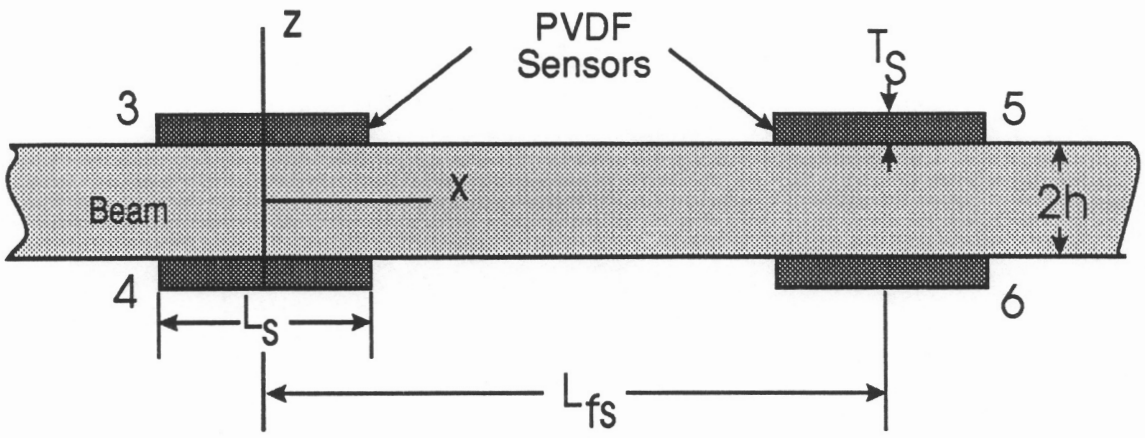

Figure 2.8 Sensor Arrangement for Flexural Wave Vector Filtering

windowing function whose sensitivity increases with frequency. As shown in Figure 2.8, the sensor length, L_s, must be less than the sensor spacing, L_{fs}. As will be discussed in detail later, L_{fs} is restricted to be less than half a wavelength at the Nyquist frequency of the digital filter network to be used in this filtering scheme. If L_s is chosen to be much less than L_{fs} then the sine function can be approximated as $(k_f L_s/2)$, and thus the windowing sensitivity is proportional to ω (as there would be a factor of k_f^2 in Equation (2.35)). By inspection of Equation (2.26), and (2.29) it can be seen that the charge produced by a piezoelectric sensor (in terms of flexure) on the upper surface of a beam is the opposite sign as that produced by an equivalent sensor mounted on the lower surface of the beam. This result can also be seen in Equation (2.35) for sensors 5 and 6, for instance. In contrast, by inspection of Equation

(2.26),and (2.29), the charge produced by a piezoelectric sensor (in terms of extension) on the upper surface of a beam is the same sign as that produced by an equivalent sensor mounted on the lower surface of the beam. Therefore, to resolve solely flexural information, the signals of two symmetrically bonded, and otherwise equivalent piezoelectric sensors will be differenced to eliminate contributions of extensional motion. To resolve only extensional information, the signals of two symmetrically bonded, and otherwise equivalent piezoelectric sensors will be summed to eliminate contributions of flexural motion. For flexural motion the two new derived signals will be:

$$\begin{aligned} q_{f34}(t) &= q_3(t) - q_4(t) \\ q_{f56}(t) &= q_5(t) - q_6(t) \end{aligned} \qquad \textbf{(2.36)}$$

Equation (2.35) can be rewritten in terms of the new quantities in matrix form as follows:

$$\begin{bmatrix} q_{f34}(t) \\ q_{f56}(t) \end{bmatrix} = -4\left(h + \frac{T_s}{2}\right) e_{31}^{o} L_y k_f \sin\left(\frac{k_f L_s}{2}\right) \begin{bmatrix} 1 & 1 \\ e^{jk_f L_{fs}} & e^{-jk_f L_{fs}} \end{bmatrix} \begin{bmatrix} A \\ B \end{bmatrix} e^{-j\omega t} \qquad \textbf{(2.37)}$$

Note that the preceding equation is simply a specific example of the general form of Equation (2.31). The above relation is then solved using the Cotangent Method and is presented as follows:

$$\begin{bmatrix} (q_{f34}+q_{f56}) + j\cot\left(\frac{k_f L_{fs}}{2}\right)(q_{f34}-q_{f56}) \\ (q_{f34}+q_{f56}) - j\cot\left(\frac{k_f L_{fs}}{2}\right)(q_{f34}-q_{f56}) \end{bmatrix} = \tag{2.38}$$

$$-16\left(h+\frac{T_s}{2}\right)e_{31}^{o} L_y k_f \sin\left(\frac{k_f L_s}{2}\right)\cos\left(\frac{k_f L_{fs}}{2}\right)\begin{bmatrix} e^{j\left(\frac{k_f L_{fs}}{2}\right)} & 0 \\ 0 & e^{-j\left(\frac{k_f L_{fs}}{2}\right)} \end{bmatrix}\begin{bmatrix} A \\ B \end{bmatrix} e^{-j\omega t}$$

The solution is shown in the schematic of Figure 2.9. As before, the top equation is proportional to the positive traveling wave, A, and the bottom equation is proportional to the negative traveling wave, B. The difficulty arises now in determining a way to produce the A and B wave estimates in real time. As will be shown, the cotangent box shown in Figure 2.9 can be approximated with a infinite impulse response filter (IIR) of three coefficients. The filter coefficients were determined using a subroutine called invfreqz of Matlab and are shown in Figure 2.10 (Math Works, 1987). Invfreqz produces a n^{th} order IIR that in a least mean square sense matches a desired frequency response. In this example, the beam and sensors had the properties shown in Table 2.1. The desired response was defined by the cotangent function at discrete frequencies from 500 Hz to 1500 Hz every 10 Hz, and the sample rate was chosen to be 5300 Hz (due to experimental implementation limitation discussed later in Chapter 4). A plot of the actual frequency response of the IIR filter

determined by Matlab versus the desired transfer function is presented in Figure 2.10. It is seen that the desired and IIR filter responses agree reasonably well (maximum variance of 0.2 dB) for frequencies between 500 Hz and 1500 Hz. If a filter network comprising the IIR plus the remaining mathematics shown in Equation (2.38), and Figure 2.8 can be constructed, then the A and B wave components can be estimated within the accuracy of the ability of the IIR filter to represent the cotangent function or (0.2 dB), in the frequency range shown.

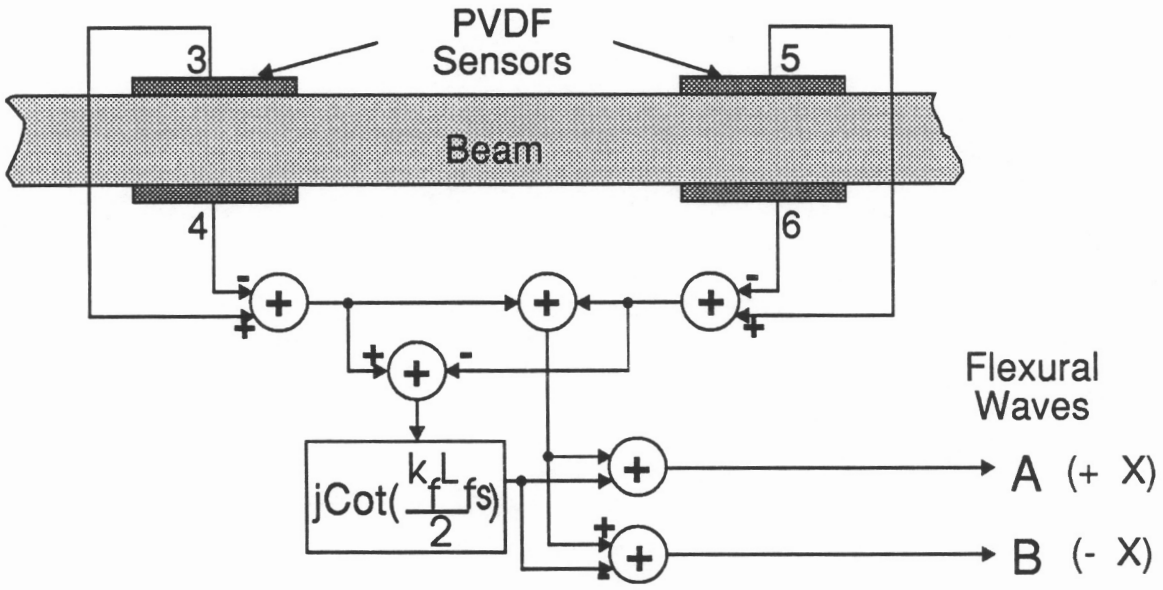

Figure 2.9 Flexural Wave Vector Filter Schematic

Note that the example shown in this section was for flexural waves which have a dispersive nature, but the method will also apply to motions that are non-

Table 2.1 Material Properties of Sensor and Beam

Name	Symbol	Value	Units
PVDF Material			
Piezoelectric Stress Coefficient	e_{31}	65.3E-3	m/V
Density	ρ	1780	kg/m^3
Elastic Modulus	E_{11}	2.0E+9	N/m^2
thickness	T_a	0.1778	mm
length	L_a	3.81	cm
Beam Material			
Density	ρ	2700	kg/m^3
Elastic Modulus	E_b	7.1E+10	N/m^2
thickness	2h	3.175	mm
width	L_y	7.62	cm

dispersive (such as extensional motion in beams). As will be shown in the next section, there is an even simpler and more accurate method of wave vector filtering for non-dispersive media.

2.3.3 Time Delay Method

The following solution to the wave vector filtering problem described in Section 2.3 is called the time delay method. A particular solution to Equation (2.31) is

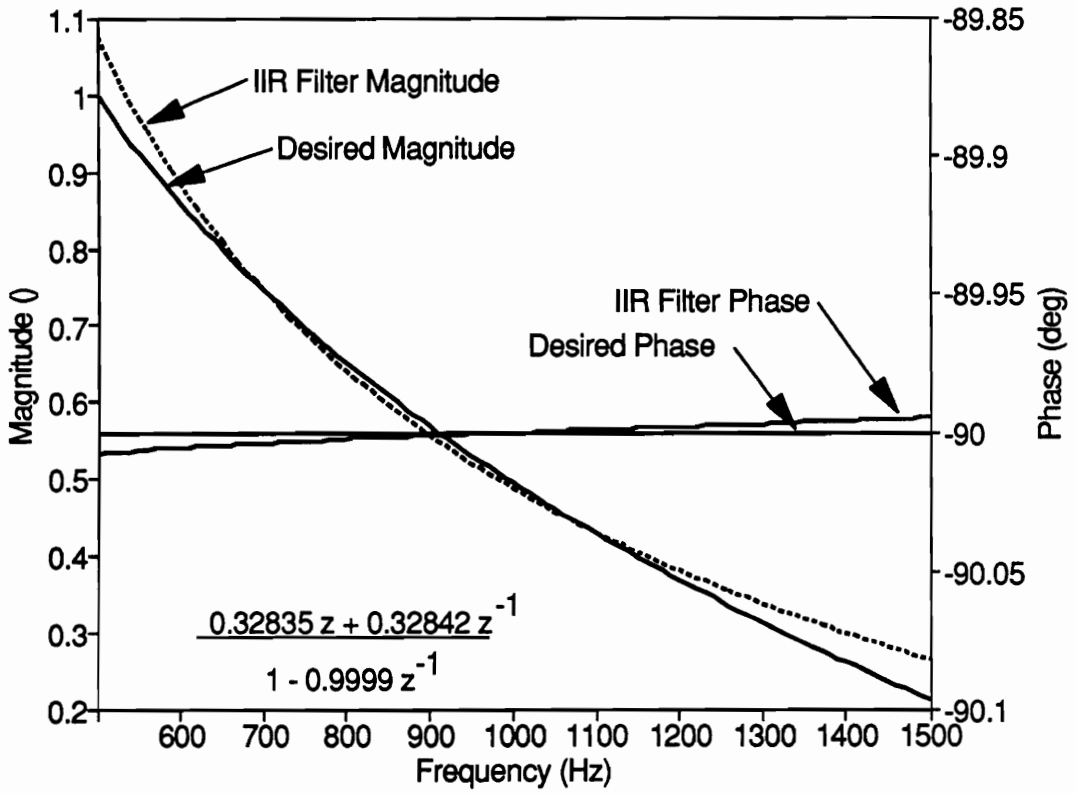

Figure 2.10 Frequency Response of the desired and actual IIR filter

presented in Equation (2.39). X_1 was arbitrarily set to zero to simplify the solution.

$$\begin{bmatrix} G_1 - G_2 e^{jkx_2} \\ G_2 - G_1 e^{jkx_2} \end{bmatrix} = \begin{bmatrix} (1 - e^{j2kx_2}) & 0 \\ 0 & j\sin(kx_2) \end{bmatrix} \begin{bmatrix} W_+ \\ W_- \end{bmatrix} e^{-j\omega t} \qquad \textbf{(2.39)}$$

It is the premise of this dissertation to adaptively control flexural and extensional waves in beams, and thus it is only necessary to obtain an estimate proportional to the traveling wave amplitudes. This estimate can then be used as an error function in an adaptive controller, and can be used to observe relative attenuation levels. Since the off diagonal terms of Equation (2.39) are zero the top entry of the left side vector is proportional to W_+, and the bottom entry of the left side vector is proportional to W_- or as reiterated below:

$$W_+(t) \propto G_1(t) - G_2(t)e^{jkx_2}$$
$$W_-(t) \propto G_2(t) - G_1(t)e^{jkx_2} \qquad \textbf{(2.40)}$$

The solution presented in Equations (2.39) and (2.40) is shown diagrammatically in the schematic of Figure 2.11. If measurement points one and two are real time signals, then W_+ and W_- can be estimated in real time provided the functions described in Equation (2.40) can be approximated.

In the previous discussion, the Time Delay Method was presented for a generic media. It will now be shown how this method is applied to the sensing and control of extensional motion in thin beams.

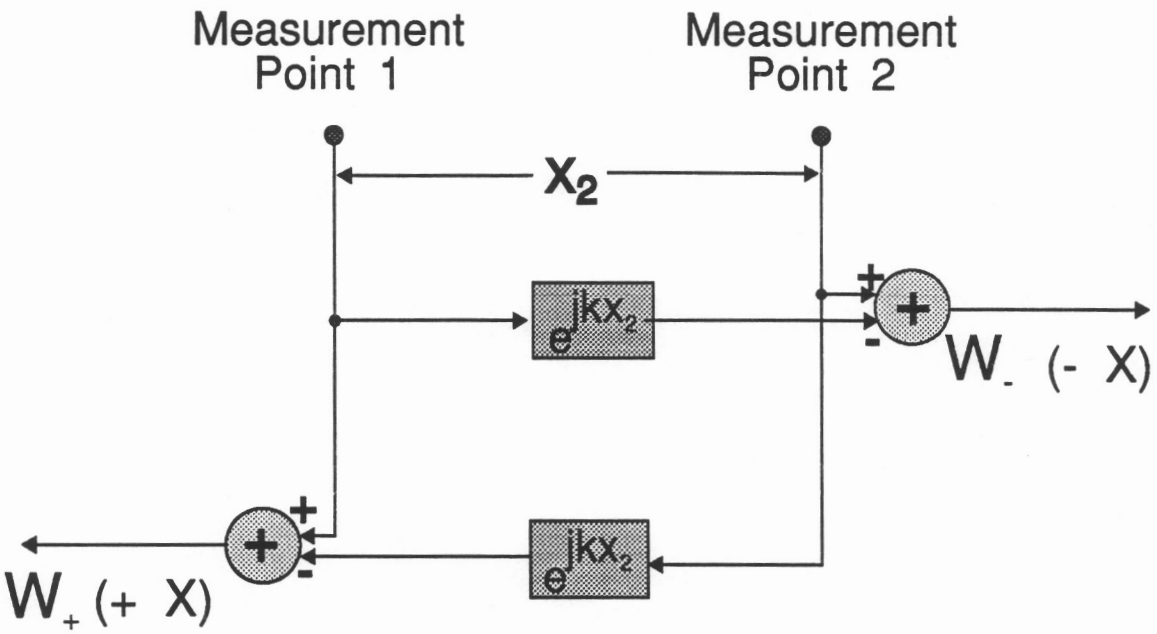

Figure 2.11 Block Diagram of Time Delay Method

2.3.4 Extensional Wave Filtering using the Time Delay Method

In a region of the beam away from discontinuities, the in-plane displacement response of the beam can be presented as follows:

$$U(x,t) = \left(Ee^{jk_e x} + Fe^{-jk_e x}\right)e^{-j\omega t} \qquad (2.41)$$

where U is the total in-plane beam displacement, k_e is the extensional wavenumber, E is the positive traveling extensional wave, F is the negative traveling extensional wave, and ω is harmonic response frequency. In this example four PVDF strips are mounted on the beam in symmetric pairs and

spaced apart by a distance L_{es} as shown in Figure 2.12. Substituting the extensional response of Equation (2.41) into the piezoelectric charge response shown in Equation (2.26) for the given configuration and integrating produces the following system of equations for the charge produced by the PVDF sensors.:

$$\begin{aligned}
q_1(t) &= -2je^{o}_{31}L_y \sin\left(\frac{k_e L_s}{2}\right)\left[E + F\right]e^{-j\omega t} \\
q_2(t) &= -2je^{o}_{31}L_y \sin\left(\frac{k_e L_s}{2}\right)\left[E + F\right]e^{-j\omega t} \\
q_5(t) &= -2je^{o}_{31}L_y \sin\left(\frac{k_e L_s}{2}\right)\left[Ee^{jk_e L_{es}} + Fe^{-jk_{ef} L_{es}}\right]e^{-j\omega t} \\
q_6(t) &= -2je^{o}_{31}L_y \sin\left(\frac{k_e L_s}{2}\right)\left[Ee^{jk_e L_{es}} + Fe^{-jk_e L_{es}}\right]e^{-j\omega t}
\end{aligned} \tag{2.42}$$

To resolve only extensional information (as described previously in Section 2.2.2), the signal of two symmetrically bonded, and otherwise equivalent piezoelectric sensors will be summed to eliminate contributions of flexural motion. For extensional motion, the two new derived signals will be:

$$\begin{aligned}
q_{e12}(t) &= q_1(t) + q_2(t) \\
q_{e56}(t) &= q_5(t) + q_6(t)
\end{aligned} \tag{2.43}$$

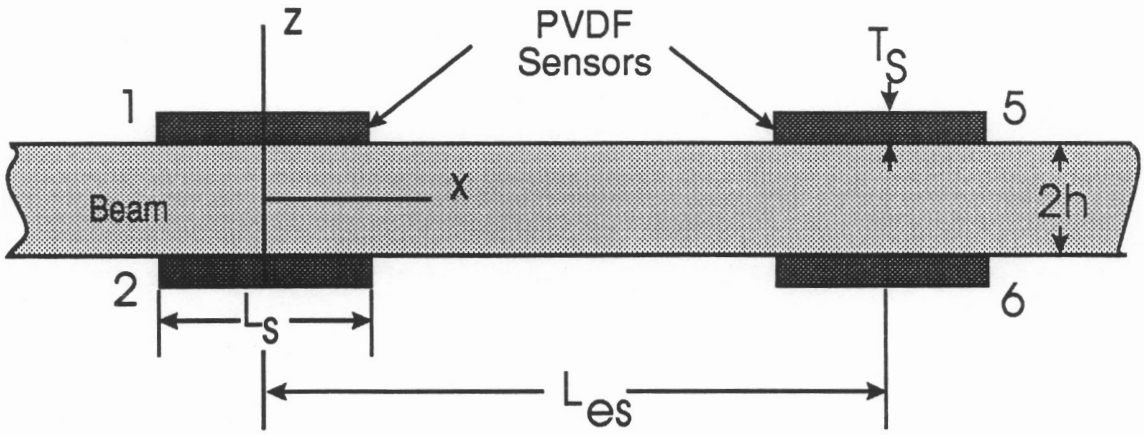

Figure 2.12 Sensor Arrangement for Extensional Wave Vector Filtering

It should be noted that it is critical that all sensors have the same sensitivity. If this is not the case, then the sensitivities should be adjusted accordingly (by amplifier gains or digitally in software). Equation (2.42) can be rewritten in terms of the new quantities in matrix form as follows:

$$\begin{bmatrix} q_{e12} \\ q_{e56} \end{bmatrix} = -4e_{31}^{o} L_y \sin\left(\frac{k_e L_s}{2}\right) \begin{bmatrix} 1 & 1 \\ e^{jk_e L_{es}} & e^{-jk_e L_{es}} \end{bmatrix} \begin{bmatrix} E \\ F \end{bmatrix} e^{-j\omega t} \qquad \textbf{(2.44)}$$

Note that the preceding equation is just a specific example of the general form of Equation (2.31). The above relation is then solved using the Time Delay Method and is presented as follows:

$$\begin{bmatrix} q_{e12} - q_{e56}e^{jk_eL_{es}} \\ q_{e56} - q_{e12}e^{jk_eL_{es}} \end{bmatrix} = -4e_{31}^{o}L_y\sin\left(\frac{k_eL_s}{2}\right)\begin{bmatrix} (1 - e^{j2k_eL_{es}}) & 0 \\ 0 & j\sin(k_eL_{es}) \end{bmatrix}\begin{bmatrix} E \\ F \end{bmatrix}e^{-j\omega t} \quad \textbf{(2.45)}$$

The solution is shown in the schematic of Figure 2.13. The difficulty arises now in determining a way to produce the E and F wave estimates in real time. However, if the sensors are discretely sampled at some sample rate, and are spaced such that they are a full wavelength apart at the sample rate frequency, then a pure time delay (represented by a [0 1] finite impulse response filter) will exactly produce the relationship desired in Equation (2.40) and (2.45). In effect, the dispersion relation that occurs physically within the beam corresponds directly with that which occurs within the FIR filter. In other words, the frequency response between two points on the beam are equated to the frequency response of the FIR filter as follows:

$$e^{jk_eL_{es}} = e^{j\omega\Delta t} \quad \textbf{(2.46)}$$

Where Δt is the sample period and L_{es} is the sensor spacing. In this example, the beam and sensors have the properties shown in Table 2.1. It is rather interesting that a simple pure time delay FIR filter is the key to an exact model to transform from extensional motion at discrete points to traveling wave amplitudes in real time for broadband excitation (up to the Nyquist frequency).

Note that the example shown in this section was for extensional waves which have a non-dispersive nature. A similar approach could be used successfully to model any media which has a non-dispersive behavior (or nearly non-dispersive behavior over a certain frequency range).

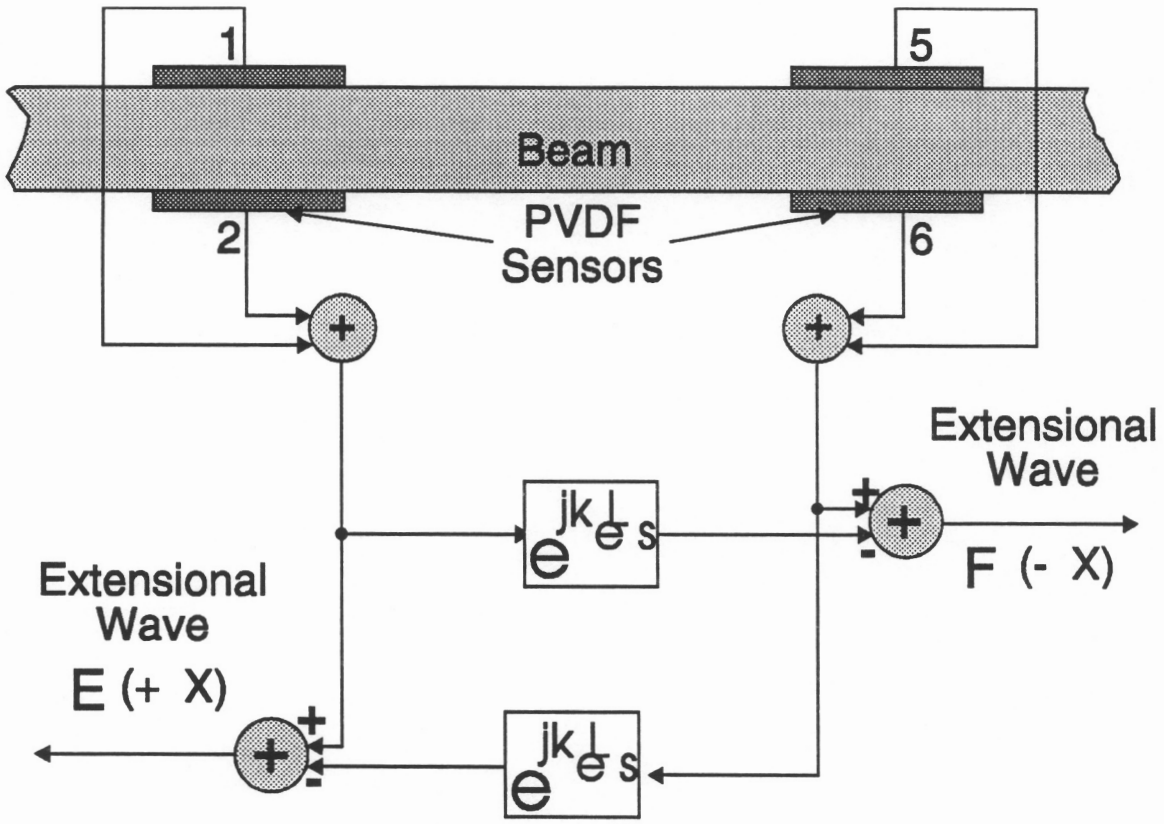

Figure 2.13 Extensional Wave Vector Filter Schematic

2.3.5 Correlation of Wave Filtering to Power Flow

Let us assume a certain section of a beam is responding in flexural motion as follows:

$$W(x,t) = (Ae^{jk_f x} + Be^{-jk_f x} + Ce^{k_f x} + De^{-k_f x})e^{-j\omega t} \quad \textbf{(2.47)}$$

where A is the coefficient of the positive traveling wave, B is the coefficient of the negative traveling wave, C is the coefficient of the negative decaying wave (nearfield), and D is the coefficient of the positive decaying wave (nearfield). Here waves C and D correspond the evanescent waves typically concentrated around discontinuities of the beam.

The power flow in this section can be described with the following relation (Cremer et al., 1973):

$$P_f(\omega) = \frac{1}{2}\mathrm{Re}(F_w V_w^* + M\dot{\Theta}^*) \quad \textbf{(2.48)}$$

where F_w is the shear force associated with the out-of-plane displacement, W, V_w is the out-of-plane velocity, M is the internal flexural moment, and Θ is the

rotational velocity. If the displacement function of Equation (2.47) is appropriately substituted into Equation (2.48) then the resulting power flow is found to be (See Appendix B for the derivation):

$$P_f(\omega) = E_b I k_f^3 \omega(|A|^2 - |B|^2 - 2\,\mathrm{imag}(CD^*)) \qquad \textbf{(2.49)}$$

It can be seen in the previous relation that the positive traveling wave, A, is proportional to the square root of the positive traveling power flow, and the negative traveling wave, B, is proportional to the square root of the negative traveling power flow. If the wave amplitude traveling in the positive direction is minimized the energy flow in that direction is also minimized. Note that the nearfields (waves C and D) do not individually contribute to the power flow, but there interaction does contribute. If the nearfields, C and D, are in-phase or out-of-phase then the power flow contribution is zero. Throughout this dissertation the contribution of power flow due to effects of the nearfield interaction found experimentally and theoretically were included but were extremely small. The wave vector filtering discussed previously in this chapter did not include filtering of the evanescent waves, and it did not allow for their presence. The wave vector filtering concept can be expanded to include the

evanescent waves, but would require four independent sensors, and a more complicated digital filter network.

Now let us assume a certain section of a beam is responding in extensional motion as follows:

$$U(x,t) = (Ee^{jk_e x} + Fe^{-jk_e x})e^{-j\omega t} \tag{2.50}$$

where E is the coefficient of the positive traveling wave, and F is the coefficient of the negative traveling wave. The power flow in this section can be described with the following relation (Cremer et al., 1973):

$$P_e(\omega) = \frac{1}{2}Re(F_u V_u^*) \tag{2.51}$$

where F_u is the in-plane force associated with the in-plane displacement U, and V_u is the in-plane velocity. If the displacement function of Equation (2.50) is appropriately substituted into Equation (2.51) then the resulting power flow is found to be (See Appendix B for the derivation):

$$P_e(\omega) = \frac{E_b a k_e \omega}{2}(|E|^2 - |F|^2) \tag{2.52}$$

It can be seen in the previous relation that the positive traveling wave, E, is proportional to the square root of the positive traveling power flow, and the

negative traveling wave, F, is proportional to the square root of the negative traveling power flow. Minimization of the traveling waves will also minimize the power flow. Using the two wave vector filtering techniques outlined in Section 2.3, the flexural and extensional power flow can thus be estimated for a broadband disturbance. It is the thrust of the control strategy to be described later in this chapter and experimentally demonstrated in Chapter 4, to minimize the square of the positive traveling wave component which by inference will minimize the power flow.

2.4 Control of Flexural and Extensional Power Flow in Thin Beams

It is the purpose of the remaining sections of this chapter to analytically demonstrate active control of flexural and extensional power flow in finite and semi-infinite beams. In this section, the flexural and extensional equations of motion are presented. These equations were solved for both semi-infinite, and finite beams (with a variable end condition) subjected to both point force and point moment (piezoelectric based) flexural excitation. In order to make a fundamental comparison with the wave based control implemented in Chapter 4, the equations are solved exclusively using the wave approach. A schematic of the beam used in this analysis is presented in Figure 2.14.

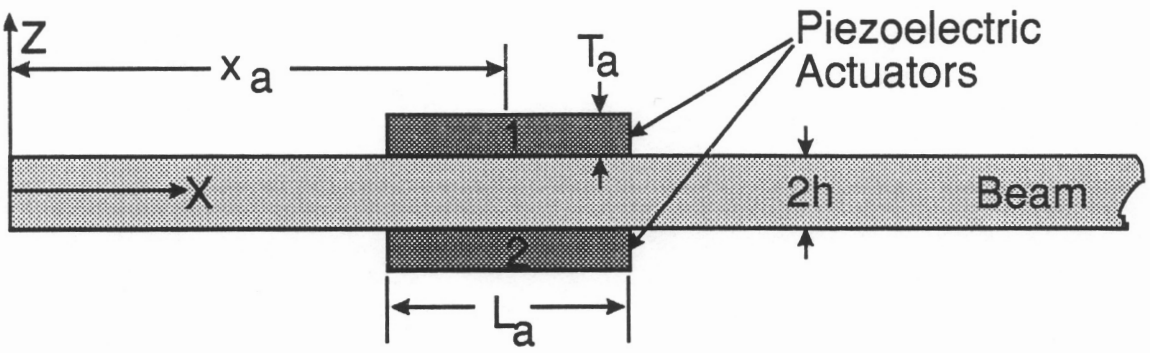

Figure 2.14 Semi-infinite Beam Schematic

2.4.1 Flexural and Extensional Equations of Motion

The Euler equation of motion will be exclusively used to model the response of a thin beam vibrating in flexure (Cremer et al., 1973). In Figure 2.14, the x-axis lies along the neutral axis of the beam. The z axis lies through the thickness of the beam in the direction of the transverse motion. The out-of-plane displacement is denoted by the variable W. The Euler beam theory assumes that the beam dimension in the z direction is much smaller than the flexural wavelengths in the structure, and thus the rotary inertia effects are small and assumed zero. Also, the rotational inertia, and shear deformations are negligibly small. These assumptions have been shown to be valid for a beam whose frequency of excitation is produces wavelengths at least six times larger than the thickness of the beam (Cremer et al., 1973). The homogeneous Euler

equation of motion for flexural vibration of the thin beam is given as follows (Cremer et al.,1973):

$$E_b I \frac{\partial^4 W}{\partial x^4} + \rho a \frac{\partial^2 W}{\partial t^2} = 0 \qquad \textbf{(2.53)}$$

When harmonic motion is assumed Equation (2.53) reduces to the following homogeneous form:

$$\frac{d^4 w}{dx^4} - k_f^4 w = 0 \qquad \textbf{(2.54)}$$

where:

$$k_f^4 = \frac{\rho a}{E_b I} \omega^2 \qquad \textbf{(2.55)}$$

The quasi-longitudinal equation of motion for extensional vibration is given as follows (Fahy, 1985):

$$\frac{\partial^2 U}{\partial x^2} - \frac{\rho}{E_b (1 - \nu^2)} \frac{\partial^2 U}{\partial t^2} = 0 \qquad \textbf{(2.56)}$$

where U is the in-plane beam displacement; and ρ is the density. The quasi-longitudinal equation of motion includes the Poisson's coupling effect which occurs with beams of finite width. The equation is valid for frequencies of excitation where the wavelength in the solid are much greater than the beam cross section.

When harmonic motion is assumed Equation (2.56) reduces to the form:

$$\frac{d^2u}{dx^2} + k_e^2 u = 0 \tag{2.57}$$

where:

$$k_e = \omega \sqrt{\frac{\rho}{E_b(1 - \nu^2)}} \tag{2.58}$$

2.4.2 Excitation and Control of Semi-Infinite Beams

In this section, the excitation of semi-infinite beams will be addressed. First, the beam will be subjected to a point force harmonic excitation located at the free end of the beam representative of the primary disturbance. The equations of motion will be solved for both flexural and extensional modes of vibration. The resultant displacement function will then be used to determine the uncontrolled power flow along the beam. This response will be the primary response which later will be actively minimized using piezoelectric control actuators. Second, the beam will be subjected to piezoelectric excitation where the piezoelectric devices are located some distance from the free end. This excitation will be considered the secondary (control) excitation. Again, the resultant displacement function will be used to determine the resulting power flow along the beam due to the control input only. Lastly, the beam will be

subjected to a combination of the two previous conditions and the net displacement will be found by superposition. The resultant power flow is considered the cost function, and is found to be quadratic with respect to the unknown complex control voltages thus having one unique minimum. The complex piezoelectric voltages are optimized such that a minimal far field power flow is obtained.

2.4.2.1 Point Force Excitation of Semi-infinite Beams

First, the beam is subjected to only the point force excitation, F, at an angle Θ with respect to the neutral axis resulting in a normal (out-of plane) component, F_f, shown in Figure 2.15. After assuming harmonic motion the flexural equation of motion is of the form:

$$\frac{d^4w}{dx^4} - k_f^4 w = F_f \delta(x) \tag{2.59}$$

The solution to this equation for all x>0 is given by the following relation (see Appendix A for the derivation):

$$w(x,t) = \frac{jF_f}{2E_b I k_f^3}(e^{jk_f x} + e^{-k_f x})e^{-j\omega t} \tag{2.60}$$

where an $e^{-j\omega t}$ time convention is assumed. The solution is obviously composed of two waves: the first is a positive traveling wave, and the second

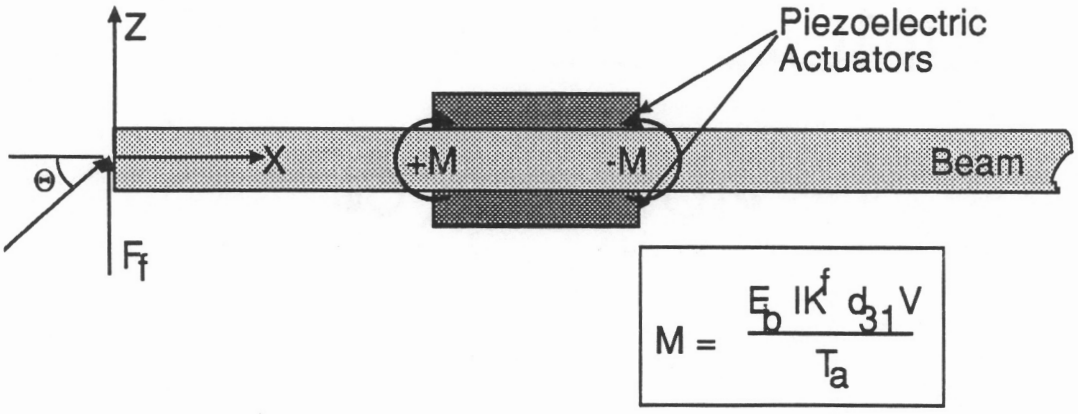

Figure 2.15 Flexural Loading Condition

is a positive decaying nearfield. Note that since the beam is semi-infinite and is excited at its free end, the response does not contain any "zeros" for all ω and x. Where a "zero" is defined as a frequency where the beam displacement is zero (similar to the presence of a node in a modally responding beam). As will be shown in the next section, if the input force (or moment for the case of a piezoelectric actuator) is moved from the free end to some positive x location, then "zeros" will be present in the response.

The power flow for flexural vibration was outlined in Section 2.3.5. The flexural power flow associated with the point force excitation of Equation (2.60) is given by:

$$P_f(\omega) = \frac{\omega |F_f|^2}{4E_b I k_f^3} \tag{2.61}$$

The in-plane component of the point force, F, is F_e, and is shown in Figure 2.16. After assuming harmonic motion, the extensional equation of motion is of the form:

$$\frac{d^2u}{dx^2} + k_e^2 u = \frac{F_e}{E_b(1 - \nu^2)a}\delta(x) \tag{2.62}$$

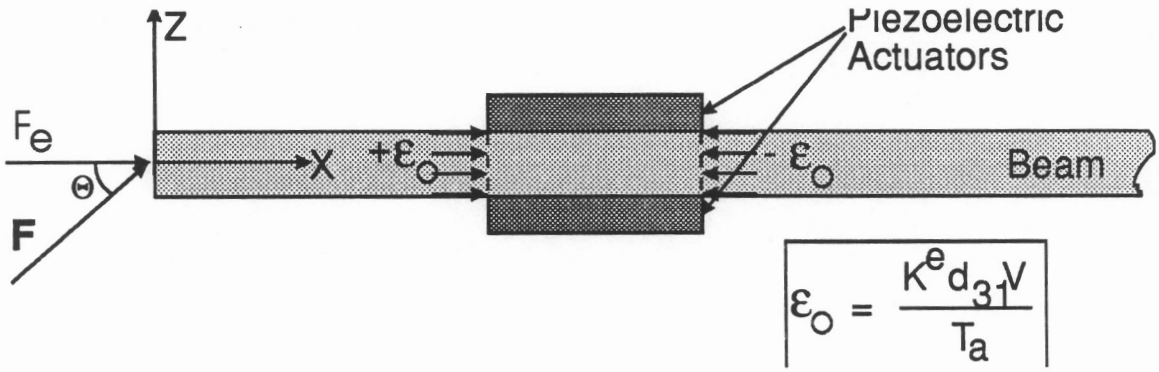

Figure 2.16 Extensional Loading Condition

The solution of Equation (2.62) consists of a single positive traveling wave of the form (see Appendix A for derivation):

$$U(x,t) = \frac{-jF_e}{E_b(1 - \nu^2)ak_e} e^{jk_e x} e^{-j\omega t} \tag{2.63}$$

Note that the extensional response of a semi-infinite beam excited by a point force at its end also does not contain zeros. The power flow for extensional vibration was also outlined in Section 2.3.5. The extensional power flow associated with the point force excitation is found by substituting Equation (2.63) into Equation (2.51), and is presented as follows:

$$P_e = \frac{\omega |F_e|^2}{2ak_e} \tag{2.64}$$

2.4.2.2 Piezoelectric Excitation of Semi-infinite Beams

In this portion of the analysis, in order to model the control field the beam is subjected to excitation by a single piezoelectric actuator bonded to the upper surface, and located at some arbitrary location, x_a, on the semi-infinite beam shown in Figure 2.14 (top actuator only). The piezoelectric actuator excites a flexural motion component with effective line moments as shown previously in Figure 2.15. The equation of motion, as previously presented in Equation (2.18), modified for the excitation of a thin beam by a single piezoelectric actuator located at a point x_a, and a length L_a is given by:

$$\frac{d^4w}{dx^4} - k_f^4 w = \frac{K^f d_{31} V}{T_a}[\delta'(x - (x_a - L_a/2)) - \delta'(x - (x_a + L_a/2))] \tag{2.65}$$

The free boundary condition at x = 0 inherent in semi-infinite beams is such that the shear force and flexural moment must be zero. This is equivalent to saying that the second and third spacial derivatives evaluated at x = 0 are zero:

$$m_y(x) = E_b I \frac{d^2w}{dx^2} = 0, \tag{2.66}$$

and

$$F_w(x) = E_b I \frac{d^3w}{dx^3} = 0 \tag{2.67}$$

The closed form solution to the above boundary valued problem is given in the following relation (see Appendix A for derivation):

for $x < x_a - L_a/2$:

$$w(x) = \frac{K^f d_{31} V}{4 T_a k_f^2} \left\{ \left(e^{\frac{-k_f L_a}{2}} - e^{\frac{k_f L_a}{2}} \right) e^{-k_f x_a} e^{k_f x} + \left[j\left(e^{\frac{-k_f L_a}{2}} - e^{\frac{k_f L_a}{2}} \right) - (2j+2)\sin\left(\frac{k_f L_a}{2} \right) e^{j k_f x_a} \right] e^{-k_f x} + \left[(j-1)\left(e^{\frac{-k_f L_a}{2}} - e^{\frac{k_f L_a}{2}} \right) + 2\sin\left(\frac{k_f L_a}{2} \right) e^{j k_f x_a} \right] e^{j k_f x} + 2j\sin\left(\frac{k_f L_a}{2} \right) e^{j k_f x_a} e^{-j k_f x} \right\} \tag{2.68}$$

for $x_a - L_a/2 < x < x_a + L_a/2$:

$$w(x) = \frac{K^f d_{31} V}{4T_a k_f^2}\left\{ e^{k_f\left(x - x_a - \frac{L_a}{2}\right)} + \right.$$

$$\left[j\left(e^{\frac{k_f L_a}{2}} - e^{\frac{-k_f L_a}{2}}\right)e^{-k_f x_a} + (-2j + 2)\sin\left(\frac{k_f L_a}{2}\right)e^{jk_f x_a} + 2e^{k_f\left(x_a - \frac{L_a}{2}\right)} \right] e^{-k_f x} + \qquad \textbf{(2.69)}$$

$$\left[(-1 + j)\left(e^{\frac{k_f L_a}{2}} - e^{\frac{-k_f L_a}{2}}\right)e^{-k_f x_a} + 2\sin\left(\frac{k_f L_a}{2}\right)e^{jk_f x_a} - 2e^{-jk_f\left(x_a - \frac{L_a}{2}\right)} \right] e^{jk_f x} +$$

$$\left. -2e^{-jk_f\left(x - x_a - \frac{L_a}{2}\right)} \right\}$$

for $x > x_a + L_a/2$:

$$w(x) = \frac{K^f d_{31} V}{4T_a k_f^2}\left\{ \left[\left(e^{k_f x_a} - je^{-k_f x_a}\right)\left(e^{\frac{-k_f L_a}{2}} - e^{\frac{k_f L_a}{2}}\right) + (2j+2)\sin\left(\frac{k_f L_a}{2}\right)e^{jk_f x_a} + 2e^{k_f\left(x_a - \frac{L_a}{2}\right)} \right] e^{-k_f x} + \right. \qquad \textbf{(2.70)}$$

$$\left. \left[(-1 + j)\left(e^{\frac{k_f L_a}{2}} - e^{\frac{-k_f L_a}{2}}\right)e^{-k_f x_a} + 2\sin\left(\frac{k_f L_a}{2}\right)\left(e^{jk_f x_a} - je^{-jk_f x_a}\right) \right] e^{jk_f x} \right\}$$

It is interesting to examine the response in the far field where $x >> x_a + L_a/2$. Under this assumption, the e^{-kfx}, term will be zero corresponding to the decay of the nearfield response. which produces the following relation:

$$w(x) = \left[(-1 + j)\left(e^{\frac{k_f L_a}{2}} - e^{\frac{-k_f L_a}{2}}\right)e^{-k_f x_a} + 2\sin\left(\frac{k_f L_a}{2}\right)\left(e^{jk_f x_a} - je^{-jk_f x_a}\right) \right] e^{jk_f x} \qquad \textbf{(2.71)}$$

If a further restriction is applied such that the actuator is located far from the free end (at a particular frequency) then the term, e^{-kfxa}, will be zero producing the following relation:

$$w(x) = 2\sin\left(\frac{k_f L_a}{2}\right)\left(e^{jk_f x_a} - je^{-jk_f x_a}\right)e^{jk_f x} \tag{2.72}$$

The response thus can be seen to contain zeros at frequencies where:

$$\left(e^{jk_f x_a} - je^{-jk_f x_a}\right) = 0, \tag{2.73}$$

and

$$\sin\left(\frac{k_f L_a}{2}\right) = 0. \tag{2.74}$$

In Equation (2.74), the zeros are produced at frequencies where the actuator is a multiple of a full flexural wavelength which is a consequence of the example shown in Section 2.1.2. A more interesting result is seen in Equation (2.73). These zeros occur when the distance from the free end to the center of the actuator, x_a, is one quarter wavelength plus a multiple of half a wavelength, λ_f, which in equation form is:

$$x_a = \left(n + \frac{1}{4}\right)\lambda_f, \tag{2.75}$$

or frequencies

$$\omega_n = \sqrt{\frac{\rho a}{E_b I}} \frac{\left(n + \frac{1}{4}\right)^2 \pi^2}{x_a^2} \qquad \text{for } n = 0,1,2,3,... \tag{2.76}$$

The zeros correspond to a negative traveling wave generated by the piezoelectric actuator reflecting of the free boundary and destructively interfering with the positive traveling wave generated by the actuator at locations downstream of the actuator. Thus, at those frequencies the beam response consists of a pure standing wave between the free end and the piezoelectric actuator, and zero traveling waves downstream of the actuator. It is noted that this zero response can only occur if the boundary (in this case free) is perfectly reflective, and thus does not absorb any wave energy. If the boundary absorbs some energy, as in most physical systems, then the zeros would not occur. In other words, the reflected wave would have a smaller amplitude, and thus could not totally cancel the positive generated wave from the actuator (at $x > x_a + L_a/2$). In order to illustrate the zero occurrences, a beam was theoretically driven by a single piezoelectric actuator with properties shown in Table 4.6 on page 178 in the same configuration as used in the experiments of Chapter 4. The semi-infinite beam is made of aluminum, and is 4 m long x 76.2 mm wide x 3.175 mm thick. The frequency response of a beam excited by a single piezoelectric actuator located at a distance 0.4m from the free end and driven with a constant 1 volt input is shown in Figure 2.17. The response is as

represented in Equation (2.71). It can be seen in Figure 2.16 that there are zeros at frequencies of about 71, 236, 491, 841, and 1281 Hz.

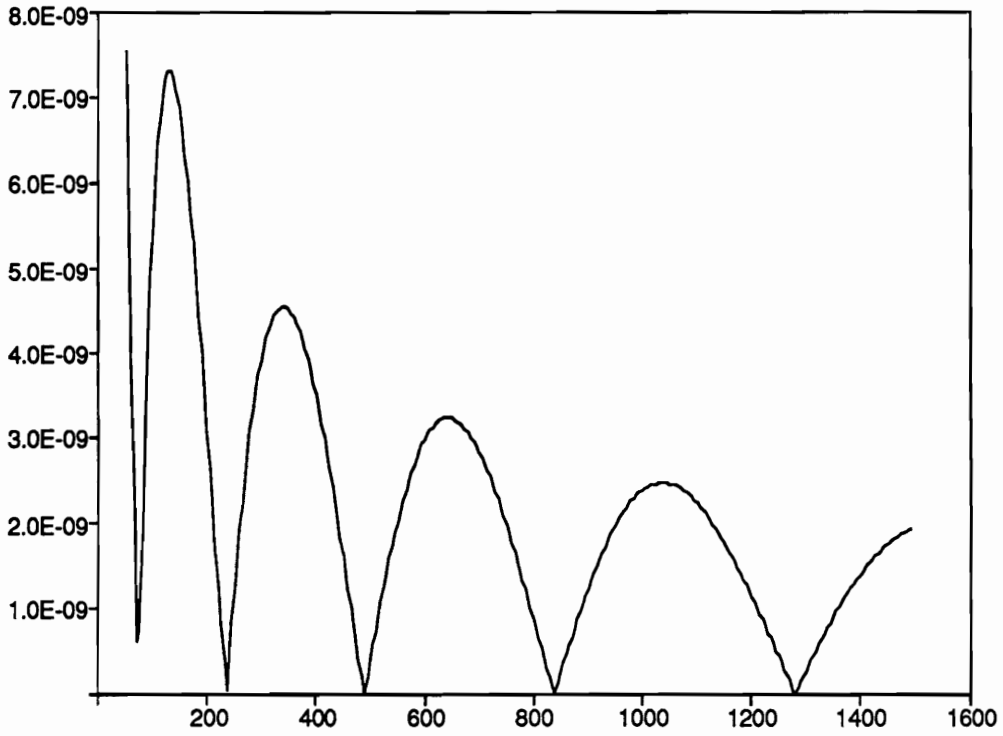

Figure 2.17 Frequency Response of Beam Downstream of the Actuator for $x >> x_a + L_a/2$

In a later section we will examine the impact of the zeros on the optimal control of power flow. At this point we will return to the excitation of the semi-infinite beam by two independent piezoelectric actuators. If two symmetrically mounted piezoelectric actuators as shown in Figure 2.15 are driven at the same

frequency with independent complex voltages, V_1 and V_2, then Equations (2.68), (2.69), and (2.70) can be modified by replacing V by $V_1 - V_2$. Thus the two piezoelectrics must be driven out of phase in order to excite pure flexural waves (at their maximum values given a fixed input voltage magnitude). If the two actuators are driven in-phase then zero flexural waves are produced (only an extensional component). The reader is referred to Section 2.1.2 for a more detailed examination of this phenomena.

The power flow for flexural vibration was outlined in Section 2.3.5. The flexural power flow past the actuator ($x > x_a + L_a/2$) associated with the excitation by a single piezoelectric actuator mounted on the upper surface is given as follows:

$$P_f(\omega) = \frac{E_b I \omega (K^f)^2 d_{31}^2}{8 T_a^2 k_f} V \left\{ 4\sin^2\left(\frac{k_f L_a}{2}\right)(1 - \sin(2k_f x_a)) + 2\sin\left(\frac{k_f L_a}{2}\right) e^{-k_f x_a}\left(e^{\frac{k_f L_a}{2}} - e^{-\frac{k_f L_a}{2}}\right)(\sin(k_f x_a) - \cos(k_f x_a) + e^{-2k_f x_a}\left(e^{k_f L_a} + e^{-k_f L_a} - 2\right)\right\}^2 \quad \textbf{(2.77)}$$

The flexural power flow past the actuator ($x > x_a + L_a/2$) associated with the excitation by both upper and lower piezoelectric actuators driven by complex voltages, V_1 and V_2, is given as follows:

$$P_f(\omega) = \frac{E_b I \omega (K^f)^2 d_{31}^2}{8T^2 k_f}\left|(V_1 - V_2)\left\{4\sin^2\left(\frac{k_f L_a}{2}\right)(1 - \sin(2k_f x_a)) + 2\sin\left(\frac{k_f L_a}{2}\right)e^{-k_f x_a}\left(e^{\frac{k_f L_a}{2}} - e^{-\frac{k_f L_a}{2}}\right)(\sin(k_f x_a) - \cos(k_f x_a) + e^{-2k_f x_a}\left(e^{k_f L_a} + e^{-k_f L_a} - 2\right)\right\}\right|^2 \quad \textbf{(2.78)}$$

The extensional equation of motion for a beam excited by a single piezoelectric actuator of length L_a, mounted on the upper surface of the beam, and located at a location x_a from the free end as shown in Figure 2.14 is presented as follows:

$$\frac{d^2u}{dx^2} + k_e^2 u = \frac{K^e d_{31} V}{T_a}[\delta(x - (x_a - L_a/2)) - \delta(x - (x_a + L_a/2))] \quad \textbf{(2.79)}$$

Here the piezoelectric effectively acts as in-plane forces acting at the ends of the piezoelectric as shown in Figure 2.16. The closed form solution for the above equation of motion is found to be (See Appendix A for derivation):

For $x < x_a - L_a/2$:

$$u(x) = -\frac{jK^e d_{31} V}{T_a k_e} e^{jk_e x_a} \sin\left(\frac{k_e L_a}{2}\right)\left[e^{jk_e x} + e^{-jk_e x}\right] \quad \textbf{(2.80)}$$

For $x_a - L_a/2 > x > x_a + L_a/2$:

$$u(x) = -\frac{jK^e d_{31} V}{2T_a k_e}\left\{\left[-2e^{jk_e x_a}\sin\left(\frac{k_e L_a}{2}\right) - e^{-jk_e\left(x_a-\frac{L_a}{2}\right)}\right]e^{jk_e x} + e^{jk_e\left(x_a-\frac{L_a}{2}\right)}e^{-jk_e x}\right\} \quad \textbf{(2.81)}$$

For $x > x_a - L_a/2$:

$$u(x) = -j\frac{2K^e d_{31} V}{T_a k_e}\sin\left(\frac{k_e L_a}{2}\right)\sin(k_e x_a)e^{jk_e x} \quad \textbf{(2.82)}$$

Again, it can be seen in Equation (2.82) that the response past the actuator ($x > x_a + L_a/2$) will contain zeros at frequencies where:

$$\sin\left(\frac{k_e L_a}{2}\right) = 0, \quad \textbf{(2.83)}$$

and

$$\sin\left(\frac{k_e x_a}{2}\right) = 0 \quad \textbf{(2.84)}$$

Equation (2.83) corresponds to frequencies where the actuator length is equal to multiples of a wavelength, and for most beams and piezoelectric actuators currently available this is not an issue due to the extreme length of extensional waves. Equation (2.84) corresponds to frequencies where a negative traveling wave reflects off the free end and interferes destructively with the positive traveling wave generated by the actuator producing zero net positive traveling

waves downstream of the actuator. The zero is produced at frequencies where the distance from the center of the patch to the free end is half a wavelength which can be written in equation form as:

$$\omega_n = \frac{2n\pi}{x_a}\sqrt{\frac{E_b(1-\nu^2)}{\rho}}, \qquad \text{for } n = 0,1,2,... \tag{2.85}$$

This phenomena of reflected waves causing cancellation will only occur if the boundary condition at x = 0 will cause total reflection (i.e. free, fixed, simply supported). If the boundary has some absorption then total cancellation at any frequency can not occur. The implications of the zeros on extensional power flow will be studied in the next section.

If the beam is excited by two symmetrically bonded piezoelectric actuators in the same axial location the in-plane displacement is found by superposition of Equation (2.82) to be:

$$u(x) = -j\frac{2K^e d_{31}(V_1 + V_2)}{k_e T_a}\sin\left(\frac{k_e L_a}{2}\right)\sin(k_e x_a)e^{jk_e x} \tag{2.86}$$

The power flow for extensional vibration was outlined in Section 2.3.5. The resultant extensional power flow of a single actuator whose response is described by Equation (2.82) is found by substituting into Equation (2.69).

$$P_e(\omega) = \frac{2E_b(1 - \nu^2)a(K^e)^2 d_{31}^2 \omega |V|^2}{k_e T_a^2} \sin^2\left(\frac{k_e L_a}{2}\right) \sin^2(k_e x_a) \qquad (2.87)$$

The resultant extensional power flow for two symmetrically bonded arbitrarily driven actuators is:

$$P_e(\omega) = \frac{2E_b(1 - \nu^2)a(K^e)^2 d_{31}^2 \omega |V_1 + V_2|^2}{k_e T_a^2} \sin^2\left(\frac{k_e L_a}{2}\right) \sin^2(k_e x_a) \qquad (2.88)$$

2.4.2.3 Optimal Control of Flexural and Extensional Power Flow in Semi-infinite Beams

In the previous sections, the displacement functions, and resultant power flow for a semi-infinite thin beam subjected to various loading conditions were determined. In this section, the relations will be applied to the control of flexural and extensional power flow in beams. In both flexural and extensional modes of vibration, the primary (or noise) field to be controlled will be generated by a force acting on the free end of the beam as previously shown in Figure 2.15 and Figure 2.16 subjected to the boundary conditions of Equations (2.66) and (2.67). The secondary (or control) field will be applied by a piezoelectric actuator pair located at some distance, x_a, from the free end.

Since the displacement function is linear in terms of both the primary and secondary fields, the power flow as presented in Equations (2.48) and (2.51) is a quadratic function of both fields. The quadratic power flow function has a unique minimum (optimal) solution in terms of the excitation voltage of the piezoelectric actuators. This solution can be obtained in one of two ways.

1. The positive power flow can be determined as a function of the primary (noise) source, and the secondary (control) source. Then, partial derivatives of the power flow cost function with respect to the real and imaginary control sources can be determined, and set equal to zero (the optimal point). This will provide unique solutions for the real and imaginary components of the secondary (control) source.

2. Since the beam is a one dimensional system, it is possible to produce a secondary displacement field which when summed (by superposition) with the primary field produce zero power flow. This case corresponds uniquely to a zero coefficient in front of the net positive traveling wave. Therefore, if the net displacement field is found with an arbitrary control voltage input, then the coefficient corresponding to the positive traveling wave can be set to zero. This complex relation will provide the unique complex control voltage value.

Since the second of the two ways is the easiest to form, it will be solely used in this dissertation. Interestingly one technique examines the problem from purely a power flow point of view, and the other examines the problem from purely a wave point of view. To better understand the concepts, lets examine the net power flow in the system as a function of the resultant net positive and negative traveling waves, A and B, respectively. The power flow can be re-written from Equation (2.49) as,

$$P_f(\omega) = E_b I k_f^3 \omega(|A|^2 - |B|^2). \tag{2.89}$$

The negative traveling wave, B, can be written in terms of the traveling wave reflection coefficient, R_{tf}, as

$$B = R_{tf}A$$

Thus the power flow can be written in terms of the traveling wave, A, and the traveling wave reflection coefficient, R_{tf}, as follows:

$$P_f(\omega) = E_b I k_f^3 \omega|A|^2(1 - |R_{tf}|^2). \tag{2.91}$$

The above relation shows that if the A wave can be set equal to zero then the power flow will also be zero resulting the aforementioned unique solution.

Since as previously discussed in Section 2.1, a single piezoelectric element can simultaneously produce both flexural and extensional waves with a fixed

relationship based on beam and actuator properties and configurations. To control arbitrary flexural and extensional primary fields it will be necessary to utilize two independent actuators. In the examples of this section the two actuators will be mounted symmetrically on the beam at a distance, x_a, from the free end. These actuators will in effect act as two independent degrees of freedom which is necessary to control the two independent mechanisms of vibration (i.e. flexural and extensional waves).

If we sum the flexural responses of the primary force of Equation (2.60) and the secondary piezoelectric excitation (with unknown optimal voltages) of Equation (2.70) modified for two symmetrically bonded piezoelectric actuators and set the positive traveling wave in region three (the coefficient of the e^{jkfx} term) equal to zero, the following relation is produced:

$$\frac{jF_f}{2E_b I k_f^3} + \frac{K^f d_{31}(V_1 - V_2)}{4T_a k_f^2}\left[(-1+j)\left(e^{\frac{k_f L_a}{2}} - e^{\frac{-k_f L_a}{2}}\right)e^{-k_f x_a} + 2\sin\left(\frac{k_f L_a}{2}\right)\left(e^{jk_f x_a} - je^{-jk_f x_a}\right)\right] = 0 \qquad \textbf{(2.92)}$$

If we sum the extensional responses of the primary force of Equation (2.63) and the secondary piezoelectric excitation for two symmetrically bonded piezoelectric actuators (with unknown optimal voltages) of Equation (2.86) and set the positive traveling wave (the coefficient of the e^{jkex} term) equal to zero, the following relation is produced:

$$\frac{-jF_e}{E_b(1-\nu^2)ak_e} - j\frac{2K^e d_{31}(V_1+V_2)}{k_e T_a}\sin\left(\frac{k_e L_a}{2}\right)\sin(k_e x_a) = 0 \qquad \textbf{(2.93)}$$

The previous two equations are solved simultaneously for the optimal piezoelectric voltages, V_1 and V_2, which will simultaneously reduce the primary excitation field to zero (in the far field) thereby isolating the beam downstream of the actuators. After much manipulation, the two complex voltages are found to be:

$$V_1 = -\frac{F_e T_a l k_f K^f\left[(-1+j)\left(e^{\frac{k_f L_a}{2}} - e^{\frac{-k_f L_a}{2}}\right)e^{-jk_f x_a} + 2\sin\left(\frac{k_f L_a}{2}\right)\left(e^{jk_f x_a} - je^{-jk_f x_a}\right)\right] + j4F_f T_a a(1-\nu^2)K^e\sin\left(\frac{k_e L_a}{2}\right)\sin(k_e x_a)}{4E_b I(1-\nu^2)K_f K^f K^e d_{31} a\left[(-1+j)\left(e^{\frac{k_f L_a}{2}} - e^{\frac{-k_f L_a}{2}}\right)e^{-jk_f x_a} + 2\sin\left(\frac{k_f L_a}{2}\right)\left(e^{jk_f x_a} - je^{-jk_f x_a}\right)\right]\sin\left(\frac{k_e L_a}{2}\right)\sin(k_e x_a)} \qquad \textbf{(2.94)}$$

$$V_2 = -\frac{F_e T_a l k_f K^f\left[(-1+j)\left(e^{\frac{k_f L_a}{2}} - e^{\frac{-k_f L_a}{2}}\right)e^{-jk_f x_a} + 2\sin\left(\frac{k_f L_a}{2}\right)\left(e^{jk_f x_a} - je^{-jk_f x_a}\right)\right] - j4F_f T_a a(1-\nu^2)K^e\sin\left(\frac{k_e L_a}{2}\right)\sin(k_e x_a)}{4E_b I(1-\nu^2)K_f K^f K^e d_{31} a\left[(-1+j)\left(e^{\frac{k_f L_a}{2}} - e^{\frac{-k_f L_a}{2}}\right)e^{-jk_f x_a} + 2\sin\left(\frac{k_f L_a}{2}\right)\left(e^{jk_f x_a} - je^{-jk_f x_a}\right)\right]\sin\left(\frac{k_e L_a}{2}\right)\sin(k_e x_a)} \qquad \textbf{(2.95)}$$

It is important to note some interesting phenomena associated with the above relations. Note that the denominator of both of the above relations contain the zeros mentioned in the last section for both flexural and extensional excitation by the single piezoelectric. These zeros now appear in the denominator of the optimal voltages, V_1 and V_2, and thus act as poles. The reason for the

occurrence of these poles is somewhat obvious. If the primary field excites the beam such that the response past the actuator is vibrating at some level at which control is desired and at a frequency near one of the poles, then the actuator in this configuration is virtually incapable of exciting the region of the beam at that frequency. The voltage required to generate a significant control field at this frequency is high because of the lack of sufficient control authority. The response of the beam upstream of the actuators will be presented for a typical beam arrangement to note the effects of the poles on the flexural response of the beam. For this example, a beam was theoretically driven by a single piezoelectric actuator with properties shown in Table 4.6 on page 178 in the same configuration as used in the experiments of Chapter 4. The semi-infinite beam is made of aluminum, and is 4 m long x 76.2 mm wide x 3.175 mm thick. The beam is subjected to a theoretical out-of-plane force, F_f, of one Newton, and the optimal solution is obtained for frequencies from 50 to 1500 Hz. As discussed earlier in this section, the optimal solution produced zero traveling waves downstream of the control actuator (note however, requiring infinite piezoelectric voltages at the poles). The frequency response of the positive traveling wave present in the beam in the region upstream of the actuator location ($0 < x < 0.4$m) under optimal control conditions is presented in Figure 2.18.

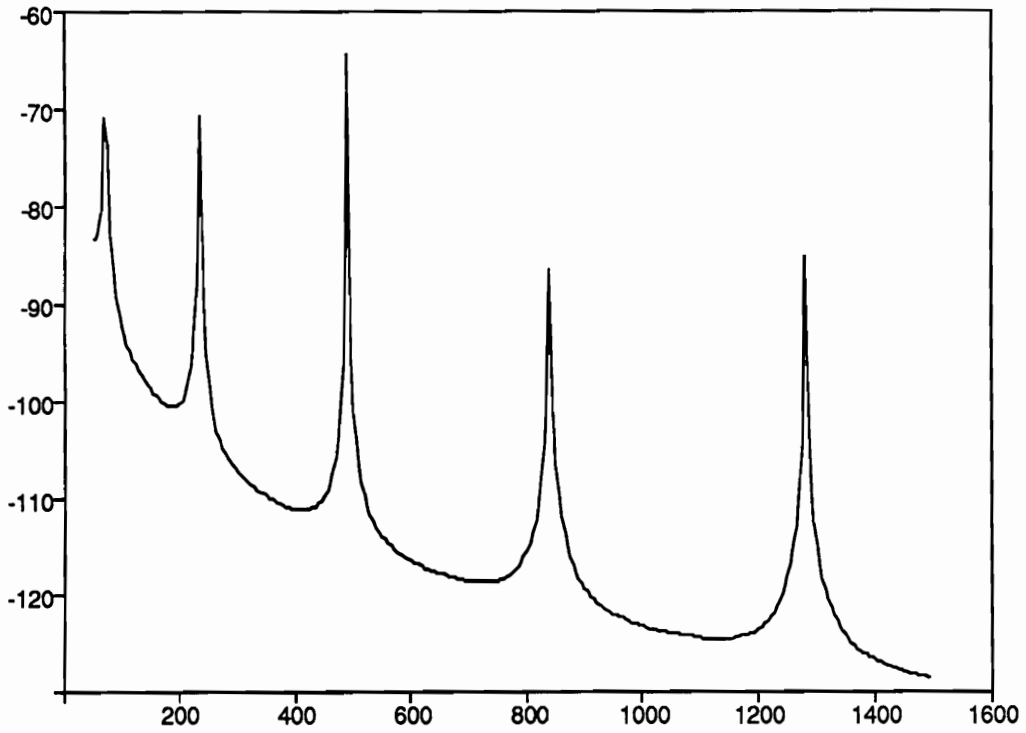

Figure 2.18 Frequency Response of the Positive Traveling Flexural Wave Under Optimal Control, for $x < x_a - L_a/2$

A comparison can now be made with the results of last section in which a beam excited by the piezoelectric actuator #1 (upper) is driven with a constant 1 volt input. The frequency response of the beam displacement downstream of the actuator was previously shown in Figure 2.17. Note that the zeros as seen in the downstream beam response shown in Figure 2.17 driven by the piezoelectric actuator correspond to the poles of the beam response shown in

Figure 2.18 upstream of the actuator under the optimal solution, and to the poles of the optimal control voltages. The poles occur because the control authority of the actuator due to its location is low at the corresponding frequencies, and although the downstream beam displacement is optimally driven to zero the upstream beam region is at "resonance," and control voltage theoretically infinite. This resonance is not a resonance of the beam, but corresponds to a synthetic resonance produced by the controller at these particular frequencies producing high optimal voltages (infinite at frequencies exactly at the pole locations), and high upstream beam responses. The complete study of the poles added by the addition of the optimal control to the beam is beyond the scope of this dissertation, and the reader is referred to excellent papers on this subject by Burdisso and Fuller (1992, 1993).

The poles occurrence is directly linked to the negative traveling wave produced by the control actuator reflecting off the free boundary and canceling the positive traveling generated by the control actuator downstream of the actuator. As stated previously, this cancellation occurs only if the boundary condition at the end of the beam upstream of the actuator (in this case free) is totally reflective or near totally reflective. For most actual beam systems this type of boundary condition may not occur, and control of the total power flow downstream of the control point at all frequencies is thus achievable. If a beam

system exists where the boundary condition is totally reflective as is the case with the free condition of this semi-infinite beam, then total power flow control is achievable in frequency regions where the controller has sufficient authority. If control of power flow is desirable in a broadband sense for these beam systems, then another pair of actuators must be utilized that will, when combined with the first pair, have control authority over the entire frequency range. The reader is referred to two papers by Miyoshi and Kaneda (1988, and 1991) that covers the control of broadband disturbances using the Multiple Input Inverse Filtering Theorem (MINT). This theorem is derived to handle the problems associated with effects control plant zeros similar to those discussed in the previous example.

2.4.3 Excitation and Control of Finite Beams

In this section, the excitation of finite beams will be analyzed. A schematic of the finite beam is shown in Figure 2.19. The beam consists of a free boundary condition at $x = 0$, and a variable boundary condition at $x = L_b$. In this particular case the boundary condition at $x = L_b$ will be described with a flexural traveling wave reflection coefficient, R_{tf}, a flexural reflected nearfield coefficient, R_{nf}, and an extensional traveling wave reflection coefficient, R_{te} defined by the following relations:

$$R_{tf} = \frac{B}{A}$$
$$R_{nf} = \frac{C}{A} \qquad (2.96)$$
$$R_{te} = \frac{F}{E}$$

where the coefficients A, B, C, E, and F are defined by Equations (2.47) and (2.50). Note that these coefficients are complex and are defined at x = 0.

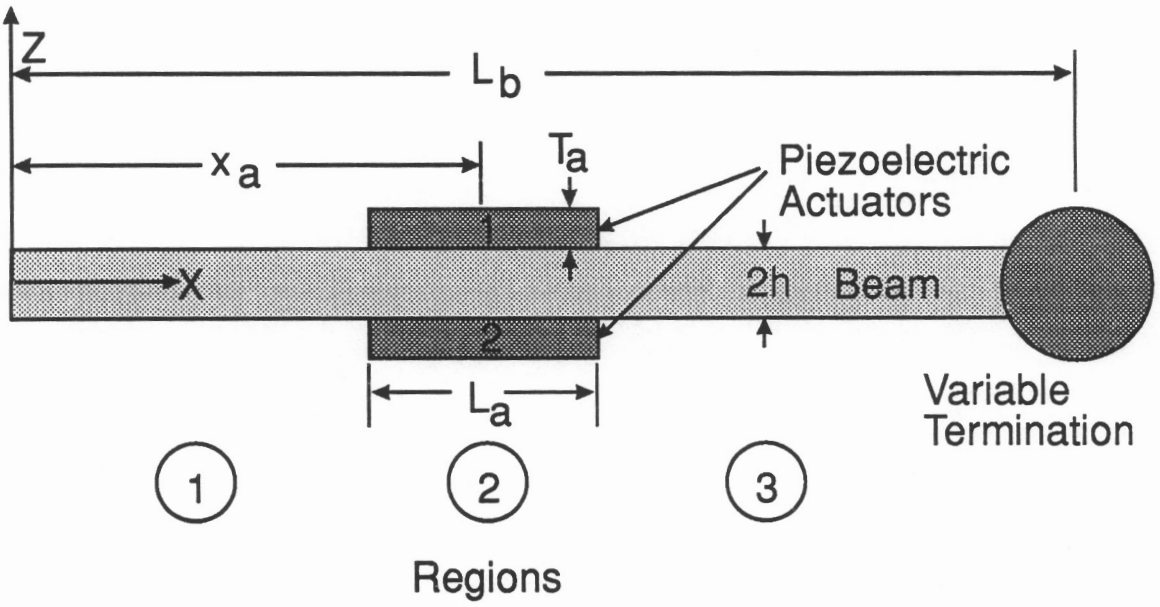

Figure 2.19 Finite Beam Schematic

The boundary condition at $x = L_b$ could be described by complex impedances or some other relation, but the reflection coefficient method provides a much simpler solution without loss of generality when a wave approach is utilized.

First, the beam will be subjected to a point force harmonic excitation located at the free end of the beam. The equations of motion will be solved for both flexural and extensional modes of vibration. The resultant displacement function will then be used to determine the power flowing along the beam. This response will be the primary (or noise) response which later will be actively minimized using piezoelectric actuators. Secondly, the beam will be subjected to piezoelectric excitation where the piezoelectric devices are located some distance from the free end. Again, the resultant displacement function will be used to determine the resulting power flow along the beam. This response will be considered the secondary (or control) response. Lastly, the beam will be subjected to a combination of the two previous conditions such that the excitation voltage of the piezoelectric actuators will be optimized to produce a minimal far field power flow.

2.4.3.1 Point Force Excitation of Finite Beams

First the finite beam as shown in Figure 2.20 will be subjected to only a point force, F, with an out-of-plane component, F_f, at the free end. The equation of motion is again described by Equation (2.59). The equation of motion is solved using the assumed waves of Equation (2.47). The resultant out-of-plane beam response is (see Appendix A for the derivation):

$$w(x) = \frac{F_f}{E_b I k_f^3 [2R_{nf} - R_{tf} - 1 + j(R_{tf} - 1)]} \left[e^{jk_f x} + R_{tf} e^{-jk_f x} + R_{nf} e^{k_f x} + (1 + R_{tf} - R_{nf} e^{-k_f x}) \right] \quad \textbf{(2.97)}$$

The power flow associated with the above relation can be found by substituting the equivalent traveling wave amplitudes A and B into Equation (2.49). The flexural power flow associated with the point force excitation using Equations (2.47) and (2.49) is found to be:

$$P_f(\omega) = \frac{\omega}{E_b I k_f^3} \frac{(|F_f|^2 - |R_{tf}|^2 |F_f|^2)}{|2R_{nf} - R_{tf} - 1 + j(R_{tf} - 1)|^2} \quad \textbf{(2.98)}$$

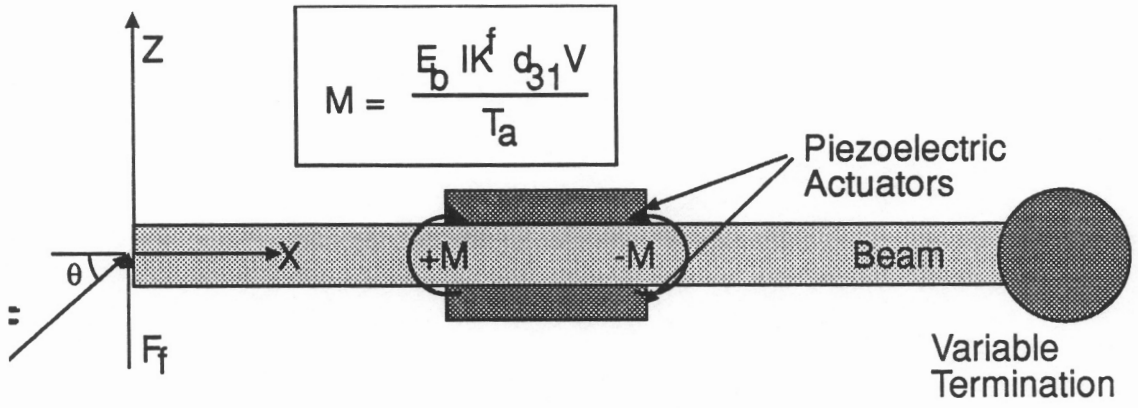

Figure 2.20 Flexural Loading Condition

In extension, the in-plane component of F is F_e as shown in Figure 2.21. The extensional equation of motion for point force excitation, F_e, is again described by Equation (2.62). The equation of motion is solved using the assumed waves

of Equation (2.50). The resultant in-plane displacement is given as follows (see Appendix A for derivation):

$$u(x) = \frac{jF_e}{E_b(1 - \nu^2)ak_e(R_{te} - 1)}\left[e^{jk_e x} + R_{te}e^{-jk_e x}\right] \qquad \textbf{(2.99)}$$

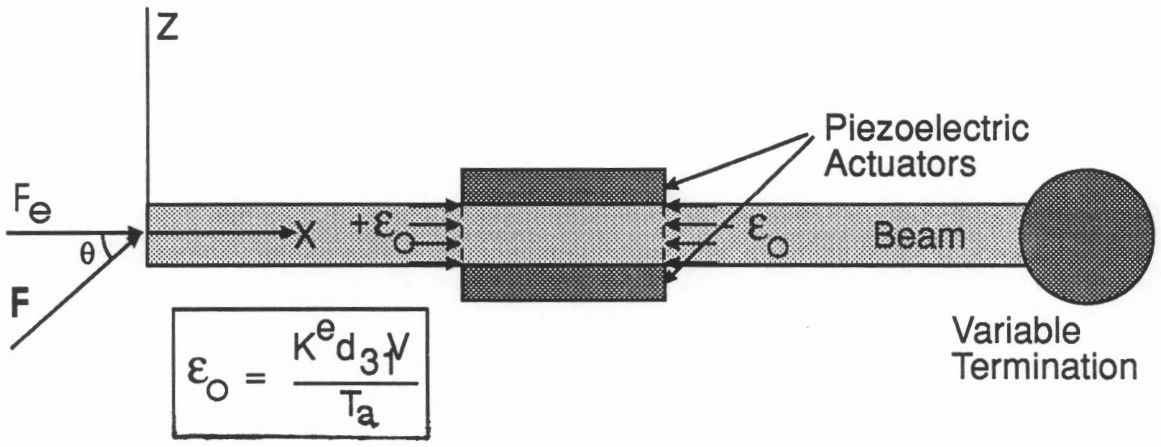

Figure 2.21 Extensional Loading Condition

The power flow associated with the response of Equation (2.99) is found by substitution of the equivalent traveling wave amplitudes of Equation (2.99) into Equation (2.51). The extensional power flow associated with the point force excitation using Equations (2.50) and (2.52) is given by:

$$P_e(\omega) = \frac{\omega(|F_e|^2 - |F_e|^2|R_{te}|^2)}{2E_b ak_e(1 - \nu^2)|R_{te} - 1|^2} \qquad \textbf{(2.100)}$$

2.4.3.2 Piezoelectric Excitation of Finite Beams

In this portion of the analysis, the beam is subjected to excitation by two piezoelectric actuators bonded to the surface, and located at some arbitrary location on a finite beam shown in Figure 2.19. The flexural equation of motion, was previously presented in Equation (2.65) for the excitation of a thin beam by two piezoelectric actuators of length L_a, symmetrically mounted, and located at a point x_a with effective moment loading as shown in Figure 2.20. The flexural equation of motion will be solved using a wave approach, where the beam is broken up into regions where discontinuities (mass, force, etc.) only lie at the boundaries of a region. Since the piezoelectric actuator effectively acts as line moments in flexure (see Figure 2.20) and in-plane point strains (see Figure 2.21) in extension at the ends of the actuator, the beam must be broken into three regions. These regions are shown in Figure 2.19. Region one is located between the free end and the left edge of the piezoelectric actuator ($0 < x < x_a - L_a/2$). Region two is located from the beginning to the end of the piezoelectric actuator ($x_a - L_a/2 < x < x_a + L_a/2$). Region three is located between the end of the piezoelectric and the end of the beam with the variable boundary condition ($x > x_a + L_a/2$). The assumed flexural response of Equation (2.47) is applied separately for each section, and the governing boundary conditions are then applied to each section. In general, this provides for four unknown waves in each section (where the subscript 1, 2, or 3 of the

wave amplitudes denote the section number). The final system of equations is given in matrix form as:

$$\begin{bmatrix} -1 & -1 & 1 & 1 & 0 & 0 & 0 & 0 & 0 & 0 & 0 & 0 \\ -j & j & 1 & -1 & 0 & 0 & 0 & 0 & 0 & 0 & 0 & 0 \\ e^{jk_f x_1} & e^{-jk_f x_1} & e^{k_f x_1} & e^{-k_f x_1} & -e^{jk_f x_1} & -e^{-jk_f x_1} & -e^{k_f x_1} & -e^{-k_f x_1} & 0 & 0 & 0 & 0 \\ je^{jk_f x_1} & -je^{-jk_f x_1} & e^{k_f x_1} & e^{-k_f x_1} & -je^{jk_f x_1} & je^{-jk_f x_1} & -e^{k_f x_1} & -e^{-k_f x_1} & 0 & 0 & 0 & 0 \\ -e^{jk_f x_1} & -e^{-jk_f x_1} & e^{k_f x_1} & e^{-k_f x_1} & e^{jk_f x_1} & e^{-jk_f x_1} & -e^{k_f x_1} & -e^{-k_f x_1} & 0 & 0 & 0 & 0 \\ -je^{jk_f x_1} & je^{-jk_f x_1} & e^{k_f x_1} & -e^{-k_f x_1} & je^{jk_f x_1} & -je^{-jk_f x_1} & -e^{k_f x_1} & e^{-k_f x_1} & 0 & 0 & 0 & 0 \\ 0 & 0 & 0 & 0 & e^{jk_f x_2} & e^{-jk_f x_2} & e^{k_f x_2} & e^{-k_f x_2} & -e^{jk_f x_2} & -e^{-jk_f x_2} & -e^{k_f x_2} & -e^{-k_f x_2} \\ 0 & 0 & 0 & 0 & je^{jk_f x_2} & -je^{-jk_f x_2} & e^{k_f x_2} & e^{-k_f x_2} & -je^{jk_f x_2} & je^{-jk_f x_2} & -e^{k_f x_2} & -e^{-k_f x_2} \\ 0 & 0 & 0 & 0 & -e^{jk_f x_2} & -e^{-jk_f x_2} & e^{k_f x_2} & e^{-k_f x_2} & e^{jk_f x_2} & e^{-jk_f x_2} & -e^{k_f x_2} & -e^{-k_f x_2} \\ 0 & 0 & 0 & 0 & -je^{jk_f x_2} & je^{-jk_f x_2} & e^{k_f x_2} & -e^{-k_f x_2} & je^{jk_f x_2} & -je^{-jk_f x_2} & -e^{k_f x_2} & e^{-k_f x_2} \\ 0 & 0 & 0 & 0 & 0 & 0 & 0 & 0 & R_{tf} & -1 & 0 & 0 \\ 0 & 0 & 0 & 0 & 0 & 0 & 0 & 0 & R_{nf} & 0 & -1 & 0 \end{bmatrix} \begin{bmatrix} A_1 \\ B_1 \\ C_1 \\ D_1 \\ A_2 \\ B_2 \\ C_2 \\ D_2 \\ A_3 \\ B_3 \\ C_3 \\ D_3 \end{bmatrix} = \begin{bmatrix} 0 \\ 0 \\ 0 \\ 0 \\ \frac{-K^f d_{31}(V_1 - V_2)}{k_f^2 T} \\ 0 \\ 0 \\ 0 \\ \frac{-K^f d_{31}(V_1 - V_2)}{k_f^2 T} \\ 0 \\ 0 \\ 0 \end{bmatrix} \tag{2.101}$$

where:

$$x_1 = x_a - \frac{L_a}{2} \tag{2.102}$$

$$x_2 = x_a + \frac{L_a}{2} \tag{2.103}$$

The unknowns in the above matrix problem are the unknown wave complex amplitudes (A_1, B_1, etc.). The solution of the above twelve by twelve system of equations is not trivial to solve, and is left to the reader for an exercise. Fortunately for the purposes of this dissertation, the solution can be found

numerically at discrete frequencies. This solution technique will be used to make direct comparisons with the experimental results of Chapter 4.

One might question the utility of such a method in comparison to the typical modal approach. There are, however, distinct advantages to this method. When a modal based solution is found, the solution is of the form of an infinite sum of modes each of which must satisfy the natural boundary conditions. In the wave approach, the solution produces only 4 wave types per region. The two traveling waves travel at the speed of motion normally associated with a flexural wave, and have wavelengths normally associated with a pure flexural wave. The infinite summation of modes in the modal approach does in the limit converge to a wave solution. This concept is directly comparable to the use of the wave vector sensors previously discussed. Here the entire motion can be described by a small group of waves instead of a infinite number of modes. In comparison with the wave filtering concept, the total energy propagating along a beam can be estimated with only two sensors, and not a infinite number of modal sensors.

After Equation (2.101) is solved at discrete frequencies, the flexural power flow in the far field is found to be:

$$P_f(\omega) = E_b I k_f^3 \omega(|A_3|^2 - |B_3|^2 - 2\,\mathrm{Imag}(C_3 D_3^*)) \quad \textbf{(2.104)}$$

Next, the extensional solution to the finite beam problem will be determined. In this portion of the analysis, the beam is subjected to excitation by two piezoelectric actuators bonded to the surface, and located at some arbitrary location on a finite beam shown in Figure 2.21. The extensional equation of motion is shown in Equation (2.79) for the excitation of a thin beam by a single piezoelectric actuator located at a point x_a, and a length L_a. The extensional equation of motion will be solve using a wave approach, where region the beam is broken up into regions where discontinuities can only occur at the boundaries of the region. The piezoelectric actuators effectively act as in-plane forces (or strains) acting at the ends of the actuator and uniformly distributed through the beam. The three regions are again shown in Figure 2.19. The assumed extensional response of Equation (2.50) is applied separately for each section, and the governing boundary conditions are then applied to each section (See Appendix A for the derivation). In general, this provides two unknown waves in each section (where the subscript 1, 2, or 3 denotes the section number, and E and F denote the positive and negative traveling waves, respectively). The solution for two collocated actuators, 1 and 2, is of the form:

for $x < x_a - L_a/2$:

$$u(x) = -\frac{K^e d_{31}(V_1 + V_2)}{k_e T_a(1 - R_{te})}\sin\left(\frac{k_e L_a}{2}\right)\left(e^{jk_e x_a} - R_{te}e^{-jk_e x_a}\right)\left(e^{jk_e x} + e^{-jk_e x}\right) \quad (2.105)$$

for $x_a - L_a/2 < x < x_a + L_a/2$:

$$u(x) = -\frac{jK^e d_{31}(V_1 + V_2)}{2k_e T_a}\left[\left[2\cos\left(\frac{k_e L_a}{2}\right)e^{jk_e x_a} + e^{-jk_e x_a}\left(e^{j\frac{k_e L_a}{2}} + R_{te}e^{-j\frac{k_e L_a}{2}}\right)\right]e^{jk_e x}\right. \quad (2.106)$$
$$\left. + \left[2R_{te}\cos\left(\frac{k_e L_a}{2}\right)e^{-jk_e x_a} + e^{jk_e x_a}\left(e^{j\frac{k_e L_a}{2}} + R_{te}e^{-j\frac{k_e L_a}{2}}\right)\right]e^{-jk_e x}\right]$$

for $x > x_a + L_a/2$:

$$u(x) = j\frac{2K^e d_{31}(V_1 + V_2)}{k_e T_a(1 - R_{te})}\sin\left(\frac{k_e L_a}{2}\right)\sin(k_e x_a)\left(e^{jk_e x} + R_{te}e^{-jk_e x}\right) \quad (2.107)$$

The extensional power flow downstream of the actuator ($x > x_a + L_a/2$) is again found using Equation (2.50) and (2.52) and determined to be:

$$P_e(\omega) = \frac{2E_b(1 - \nu^2)a\omega(K^e)^2 d_{31}^2}{k_e T_a^2}\left|\frac{V_1 + V_2}{1 - R_{te}}\right|^2 \sin^2\left(\frac{k_e L_a}{2}\right)\sin^2(k_e x_a) \quad (2.108)$$

2.4.3.3 Optimal Control of Flexural and Extensional Power Flow in Finite Beams

In the previous sections, the displacement functions, and resultant power flow for a finite beam (with a variable boundary condition at one end) subjected to

various loading conditions were determined. In this section, the relations will be applied the control of flexural and extensional power flow in thin beams. In both flexural and extensional modes of vibration, the primary (or noise) field to be controlled will be generated by a force acting on the free end of the beam as previously shown in Figure 2.20 and Figure 2.21. The secondary (or control) field will be applied by a piezoelectric actuator pair located at some distance, x_a, from the free end.

Again in this section the optimal solution will be determined by superimposing the primary (force input) response and the secondary (piezoelectric input) response. The optimal solution for the complex piezoelectric voltages, V_1 and V_2, again occurs when the two superimposed responses produce a zero amplitude positive traveling wave in region three. This optimal point will also produce a zero amplitude net negative traveling wave in region three because the negative wave amplitude is just the flexural traveling wave reflection coefficient times the positive traveling wave. Since the response due to piezoelectric excitation is solved at discrete frequencies using Equation (2.101), it is advantageous to let the term $(V_1 - V_2)$ be equal to one. When this substitution is made, and Equation (2.101) is solved for A_3, the solution will be directly proportional to $(V_1 - V_2)$. When the primary flexural response of Equation (2.97) is superimposed with the solution of the secondary response of

Equation (2.101) (with a unity V_1 - V_2 input term), and the coefficient of the positive traveling wave of region three (the coefficient of the e^{jkfx} term) is set to zero reduces to the following relation:

$$\frac{F_f}{E_b I k_f^3 [2R_{nf} - R_{tf} - 1 + j(R_{tf} - 1)]} + A_3(V_1 - V_2) = 0 \qquad \textbf{(2.109)}$$

Where A_3 is solved at discrete frequencies of interest. When the primary extensional response of Equation (2.99) is superimposed with the secondary response of Equation (2.107), and the coefficient of the positive traveling wave of region three (the coefficient of the e^{jkex} term) is set to zero reduces to the following relation:

$$j\frac{2K^e d_{31}(V_1 + V_2)}{k_e T_a(1 + R_{te})}\sin\left(\frac{k_e L_a}{2}\right)\sin(k_e x_a) + \frac{jF_e}{E_b(1 - \nu^2)ak_e(R_{te} - 1)} = 0 \qquad \textbf{(2.110)}$$

The previous two equations must be solved for the optimal voltages, V_1 and V_2 as,

$$V_1 = \frac{-2F_f K^e d_{31} ak_e(1-\nu^2)(R_{te}-1)\sin\left(\frac{k_e L_a}{2}\right)\sin(k_e x_a) - F_e k_f^3 I T_a A_3(1+R_{te})(2R_{nf}-R_{tf}-1+j(R_{tf}-1))}{4A_3 E_b I k_f^3 K^e d_{31} a(1-\nu^2)(R_{te}-1)\sin\left(\frac{k_e L_a}{2}\right)\sin(k_e x_a)} \qquad \textbf{(2.111)}$$

$$V_2 = \frac{2F_f K^e d_{31} a k_e (1-\nu^2)(R_{te}-1)\sin\left(\frac{k_e L_a}{2}\right)\sin(k_e x_a) - F_e k_f^3 I T_a A_3 (1+R_{te})(2R_{nf}-R_{tf}-1+j(R_{tf}-1))}{4A_3 E_b I k_f^3 K^e d_{31} a (1-\nu^2)(R_{te}-1)\sin\left(\frac{k_e L_a}{2}\right)\sin(k_e x_a)} \quad \textbf{(2.112)}$$

The theoretical developments presented in this chapter form a basis for the study of the excitation and control of flexural and extensional motion in thin beams. The analysis techniques presented here will be used in Chapter 4 to compare the theoretical response and active control of semi-infinite and finite beams to those obtained experimentally.

Chapter 3

Control Concepts

In this chapter, a feedforward adaptive linear control approach will be presented. The chapter will first present the fundamental part of the feedforward controller, namely the finite impulse response (FIR) filter. This filter can be made adaptive such that its characteristics (i.e. frequency response) can be changed as desired within certain limitations. Next, the application of this filter to the measurement (or model) of a physical plant will be discussed. Finally, multiple adaptive FIR filters, will be combined to implement what is commonly known as the Filtered-x Adaptive LMS Algorithm. Briefly, the implementation of the controller to the control of flexural and extensional power flow in beams will be discussed, and several experimental results are then presented in the next chapter.

3.1 The Adaptive Finite Impulse Response Filter

The n-coefficient digital Finite Impulse Response (FIR) filter is defined by (Widrow and Stearns, 1985):

$$\Psi(n) = \sum_{i=0}^{N-1} \beta_i \chi(n - i) \qquad (3.1)$$

where $\Psi(n)$ is the output of the FIR filter at the n^{th} time step, β_i is the i^{th} coefficient of the FIR filter, and $\chi(n - i)$ is the n-i time step of the input sequence. The impulse response of a discretized system is defined to be the output response of a system whose input is unity at t=0, and zero at all other times. Therefore, by inspection of Equation (3.1), the i^{th} filter coefficient can be thought of as the impulse response at the i^{th} time step after the unit impulse.

The continuous frequency response function of the FIR filter is found to be:

$$H(\omega) = \sum_{i=0}^{N-1} \beta_i e^{-j\omega\Delta t} \qquad (3.2)$$

where ω is the circular frequency, and Δt is the sample period.

The basic concept behind the adaptive FIR filter is to make the N coefficients of the FIR filter variable such that some desired filter characteristic is achieved. For example, the coefficients, β, may be chosen such that the frequency response of the FIR over some band of frequencies best fits (in a least mean squares sense) some desired frequency response.

3.2 The Single Input/Output LMS Algorithm

One of the simplest uses of the adaptive FIR filter is in the plant modeling configuration of the LMS Algorithm as shown in the schematic of Figure 3.1. In this case, there exists a plant to which the input and output time domain signals are known or can be generated. An adaptive filter is placed in parallel with the unknown plant. The output of the plant is known as the desired, and the output of the adaptive FIR filter is known as the estimate. The idea here is to decide the number of coefficients of the FIR filter and to determine their optimal values such that the derived error signal is minimized in some sense. This yields an adaptive filter coefficient set that represents the plant. Some thoughts on the selection of the number of coefficients for the FIR filter will be discussed later. It is the purpose of this section to present the LMS algorithm, and to discuss how it determines or searches for the optimal weight vector. A more rigorous derivation is presented by Widrow and Stearns (1985).

As shown in Figure 3.1, the error at time step n, e(n), can be written in terms of the desired, d(n), and the adaptive filter output as follows:

$$e(n) = d(n) - \sum_{i=0}^{N-1} \beta(n)\chi(n - i) \qquad \textbf{(3.3)}$$

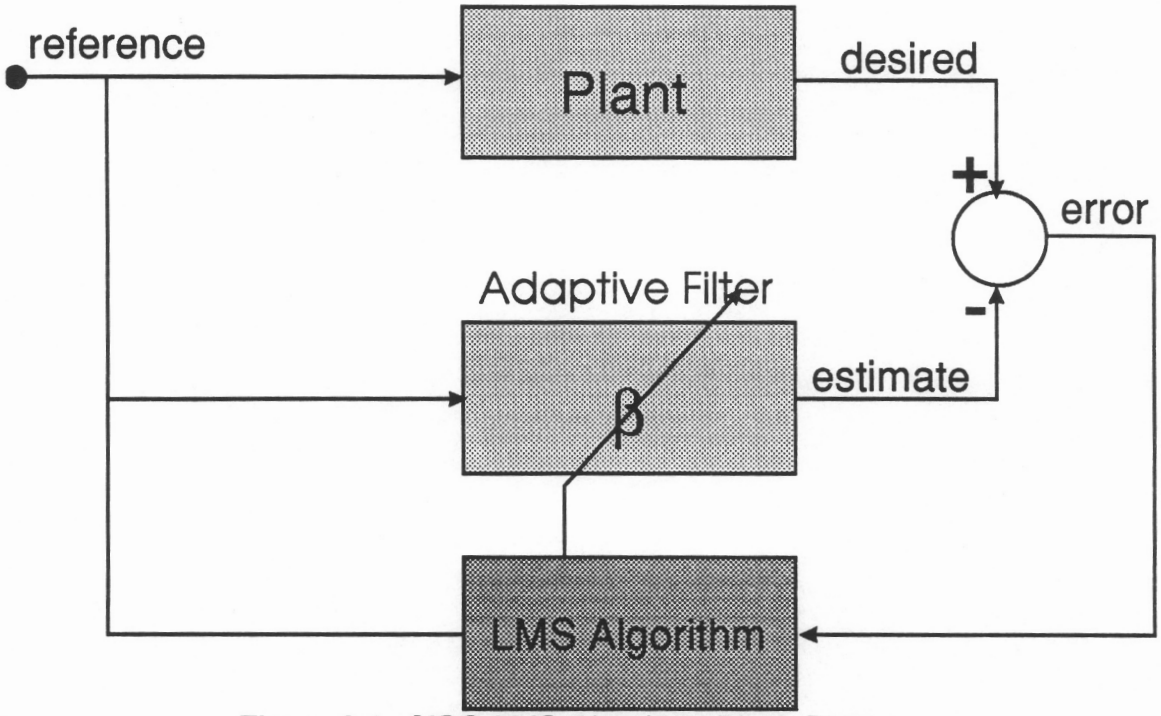

Figure 3.1 SISO LMS Algorithm Block Diagram

It is desired to minimize the expected value of the mean squared error presented in the following relation:

$$J = E[e(n)^2] \tag{3.4}$$

In this algorithm, the instantaneous value of the squared error is used as an estimate of the expected value, and in the mean provides an accurate estimate (Widrow and Stearns, 1985). The i^{th} component of the estimate of the gradient of the function, J, is presented as follows:

$$\nabla_i e(n)^2 = \frac{\partial e(n)^2}{\partial \beta_i} = 2e(n)\frac{\partial e(n)}{\partial \beta_i} = -2e(n)\chi(n - i) \qquad \textbf{(3.5)}$$

The total gradient can be thought of as a vector pointing (in an instantaneous sense) toward the minimum solution. We now update the adaptive filter weights, β_i, in the direction of this gradient using a steepest decent type algorithm as follows:

$$\beta_i(n+1) = \beta_i(n) + 2\mu e(n)\chi(n-i) \qquad \textbf{(3.6)}$$

In this case μ is called the convergence parameter. Its purpose is to control the rate at which the algorithm updates the coefficients, β. The values can range between 0.0 and 1.0 where 0.1 to 0.2 are typical. The value must be selected to achieve the desired solution in a timely manner without introducing instability (Widrow and Stearns, 1985).

The selection of the number of coefficients for the adaptive FIR filter depends on the nature of the reference signal (i.e. spectrally white, pure tone , multiple pure tones, etc.) and the desired quality of estimate by the adaptive filter. In Chapter 4 of this dissertation, experimental verification of the concepts of Chapter 2 are demonstrated at a multiple of pure frequencies. The transfer function of the filter is defined in a continuous sense (see Equation (3.2)). The weights of the adaptive filter can be thought of in terms of degrees of freedom.

If the reference signal, for example contains only three pure tones, then the adaptive filter need only estimate the transfer function of the plant at those frequencies. This estimation can be accomplished with a minimum of six weights. The six weights will provide six independent degrees of freedom in Equation (3.2) which can uniquely produce the complex transfer function at three discrete frequencies.

3.3 The Multiple Input/Output Filtered-x LMS Algorithm

In this section, a expanded version of the LMS algorithm will be presented. A schematic of the control system for two controllers, and two error sensors is shown in Figure 3.2.

This version will provide for multiple control inputs to the plant, and alleviate some problems associated with control input to error output time delays. In real systems, there is typically an inherent time delay between a control input and the error output of the plant. This delay was not modelled in the preceding section, and is the driving factor for the filtered-x portion of the algorithm presented here. The multiple input multiple output filtered-x LMS algorithm was

first presented by Elliott et al., (1987), and will be presented here. The output of an error sensor can be modelled at the n^{th} time step as:

$$e_l(n) = d_l(n) + \sum_{m=1}^{M} \sum_{j=0}^{N-1} P_{lmj} \sum_{i=0}^{N-1} \beta_{mi}(n - j)\chi(n - i - j) \qquad (3.7)$$

where:

$d_l(n)$ = l^{th} error sensor output due to the primary or noise source alone

$\chi(n)$ = input reference source

β_{mi} = the coefficients of the adaptive control filters

P_{lmj} = the j^{th} coefficient of the transfer function between the output of the m^{th} adaptive filter and the l^{th}error sensor

m = actuator number

l = error sensor number

i = filter coefficient number

n = time step

M = number of control actuators

N = number of filter coefficients.

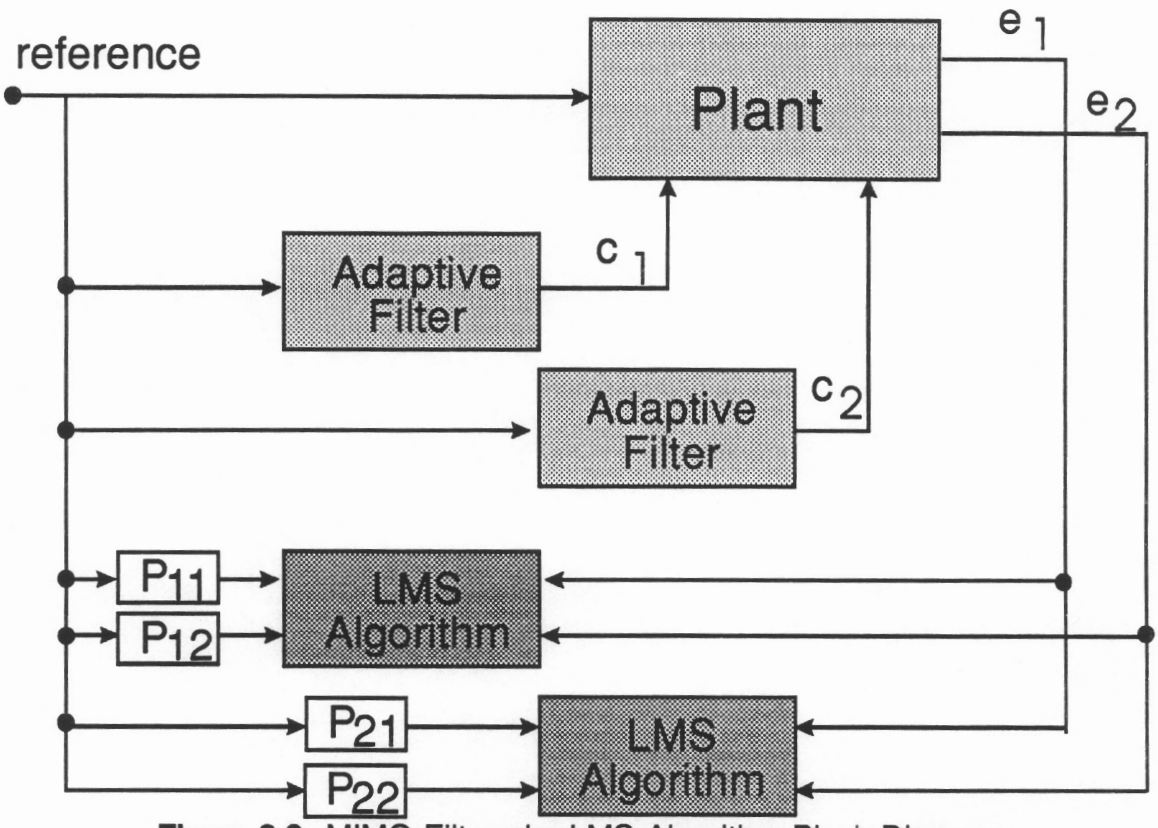

Figure 3.2 MIMO Filtered-x LMS Algorithm Block Diagram

The object is to minimize the expected value of the summation of the squared errors defined to be:

$$J = E\left[\sum_{l=1}^{L} e_l^2(n)\right] \tag{3.8}$$

where E is the expectation operator. The error function can be shown to be quadratic and thus theoretically has one minimum solution.

At each time n, the output of the compensating filters, P_{lmj}, are used by the LMS algorithm to minimize J by individually updating each adaptive filter coefficients according to the following relation:

$$\beta_{mi}(n + 1) = \beta_{mi}(n) - \mu \sum_{l=1}^{L} e_l(n) r_{lm}(n - i) \qquad \textbf{(3.9)}$$

where:

L = total number of error sensors

r_{lm} = output of compensating filter P_{lm} and defined as:

$$r_{lm}(n - i) = \sum_{j=0}^{N-1} P_{lmj} \chi(n - i - j) \qquad \textbf{(3.10)}$$

The compensating filter coefficients, P_{lmj}, provide an estimate of the plant from the respective control input to error sensor output of the system typically measured before the employment of the adaptive process. It is interesting that the plant which occurs downstream of the control filters is used to pre-filter the reference signal before it is used in the update equation. The pre-filtering of the χ is where the Filtered-x portion of the name originates. Again the instantaneous error function, $e_l(n)$, is taken as an estimate of the expected value of $e_l(n)$. This function provides an estimate of the expected value of $e_l(n)$ at every sample and convergence is found in the mean.

3.4 The MIMO Filtered-x LMS Algorithm with Real Time Wave Vector Filtering

In this section, the wave vector filtering scheme of Chapter 2 will be combined with the multiple input/output Filtered-x LMS algorithm. A schematic of this control system is shown in Figure 3.3.

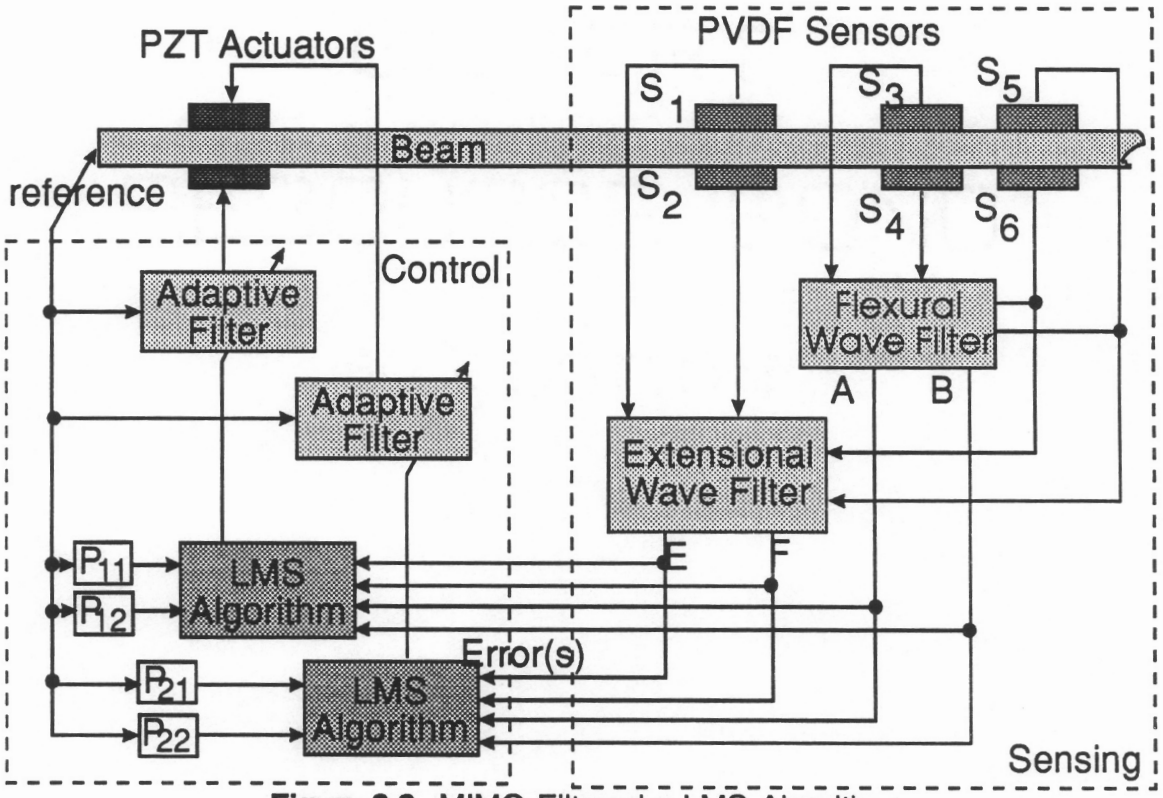

Figure 3.3 MIMO Filtered-x LMS Algorithm with Real Time Wave Vector Filtering

The equations describing the control scheme are the same as outlined in the previous section except as outlined below. The error signals are no longer measured quantities, but are derived from structural measurements. In this case the derived error signals correspond to real time estimates of the positive and negative traveling flexural and extensional waves in the beam. Piezoelectric sensors in conjunction with a digital filter scheme are used to estimate the traveling waves in the time domain as outlined in Section 2.3 of Chapter 2. The derived error signals are determined as follows:

$$
\begin{aligned}
e_1(n) &= A(n) = [s_3(n)-s_4(n)+s_5(n)-s_6(n)] + [s_3(n)-s_4(n)-s_5(n)+s_6(n)]Q_{n1} + \\
&\quad [s_3(n-1)-s_4(n-1)-s_5(n-1)+s_6(n-1)]Q_{n2} - e_1(n-1)Q_{d1} \\
e_2(n) &= B(n) = [s_3(n)-s_4(n)+s_5(n)-s_6(n)] - [s_3(n)-s_4(n)-s_5(n)+s_6(n)]Q_{n1} - \\
&\quad [s_3(n-1)-s_4(n-1)-s_5(n-1)+s_6(n-1)]Q_{n2} + e_1(n-1)Q_{d1} \\
e_3(n) &= E(n) = [s_1(n)+s_2(n)] - [s_5(n-1)+s_6(n-1)] \\
e_4(n) &= F(n) = [s_5(n)+s_6(n)] - [s_1(n-1)+s_2(n-1)]
\end{aligned}
\tag{3.11}
$$

where e_1, e_2, e_3, and e_4 are estimates of the true wave amplitudes A, B, E, F, respectively. The Cotangent Method of Section 2.3 of Chapter 2 is used to perform the flexural wave estimation, and the Time Delay Method of Section 2.3 of Chapter 2 is used to estimate the extensional waves. Q_{n1} and Q_{n2} are the numerator coefficients of the Infinite impulse response filter used in the Cotangent Method of Section 2.3 of Chapter 2. Q_{d1} is the denominator coefficient of the Infinite impulse response filter used the Cotangent Method of Section 2.3 of Chapter 2. For further information concerning the details of the

Time Delay Method and the Cotangent Method the reader is referred to Section 2.3 of Chapter 2.

It should be noted that the compensating filters, P_{lm}, now include the complete time delay from the control input to the derived error sensor output which includes the delay through the wave vector filters. Experimental verification of this control system will be demonstrated in Chapter 4.

Chapter 4

Experimental Work

In this chapter, control of flexural and extensional power flow in thin beams will be experimentally verified. In the first part of the chapter, techniques which are used as controller independent verification of beam response in both flexure and extension are discussed. In the next three main sections, results of three different active control experiments are presented. In all cases piezoceramic actuators are used as control inputs to the beam system. The first set of experiments deals with the control of flexural motion in both semi-infinite and finite beam systems using the output of simple piezoelectric sensors as the error function for an adaptive LMS controller. In this set of experiments, the piezoelectric error sensors are placed in the semi-infinite portion of the beam, and are thus only sensitive to the flexural waves traveling into the anechoic termination. In this configuration, the sensors can estimate the total power flow in the beam.

It will be shown in the second set of experiments that sensing and control of finite beams is possible where the sensors are placed in the finite section of the

beam provided the beam does not contain vibration sources between the error sensor and the passive termination, and the sensor is not placed near a nodal line. The second set of experiments demonstrate the simultaneous control of flexural and extensional power flow using simple piezoelectric sensors as error functions for an adaptive controller. In both the first and second set of experiments, the sensors measure the surface strain on opposite sides of the beam at a single beam axial location. Global control is achieved without the direct measurement of traveling waves or power flow since the error sensors are not positioned on nodal lines of the beam structure.

A different sensing scheme is required for general beam systems where one of the following is true: the boundary conditions and subsequent nodal lines are unknown and subject to change, or the primary disturbance(s) are located on either side of the error sensor. Under these conditions, a real time wave vector filtering technique can be used to filter out positive and negative traveling waves from time domain structural measurements. In the last set of experiments, flexural and extensional power flow are controlled simultaneously using real time traveling wave vector estimates as the error functions for the multi-channel LMS controller discussed in Chapter 3. This technique directly (in real time) observes, and controls the flexural and extensional power flow.

4.1 Out-of-Plane Velocity Measurements

Past work relies on determining flexural power flow using signals from surface mounted accelerometers (Downing and Shepard, 1988). However, this approach suffers from a number of disadvantages among which are: added mass to the structure, inadequacy of location, sensitivity to rotation, and phase calibration errors. For all experimental results discussed in this chapter, a Dantec Laser Vibrometer was used as an independent form of out-of-plane response measurement without the problems listed above (Dantec Elektronik, 1984). A schematic of this arrangement is shown in Figure 4.1. The laser vibrometer emits a laser beam which strikes the vibrating surface of the beam, and is partially reflected. The reflected beam is of a slightly different frequency based on the doppler effect. The system outputs a voltage signal proportional to the instantaneous out-of-plane velocity of the vibrating beam. A data acquisition program was written which allows the vibrometer to axially scan the beam, and pause at discrete locations so that a B&K 2032 spectrum analyzer could determine the resultant velocity. For all experiments in this chapter, velocity measurements were taken at 1 cm intervals along the full length of the test beam. Two basic techniques were then used to analyze the resulting information, and determine the power flow in various regions along the beam. These two techniques will be outlined in the following sections.

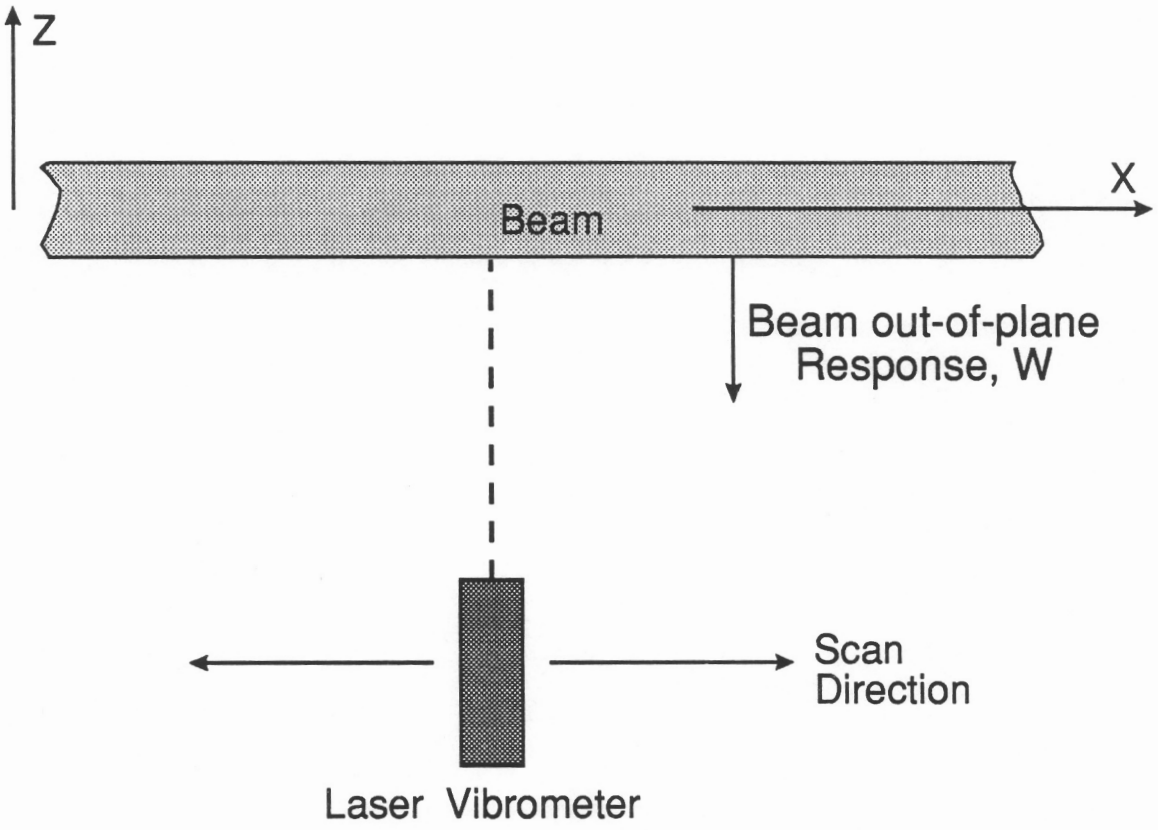

Figure 4.1 Scanning Laser Vibrometer Schematic

4.1.1 Power Flow Estimation using Two Point Finite Difference Technique

For the work considered here only propagating flexural waves were considered; flexural nearfields generated at discontinuities were assumed to be decayed to zero.

The beam equation can thus be written in reduced form as:

$$\frac{d^2w}{dx^2} + k_f^2 w = 0 \qquad \textbf{(4.1)}$$

were w(k) is the spectral content of the beam transverse response and the flexural wavenumber:

$$k_f^4 = \frac{\rho a \omega^2}{E_b I} \qquad \textbf{(4.2)}$$

where ρ is the density, ω is the frequency of excitation and E_bI is the flexural rigidity term. The power flow is the time averaged sum of the shear and flexural moment components, as follows (Downing and Shepard, 1988):

$$P_f = \langle F_w \dot{w} \rangle_t + \langle M \dot{\Theta} \rangle_t \qquad \textbf{(4.3)}$$

The moment is related to the out-of-plane displacement using the following relation (Fahy, 1985):

$$M = E_b I \frac{d^2w}{dx^2} \approx E_b I k_f^2 w \qquad \textbf{(4.4)}$$

Under free-field conditions, the total power flow is shared equally by the shear and flexural components (Cremer et al., 1973). Thus, Equations (4.3) and (4.4) can be combined and reduced to:

$$P_f = 2E_b I k_f^2 \langle w \dot{\Theta} \rangle_t \qquad \textbf{(4.5)}$$

The following finite difference approximations allow the displacement and rotational velocity to be approximated:

$$\begin{aligned} w &\approx [w_1 + w_2]/2 \\ \dot{\Theta} &\approx [\dot{w}_1 - \dot{w}_2]/L_v \end{aligned} \tag{4.6}$$

where L_v is the spacing between adjacent measurements. Substituting the finite difference relations into Equation (4.5), the result is:

$$P_f = \frac{E_b I k_f^2}{L_v}[\langle w_1 \dot{w}_1 \rangle_t + \langle w_2 \dot{w}_1 \rangle_t - \langle w_1 \dot{w}_2 \rangle_t - \langle w_2 \dot{w}_2 \rangle_t] \tag{4.7}$$

If Equation (4.7) is written in terms of acceleration instead of displacement and velocity and the Fourier transform is taken the resulting power flow is (Downing and Shepard, 1888)

$$P_f(\omega) = - \frac{E_b I k_f^2}{L_v \omega^3} \mathrm{Imag}(S_{21}) \tag{4.8}$$

where S_{21} is the cross spectrum between the acceleration response at two points on the beam. In order to process the velocity information of the laser vibrometer, Equation (4.8) can be re-written as:

$$P_f(\omega) = \frac{E_b I k_f^2}{L_v \omega} \mathrm{Imag}(S'_{21}) \tag{4.9}$$

where S'_{21} is the cross spectrum of the velocity response.

In the actual experimental setup the Dantec laser vibrometer was interfaced to a B&K 2032 spectral analyzer. The scanning drive and the B&K analyzer were controlled by an IBM AT computer. Since there was only one vibrometer, the S'_{21} was derived by taking the cross spectrum of each respective point relative to a constant coherent signal (from the signal generator), and calculating their relative cross spectrum, S'_{21}, from the results.

4.1.2 LMS Flexural Wave Decomposition

Discontinuities such as lumped mass, simple supports, etc. impart boundary conditions on the beam which result in the generation of nearfields. The general flexural beam response is composed of 4 terms (waves):

$$W(x,t) = \left(Ae^{jk_f x} + Be^{-jk_f x} + Ce^{k_f x} + De^{-k_f x}\right)e^{-j\omega t} \qquad \textbf{(4.10)}$$

where A is the positive traveling flexural wave, B is the negative traveling flexural wave, C is the negative decaying flexural nearfield, and D is the positive flexural decaying nearfield.

The method described in this section will attempt to fit (in a least mean squares sense) the four wave types of Equation (4.10) using velocity information from the laser vibrometer. Equation (4.10) can be written in terms of velocity as follows:

$$\dot{W}(x,t) = -j\omega\left(Ae^{jk_f x} + Be^{-jk_f x} + Ce^{k_f x} + De^{-k_f x}\right)e^{-j\omega t} \tag{4.11}$$

The response at a particular location, k, can be written without the time dependence as follows:

$$\dot{W}_k(x) = -j\omega\left(Ae^{jk_f x_k} + Be^{-jk_f x_k} + Ce^{k_f x_k} + De^{-k_f x_k}\right) \tag{4.12}$$

The discretized version can be written for multiple points in matrix form:

$$\begin{bmatrix} \dot{w}_1 \\ \dot{w}_2 \\ \vdots \\ \dot{w}_n \end{bmatrix} = -j\omega \begin{bmatrix} e^{jk_f x_1} & e^{-jk_f x_1} & e^{k_f x_1} & e^{-k_f x_1} \\ e^{jk_f x_2} & e^{-jk_f x_2} & e^{k_f x_2} & e^{-k_f x_2} \\ \vdots & \vdots & \vdots & \vdots \\ e^{jk_f x_n} & e^{-jk_f x_n} & e^{k_f x_n} & e^{-k_f x_n} \end{bmatrix} \begin{bmatrix} A \\ B \\ C \\ D \end{bmatrix} \tag{4.13}$$

The assumed wave distribution is only valid in regions of the beam where discontinuities lie at the ends of the region. Thus the assumed nearfields provide adequate modeling of the localized effects of the discontinuities. For situations where n>4 the system is over-defined, and a solution is desired in a least squares sense. Several methods exist for solution of over-defined problems, but the most robust solution technique is the QR decomposition (Golub and Van Loan, 1989). For the experiments in this chapter the QR method will be solely used. Once the wave amplitudes, A, B, C and D, are estimated (in the least squares sense), then the power flow can be estimated using the aforementioned relation:

$$P_f(\omega) = E_b I k_f^3 \omega (|A|^2 - |B|^2 - \text{Imag}(CD^*)) \quad (4.14)$$

It is noted again that the decaying nearfields by themselves do not contribute contribute to the real (resistive) power flow, but the interaction of two nearfields decaying in opposite directions does contribute. This effect was found to be small in most of the experimental work presented in this dissertation. If the nearfields are generated due to discontinuities more than a few wavelengths apart then their interactions become small.

4.1.3 Comparison of the Finite Difference and Wave Deconvolution Techniques

The finite difference based and wave deconvolution techniques both provide estimates to the power flow in a one dimensional beam. In this section, a basic comparison of the two techniques will be made. It is noted that the comparison will not be complete, but will only provide some insight into the benefits and drawbacks of each technique.

Obviously, both techniques require velocity information with a relatively high signal to noise ratio to provide accurate results. It is not the purpose of this section to make a comparison of the two techniques in their relative accuracies under circumstances of low signal to noise ratio. Since the wave deconvolution

technique is designed to use four or more data points spatially located, it will tend to average out problems associated with random measurement noise. However, the technique tends to provide power flow from a global point of view, where the finite difference based technique tends to provide a local estimate. However, if two measurements are used, the wave deconvolution technique can also be used as a local estimator (where C and D are assumed zero). It is in this case that the two will be compared. In regions where the nearfields are negligible, Equation (4.13) can be re-written as follows:

$$\begin{bmatrix} \dot{w}_1 \\ \dot{w}_2 \end{bmatrix} = -j\omega \begin{bmatrix} e^{jk_f x_1} & e^{-jk_f x_1} \\ e^{jk_f x_2} & e^{-jk_f x_2} \end{bmatrix} \begin{bmatrix} A \\ B \end{bmatrix} \tag{4.15}$$

If this matrix is solved in a similar fashion to that of the Time Delay method of Chapter 2, and the resulting wave amplitudes are substituted into Equation (4.14) produce, after much manipulation, the following result is obtained:

$$P_f = \frac{E_b I k_f^3}{\omega \sin(k_f L_v)} \mathrm{Im}(S'_{21}) \tag{4.16}$$

Where L_v is the spacing between data points (x_2 - x_1). It can be seen that for small $k_f L_v$ (small angle assumption where $\sin(k_f L_v) = k_f L_v$) Equation (4.16) reduces to the same form as that of Equation (4.9). The finite difference technique, that is a main assumption in the derivation of Equation (4.9), is only

accurate for relatively small data point spacing. However, small spacing is inherently prone to phase errors. It is believed that if a larger spacing is used (i.e. a quarter wavelength at the frequency of interest), and Equation (4.16) is used in lieu of Equation (4.9) that the phase error problems will be minimized without suffering from the inaccuracies associated with the finite difference technique with large data point spacing.

Both of the aforementioned techniques can be used to estimate the power flow in a one dimensional beam, but the wave deconvolution technique appears to be more robust. The wave deconvolution technique can be used as a local or global estimate of all four wave types present in a vibrating beam. The results can then be used to estimate the power flow in a region of the beam. The technique does not require that the data points be closely spaced, in fact the data can extend over several flexural wavelengths. The technique also tends to improve problems associated with experimental errors through the inherent spatial averaging that a LMS type approach provides.

4.2 In-Plane Strain Measurements

In order to have independent verification of the control of the extensional beam motion, in-plane strain measurements were taken at various locations along the

test beam. The strain measurements were taken using semi-conductor strain gages having a gage factor of 100, and arranged as a group of four gages at each axial location. Two gages were mounted on opposite sides of the beam and oriented as to be sensitive to axial beam strain. These two gages were inserted in opposite legs of a standard Wheatstone bridge. The other two strain gages were mounted on opposite sides of the beam and oriented such that they were sensitive two Poisson's coupling (normal to the axis of the beam). These two gages were inserted in the remaining opposite legs of the Wheatstone bridge. The strain gage arrangement and placement in the Wheatstone bridge provided a combination only sensitive to in-plane strains with a maximum sensitivity. These measurements are then used to estimate the extensional wave behavior in the beam, and the corresponding power flow.

Discontinuities in the beam cause boundary conditions to be imparted on the beam such that wave amplitudes on one side of the discontinuity are different than those on the other side. Thus, for example, a concentrated mass on a beam can cause the beam to respond with one set of traveling extensional waves on one side of the mass and completely different wave amplitudes on the other side. It is necessary to break the beam up into sections where discontinuities can only occur at the ends of the region.

In regions between discontinuities, the in-plane displacement, U, can be written in terms of a wave approach as:

$$U(x,t) = \left(Ee^{jk_e x} + Fe^{-jk_e x}\right)e^{-j\omega t} \tag{4.17}$$

where E is the positive traveling extensional wave, F is the negative traveling extensional wave, and k_e is the extensional wavenumber at the frequency ω.

The corresponding strain distribution, ε, is found by taking the first partial derivative with respect to x as follows:

$$\varepsilon(x,t) = jk_e\left(Ee^{jk_e x} - Fe^{-jk_e x}\right)e^{-j\omega t} \tag{4.18}$$

The response at a particular location, k, can be written without the time dependence as follows:

$$\varepsilon_k(x) = jk_e\left(Ee^{jk_e x_k} - Fe^{-jk_e x_k}\right) \tag{4.19}$$

The discretized version of this relation for multiple points can be written in matrix form:

$$\begin{bmatrix} \varepsilon_1 \\ \varepsilon_2 \\ \vdots \\ \varepsilon_n \end{bmatrix} = jk_e \begin{bmatrix} e^{jk_e x_1} & -e^{-jk_e x_1} \\ e^{jk_e x_2} & -e^{-jk_e x_2} \\ \vdots & \vdots \\ e^{jk_e x_n} & -e^{-jk_e x_n} \end{bmatrix} \begin{bmatrix} E \\ F \end{bmatrix} \tag{4.20}$$

where as previously stated, the wave amplitudes are only valid in sections of the beam free from discontinuities. If the beam has discontinuities other than those found at the ends, then the beam should be broken into sections each of which contains a separate E and F coefficient.

For situations where n>2 the system is over-defined, and a solution is desired in a least squares sense. Again, for the experiments in this chapter the QR method of solution will be solely used. Once the wave amplitudes, E, and F are estimated (in the least squares sense), then the power flow can be estimated using the aforementioned relation:

$$P_e(\omega) = \frac{E_b(1 - \nu^2)ak_e\omega}{2}(|E|^2 - |F|^2) \qquad \textbf{(4.21)}$$

The methods presented in this section will be used to estimate the in-plane beam response, and corresponding power flow, both before and after control.

4.3 Control of Flexural Power Flow using Piezoelectric Error Sensors

The active control of flexural power flow in both semi-infinite and finite elastic beams is experimentally investigated. The experimental results demonstrate

that piezoceramic transducers when used in conjunction with an adaptive least mean squares narrow band controller, can effectively control flexural power flow at steady state single frequencies in thin beam systems. The piezoceramic transducers offer distinct size and weight advantages over conventional transducers. The experiments also demonstrate the use of an axial scanning laser vibrometer to determine out-of-plane velocity and power flow.

4.3.1 Experimental Arrangement

A schematic for the test arrangement used in the following experiments is presented in Figure 4.2. The beam is made of aluminum, and is 4 m long x 76.2 mm wide x 3.175 mm thick. The beam is fitted at one end with an anechoic termination which has been tested to have a power reflection coefficient of less than 0.1 for frequencies above 150 Hz. A photograph of the experimental arrangement is shown in Figure 4.3.

The primary source (noise source) is applied as a point force at the free end perpendicular to the surface of the beam. In order to provide control input to the beam, two piezoceramic elements were bonded symmetrically to the beam at a distance of 0.4 m from the free end. These elements were made of Lead Zirconate Titante material (Piezo Systems, 1987) and had the dimensions 38.1 mm x 21.1 mm x 0.18 mm and were hard wired 180° out of phase to induce a

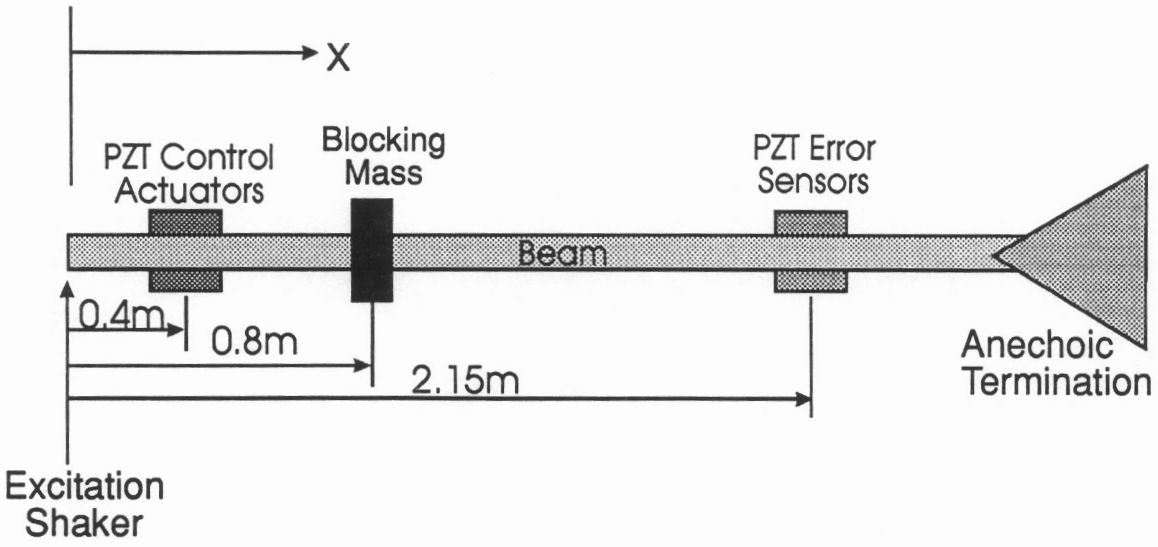

Figure 4.2 Experimental Schematic

flexural moment on the beam (as shown in Chapter 2). It is assumed that these transducers have similar sensitivity. If the transducers do not have the same sensitivity then the output will actually include spillover in the form of extensional motion.

Two similar transducers were bonded 2.15 m from the free end, and were used as the flexural wave error sensors. When these sensors are wired so that their outputs are summed 180° out of phase they produce an oscillating signal which is proportional to the response of the flexural wave motion (see Chapter 2).

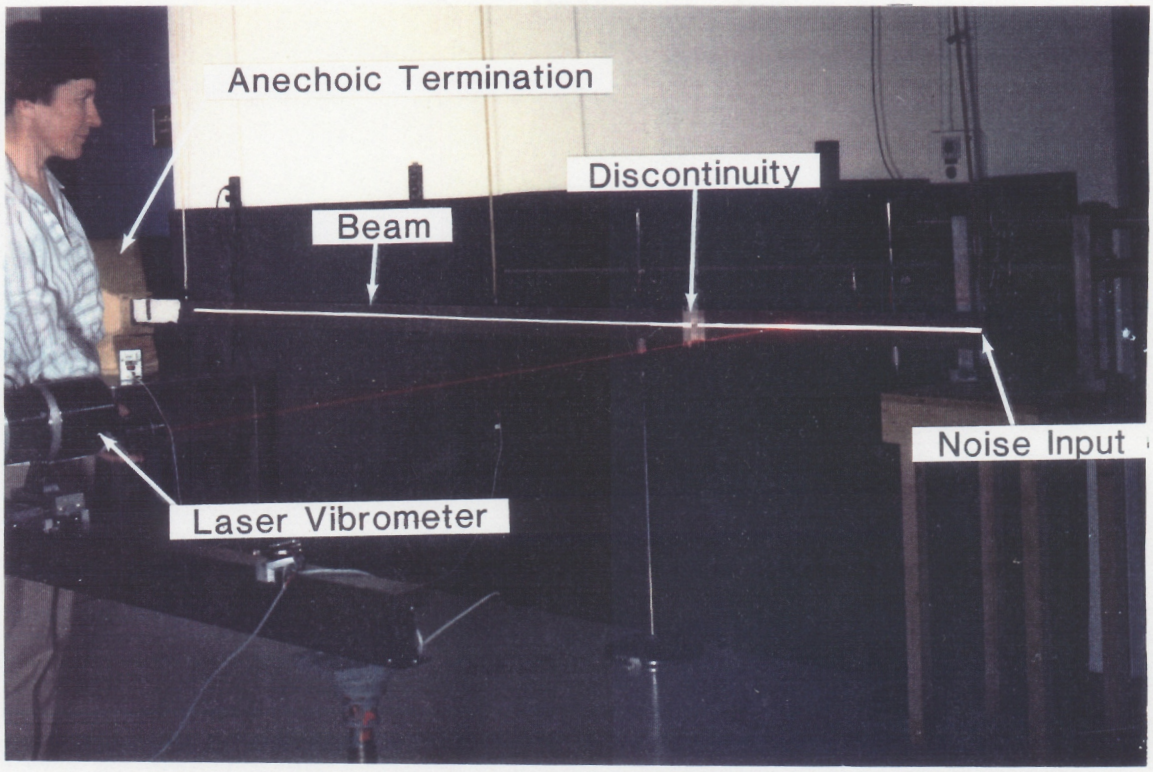

Figure 4.3 Photograph of Experimental Arrangement

In order to have independent verification of the control of the flexural wave and measure the flexural power flow distribution along the beam, an axial scanning laser vibrometer was used to measure out-of-plane velocity. Using cross-spectral information from two separate velocity measurements (located away from discontinuity nearfields) the net flexural power flow was calculated as outlined in Section 4.1.1.

4.3.2 Control Implementation

A schematic of the adaptive control system used in these series of experiments is shown in Figure 4.4. The control system uses the adaptive Filtered-X least mean squares technique to adapt the coefficients of a FIR control filter based upon reference and error signals as detailed in Chapter 3 and Widrow and Stearns (1985). The control algorithm was implemented using a TMS 320C25 signal processing chip with an IBM AT as a host computer. The sampling rate was fixed at 8 kHz. In the following tests, the noise input was a pure tone sinusoid. For convenience, the reference signal was taken from the same signal generator as the noise signal. In practice, the reference signal could be measured directly from the exciting machinery or synthesized from information related to machinery shaft speed. For the following experiments, the length of the adaptable FIR control filter was set to two, thus limiting the controller to narrow band (single frequency).

As discussed in Chapter 3, the adaptive LMS algorithm uses a cost function which is based on the mean square amplitude of the error signal. Thus, as the error signal is proportional to flexural strain, the control cost function is related to the square of the flexural strain integrated under the control error sensors. With sources only to the left of the error sensors and R_{tf} fixed, the error is proportional to the net wave field under the sensor or A (1 + R_{tf}) which is

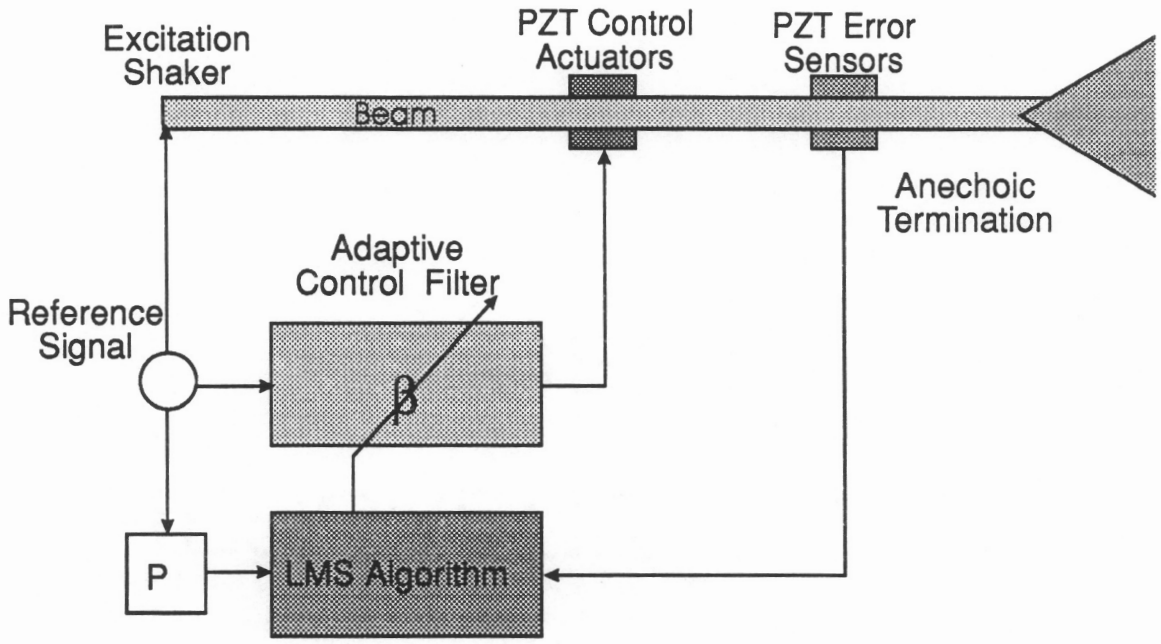

Figure 4.4 Control Block Diagram

generally proportional to A. The problem arises when the sensor is located on top of a null of the standing wave when R_{tf} is approximately equal to one.

4.3.3 Experimental Procedure

For the experiment, two different beam arrangements were tested. For the first arrangement, the beam was in a semi-infinite setup. For the semi-infinite case, frequencies of 302 Hz and 802 Hz were tested. These values were chosen to demonstrate control performance over a range of frequencies. For the baseline response, no control was exercised over the primary excitation. Using the Dantec laser vibrometer, out-of-plane velocity versus position was measured

every 1 cm along the beam. Control was then applied to the system, and the axial velocity distribution was measured to compare to the no control case.

The second arrangement involved the addition of a blocking mass (0.388 kg) located 0.8 m from the free end to provide a finite section of the beam. In this case, the blocking mass causes a discontinuity on the beam which leads to reflection of waves and associated modal response. However, the impedance discontinuity that the beam sees is complex and waves (and thus flexural power flow) are transmitted through it. The arrangement thus approximates a finite beam section joining to (for example) a more complex structure. Rather than reducing the vibration in the finite beam section, we are interested in trying to reduce the power flow leaving the beam at the discontinuity thus controlling it before it spreads into the more complex supporting structure. The blocking mass has properties given in Table 4.1 and were clamped symmetrically on each side of the beam by bolts. As the wavelength of the motion is long compared to their width the masses were assumed to be representative of line constraints. However, later results show some evidence of wave conversion phenomena suggesting they may also have some distributed characteristics. Frequencies of 412 Hz and 802 Hz were selected for the test to demonstrate control over a range of different frequencies. Again, a baseline response was tested for both frequencies with no control over the primary excitation. The

laser vibrometer was used to measure the axial velocity distribution. Then, control was applied, and the axial velocity distribution was again measured.

Table 4.1 Blocking Mass Properties

Length	0.0256 m
Width	0.102 m
Thickness	0.005 m
Young's Modulus	71.1 GPa
Density	2700 kg/m^3
Mass	0.388 kg

In addition, a force transducer was inserted in line with the primary shaker attachment. The force transducer output was used in conjunction with the velocity measurement at the drive point to determine the characteristics of the input impedance under the different test cases. The input impedance is defined to be the complex input force divided by the complex velocity at the drive point.

The force and velocity transducers were phase calibrated by placing the force transducer between a mass and a shaker. The vibrometer was used to measure normal beam velocity along the axis of the force transducer, and was assumed to be a purely reactive system producing a 90 degree phase difference. The H_1 transfer function was measured and the phase variance

from 90 degrees was determined and used to compensate actual experimental data.

4.3.4 Semi-Infinite Beam Results

The out-of-plane velocity for the semi-infinite 302 Hz test case is shown in Figure 4.5. As mentioned previously, the primary shaker was located at the free end (0.0 m). The control piezoceramics were located at 0.4 m from the free end, and the simple error sensor piezoceramics were located at 2.15 m. From Figure 4.5 it appears from the no control case that the termination is ineffective at this frequency. However, calculation of the amplitude reflection coefficient from the standing wave ratio (Morse and Ingard, 1968) provides an amplitude reflection coefficient of approximately 0.2 and thus a power reflection coefficient of less than 0.05. Thus in terms of power, the termination performs quite effectively at this frequency.

When control is applied to the beam, the velocity between the control actuator and the termination is attenuated on the order of 35 dB. Between the free end and the control actuator location, the magnitude of the velocity does not change significantly however there is significant increase in its standing wave component.

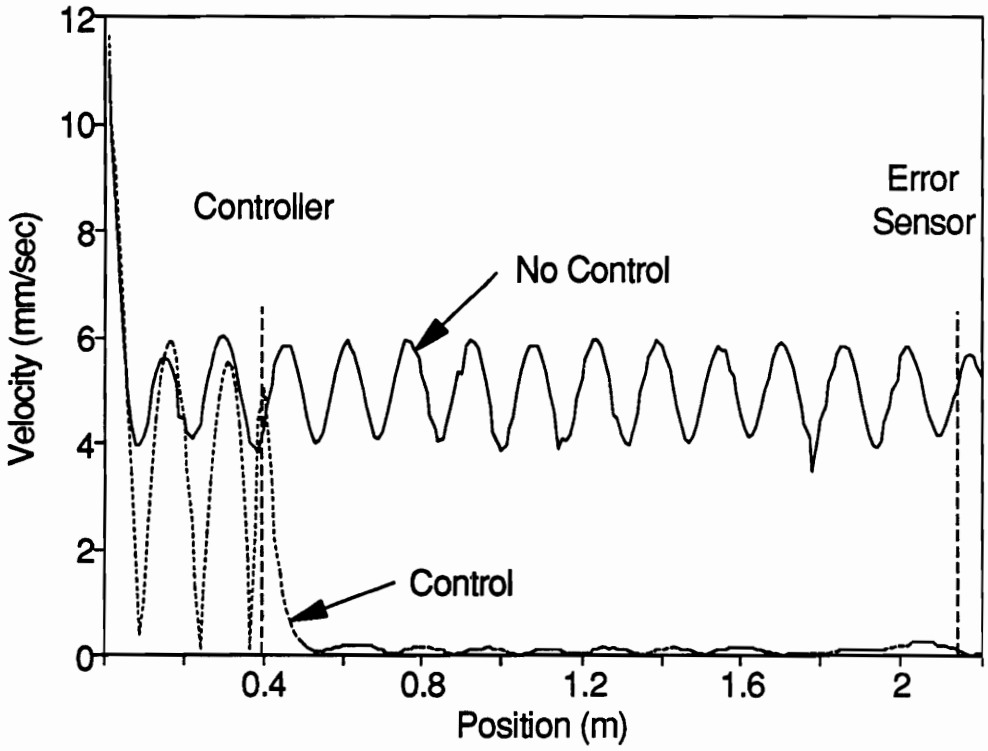

Figure 4.5 Flexural Velocity Distribution
302 Hz, Semi-infinite Beam

Figure 4.6 shows the power flow distribution for the 302 Hz test case as calculated from the aforementioned velocity magnitude and phase information (as discussed in Section 4.1.1). The power flows discussed in this section are referenced to 10^{-12} Watts. The power flow calculation is accurate except in the proximity of discontinuities on the beam where flexural wave nearfields are generated. When control is applied, the power flow between the primary

source and the controller drops about 20 dB. The controller forces the input impedance that the primary shaker sees to become very reactive causing real input power flow to drop. As can also be seen in Figure 4.6, the power flow measured between the controller and the error sensor drops an additional 20 dB. This behavior is believed to be associated with nearfield effects not modeled by the power flow estimate. It is noted that the theory derived in Chapter 2 does not predict absorption by the control actuator.

Table 4.2 shows the real and imaginary portion of the input impedance that the primary shaker sees which was determined as mentioned previously with a force transducer mounted in line with the shaker and the velocity at the drive point. Table 4.2 only shows a 9.5 dB drop in the real portion of the input impedance of the primary shaker, and this agrees well with the 10 dB drop in input power shown in Figure 4.6. The control actuator is seen to provide downstream attenuation of flexural power flow by creating a largely reactive boundary condition which reflects waves back towards the source, leading to increasing standing wave response, and causing the resistive input impedance to fall with an associated drop in input power. Note also the performance of the controller is unaffected by the standing wave present in the beam velocity before control. As long as the error sensor is located downstream of the control actuator the beam motion is attenuated past the control actuator

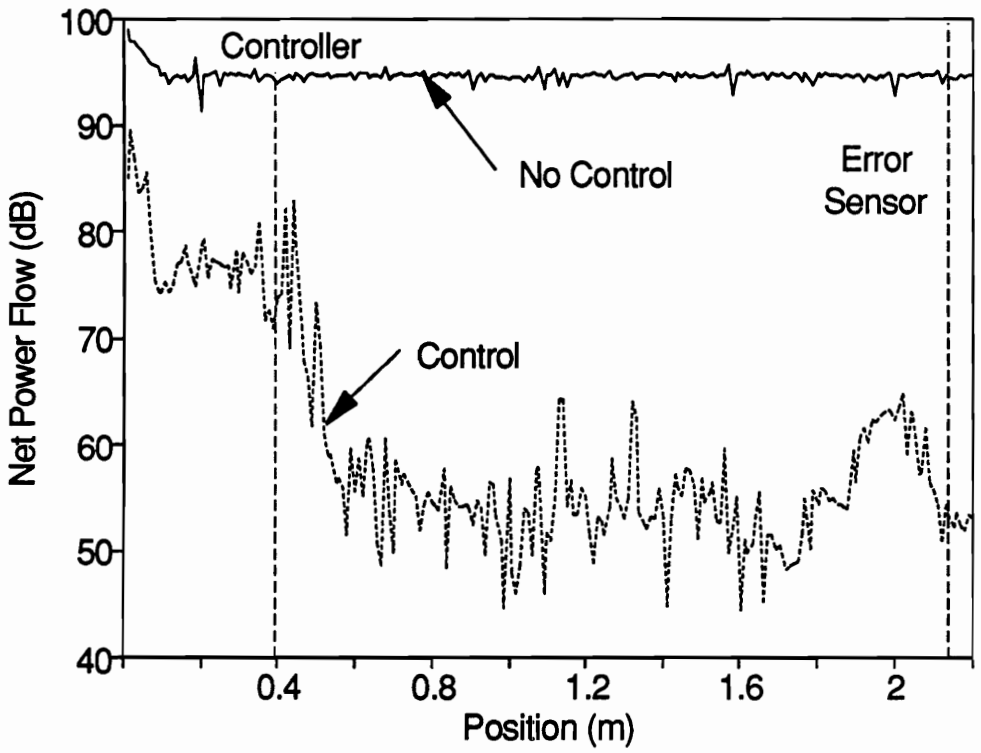

Figure 4.6 Power Flow Distribution
302 Hz, Semi-infinite Beam

whether the termination is anechoic or not. As the piezoelectric actuator senses the integral of the strain field under the element, the error signal is proportional to the summation of the two traveling waves (i.e. A + B). Since the error can then be written in terms of the flexural traveling wave reflection coefficient as A (1 + R_{tf}), then it can be seen that the error function can observe the flexural traveling waves and corresponding power flow as long as the

sensor is not placed on top of a null in the standing wave when R_{tf} is near one. The result also highlights an advantage of using a piezoceramic element as a sensor. Being distributed it is less affected by nodes than point sensors. Previous testing has found, for example, that accelerometers are very sensitive to nodal lines giving error signals that flip 180° in-phase leading to control instabilities.

Table 4.2 Shaker Input Impedance
Semi-infinite Beam

Frequency (Hz)	Input Impedance (N-sec/m)			
	No Control		Control	
	Real	Imag.	Real	Imag.
302	2.32	8.47	0.26	9.28
802	2.78	20.15	1.09	16.91

The flexural velocity distribution for the 802 Hz test case is shown in Figure 4.7. Although the termination is more anechoic at this frequency than the 302 Hz case, there is still a small standing wave present on the no control curve which corresponds to a flexural traveling wave reflection coefficient of about 0.13. When control is applied the transverse beam velocity drops from about 4 mm/sec to about 0.05 mm/sec downstream of the control actuator providing an attenuation of the order of 38 dB. Also it is noted that the flexural velocity

between the controller and the primary shaker actually increases in this case when control is applied. The increase in response of the beam section between the controller and the free end was thought to be due to this section being near to resonance with this test frequency and controller input (under closed loop conditions). Previously in Chapter 2, the theoretical optimal control of a semi-infinite beam was examined, and resonances associated with the controlled system upstream of the controller were noted. The theoretical frequency response of the semi-infinite beam upstream of the control actuator location under optimal control in the same beam and actuator configuration as in this experiment was presented in Figure 2.18 on page 93. Note that the 802 Hz excitation frequency is near the theoretical resonance of 841 Hz.

The power flow distribution for the 802 Hz semi-infinite case is presented in Figure 4.8. When control is applied the power flow near the error sensor decreases about 30 dB because the primary shaker input impedance becomes more reactive as can be seen in Table 4.2. The sharp dips in the power flow distribution were thought to be due to the laser vibrometer losing a lock on the reflected laser light which occurs more frequently when the out-of-plane response is small (i.e. under controlled conditions). The real part of the input impedance now shows an attenuation on the order of 4 dB compared to the measured drop in input power at the drive point (Figure 4.8) of 10 dB. This

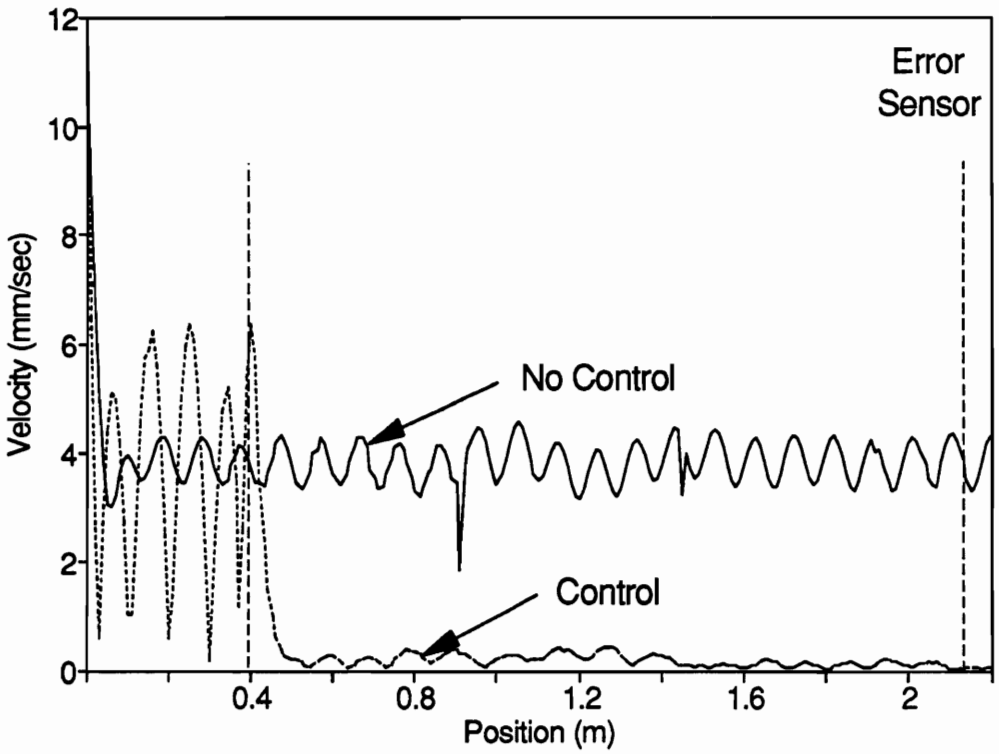

Figure 4.7 Flexural Velocity Distribution
802 Hz, Semi-infinite Beam

discrepancy is attributed to the error in phase matching the force and velocity measurements such that they are accurate to within one degree or less. Nonetheless, the table provides an qualitative assessment of the input impedance changes after control is applied. Note when the input impedance is very reactive, as in this test case, the force and velocity are in quadrature

hence very small changes in phase angle will have a large effect on the real part of the input impedance.

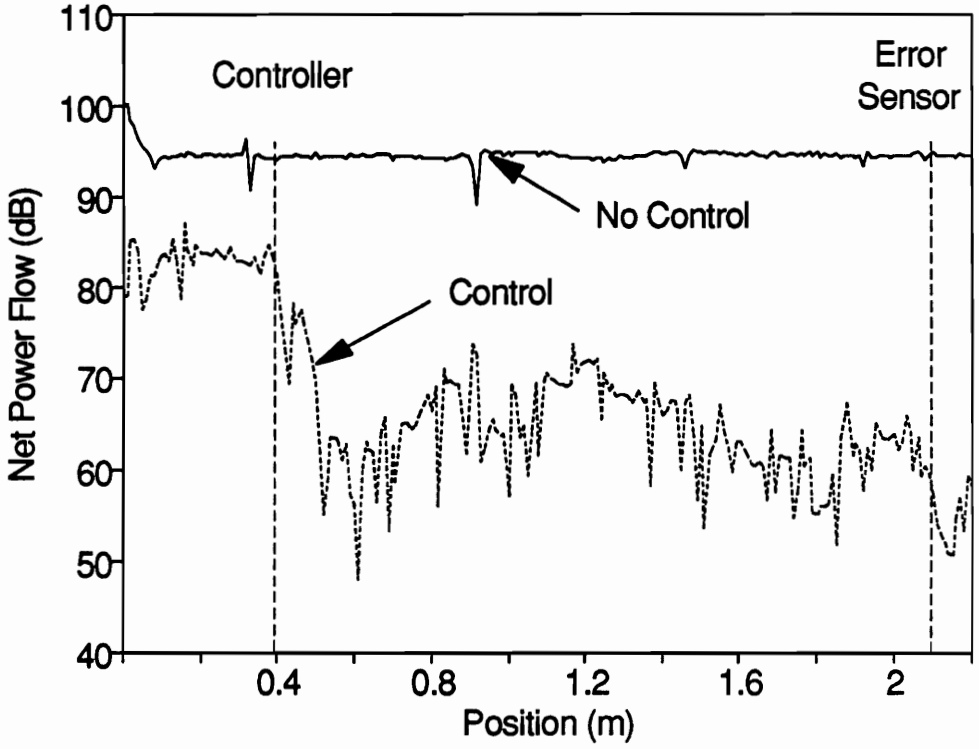

Figure 4.8 Power Flow Distribution
802 Hz, Semi-infinite Beam

4.3.5 Finite Beam Results

The remaining results are with the beam configured with the blocking mass installed. In this case we have a finite beam section between the free end and

the blocking mass. The velocity distribution for the 412 Hz case is shown in Figure 4.9. The blocking mass is located at 0.8 m from the free end as can be seen by the relatively low beam velocity at that point on the no control curve. With no control, a larger standing wave is present between the primary shaker and the blocking mass due to the presence of the blocking mass discontinuity. When control is applied, the velocity between the controller and the error sensor is attenuated on the order of 35 dB showing the effectiveness of the controller. The velocity of the beam between the primary shaker and the controller also drops. The controller imparts a boundary condition on the system which causes the finite portion of the beam to have a lower response. This result was thought to be due to the fact that the finite section of the beam is being driven off resonance. The upstream resonance behavior was studied theoretically in Chapter 2 for a semi-infinite beam under optimal controlled conditions. If the finite beam under optimal control produces near zero response downsteam of the control actuator, then the author believes that the presence (or dynamics) of the blocking mass does not affect the vibration upstream of the controller. The resonances of the upstream beam portion associated with the optimal control under this assumption would be unchanged, and could be compared to the theoretical resonances observed in Figure 2.18 on page 93. Note in the figure that 412 Hz is off resonance for the theoretical

case. Similar results have been observed in theoretical calculations using point force actuators.

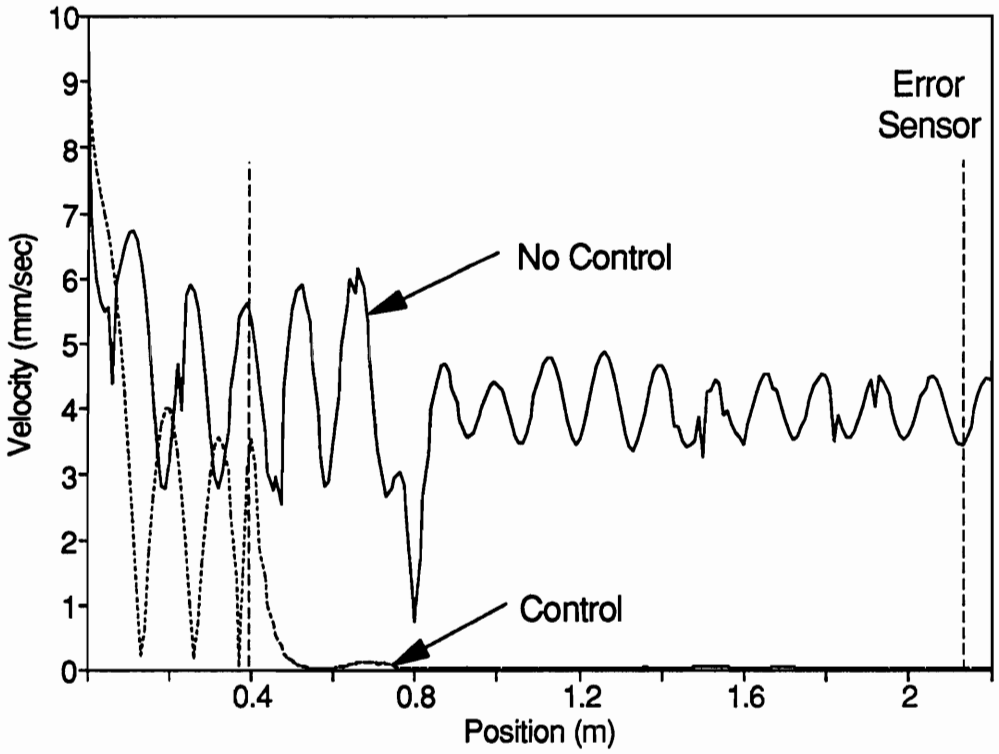

Figure 4.9 Flexural Velocity Distribution
412 Hz, Blocking Mass

The power flow distribution for the 412 Hz case is shown in Figure 4.10. Table 4.3 presents the real and imaginary portion of the input impedance at the primary input point. As seen in previous results, the power flow in regions downstream of the controller is reduced about 35 dB because of a reduction of

the real portion of the primary input impedance (see Table 4.3). The overall reduction in power flow at the error sensor was measured to be greater than 50 dB. Again it is believed that phase calibration errors between the force and velocity transducers caused the discrepancy between the the results of Table 4.3 and Figure 4.10.

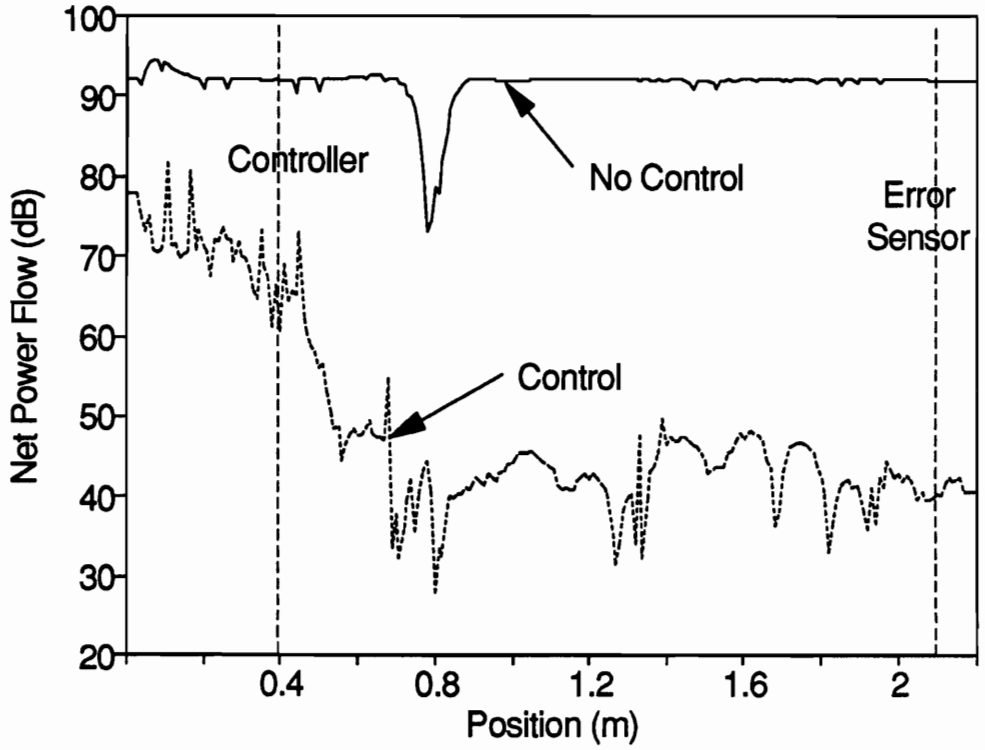

Figure 4.10 Power Flow Distribution
412 Hz, Blocking Mass

Table 4.3 Shaker Input Impedance
Blocking Mass

Frequency (Hz)	Input Impedance (N-sec/m)			
	No Control		Control	
	Real	Imag.	Real	Imag.
412	46.0	266.	3.66	235.
802	2.78	17.3	1.58	18.2

Note that the power flow distribution shows a large dip at the blocking mass location. This is due to the fact that, as discussed in Section 4.1.1, the power flow equations are based on a second order beam equation and thus does not include flexural nearfields. The results in Figure 4.10 thus imply that there are significant nearfields generated by the blocking mass.

It is also apparent by observing the large standing wave of Figure 4.9 that the vibration is attenuated immediately after the control actuator even though the error sensor is located out of the finite section of the beam. This result highlights the observation that if a power based cost function is used then control of the finite beam can be achieved with a single pair of actuators.

The velocity distribution for the 802 Hz case is presented in Figure 4.11. For the no control case, the standing wave between the primary shaker and the blocking mass is larger than previous cases because 802 Hz appears to be near a resonance of the finite portion of the beam. When control is applied, the velocity in the region between the blocking mass and the error sensor is attenuated on the order of 35 dB over the no control case. The velocity distribution can also be seen to be markedly reduced past the control actuator leading to a global reduction in beam response with one actuator pair.

The power flow distribution for the 802 Hz case is shown in Figure 4.12. The controller forces the input impedance of the primary shaker to be more reactive which reduces the power flow in the region downstream of the controller to be attenuated by about 40 dB.

It may appear as though the control actuators are absorbing energy (see Figure 4.10 for example). The apparent drop of the power flow distribution in the proximity of discontinuities such as the controller location and the blocking mass result is considered an anomaly, and is due to the nearfields associated with the discontinuity which are not modeled by the two point power flow estimation technique. It is also noted that the theoretical results in Chapter 2 for a semi-infinite beam only allow the control actuator to reflect the incoming

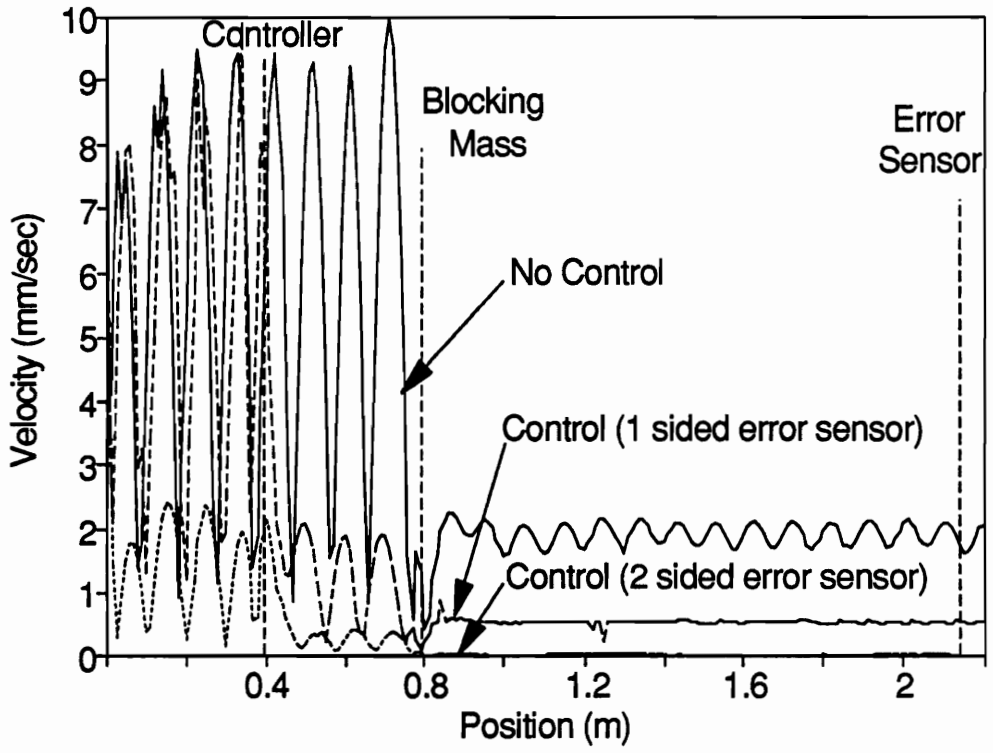

Figure 4.11 Flexural Velocity Distribution
802 Hz, Blocking Mass

waves back to the primary source producing a reactive input impedance at the primary shaker, and zero power flow throughout the beam. The theoretical results due not allow for the absorption of power flow by the controller.

It is also interesting to note the apparent drop in power flow across the blocking mass for the no control case. If there is conservation of energy on the beam,

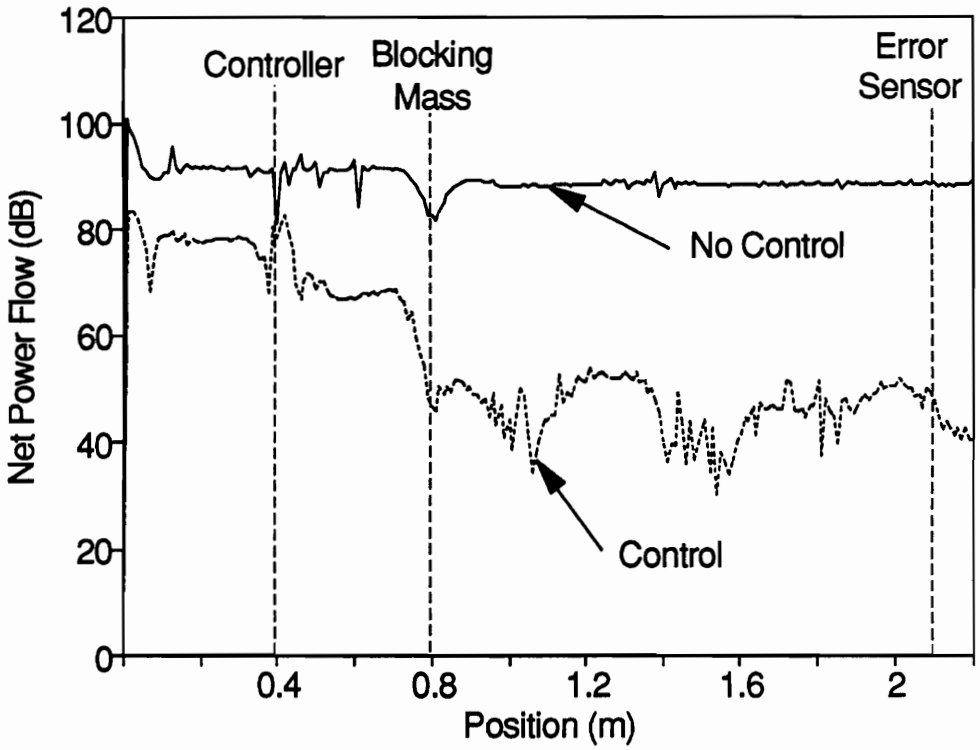

Figure 4.12 Power Flow Distribution
802 Hz, Blocking Mass

and there is only flexural motion then these values should be the same as the power flow technique measures net power flow. It was thought that a wave conversion phenomena was occurring at the blocking mass discontinuity. Due to the distributed nature of the blocking mass, flexural waves were thought to be coupling into extensional waves on the beam at the mass discontinuity location. As these waves are largely unobservable by the laser vibrometer and

can carry high power (due to the beam being stiffer in extension), the measured power flow falls by around 5 dB. The power flow drop across the blocking mass could also be caused by air damping of the mass discontinuity or mechanical damping associated with the clamped interface between the mass and the beam.

Extensional waves were also found to be present on the error sensors. Figure 4.11 shows the velocity distribution of the beam driven at 802 Hz with blocking mass number one on the beam for three different situations. When a single error sensor element was used on one side of the beam, while the error signal was attenuated by 40 dB, the laser vibrometer showed attenuations of only on the order of 10 dB. The error signal was thought to be comprised of a flexural wave superposed with an extensional wave, and the controller reduced the superposed signals at the error sensor location by 40 dB while neither component was necessarily reduced by as much. This problem was cured by using two matched piezoceramic elements in symmetric pairs with their signals summed 180° out of phase as shown in Figure 4.11. As will be shown in the next section, simultaneous control of flexural and extensional waves is demonstrated by letting the symmetric elements of the actuator and sensor be floating transducers of a two channel adaptive controller.

4.3.6 Discussion

The active control of flexural vibrations and power flow has been experimentally studied. In particular, the proceeding experiments demonstrated attenuations in flexural power flow and vibrations in both semi-infinite and finite beams on the order of 30 dB or more using piezoceramic transducers bonded symmetrically on each side of the beam, and hard wired out-of-phase, in conjunction with an adaptive LMS controller. The approach used in the experiments has also been demonstrated to be robust with high attenuations obtained over a wide range of frequencies and differing beam configurations.

In conjunction with the control experiments, the use of a laser vibrometer as a non-contacting sensor to measure beam out-of-plane velocity and more importantly flexural power flow has been demonstrated. This device shows much potential for research in structural energy flows.

The work clearly demonstrates that piezoceramic elements have much potential for active/adaptive control of power flow in structures. These elements have both size and weight advantages over conventional transducers and in conjunction with multi-channel controllers are a step towards the creation of highly integrated distributed control systems.

4.4 Simultaneous Control of Flexural and Extensional Power Flow using Piezoelectric Error Sensors

In this section the simultaneous control of flexural and extensional vibrations in thin elastic beams is experimentally investigated. The results demonstrate that using pairs of piezoelectric transducers, whose elements are symmetrically located and independently controlled by means of a two channel controller, enables the high attenuation of both flexural and extensional power flow. This capability is due to the nature of the piezoelectric element, which when bonded to the surface of the structure and electrically excited, exerts a surface strain on the structure (see Chapter 2). The strain enables input of both in-plane forces, and flexural moments into the structural system.

4.4.1 Experimental Arrangements

The experimental arrangement used in the following experiments is shown diagrammatically in Figure 4.13. A photograph of the experimental arrangement is presented in Figure 4.14. The beam is thin aluminum and is dimensionally identical to that presented in the previous sections. The sand anechoic termination (for flexural waves only) has been demonstrated to have a

flexural power flow reflection coefficient of less than 0.1 for frequencies greater than 150 Hz. The primary source was applied as a point force at the free end. In order to generate a combination of flexural and extensional waves the angle at which the force was applied relative to the neutral axis was set to 10^{o}. For all tests described in this section, the primary signal consists of a pure tone sinusoid.

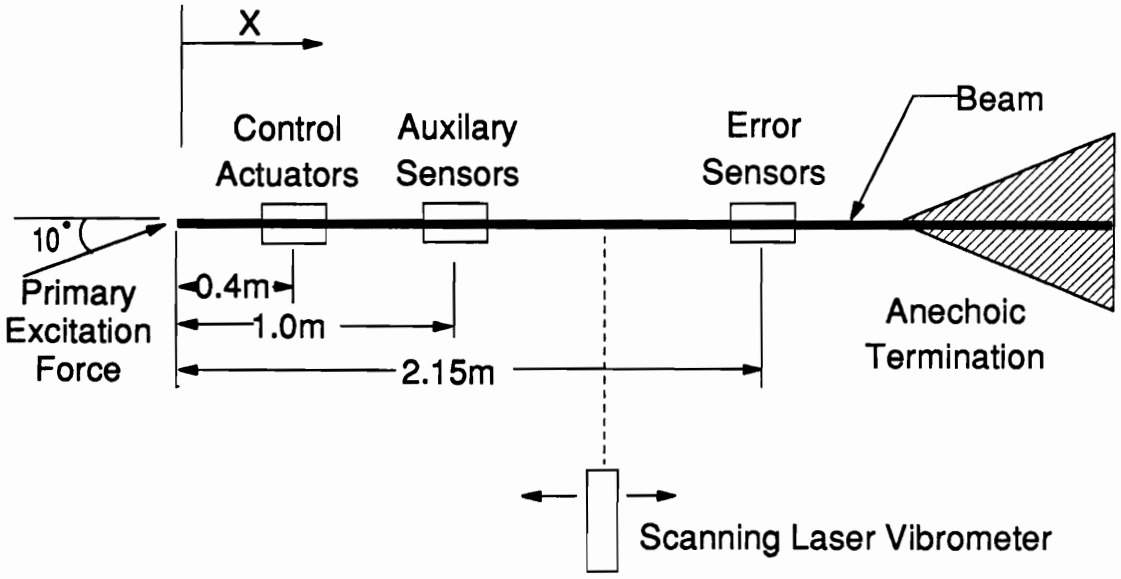

Figure 4.13 Experimental Schematic

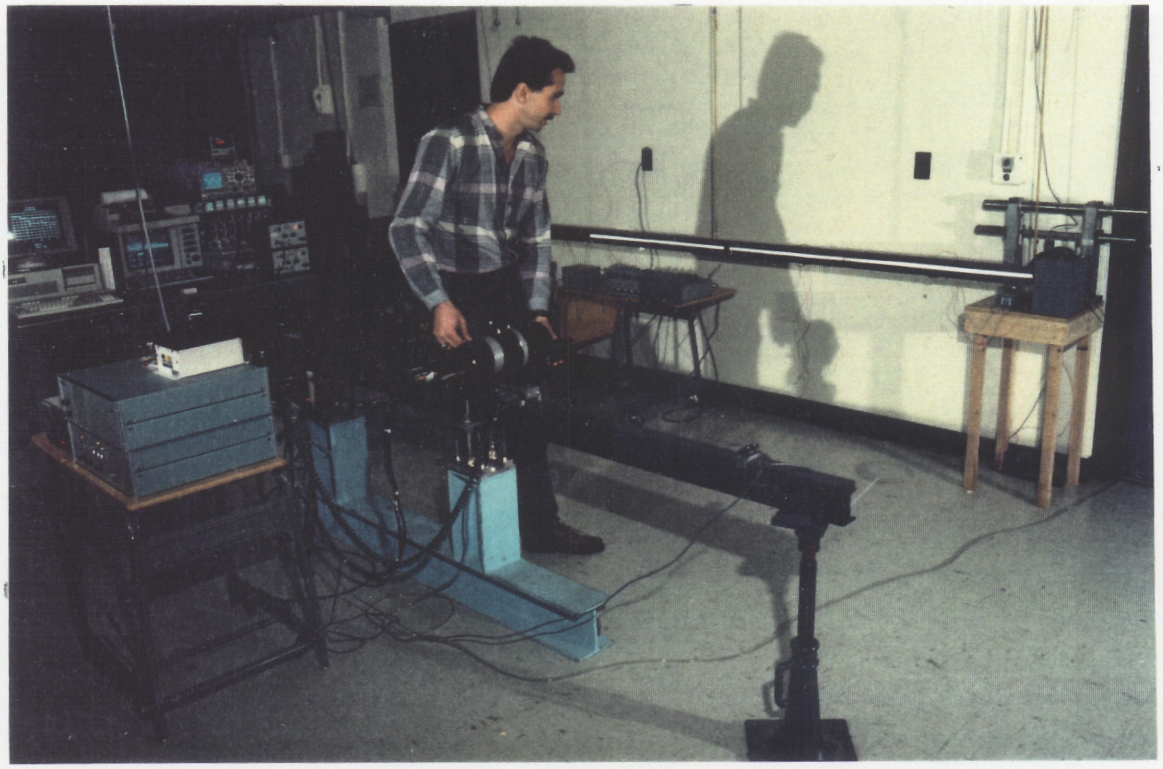

Figure 4.14 Photograph of Experimental Arrangement

In order to provide control inputs to the beam, two symmetrically bonded piezoelectric elements were bonded to the surface of the beam at a distance of 0.4m from the free end of the beam. These elements were 38.1mm x 22.2mm x 0.18mm in size and were made of Lead Zirconate Titanate material (Piezo Systems, 1987). The two actuators were driven from two independent output channels of an adaptive control system through B&K power amplifiers and 9 to 1 transformers (used to increase the voltage output of the B&K amplifiers from a maximum of about 40 volts peak to peak to about 360 volts peak to peak).

At a distance of 2.15m from the free end, two additional like size elements were bonded symmetrically on either side of the beam and used as independent control error sensors. An additional pair of piezoelectric transducers were located at 1m from the free end. These sensors provided independent verification that the controller was indeed performing as indicated by the error sensors (driving error signals to small values does not necessarily imply global control of the beam vibration). The out-of-plane velocity of the beam was measured with an axial scanning laser vibrometer. This instrument was used to provide independent measurements at 1 cm intervals along the beam.

4.4.2 Control Implementation

The active control system used in this experiment implemented the multiple channel Filtered-x LMS control algorithm discussed in Chapter 3. The control system is depicted in block diagram form in Figure 4.15. The function of the controller is to optimize (in terms of magnitude and phase) the control voltages from the control actuators such that the mean square amplitudes of the error signals are minimized. For the tests presented in this section, a steady state sinusoid was used as the noise signal. It was taken from a reference oscillator that provided the training or reference signal for the LMS adaptive controller. The adaptive control algorithm was implemented on a PC based TMS320C25 digital signal processing board using assembly language. The sample rate was

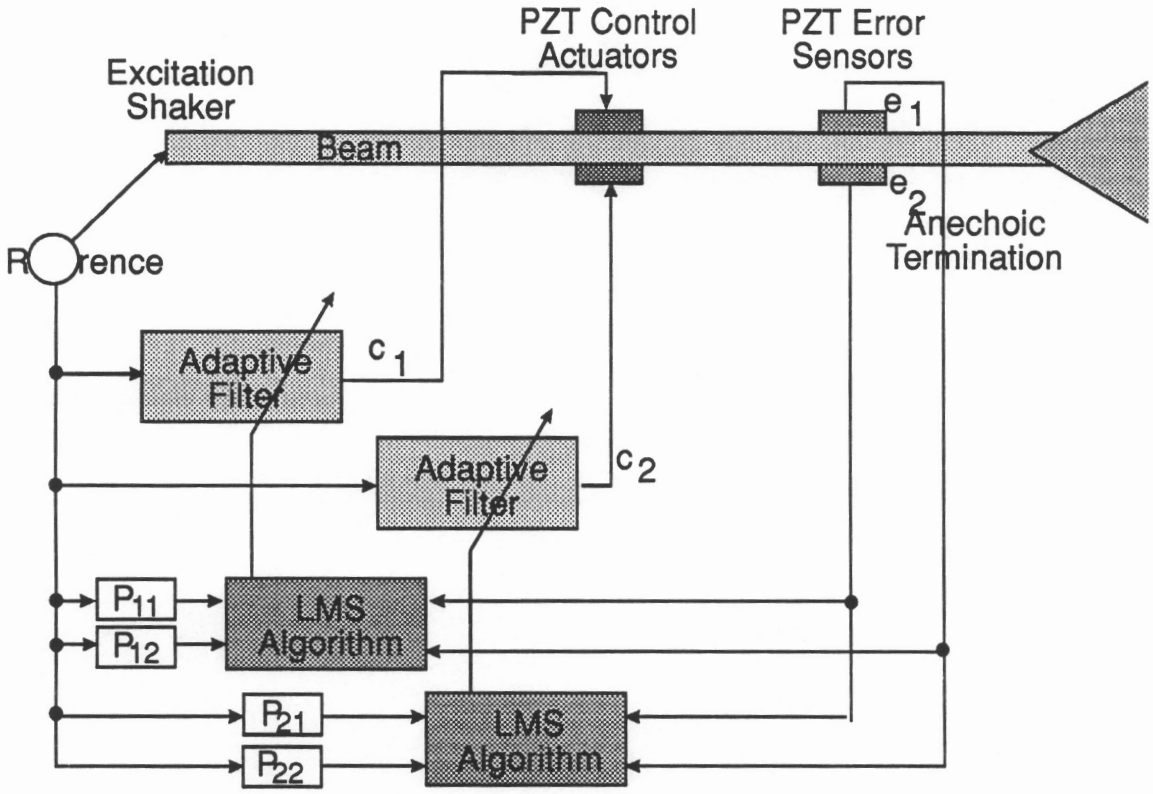

Figure 4.15 Controller Block Diagram

fixed at 5 kHz. It should be noted that the variable being minimized is the square of the voltage of the error signals. As was shown in Chapter 2. this variable is proportional to the square of the surface strain in the beam. Thus, the function to be minimized can be seen to be proportional to the vibrational energy integrated under the sensor. Minimizing this variable globally, or at a number of points implies control of vibrational power flow for flexure and extension in this semi-infinite configuration.

4.4.3 Experimental Procedure

In order to determine reasonable test conditions, the beam response to separate extensional and flexural excitations was examined. The signals corresponding to the outputs of the symmetric pairs of piezoelectric elements were matched by the following procedure. First, the beam was subjected to a point force at the free end normal to the surface of the beam and well off resonance of extensional motion (see Figure 4.16), thus producing primarily flexural motion. Next the output of each sensor was passed through an ithaco amplifier with variable gain, and the outputs were adjusted to have comparable magnitudes. The phase was observed to be 180 degrees plus or minus 2 degrees. This method was thought to be the best available to match the sensors considering the difficulty in measuring (and calibrating sensors for) extensional strains on the order of 1 μs. Finally, the electrical signals from each pair of adjacent sensor elements was summed and differenced which provided signals corresponding to extensional and flexural wave components, respectively. The appropriate response derived for the error array (2.15m) is shown in Figure 4.16 for two excitation conditions. The extensional wave excitation was obtained by inputing random noise to the control actuators with both being driven in-phase. This technique produced a response that was primarily extensional, and had strong resonant peaks implying that the termination is not effective for extensional waves. These extensional

resonances were at frequencies of 675 Hz and 1312 Hz. The response is normalized to the peak value for this excitation.

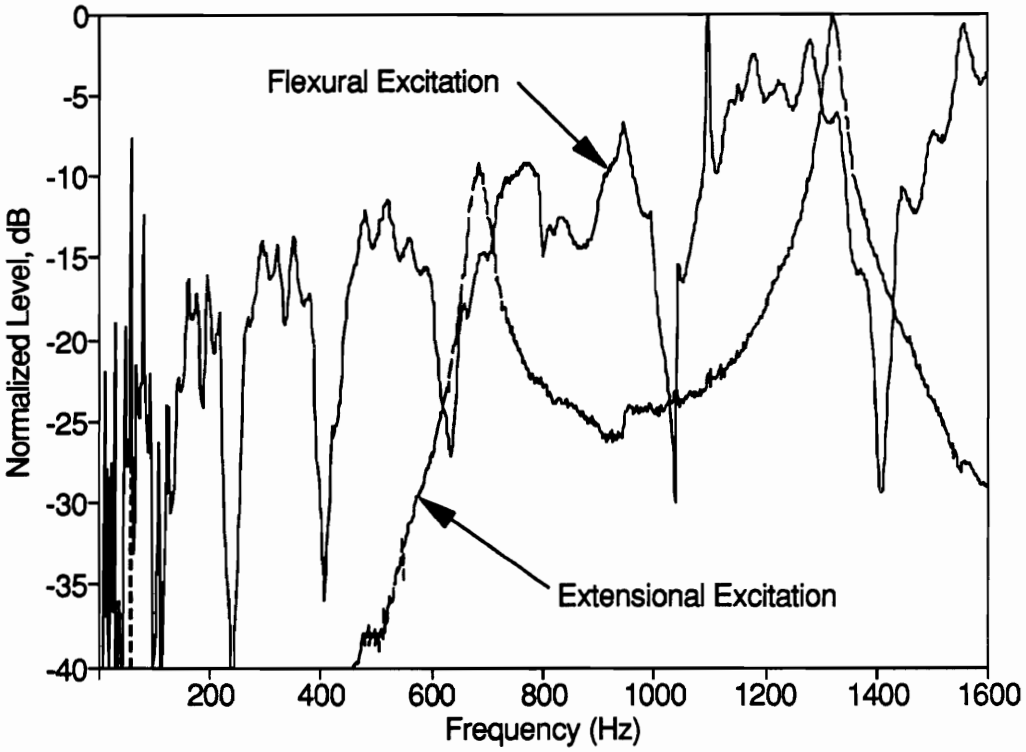

Figure 4.16 Normalized Response of Beam to Broad Band Extensional and Flexural Excitation by Control Transducers

To examine the flexural response, the control actuators were again excited by random noise but this time with inputs 180 degrees out-of-phase. This produced differenced output at the error sensor array corresponding to the flexural wave response. The response is normalized to the peak value for this

excitation and clearly demonstrates the effectiveness of the termination to flexural waves. The nulls in the response correspond to the reflections of waves from the primary end superimposing exactly out-of-phase with waves generated by the piezoelectric actuators traveling toward the termination. These nulls are not present in the responses driven by the primary shaker only.

Using these results, frequencies of 704 Hz and 1312 Hz were chosen as test conditions because the extensional and flexural motions excited by the piezoceramic control actuators were of comparable magnitudes near extensional resonances. These frequencies allow for the limited excitation capability of the piezoceramic actuators when driving relatively long wavelength extensional waves (see Section 2.1.2).

For the baseline response no control was exercised over the primary excitation. The extensional and flexural responses from the summed and differenced sensor outputs provided the baseline against which control cases were measured. The results in Table 4.4 and Table 4.5 are normalized to this baseline response. In order to control the flexural response, the two piezoceramic actuators inputs were hard wired so as to be driven 180 degrees out-of-phase to create a single flexural control actuator. Similarly, the differenced output of the error sensors was used as the single error variable

with the output of the controller driving the above control excitation. To control the extensional response, the two piezoceramic actuators inputs were hard wired in-phase to create a single extensional control actuator. This arrangement was used in a single channel controller to drive the summed error sensors to a minimum resulting in control of the extensional wave response.

Finally, simultaneous control of both flexural and extensional response was implemented driving each control actuator as an independent control variable and using the output of each error sensor as an error signal. In this configuration, no derived signals were used in the control implementation, and thus a coupled controller where each actuator and sensor can couple into both flexural and extensional motion was created. This configuration resulted in better equalization of error sensor levels and excitation voltages than if the summed and differenced signals had been used. The configuration is less susceptible to spillover problems which occur, for example, when a particular wave type (i.e. flexural) is created by the imperfections of an actuator pair hard wired in-phase to excite pure extension.

4.4.4 Experimental Results

Table 4.4 presents the summed and differenced voltage outputs of the

piezoceramic sensors located at 1.0m and 2.15m at an excitation frequency of 704 Hz. As stated previously, the transducer at 2.15m was used to provide the error signals for the adaptive controller. The results are presented in terms of the attenuation in decibels relative to that sensor output with no control applied. For no control the flexural response was 11.8 dB less than the extensional at 1.0m and 16.1 dB less at 2.15m.

Table 4.4 Attenuation (dB re no control) at 704 Hz

Sensor Position	1.0 m		2.15 m	
Test Condition	Extensional (Summed)	Flexural (Differenced)	Extensional (Summed)	Flexural (Differenced)
Flexural Control	0.054	17.0	0.0055	31.0
Extensional Control	39.1	-12.8	32.6	-4.79
Flexural-Extensional Control	34.6	25.4	36.3	20.5

When the flexural vibrations were controlled, the summed error signals corresponding to the extensional motions show little attenuation whereas the differenced outputs corresponding to the flexural motion showed attenuations of 17 and 31 dB at beam locations of 1.0m and 2.15m, respectively. This attenuation implies a significant reduction of flexural motion with little control of

extensional as dictated by the fixed out-of-plane relationship of the control transducers sensing and actuating primarily flexural motion.

For control of extensional motion the reverse situation is true, with attenuations of 39.1 and 32.6 dB of the extensional response and an increase in flexural motion of 12.8 and 4.8 dB at 1.0m and 2.15m locations, respectively. Here the fixed in-plane relationship of the control transducers allowed control of only extensional motion, although some flexural motion was thought to be excited by the controller spillover. This spillover can occur if either control actuator is of a slightly different size, axial position, thickness, or different material property with respect to the other. Since the actuators are excited with the same voltage but are asymmetric as a pair (due to the aforementioned reasons) with respect to the beams neutral axis, then they will produce a slightly asymmetric strain distribution in the beam resulting in flexural motion. The spillover is confirmed by the increase in the sensor outputs of over 4.8 dB in flexure for the extensional control case as seen in Table 4.4.

Finally when simultaneous control of both motions was exerted, attenuations of 20.5 dB or greater in flexure and 34 dB or greater in extension was observed. In this case the control transducers (both actuators and sensors) are used independently and the controller finds its optimal solution by driving both error

signals to low values simultaneously. The similar trends of both piezoceramic sensor arrays indicated that an overall reduction of power flow beyond the control actuator has occurred as the sensors are not spaced at a multiple of half a wavelength in flexure or extension, and thus both locations can not be at a node.

As a further conformation of the extent of control, the axial distribution of the beam out-of-plane velocity is shown in Figure 4.17. This was measured by the axial scanning laser vibrometer. The results show that the beam velocity is reduced significantly for both cases of flexural control alone and simultaneous flexural-extensional control. It is also interesting to note that for the no control case there is a significant standing wave on the beam (for flexural motion) that is significantly reduced when extensional control is used corresponding to flexural traveling wave reflection coefficients, R_{tf}, of approximately 0.38 and 0.1, respectively. This result illustrates the wave conversion phenomena discussed previously and is most likely due to extensional waves reflected as flexural motion at the beam termination (as the termination is not anechoic for extension). Note the standing wave re-appears when flexural control is employed and is suppressed when both flexural and extensional control is used corresponding to flexural traveling wave reflection coefficients, R_{tf}, of approximately 0.42 and 0.2, respectively.

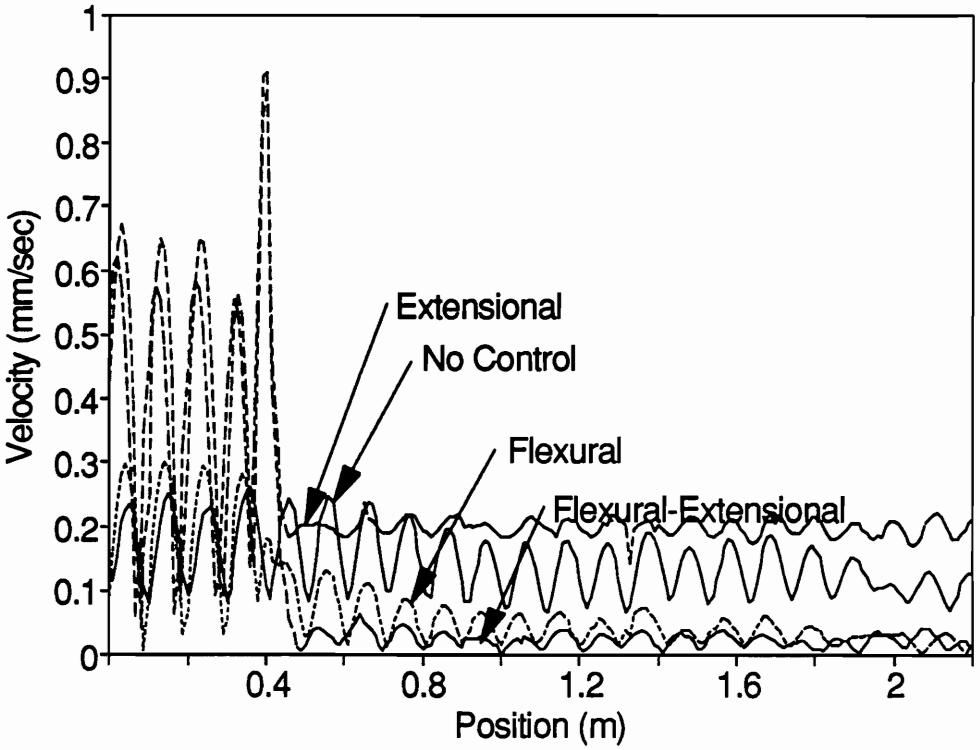

Figure 4.17 Flexural Velocity Distribution, 704 Hz

It is also apparent from Figure 4.17 that although there is significant standing wave on the "semi-infinite" beam, the control inputs drive the beam response to zero past their location. This result should be contrasted to the modal approaches (Meirovitch and Norris, 1984) in which as many control inputs as modes are required. As the beam displacement in both extension and flexure

is highly attenuated along the beam length, one can conclude that the total vibrational power in the beam (excluding torsional) has been controlled.

Similar results were found for the 1312 Hz case. These results are presented in Table 4.5 for both the sensor array at 1.0m and the error sensor at 2.15m. For control of flexural response, attenuations of 33.0 and 41.7 dB were recorded at 1.0m and 2.15m, respectively. Little change was affected at either location for the extensional response in this case. As expected for the extensional motion control, the reverse was found to be true with attenuations of greater than 10 dB for the extensional response and less than 1 dB for the flexural response. The case for simultaneously controlling both extensional and flexural response shows excellent control with the extensional response attenuated by 24 dB or greater, and the flexural response attenuated by 36 dB or greater. The axial out-of-plane velocity distributions measured by the laser vibrometer shown in Figure 4.18 yield similar results to Figure 4.17 except that the flexural response did not measurably increase for the extensional control case. This result is also apparent in the results of Table 4.5. In Figure 4.18 little change in the out-of-plane distribution is observed when extensional control is applied. It may be deduced that for this frequency little flexural-extensional coupling is occurring, most likely due to direct flexural reflection. However, it should be noted that this standing wave ratio of approximately 0.25

leads to a flexural power reflection coefficient of approximately 0.06. Thus, the termination is still relatively effective, in terms of power, at this frequency.

Table 4.5 Attenuation (dB re no control) at 1312 Hz

Sensor Position	1.0 m		2.15 m	
Test Condition	Extensional (Summed)	Flexural (Differenced)	Extensional (Summed)	Flexural (Differenced)
Flexural Control	-0.81	33.0	0.51	41.7
Extensional Control	9.8	0.25	46.4	-0.05
Flexural-Extensional Control	23.9	36.6	27.7	40.2

4.4.5 Discussion

In this section, the results show that by using two symmetrically located piezoceramic elements as actuators and sensors in conjunction with a multi-channel adaptive controller, simultaneous attenuation of both extensional and flexural motion is achievable. This ability is due to the nature of the each piezoelectric element which, when bonded to the surface of a structure and activated by an oscillating voltage, generates corresponding oscillating stress distributions which couple to both flexural moments and in-plane forces within

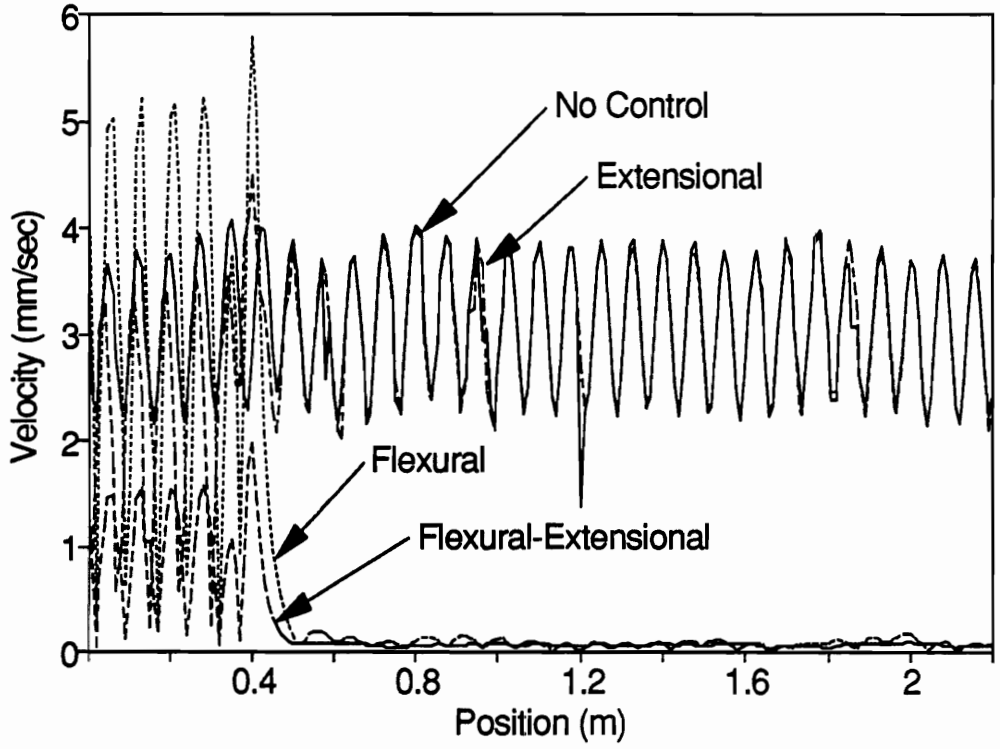

Figure 4.18 Flexural Velocity Distribution, 1312 Hz

the structure. These relatively small light weight devices can effectively actuate and sense both flexural and extensional beam motions.

4.5 Simultaneous Control of Flexural and Extensional Power Flow using Real Time Wave Vector Filtering

In this section, control of both flexural and extensional power flow in a test beam using real time wave vector filtering (as introduced in Chapter 2) will be demonstrated. The wave vector filtering discriminates the net positive traveling flexural waves from the net negative traveling flexural waves for band limited spectra in real time. The same is true for the extensional case. The results will show this to be an extremely efficient method to sense and control flexural and extensional power flow in finite or semi-infinite beams. The experimental results discussed in this section will be compared to the corresponding theoretical beam responses (both before and after control) predicted using the analysis outlined in Chapter 2. Comparisons will be made in terms of beam out-of-plane velocity distributions, in-plane strain distributions, traveling flexural and extensional wave amplitudes, and flexural and extensional power flow.

In this set of experiments, the wave vector filters were used to control flexural and extensional power flow at single or multiple frequencies. It is noted that the wave vector filters are designed for broadband excitation, and were not re-

designed as the experimental arrangement or frequency varied during the experiment.

4.5.1 Experimental Arrangement

A schematic for the experiment is shown in Figure 4.19, and a photograph of the experiment is shown in Figure 4.20. The beam is made of aluminum, and is 4 m long x 76.2 mm wide x 3.175 mm thick. The beam is fitted with a termination consisting of a diverging wooden box filled with sand. The diverging box has an initial inside dimension of approximately 5 cm by 8.75 cm and diverges to approximately 45 cm x 45 cm over a length of 45 cm of the beam. The termination has been previously tested have a flexural power reflection coefficient of less than 0.1 for frequencies above 150 Hz. Due to the extreme length of extensional waves the termination was ineffective at absorbing extensional energy. For the first set of experiments the beam is denoted semi-infinite, and the termination was used in its standard configuration. For the second part of the experiments the beam is denoted finite, and aluminum blocks were inserted into the termination at the entrance to cause the termination to be much more reflective. For the configuration presented in this paper, the termination had a flexural traveling wave reflection coefficient of about 0.5, and an extensional wave reflection coefficient of about 0.9 at 608 Hz.

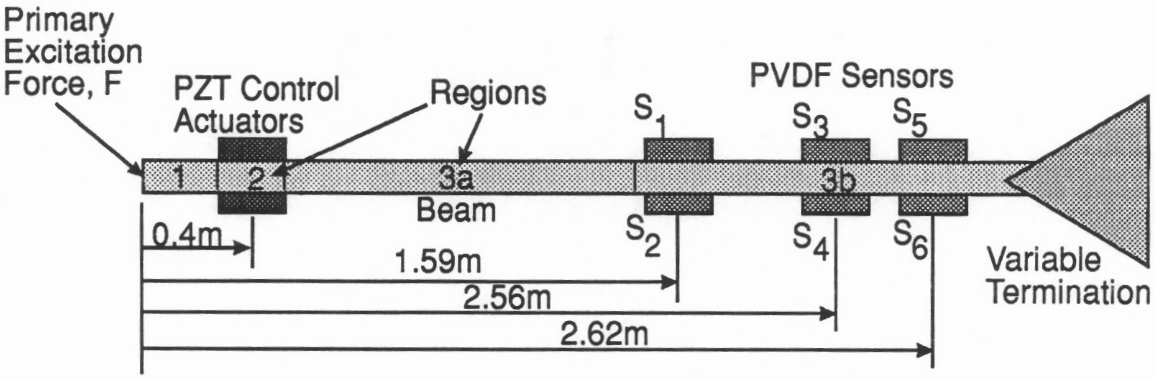

Figure 4.19 Schematic of the Experimental Arrangement

The primary source (noise source) was applied at a 40 degree angle relative to the neutral axis of the beam. Two piezoelectric (PZT) actuators shown in Figure 4.21 were bonded 0.4m from the free end of the beam and were driven independently. As detailed in Chapter 2, these actuators can simultaneously excite both flexural and extensional waves with arbitrary amplitudes. These actuators were bonded to the surface of the beam using an epoxy adhesive. Copper foil strips were soldered to either side of the PZT providing a solder attachment location for the 18 gage copper wire leads. These control actuators have size and material properties listed in Table 4.6.

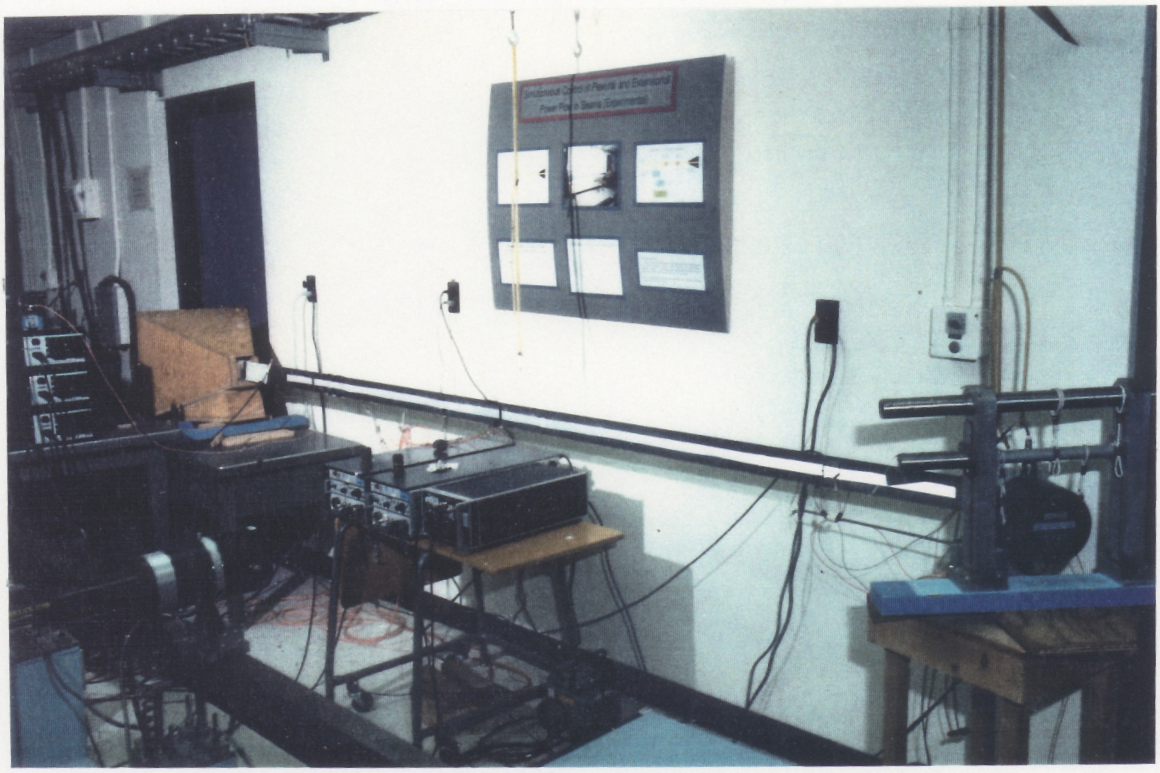

Figure 4.20 Photograph of Experimental Arrangement

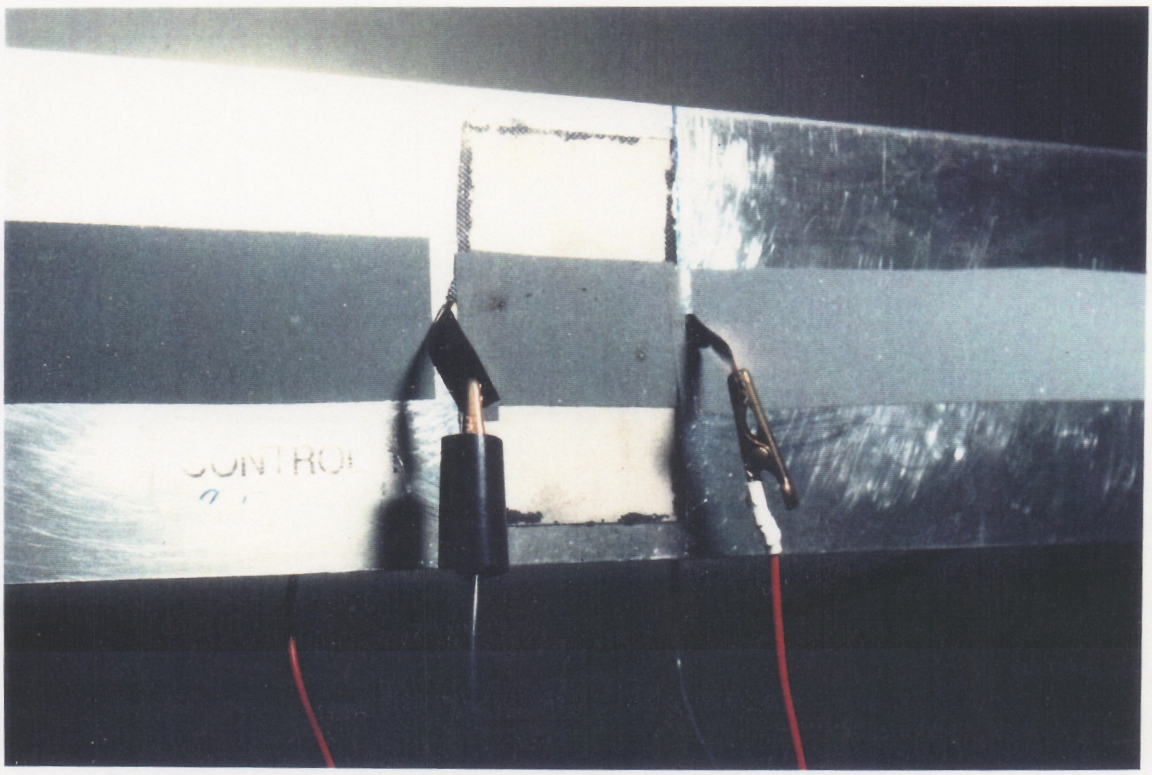

Figure 4.21 Photograph of Piezoelectric Control Actuators

The beam was also fitted with an array of 6 PVDF sensors as shown in Figure 4.19 and Figure 4.22 that were used in conjunction with a digital filter network (as outlined in Chapter 2) to provide a real time estimate of the traveling flexural and extensional waves in the beam. These sensors had dimensions and material properties listed in Table 4.7. The PVDF sensors were bonded to the beam using Tuck double sided tape. A single 3M 0.025 mm thick copper foil strip coated with conductive adhesive was used to attach 18 gage wire to either side of the fragile PVDF sensor.

Table 4.6 Material Properties of Piezoelectric Material G-1195

Name	Symbol	Value	Units
Piezoelectric Strain Coefficient	d_{31}	166E-12	m/V
Density	ρ	7600	kg/m^3
Elastic Modulus	E_{33}	4.9E+10	N/m^2
Elastic Modulus	E_{11}	6.3E+10	N/m^2
thickness	T_a	0.1778	mm
length	L_a	3.81	cm
width	L_y	6.35	cm

Table 4.7 Material Properties of Polyvinylidene Fluoride (PVDF)

Name	Symbol	Value	Units
Piezoelectric Stress Coefficient	e_{31}	65.3E-3	C/m^2
Density	ρ	1780	kg/m^3
Elastic Modulus	E	2E+9	N/m^2
Permitivity	ε	106E-12	F/m
thickness	T_s	0.028	mm
length	L_s	1.0	cm
width	L_y	7.62	cm

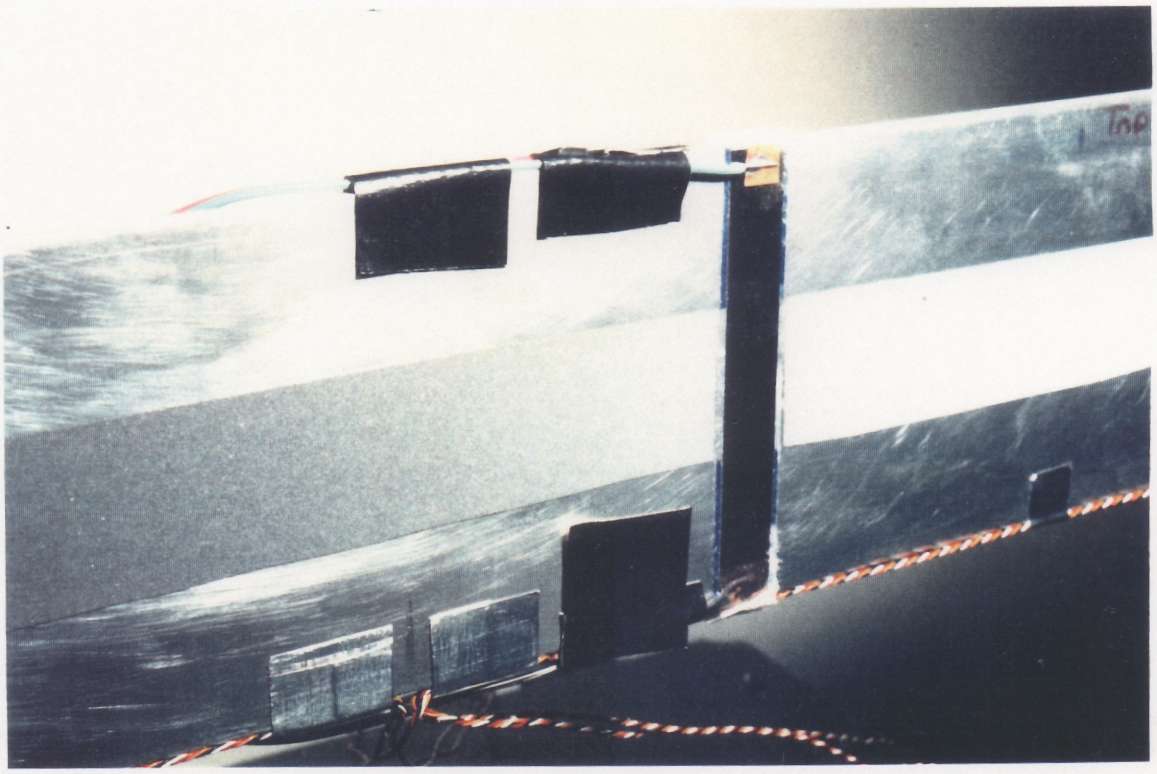

Figure 4.22 Photograph of PVDF Sensors

The beam is also fitted with semi-conductor strain gages configured to measure in-plane motion only as shown in Figure 4.23. At each strain gage station there are four strain gages (two per side) mounted at the same axial location. These strain gages are mounted in each of four arms of a Whetstone bridge. Two of the gages are configured to measure axial strain, and are located in opposite legs of the bridge. The remaining two strain gages are mounted in the y direction as to be sensitive to Poisson's coupling effect, and are mounted in the remaining opposite arms of the bridge. This configuration provides the most

sensitive bridge arrangement for measuring in-plane motion. There are a total of four stations located axially on the beams at points, 0.6m, 1.4m, 1.9m, and 2.7m from the free end. All of the gages are of the semi-conductor type and have an extremely high gage factor of 100.

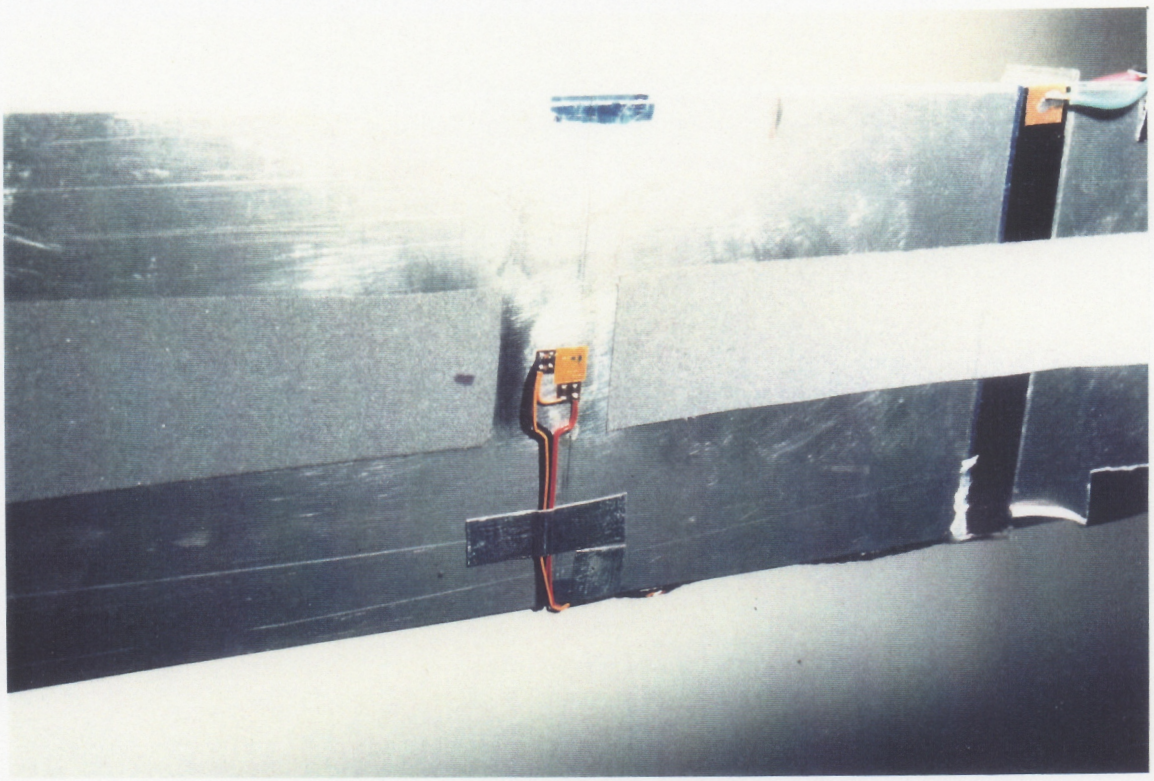

Figure 4.23 Photograph of Semi-Conductor Strain Gage Station

An axial scanning Dantec laser vibrometer was also used to measure out-of-plane velocity. The beam was scanned at discrete locations starting at the free end and continuing at 1 cm increments to a distance of 2.7m from the free end. The complex velocities were determined by a B&K 2032 signal analyzer. The

scanning was controlled by a IBM compatible computer which simultaneously manipulated the B&K analyzer, and the scanning stepper motor as well as being the host for the digital control board. The velocity results were later processed to estimate the flexural waves present using the deconvolution technique and subsequent power flow as outlined in Section 4.1.

Additionally there is a force transducer mounted between the primary shaker and the beam to determine the primary input force both before and after control. This force will be used to determine the theoretical beam response before and after control such that a comparison can be made between the experimental and theoretical beam in-plane and out-of-plane motion and power flow.

4.5.2 Control Implementation

A schematic of the adaptive control system used in this portion of the experiments is shown in Figure 4.24. The controller uses the Filtered-x LMS adaptive technique discussed in Chapter 3. This algorithm is a time domain adaptive algorithm which requires a time domain error signal correlated with the function to be minimized. In these experiments, the new time domain sensing technique termed wave vector filtering outlined in Chapter 2 is used to provide real time estimates of the net positive and net negative traveling flexural and extensional waves from PVDF based surface strain measurements. The wave

vector filtering scheme provides an estimate of the traveling waves in a structure in the time domain. Determination of wave estimates traditionally would require post processing of frequency domain data. In the configuration used in this experiment, PVDF sensors are mounted on the beam to provide 6 independent measurements of beam response. Sensors 1 and 2, as well as sensors 5 and 6, are summed in order to provide voltages proportional to extensional motion only. These two stations are input to a digital filter network implementing the Time Delay method as described in Chapter 2. The digital filter network outputs two signals proportional to the complex positive and negative traveling extensional waves (waves E, and F from Equation (2.41), respectively). As derived in Chapter 2, the Time Delay Method only provides extremely accurate wave filtering for non-dispersive media (or relatively non-dispersive over some frequency range). Secondly, sensors 3 and 4, as well as 5 and 6, are differenced in order to only provide voltage signals proportional to flexural motion. These two stations are input into another parallel digital filter network which estimates the positive and negative traveling flexural waves (with amplitudes A and B from Equation (2.34), respectively) using the Cotangent Method as derived in Chapter 2. The Cotangent Method previously discussed in Chapter 2 is used to filter traveling waves in both dispersive and non-dispersive media. However, the Time Delay Method is used for non-dispersive media because of its increased accuracy and lower overhead (as discussed in

Chapter 2). The wave vector filtering network effectively synthesizes wave vector estimates which will be input as the error signals of the Filtered-x LMS adaptive algorithm for both flexural and extensional traveling waves.

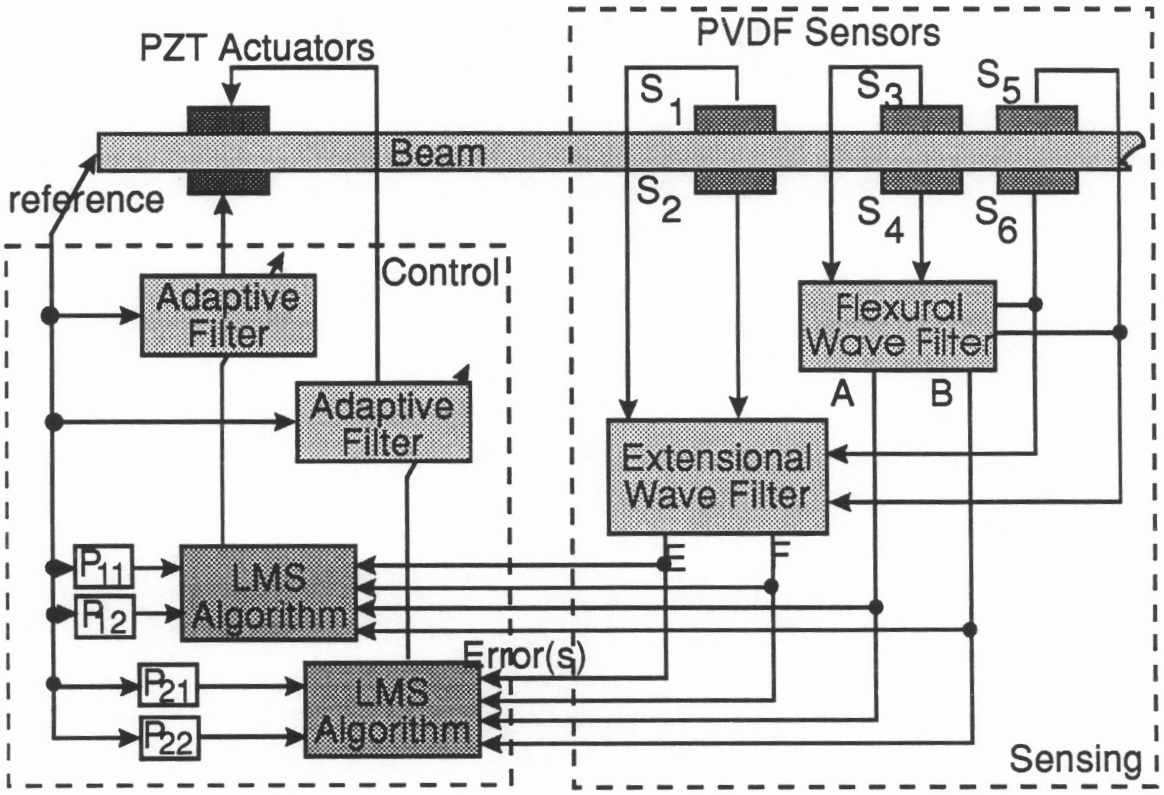

Figure 4.24 Controller Block Diagram

In this experiment, the controller will be configured to use the wave vector estimates A and E as error signals for the controller. The controller will minimize the square of the flexural and extensional waves traveling into the termination. The error signals are proportional to the traveling flexural and extensional waves, and as discussed in Chapter 2 are proportional to the

square root of the power flowing in the beam. The exact details of the control algorithm were previously presented in Chapter 3. The control algorithm was implemented using a TMS 320C25 signal processing board resident in an IBM compatible PC computer. The sampling rate was fixed at 5.3 kHz corresponding to the maximum possible value in order to complete all the computational tasks required by this control system on the TMS 320C25 signal processing board. Note that the Time Delay Method requires the corresponding structural sensors to be half a wavelength at the Nyquist frequency (2650 Hz in this case). Since extensional waves are relatively long, the spacing of 1.03m was required as shown in Figure 4.19. If a larger sample rate is achievable then a proportionally shorter spacing could be used. The primary (noise) input was driven by a 10 pound B&K shaker with a pure tone sinusoidal input. The pure tone was also used as the reference signal for the control algorithm, but in general this reference signal can be measured from exciting machinery or synthesized from information related to the vibrational frequency.

4.5.3 Experimental Procedure

For this experiment the beam was tested under two different configurations. In the first configuration termed "semi-infinite," the termination was made to absorb as much flexural wave energy as possible, and thus appeared nearly semi-infinite for flexural waves (the largest flexural traveling wave amplitude reflection

coefficient for all test frequencies was 0.18). The beam response before control for the semi-infinite case consisted primarily of a single positive flexural wave traveling into the termination.

In the second configuration, the termination was configured to reflect a large portion of the flexural energy back towards the source. This configuration is called the "finite" beam case, and has a flexural traveling wave reflection coefficient greater than 0.46 for all test frequencies. The beam response due to the primary excitation consisted of large positive and negative traveling flexural waves providing a more stringent test for the wave vector filtering.

In both configurations, the beam was highly resonant in extension which again corresponds to large positive and negative traveling extensional wave components. In a general beam structure containing multiple beam elements connected by various boundary connections, the nature of the wave reflection coefficients can vary greatly. It is desirable to be able to control the energy transmission for beam systems with variable termination impedances. As was shown in Chapter 2, it is possible to isolate all energy transmission in a beam downstream of the control point for a beam with a point force primary excitation at the free end and secondary piezoelectric excitation at an arbitrary location

along the beam. The finite and semi-infinite configurations are used to demonstrate control robustness over a range of boundary conditions.

For the semi-infinite case, frequencies of 608 Hz, and 1120 Hz were tested. For the baseline response, no control was exercised over the Primary excitation. The out-of-plane velocity distribution along the beam, the in-plane strain at the strain gage locations, and the PVDF sensor complex amplitudes were measured. Control was then applied to the system, and after steady state was reached, the same measurements were made to compare with the no-control case.

For the second case, the termination was partially blocked off resulting in a more resonant primary field. A frequency of 608 Hz was tested. Again, the baseline response was a function of the primary excitation only. The out-of-plane velocity distribution along the beam, the in-plane strain at the strain gage locations, and the PVDF sensor complex amplitudes were measured both before and after control.

4.5.4 Data Analysis

In this section the data analysis and data reduction will be described. As stated previously, the out-of-plane velocity distribution along the beam was recorded

both before and after control. This data will be used to determine the positive and negative flexural traveling wave components, and subsequent power flow in various regions of the beam. In Section 4.1.2, the deconvolution of flexural traveling waves and nearfields from velocity data was described in detail. In this section the application of this technique to the data obtained experimentally will be examined. The wave decomposition technique will in a least mean squares sense fit two traveling flexural waves and two flexural decaying nearfields to the data in regions of the beam between discontinuities. The known discontinuities associated with this beam are: the primary excitation point at the free end, the control actuator location (when control is applied), and the variable sandbox termination. For the no control case, the only beam discontinuities are located at the primary excitation point and at the termination. Thus there is only one region of the beam between discontinuities corresponding to the entire beam from the primary excitation point to the sandbox termination (or in this case the end of the available velocity data, x = 2.7m). For the control case, there are two regions of the beam that are between discontinuities. The first region lies between the primary excitation point and the control actuator, and the second lies between the control actuator and the sandbox termination (or in this case the end of the available velocity data, x = 2.7m).

In order to determine the wave deconvolution for the entire beam, the velocity data from the aforementioned regions is used to determine a separate wave deconvolution for each region as outlined in Section 4.1.2. The beam response for each region can be reconstructed using Equation (4.10) and substituting the wave complex amplitudes determined from the LMS wave deconvolution. The net beam response can thus be reconstructed by combining the responses for each region. The technique was used to determine the flexural traveling wave amplitudes and corresponding net beam response for all of the test frequencies under the no control condition.

After reviewing the plots of the actual velocity measurements compared to the curve fit of the net beam response from the wave deconvolution it was apparent that there existed another waveform of a distinctly different wavelength superimposed with the flexural response. This unknown wave form appeared to have a discontinuity at approximately x = 1.6m which corresponded to the location of a beam support (see Figure 4.20). It was determined after further review of the actual velocity data that a torsional wave corresponding to the test frequency had a near identical wavelength to the unknown wave. Since the aforementioned support at x = 1.6m was not attached to the beam at its neutral axis, it was conceivable that the asymmetry of the support was causing the generation of a torsional wave from an incoming flexural wave.

The next step was to curve fit the actual velocity data with corresponding flexural and torsional waves. The beam support provided another discontinuity at x = 1.6m, and therefore, the beam was broken into a total of three regions between discontinuities as shown in Figure 4.19. The first region, 1, lies from the primary force input at x = 0 to the control actuator location at x = 0.4m. The second region, 3a, lies between the control actuator location at x = 0.4 to the beam support at x = 1.6m. The third and final region, 3b, lies between the support at x = 1.6m and the end of the velocity data at x = 2.7m. In each of these regions the response of the beam was assumed to be comprised of 4 flexural waves and two torsional waves as follows:

$$W(x,t) = \left(Ae^{jk_f x} + Be^{-jk_f x} + Ce^{k_f x} + De^{-k_f x}\ T_+e^{jk_t x} + T_-e^{-jk_t x}\right)e^{-j\omega t} \quad \textbf{(4.22)}$$

where T_+ is the positive traveling torsional wave, T_- is the negative traveling torsional wave, and k_t is the torsional wavenumber defined as (Cremer et al., 1973):

$$k_t = \frac{\omega L_w}{4h}\sqrt{\frac{\rho}{G}} \quad \textbf{(4.23)}$$

where L_w is the width of the beam, and G is the shear modulus.

In a similar approach to that used in Section 4.1.2, the beam velocity at discrete locations can be written in matrix form as follows:

$$\begin{bmatrix} \dot{w}_1 \\ \dot{w}_2 \\ \vdots \\ \dot{w}_n \end{bmatrix} = -j\omega \begin{bmatrix} e^{jk_f x_1} & e^{-jk_f x_1} & e^{k_f x_1} & e^{-k_f x_1} & e^{jk_t x_1} & e^{-jk_t x_1} \\ e^{jk_f x_2} & e^{-jk_f x_2} & e^{k_f x_2} & e^{-k_f x_2} & e^{jk_t x_2} & e^{-jk_t x_2} \\ \vdots & \vdots & \vdots & \vdots & \vdots & \vdots \\ e^{jk_f x_n} & e^{-jk_f x_n} & e^{k_f x_n} & e^{-k_f x_n} & e^{jk_t x_n} & e^{-jk_t x_n} \end{bmatrix} \begin{bmatrix} A \\ B \\ C \\ D \\ T_+ \\ T_- \end{bmatrix} \quad \textbf{(4.24)}$$

For situations where n>6 the system is over-defined, and a solution is desired in a least squares sense. Several methods exist for solution of over-defined problems, but the most robust solution technique is the QR decomposition (Golub and Van Loan, 1989). For the experiments in this chapter the QR method will be solely used. Once the wave amplitudes, A, B, C, D, T_+, and T_- are estimated (in the least squares sense), then the flexural power flow can be estimated using Equation (4.14). The net displacement function can create what is called a "curve fit" by substituting the wave amplitude estimates A, B, C, D, T_+, and T_- into Equation (4.22).

An LMS wave deconvolution was performed using the assumed 6 waves for all velocity data for the experiments, and provided an extremely accurate curve fit of the actual velocity data (see Figure 4.25 for example). The complex flexural wave reflection coefficients associated with the termination can now be estimated using the wave amplitude estimates A and B for region 3b, and are presented as follows:

$$R_{tf} = \frac{B}{A} \tag{4.25}$$

$$R_{nf} = \frac{C}{A} \tag{4.26}$$

These values can now be used as parameters defining the termination characteristics which are necessary to determine the theoretical flexural response of the beam as outlined in Chapter 2.

The in-plane strain measurements taken from the 4 strain gage stations along the beam were used to determine the positive and negative traveling extensional waves, E and F, both before and after control using the technique outlined in Section 4.2. In this case, the discontinuities again are: the primary force location, the control actuator location (when control is applied), and the termination. The strain gages only lie in the region between the control actuator and the termination, and thus only provide information on this region. However, since under the no control condition the control actuator does not cause a discontinuity in the beam, the wave deconvolution determined from the four strain gages was considered valid over the entire beam. Under the control condition, the extensional wave deconvolution as outlined in Section 4.2 is found in a single region called (3a + 3b) from the control actuator location at x = 0.4m to the end of the data at x = 2.7m. It is noted that under control

conditions, no strain data is available for region 1 of the beam (between x = 0 and x = 0.4m).

The complex extensional wave reflection coefficient associated with the termination can now be estimated using the wave amplitude estimates E and F, and is presented as follows:

$$R_{te} = \frac{F}{E} \tag{4.27}$$

This value can now be used as a parameter defining the termination characteristics which are necessary to determine the theoretical extensional response of the beam as outlined in Chapter 2.

4.5.5 Results

4.5.5.1 Semi-infinite Beam Flexural Response, 608 Hz

The out-of-plane velocity magnitude versus beam axial position for the no-control case is shown in Figure 4.25. The curve denoted as "Experimental" is the actual velocity magnitude determined in the experiment. Unknown flexural wave amplitudes for regions 1, 3a, and 3b were determined using the technique described by Section 4.5.4. The resulting curve fit of the torsional and flexural waves is shown as "Curve fit" in Figure 4.25.

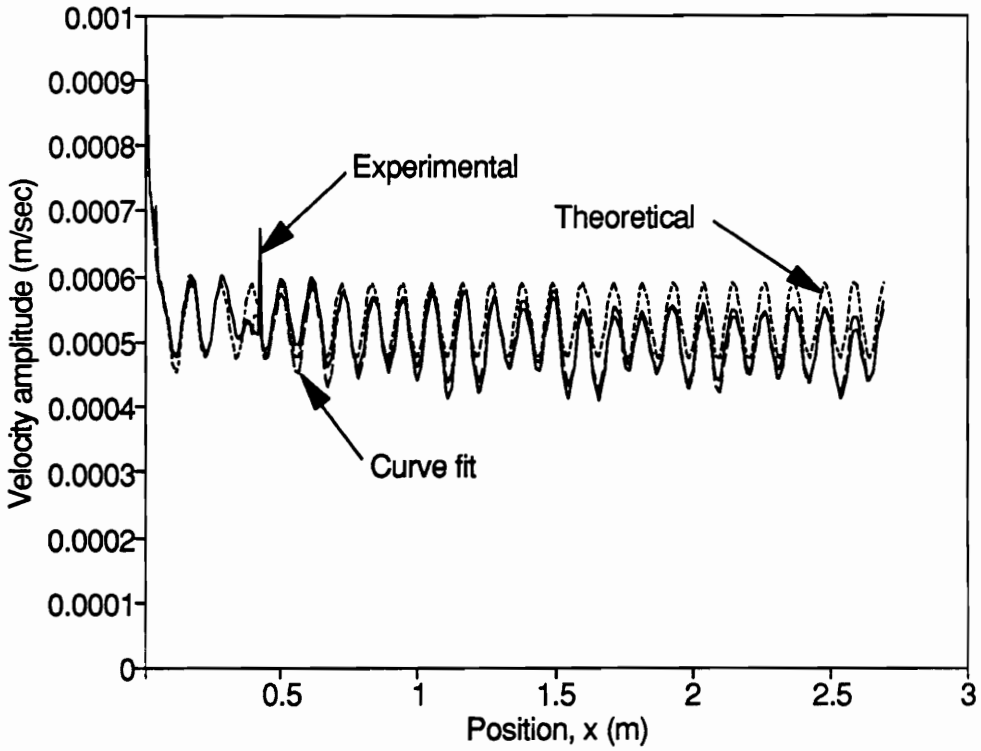

Figure 4.25 Flexural Velocity Distribution
No Control, 608 Hz, Semi-infinite

A comparison can now be made between the results determined experimentally and those derived theoretically, as discussed in Chapter 2, for the excitation of a free beam subjected to a point force at the free end. The theoretical beam response of a finite beam subjected to a point force at the free end and a variable boundary condition at the other was previously presented in Equation (2.97) of Chapter 2. In this case, the point force measured at the input of the

primary shaker is used as the input of Equation (2.97). The termination is described by its traveling wave reflection coefficient, R_{tf}, and its nearfield reflection coefficient, R_{nf}, which are found from the curve fit of the velocity data as described in Section 4.5.4. In other words, the curve fit is used to determine the nature of the beam termination in flexure, and these results are used to predict the theoretical beam motion with that type of termination. The resulting theoretical flexural beam response is labeled "Theoretical" in Figure 4.25. The theoretical and experimental data are generally in good agreement, except Figure 4.25 shows a slight decay in experimental beam response with position which is probably due to a combination of internal material damping, as well external air damping of the beam response. This was not included in the theoretical response depicted in the "Theoretical" curve, and thus the roll off is not seen in the prediction.

The plot of the controlled velocity distribution is shown in Figure 4.26. When control is applied to the beam the velocity distribution between the control point (0.4m) and the termination is attenuated on the order of 45 dB over the no control case. Again, the curve labeled "Experimental" is the actual measured velocity magnitude. Although the response between the control point and the termination is extremely low, the beam is still broken into the same three regions as used previously (see Section 4.5.4). In this case all three regions

are assumed to have the four flexural waves (two traveling, and two nearfields), and no torsional waves are assumed present. The LMS fit of the flexural wave response is depicted as the "Curve fit" shown in Figure 4.26. Since there very little response in the area of the support (1.6m), there is no significant torsional wave conversion. Even though the controller was incapable of sensing or exciting torsional waves, the torsional response was reduced because the flexural (and extensional) energy was stopped at the control point and thus not allowed to convert to torsional at the support (1.6m). In other words, since the traveling flexural waves never reach the support location, there is very little torsional wave conversion.

A comparison can now be made between the results determined experimentally and those derived theoretically, as discussed in Chapter 2, for the excitation of a free beam subjected to a point force at the free end, and also subjected to an optimal control input by two optimally driven piezoelectric actuators. The theoretical beam response of a finite beam subjected to a point force at the free end and a variable boundary condition at the other was previously presented in Equation (2.97) of Chapter 2. In this case, the point force measured at the input of the primary shaker (while control is exercised) is used as the input of Equation (2.97) in order to allow for the change of beam input impedance under control affecting shaker output force (i.e. the shaker is not an infinite input

impedance source). Then the optimal control of the beam subjected to the primary force and secondary piezoelectric excitation as detailed in Section 2.4.3.3 is determined. The theoretical response corresponding to the optimal control exercised over the theoretical distribution shown in Figure 4.25 is also shown as the "Theoretical" curve of Figure 4.26. Qualitatively speaking, the theoretical and experimental plots agree quite well. The difference in the amplitude is attributed to the fact that the boundary condition at the free end is not exactly free in the rotational sense as the primary shaker does impart some rotational impedance (as the stinger was fairly stiff). Overall the nature of the theoretical model of the control from a wave point of view tends to mimic the actual experimental results. Note that the boundary condition that the control actuator imparts on the beam causes the out-of-plane response between the free end and the control point to rise significantly (as compared to the no control case of Figure 4.25), but as will be shown later in corresponding tabulated power flow, the increased response does not correspond to an increase in power flow.

For example, consider the case of a theoretically responding simply supported beam. In this case the net power flow is zero. The response consists of two equal magnitude but opposite traveling flexural waves, each of which carries equal amounts of energy. However, since they travel in opposite directions the

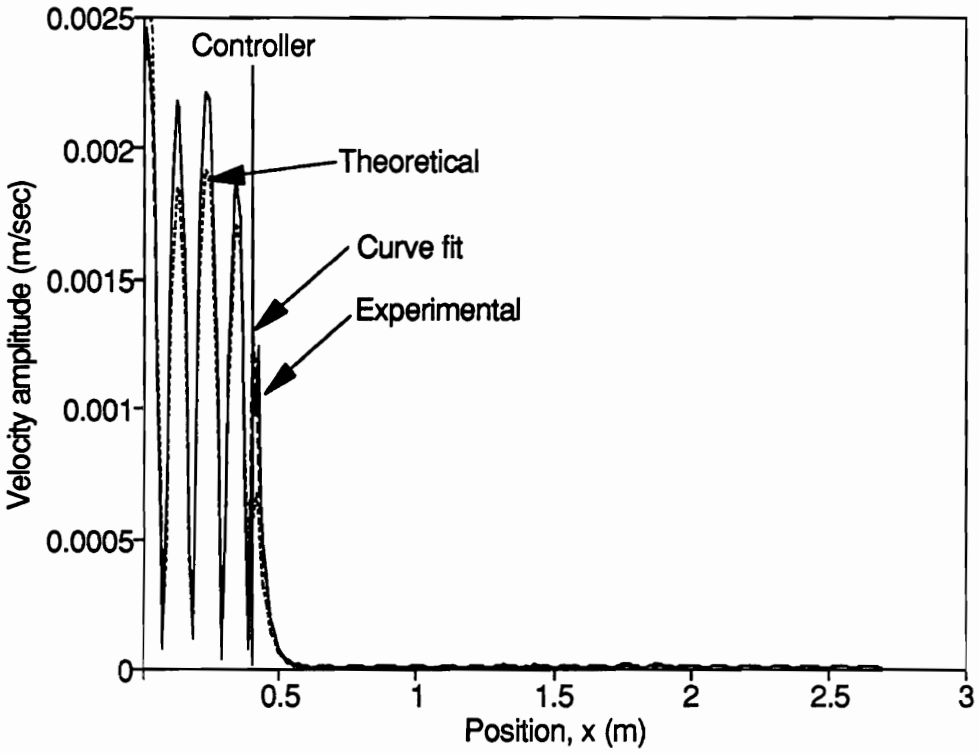

Figure 4.26 Flexural Velocity Distribution
Control, 608 Hz, Semi-infinite

net power flow is zero (see Equation (4.14)). This can be related to the experiment, where large standing waves correspond to little power flow.

The flexural traveling wave amplitudes for the no control case corresponding to the velocity response plots shown in Figure 4.25 are shown in Table 4.8. The wave amplitudes are given in terms of displacement in meters. The beam

regions are shown in Figure 4.19 for reference. The theoretical curves were determined based on the experimental traveling wave reflection coefficient of region 3b which equals 0.11. The experimental wave amplitudes tend to decrease slightly as the region number increases which can also be seen in the corresponding velocity plot of Figure 4.25. The experimental traveling wave reflection coefficients for all regions fall between 0.09 and 0.12.

Table 4.8 Flexural Traveling Wave Amplitudes
No Control, 608 Hz, Semi-infinite Beam

Region	Theoretical			Experimental Curve Fit		
	A	B	R_{tf}	A	B	R_{tf}
	m x 10^{-9}	m x 10^{-9}	--	m x 10^{-9}	m x 10^{-9}	--
1	139	15.1	0.11	145	13.0	0.09
2	139	15.1	0.11	NA	NA	NA
3a	139	15.1	0.11	134	16.1	0.12
3b	139	15.1	0.11	129	14.0	0.11

The flexural traveling wave amplitudes for the control case corresponding to the velocity response plots shown in Figure 4.26 are shown in Table 4.9. The wave coefficient amplitudes are again given in terms of displacement in meters. The theoretical curves were determined based on the experimental traveling wave reflection coefficient of region 3b which equals 0.11. It is seen that the theoretical optimal control solution provides zero traveling wave amplitudes at

axial positions past the control point. Experimentally the wave amplitudes are over 40 dB less than they were before control, and thus the velocity measurements are only a few dB above the noise floor of the measurement system. In region 1 the theoretical wave amplitudes are about 17 percent less than their respective experimental values.

Table 4.9 Flexural Traveling Wave Amplitudes
Control, 608 Hz, Semi-infinite Beam

Region	Theoretical			Experimental Curve Fit		
	A	B	R_{tf}	A	B	R_{tf}
	m x 10^{-9}	m x 10^{-9}	--	m x 10^{-9}	m x 10^{-9}	--
1	251	251	1.0	291	286	0.98
2	242	242	1.0	NA	NA	NA
3a	0	0	0.11	1.34	1.73	1.29
3b	0	0	0.11	1.83	1.98	1.07

Table 4.10 details the flexural power flow corresponding to the velocity distributions shown in Figure 4.25 and Figure 4.26. In this case the power flow is given in both Watts and dB relative to the experimental no control case. Note also that the scaling exponent corresponding to the controlled column is 1000 times smaller than that used in the no control column. It is seen in Table 4.10, in the no control case, that the power flow both experimentally and theoretically agree within 0.4 dB. For the modeled situation, theoretically the

power flow can be totally nulled by the controller in all regions of the beam, by totally reflecting the incoming waves back and creating a purely reactive input impedance at the primary source. Experimentally, the power flow downstream of the controller location (regions 3a and 3b) is reduced by over 40 dB. The experimental case showed only a reduction of 17.68 dB between the free end and the control location. The discrepancy is thought to be caused by increased material and air damping due to the increased beam response in this region. Note that the slight power flow in this region corresponds to traveling wave reflection coefficient of 0.98 Thus, the reflected wave is only 2% less than the incident wave.

This finishes the experimental results for the flexural response of the semi-infinite beam at 608 Hz, The next section will make a similar examination of the extensional experimental results at 608 Hz.

4.5.5.2 Semi-Infinite Beam Extensional Response, 608 Hz

Flexural and extensional power flow was simultaneously controlled, but the data will be presented separately for each wave type. In this section, the experimental results for the control of extensional waves at 608 Hz will be presented. The in-plane strain magnitude versus beam axial position for the no-control case is shown in Figure 4.27. The curve denoted as "Experimental"

Table 4.10 Flexural Power Flow, 608 Hz, Semi-infinite

Region	No Control		Control	
	Theoretical	Experimental Curve Fit	Theoretical	Experimental Curve Fit
	Watts $x10^{-6}$ (dB)	Watts $x10^{-6}$ (dB)	Watts $x10^{-9}$ (dB)	Watts $x10^{-9}$ (dB)
1	24.4 (0.66)	26.6 (1.02)	0.00 (-∞)	358.0 (-17.68)
2	24.4 (0.66)	NA (NA)	0.00 (-∞)	NA (NA)
3a	24.4 (0.66)	22.6 (0.32)	0.00 (-∞)	-1.51 (-41.4)
3b	24.4 (0.66)	21.0 (0.00)	0.00 (-∞)	-6.71 (-45.0)

is the actual strain magnitude determined in the experiment. The strain distribution was curve fit with two opposite traveling extensional wave components (amplitudes E and F) as outlined in Section 4.2 and Section 4.5.4. In this curve fit, the two extensional waves were assumed to be present, and the wave amplitudes were determined which fit the actual four point strain distribution in a least squares sense. An expansion of these extensional wave components is shown as "Curve fit" in Figure 4.27. The number of strain gages was limited to four due to the relative expense of purchasing and mounting semi-conductor strain gages.

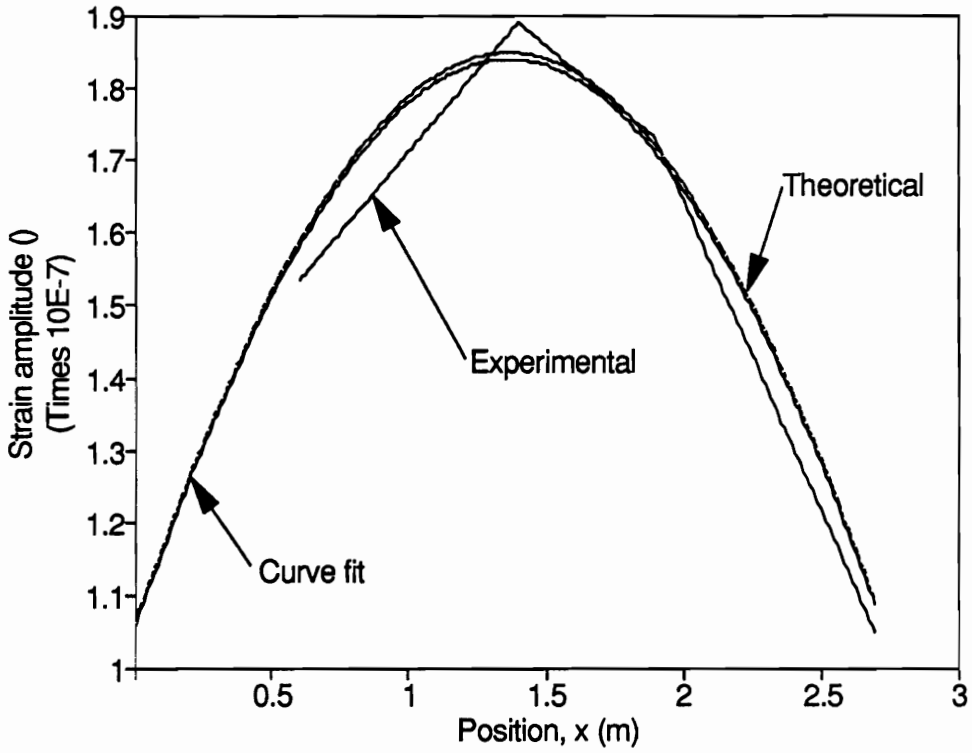

Figure 4.27 Extensional Strain Distribution
No Control, 608 Hz

A comparison can now be made between the results determined experimentally and those derived theoretically, as discussed in Chapter 2, for the excitation of a free beam subjected to a point force at the free end. The theoretical extensional beam response of a finite beam subjected to a point force at the free end and a variable boundary condition at the other was previously presented in Equation (2.99) of Chapter 2. In this case, the point force

measured at the input of the primary shaker is used as the input of Equation (2.99). The resulting theoretical extensional strain response is labeled "Theoretical" in Figure 4.27. In this case the termination is described by its traveling wave reflection coefficient, R_{te}, as defined in Chapter 2. This value were set equal to the reflection coefficient determined from the aforementioned curve fit as outlined in Section 4.5.4. In other words, the curve fit is used to determine the nature of the beam termination in extension, and these results are used to predict the theoretical beam motion with that type of termination. Note the good agreement between "theoretical" and "Curve fit" plots. The excellent match requires both the variable termination to be modeled correctly (which was forced to occur by the complex reflection coefficient), and the forced end condition to be modeled correctly. It is interesting to note that the beam is being driven slightly below its first mode resonance in extension at a frequency of 675 Hz as previously presented in Section 4.4. As the termination is ineffective in terms of absorbing extensional energy, both ends of the beam could be modeled as free. Note the general shape of the curve resembles the first half period of a sine wave which corresponds to the strain distribution of the first mode of a free - free beam in extension.

When control is applied to the beam the strain between the control point (0.4m) and the termination is attenuated on the order of 27 dB. The plot of the

controlled strain distribution is shown in Figure 4.28. Again, the curve labeled "Experimental" is the actual measured strain magnitude. The curve labeled "Curve fit" is a plot of the LMS wave deconvolution response determined as discussed in Sections 4.2 and 4.5.4 which is only valid in the proximity of the strain data locations, region 3. In this case, the combination of the real time wave vector filter and the filtered-x LMS adaptive controller provides an effective means of reducing the strain between the control actuator and the termination in a highly resonant condition (R_{te} = 0.9). The advantage of the real time wave vector filter is that it is capable of discriminating positive and negative extensional waves in the time domain regardless of the boundary conditions.

A comparison can now again be made between the results determined experimentally and those derived theoretically, as discussed in Chapter 2, for the excitation of a free beam subjected to a point force at the free end, and also subjected to an optimal control input by two optimally driven piezoelectric actuators. As previously, the primary input force measured in the experiments under the controlled case, and the experimentally derived extensional wave reflection coefficient calculated as described in Section 4.5.4 were used as the input to the theoretical model of Chapter 2. The theoretical extensional strain distribution corresponding to the optimal control of the theoretical distribution

shown in Figure 4.27 is also shown as the "Theoretical" curve of Figure 4.28. Overall the nature of the theoretical model of the control from a wave point of view tends to mimic the actual experimental results in terms of distribution and absolute values. Note that the scale of the control strain plots was decreased by over an order of magnitude in order to visualize the residual wave field after control. Also notice that the strain peak under the actuator is off scale and actually reaches a maximum of 1.44E-5 due to the relatively short actuator length compared to the extensional wavelength. The piezoelectric actuator is theoretically modeled with equal and opposite in-plane forces acting at the ends of the actuator. Since the actuator is relatively short compared to the extensional wavelength the in-plane forces tend to cancel each other out (similar to an acoustic dipole), which requires much higher input strain levels to correspond to the required wave field away from the actuator.

The extensional traveling wave amplitudes for the no control case corresponding to the strain distributions shown in Figure 4.27 are shown in Table 4.11. The wave amplitudes are given in terms of in-plane displacement in meters. The theoretical curves were determined based on the experimental traveling wave reflection coefficient of region 3 which equals 0.90. The value of 0.9 is quite high, and is attributed to the fact that the sand termination is ineffective at absorbing extensional waves.

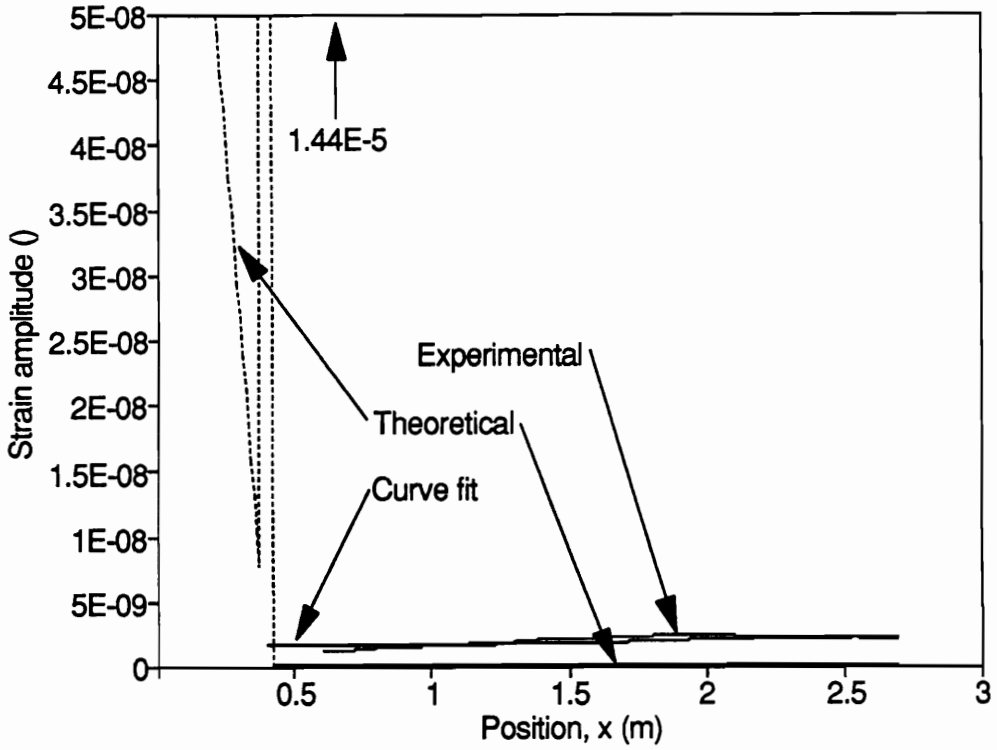

Figure 4.28 Extensional Strain Distribution
Control, 608 Hz

The extensional traveling wave amplitudes for the control case corresponding to the strain distributions shown in Figure 4.28 are shown in Table 4.12. The wave amplitudes are given in terms of in-plane displacement in meters. The theoretical curves were determined based on the experimental traveling wave reflection coefficient of region 3 which equals 0.90 as above. It is seen in both Figure 4.28 and Table 4.12, that the theoretical optimal control solution provides

Table 4.11 Extensional Traveling Wave Amplitudes
No Control, 608 Hz

Region	Theoretical			Experimental Curve Fit		
	E	F	R_{te}	E	F	R_{te}
	m x 10^{-9}	m x 10^{-9}	--	m x 10^{-9}	m x 10^{-9}	--
1	139	124	0.90	NA	NA	NA
2	139	124	0.90	NA	NA	NA
3	139	124	0.90	138	124	0.90

zero traveling wave amplitudes at axial positions past the control point. Experimentally the wave amplitudes are over 34 dB less than they were before control. For region 1 comparing Table 4.11 and Table 4.12, the theoretical wave amplitudes increased under control about 6.0 dB.

Table 4.12 Extensional Traveling Wave Amplitudes
Control, 608 Hz

Region	Theoretical			Experimental Curve Fit		
	E	F	R_{te}	E	F	R_{te}
	m x 10^{-9}	m x 10^{-9}	--	m x 10^{-9}	m x 10^{-9}	--
1	274	274	1.0	NA	NA	NA
2	10200	10200	1.0	NA	NA	NA
3	0	0	0.90	2.77	0.404	0.15

Table 4.13 details the extensional power flow corresponding to the strain distributions shown in Figure 4.27 and Figure 4.28. In this case the power flow is given in both Watts and dB relative to the experimental no control case. It is seen in Table 4.13 that in the no control case, the power flow in both experimentally and theoretically agree within 0.04 dB. For the modeled situation, theoretically the power flow can be totally attenuated by the controller in all regions of the beam, by totally reflecting the incoming waves back to the drive point and creating a reactive input impedance at the primary source. Experimentally, the power flow downstream of the controller location (region 3) is reduced by over 26 dB.

Table 4.13 Extensional Power Flow, 608 Hz

Region	No Control		Control	
	Theoretical	Experimental Curve Fit	Theoretical	Experimental Curve Fit
	Watts $x10^{-6}$ (dB)	Watts $x10^{-6}$ (dB)	Watts $x10^{-6}$ (dB)	Watts $x10^{-6}$ (dB)
1	173 (0.04)	NA (NA)	0.00 (-∞)	NA (NA)
2	173 (0.04)	NA (NA)	0.00 (-∞)	NA (NA)
3	173 (0.04)	171 (0.0)	0.00 (-∞)	0.35 (-26.9)

It is thus experimentally verified that the flexural and extensional power flow along a beam can be significantly reduced with a single pair of piezoelectric actuators and a sensor array and filter network that discriminates the net

positive and negative traveling flexural and extensional waves in real time. As discussed in Chapter 2, the traveling wave can be thought of as a carrier of energy in an amount proportional to the square of the waves amplitude. The wave vector filter is capable of estimating the traveling waves complex amplitude, and thus the square root of the power flow in that direction in real time. This unique time domain estimate when coupled with an adaptive controller enables the control of flexural and extensional beam vibration directly from a power flow point of view. This is in contrast to the modal approach where an attempt is made to observe and control a finite number of modes with an (usually) equal number of actuators and sensors. For general beam excitation, the response can be quite modally rich, and therefore, to perform modal based control it would be necessary to observe and excite all of the significantly responding modes. The modal approach under these conditions would require a vastly complex arrangement of actuators, sensors, and computer hardware as compared to the results achievable with the relatively simple wave based control system. Thus the wave approach proves to be an efficient scheme to examine and control the flexural and extensional power flow in both finite and semi-infinite beams. In the next section, the performance of the wave vector filtering portion of the control system will be examined in more detail.

4.5.5.3 Wave Filter Performance Studies, Semi-Infinite Beam, 608 Hz

In the previous two sections, the wave vector filter proved to be an extremely useful element in the control flexural and extensional power flow in thin beams. In this section, the experimental performance of the wave vector filtering portion of the control system will be examined in more detail. The sensor/filter will be examined using three types of data. First, the wave vector filter amplitudes will be presented based on the actual PVDF sensors used in the experiment. This data corresponds to the actual PVDF signals which were used by the wave vector filters to estimate the traveling waves. Secondly, wave amplitudes will be examined based on the "curve fits" of the actual experimental data (velocity for flexural and strain for extension). The wave amplitudes obtained from the "curve fits" for the purpose of this study, will be considered the actual wave amplitudes present on the beam. Lastly, the "curve fit" wave amplitudes will be passed through wave vector filters equivalent to those used in this experiment. This portion of the study is included to show the slight modeling errors associated with the IIR filters used in the Cotangent Method of wave vector filtering. These model errors are evident in the comparison between the IIR filter and desired frequency response functions depicted in Figure 2.10.

Table 4.14 shows the performance of the flexural wave vector filtering scheme used during the experiment at 608 Hz. These filters provided real time estimates of the traveling waves on a beam, and were the error signals for this portion of the active control experiments. The first three columns contain the wave estimates corresponding to the actual PVDF sensors used in the experiment. As discussed in the detail in Section 2.3.1, the wave vector filter (the Cotangent Method in the case of flexure) provides an estimate proportional to the traveling waves but not there actual values. In order to make a direct comparison, the data taken PVDF sensors used in this experiment was multiplied by the proportionality constant given in Equation (2.38). The second set of three columns correspond to the experimental curve fit data which is to be considered the actual waves present on the beam, and was presented previously in Table 4.8 and Table 4.9. The last set of three columns corresponds to the experimental curve fit data that has been processed through ideal wave vector filters (in this case the filters corresponding to the Cotangent Method) to determine how the actual waves present on the beam would be estimated by the Cotangent Method for this particular test case.

It can be seen that the experimental positive traveling wave, A, is about 8.5 % larger than the actual A wave present on the beam. The negative traveling flexural wave estimate, B, is about 3 % lower than the actual wave. Thus the estimated wave have a corresponding slightly lower reflection coefficient of

Table 4.14 Flexural Wave Vector Filtering, 608 Hz

Test Case	Experimental Estimated Amplitudes			Curve Fit Amplitudes			Curve Fit Amplitudes acting through Ideal Filters		
	A	B	R_{tf}	A	B	R_{tf}	A	B	R_{tf}
	m x 10^{-9}	m x 10^{-9}	--	m x 10^{-9}	m x 10^{-9}	--	m x 10^{-9}	m x 10^{-9}	--
No Control	140	13.6	.097	129	14.0	.11	130	12.6	.096
Control	1.27	2.83	2.2	1.84	1.98	1.07	1.88	2.02	1.07

0.097 versus the actual of 0.11. Since the control system attenuated the traveling waves by over 40 dB for the corresponding control case, the signals were only a few dB above the noise floor of the laser vibrometer, and the amplifiers. The corresponding wave estimates after control reflect the inherent low signal to noise ratio, and thus vary by as much as 50%.

Table 4.15 shows the extensional wave vector filtering performance for the 608 Hz case. The first three columns contain the wave estimates corresponding to the actual PVDF sensors used in the experiment. As was shown in Section 2.3.3, the wave vector filter (the Time Delay Method in the case of extension) provides an estimate proportional to the traveling waves but not there actual values. In order to make a direct comparison, the data taken from the PVDF

sensors used in this experiment were multiplied by the proportionality constant given in Equation (2.45). The second set of three columns correspond to the extensional waves based on the experimental curve fit strain gage data which is to be considered the actual waves present on the beam, and was presented previously in Table 4.11 and Table 4.12. The last set of three columns corresponds to the experimental curve fit data that has been processed through ideal wave vector filters (in this case the filters corresponding to the Time Delay Method) to determine how the actual waves present on the beam would be estimated by the Time Delay Method for this particular test case.

The positive traveling extensional wave estimate, E, is approximately 9 % lower than the actual wave. The negative traveling extensional wave estimate, F, is about 9 % higher than the actual wave. This slight discrepancy can be attributed to slight variations in PVDF film, bonding, or charge amplifier transfer functions between the four corresponding PVDF sensors. As was seen in the flexural control case, the low signal to noise ratio prevents accurate wave estimation. The right hand set of six columns are in exact agreement because the Time Delay Method provides a method of exact wave vector filtering, and is not subjected to the slight modeling errors associated with the Cotangent Method.

Table 4.15 Extensional Wave Vector Filtering, 608 Hz

Test Case	Experimental Estimated Amplitudes			Curve Fit Amplitudes			Curve Fit Amplitudes acting through Ideal Filters		
	E	F	R_{te}	E	F	R_{te}	E	F	R_{te}
	m x 10^{-9}	m x 10^{-9}	--	m x 10^{-9}	m x 10^{-9}	--	m x 10^{-9}	m x 10^{-9}	--
No Control	126	136	1.08	138	124	.897	138	124	.897
Control	2.71	1.36	.502	2.77	.404	.146	2.77	.404	.146

4.5.5.4 Semi-infinite Beam Flexural Response, 1120 Hz

In this and the following section, the experimental results for the simultaneous control of flexural and extensional power flow with the beam in the semi-infinite configuration will be presented at 1120 Hz. As for the 608 Hz case, real time wave vector filters are used to provide an estimate of the positive and negative flexural and extensional traveling wave amplitudes. The controller again will attempt to minimize only the flexural and extensional waves traveling into the termination. The results are very similar to those obtained for 608 Hz, and demonstrate the control performance is robust over a range of frequencies.

The out-of-plane velocity magnitude versus beam axial position for the no-control case is shown in Figure 4.29. As presented previously for the 608 Hz case, the curve denoted as "Experimental" is the actual velocity magnitude determined in the experiment. A curve fit was performed as described in Section 4.5.4. The resulting curve fit of the experimental data is shown as "Curve fit" in Figure 4.29. Note the exceptional agreement between the actual velocity data and the resultant curve fit. The one extremely high data point at about x = 0.4m is erroneous caused by the poor laser light reflection (or speckle) at the edge of the piezoelectric actuator.

Again, a comparison is now made between the theoretical and experimental flexural beam response subjected to only the primary force. The theoretical response is again determined using the input force measured experimentally as discussed previously for the 608 Hz case. The last curve labeled "Theoretical" in Figure 4.29 is the theoretical response of the beam to a point force excitation at the free end, and a variable termination at the other end as detailed in Chapter 2. Again, the termination is described by its traveling wave reflection coefficient, R_{tf}, and its nearfield reflection coefficient, R_{nf}, as defined in Chapter 2. These values were set equal to the reflection coefficients determined from the aforementioned curve fit as discussed in Section 4.5.4. In other words, the curve fit is used to determine the nature of the beam termination in flexure, and

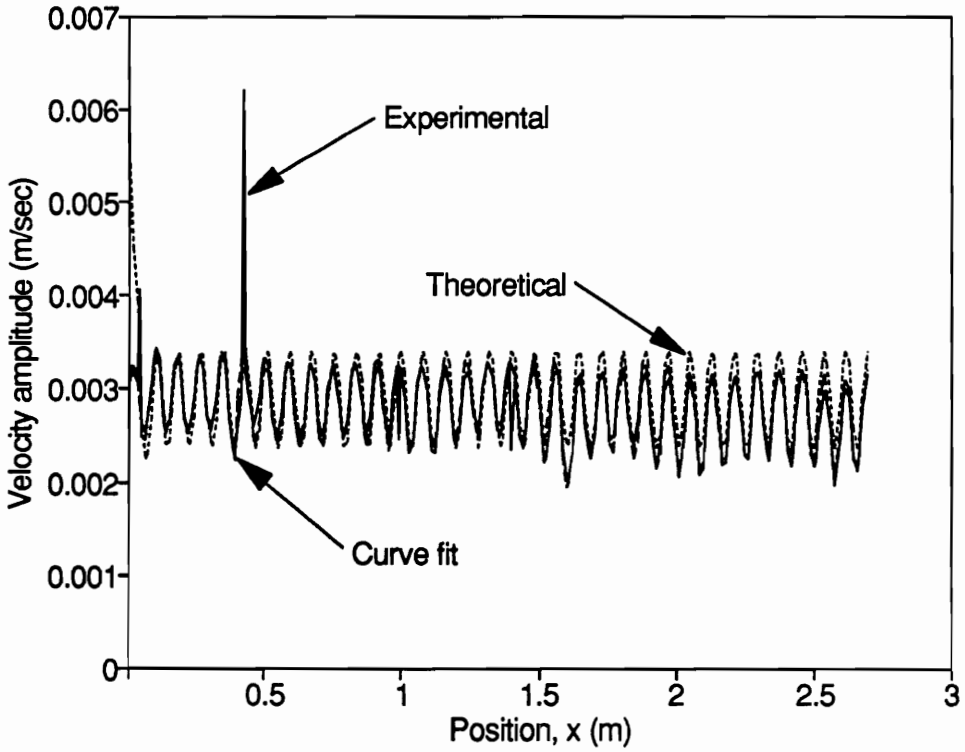

Figure 4.29 Flexural Velocity Distribution
No Control, 1120 Hz, Semi-infinite Beam

these results are used to predict the theoretical beam motion with that type of termination.

Figure 4.29 shows, a slight decay in experimental beam response with position which is probably due to a combination of internal material damping, as well external air damping of the beam response. This was not included in the

theoretical model presented in Chapter 2, or the response depicted in the "Theoretical" curve.

When control is applied to the beam the velocity distribution between the control point (0.4m) and the termination is attenuated by the action of the control system on the order of 32 dB. The plot of the controlled velocity distribution is shown in Figure 4.30. Again, the curve labeled "Experimental" is the actual measured velocity magnitude. The LMS fit of the flexural wave response depicted as the "Curve fit" shown in Figure 4.30 was constructed using the LMS wave deconvolution response determined as discussed in Section 4.5.4.

The theoretical optimal control of the beam is determined as outlined previously for the 608 Hz test case. The theoretical response corresponding to the optimal control over the theoretical distribution shown in Figure 4.29 is also shown as the "Theoretical" curve of Figure 4.30. In this case however, the actual primary force measured under controlled conditions was considered to be the input to allow for changes in disturbance source loading. The difference in the amplitude is attributed to the fact that the boundary condition at the free end is not exactly free in the rotational sense as the primary shaker does impart some rotational impedance. Overall the nature of the theoretical model of the control

from a wave point of view tends to mimic the actual experimental results. Note that the boundary condition that the controller imparts on the beam causes the response between the free end and the control point to rise by a factor of two (as compared to the no control case of Figure 4.29), but as will be shown later, the increased response does not correspond to an increase in power flow in this region. Again it can be seen in Figure 4.30 that the torsional motion generated by the support at 1.6 m is also controlled strictly because the controller eliminates virtually all flexural (and extensional) energy past the control point which prevents the generation of the torsional waves.

The flexural traveling wave amplitudes for the no control case corresponding to the velocity response plots shown in Figure 4.29 are shown in Table 4.16. The wave amplitudes are given in terms of displacement in meters. As stated previously, the theoretical curves were determined based on the experimental traveling wave reflection coefficient of region 3b which equals 0.18. The experimental wave amplitudes tend to decrease slightly as the region number increases which can also be seen in the corresponding velocity plot of Figure 4.29. The experimental traveling wave reflection coefficients for all regions fall between 0.14 and 0.18.

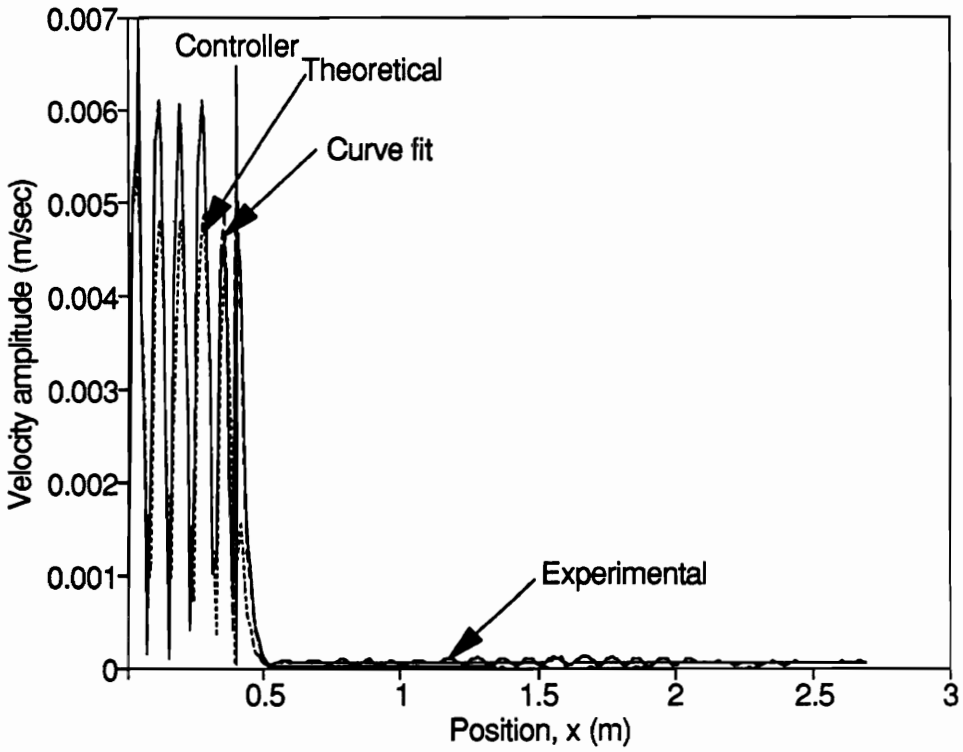

Figure 4.30 Flexural Velocity Distribution
Control, 1120 Hz, Semi-infinite Beam

The flexural traveling wave amplitudes for the control case corresponding to the velocity response plots shown in Figure 4.30 are shown in Table 4.17. It is seen that the theoretical optimal control solution provides zero traveling wave amplitudes at axial positions past the control point. Experimentally the wave amplitudes are over 18 dB less than they were before control, and thus the velocity measurements are only a few dB above the noise floor of the

Table 4.16 Flexural Traveling Wave Amplitudes
No Control, 1120 Hz, Semi-infinite Beam

Region	Theoretical			Experimental Curve Fit		
	A	B	R_{tf}	A	B	R_{tf}
	m x 10^{-9}	m x 10^{-9}	--	m x 10^{-9}	m x 10^{-9}	--
1	409	72.8	0.18	426	59.4	0.14
2	409	72.8	0.18	NA	NA	NA
3a	409	72.8	0.18	403	58.8	0.15
3b	409	72.8	0.18	379	67.4	0.18

measurement system. In region 1 the theoretical wave amplitudes are about 26 percent less than their respective experimental values.

Table 4.17 Flexural Traveling Wave Amplitudes
Control, 1120 Hz, Semi-infinite Beam

Region	Theoretical			Experimental Curve Fit		
	A	B	R_{tf}	A	B	R_{tf}
	m x 10^{-9}	m x 10^{-9}	--	m x 10^{-9}	m x 10^{-9}	--
1	346	346	1.0	431	433	1.00
2	258	258	1.0	NA	NA	NA
3a	0	0	0.18	0.25	10.0	40.8
3b	0	0	0.18	1.13	8.52	7.51

Similar to the results presented for the 608 Hz case, Table 4.18 details the flexural power flow corresponding to the velocity distributions shown in

Figure 4.29 and Figure 4.30. In this case the power flow is given in both Watts and dB relative to the experimental no control case. As shown in Table 4.18 for the no control case, the experimental and theoretical power flow agree within 0.7 dB. Theoretically the power flow can be totally nulled by the controller in all regions of the beam, by totally reflecting the incoming waves back and forcing a reactive input impedance at the primary source. Experimentally, the power flow downstream of the controller location (regions 3a and 3b) is reduced by over 30 dB. It is interesting to note that under the control case the energy is coming out of the sand termination in an amount of 0.42E-6 Watts. Since there is no source within the sand termination, the energy is most likely due to wave conversion from extensional motion occurring at the termination. Under the controlled case, there is still 68.1E-6 Watts of energy entering the termination as extensional motion (see Table 4.21). Since the signal to noise ratio is lower in this region under control the evidence is not strong. However, in the next section, both the strain gage data and the PVDF sensor data suggests that there is a strong wave conversion going on in the uncontrolled case. These signals had high signal to noise ratios, and coherence values consistently above 0.97 (as determined by the B&K analyzer) , and cannot be discredited because of poor signal quality.

Table 4.18 Flexural Power Flow, 1120 Hz, Semi-infinite

Region	No Control		Control	
	Theoretical	Experimental Curve Fit	Theoretical	Experimental Curve Fit
	Watts $x10^{-6}$ (dB)	Watts $x10^{-6}$ (dB)	Watts $x10^{-6}$ (dB)	Watts $x10^{-6}$ (dB)
1	953 (0.67)	1050 (1.08)	0.00 (-∞)	-8.37 (-19.9)
2	953 (0.67)	NA (NA)	0.00 (-∞)	NA (NA)
3a	953 (0.67)	933 (0.58)	0.00 (-∞)	-0.59 (-31.4)
3b	953 (0.67)	817 (0.00)	0.00 (-∞)	-0.42 (-32.9)

4.5.5.5 Semi-Infinite Beam Extensional Response, 1120 Hz

In this section, the performance of the extensional power flow control for the 1120 Hz case will be presented. The in-plane strain magnitude versus beam axial position for the no control case is shown in Figure 4.31. Similar to the format used in the 608 Hz test case, the curve denoted as "Experimental" is the actual strain magnitude determined in the experiment. The strain distribution was curve fit with two opposite traveling extensional waves (amplitudes E and F) as outlined in Section 4.2 and Section 4.5.4. The resulting reconstruction of the strain distribution of the extensional waves is shown as "Curve fit" in Figure 4.31. The LMS curve fit of the experimental data shows that the extensional wave reflection coefficient, R_{te}, is 1.5. One may ask how is this

possible? The answer lies in the realization that there is wave conversion between flexural and extensional waves at the termination. Since the termination is passive and can only absorb energy, the net flow of energy must be into the termination (and subsequently dissipated by absorption). As will be seen later, there is approximately 3 times more flexural energy entering the termination than exiting the termination as extensional energy.

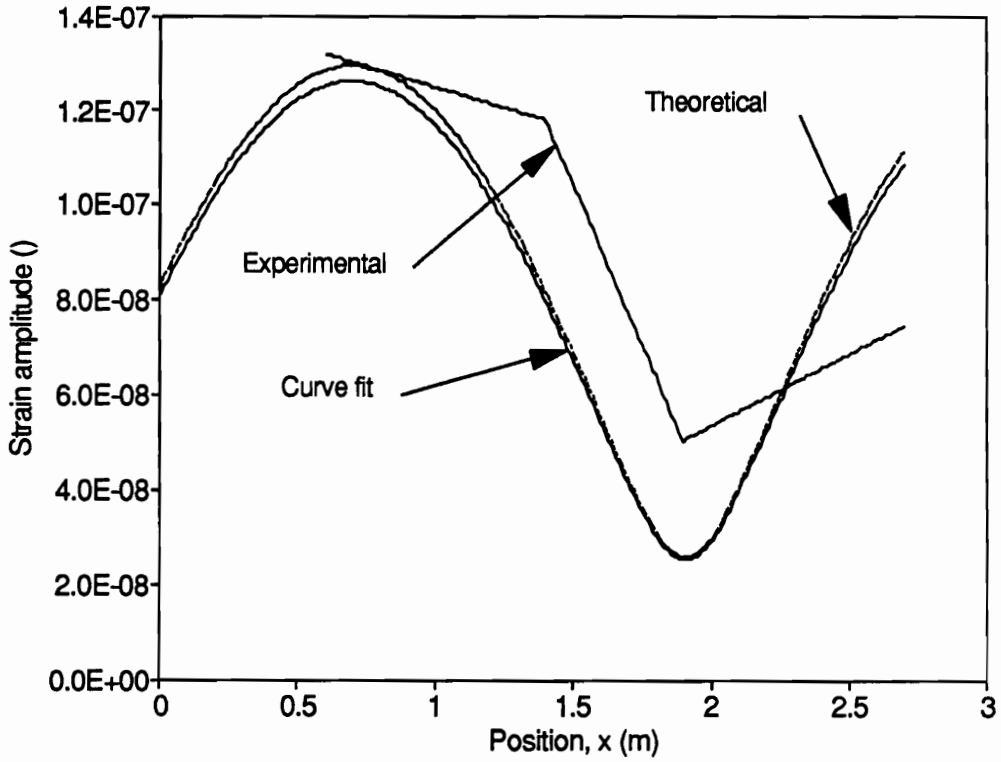

Figure 4.31 Extensional Strain Distribution
No Control, 1120 Hz

As detailed previously for the uncontrolled 608 Hz extensional case, the theoretical beam response is determined using the experimentally measured primary input force. The last curve labeled "Theoretical" in Figure 4.31 is the theoretical response of the beam to a point force excitation at the free end, and an variable termination at the other end as detailed in Chapter 2. In this case the termination is described by its traveling wave reflection coefficient, R_{te}, as defined in Chapter 2. This value were set equal to the reflection coefficient determined from the aforementioned curve fit (1.5) as discussed previously in Section 4.5.4.

When control is applied to the beam, the strain in the region between the control point (0.4m) and the termination is reduced by the action of the controller on the order of 26 dB. The plot of the controlled velocity distribution is shown in Figure 4.32. Again, the curve labeled "Experimental" is the actual measured velocity magnitude. The LMS fit of the extensional wave response is depicted as the "Curve fit" shown in Figure 4.32.

The theoretical response corresponding to the optimal control of the theoretical uncontrolled distribution is also shown as the "Theoretical" curve of Figure 4.32. This response was again determined using the primary input force while the beam was under control as discussed previously for the 608 Hz case. Note

that the scale of the control strain plots was decreased by over a factor of two in order to visualize the residual wave field after control. Also notice that the strain peak under the actuator is off scale and actually reaches a maximum of 1.3E-6 due to the relatively short actuator length compared to the extensional wavelength. This value is over ten times lower for 1120 Hz than it was for 608 Hz for approximately the same level of control input (in terms of displacement in region 3). This lower value occurs because the actuator is almost twice as long relative to a wavelength at 1120 Hz than 608 Hz. The effects of actuator length were discussed from a theoretical standpoint in Section 2.1.2.

The extensional traveling wave amplitudes for the no control case corresponding to the strain distributions shown in Figure 4.31 are shown in Table 4.19. The wave amplitudes are given in terms of in-plane displacement in meters. It is seen that the traveling wave exiting the termination is 50% larger than the wave entering the termination. This is only possible if there is a wave conversion between flexural and extensional occurring at the termination. Further evidence of this behavior is shown in both the resulting power flows (of both wave types), and the PVDF sensor/wave filter outputs. The theoretical curves were determined based on the experimental traveling wave reflection coefficient, R_{te}, of 1.5 in order to allow for the wave conversion mechanism.

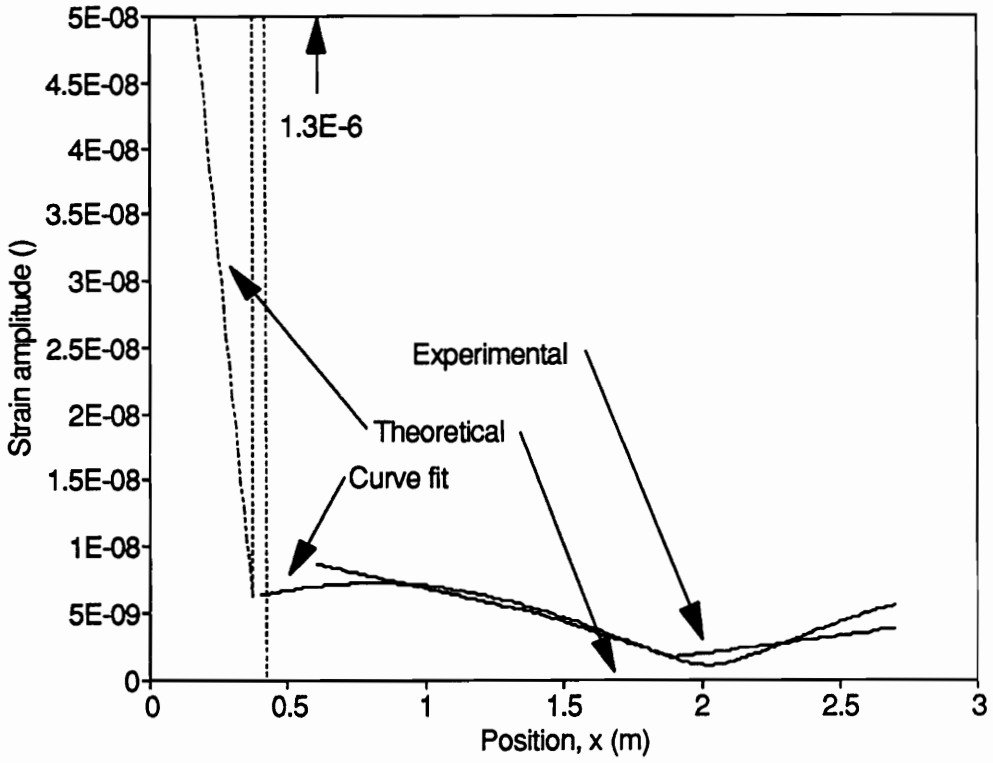

Figure 4.32 Extensional Strain Distribution
Control, 1120 Hz

The extensional traveling wave amplitudes for the control case corresponding to the strain distributions shown in Figure 4.32 are shown in Table 4.20. The wave amplitudes are given in terms of in-plane displacement in meters. The theoretical curves were determined based on the experimental traveling wave reflection coefficient of region 3 which equals 1.50. It is seen that the theoretical optimal control solution provides zero traveling wave amplitudes at

Table 4.19 Extensional Traveling Wave Amplitudes
No Control, 1120 Hz

Region	Theoretical			Experimental Curve Fit		
	E	F	R_{te}	E	F	R_{te}
	m x 10^{-9}	m x 10^{-9}	--	m x 10^{-9}	m x 10^{-9}	--
1	40.0	60.0	1.50	NA	NA	NA
2	40.0	60.0	1.50	NA	NA	NA
3	40.0	60.0	1.50	39.0	58.4	1.50

axial positions past the control point. Experimentally the wave amplitudes are over 22 dB less than they were before control. In region 1 the theoretical wave amplitudes increased under control about 4.2 dB.

Table 4.20 Extensional Traveling Wave Amplitudes
Control, 1120 Hz

Region	Theoretical			Experimental Curve Fit		
	E	F	R_{te}	E	F	R_{te}
	m x 10^{-9}	m x 10^{-9}	--	m x 10^{-9}	m x 10^{-9}	--
1	64.7	64.7	1.0	NA	NA	NA
2	1310	1310	1.0	NA	NA	NA
3	0	0	1.50	3.17	2.39	0.75

Table 4.21 details the extensional power flow corresponding to the strain distributions shown in Figure 4.31 and Figure 4.32. In this case the power flow

is given in both Watts and dB relative to the experimental no control case. As shown in the no control case of Table 4.21, the experimental and theoretical power flow in both agree within 0.22 dB. As was evident in the 608 Hz case, theoretically the power flow can be totally attenuated by the controller in all regions of the beam, by totally reflecting the incoming waves back and forcing a reactive input impedance at the primary source. Experimentally, the power flow downstream of the controller location (region 3) is reduced by over 26 dB.

Power in the amount of 297E-6 Watts is exiting the termination in extensional motion. In the flexural case before control, flexural energy was entering the termination in an amount of 817E-6 Watts. Thus, a portion of this flexural energy was being absorbed by the termination (538E-6 Watts), and a smaller portion (297E-6 Watts) was converted to a net extensional energy by the termination. Possible wave conversion is further confirmed by the output of the wave vector filters used as the error sensors for this experiment as is shown in the next section.

This test frequency demonstrates the effective use of wave vector filters in conjunction with a feedforward adaptive controller to simultaneously control flexural and extensional power flow in thin beams including wave conversion phenomena. The wave vector filters provide an alternative approach to the

Table 4.21 Extensional Power Flow, 1120 Hz

Region	No Control		Control	
	Theoretical	Experimental Curve Fit	Theoretical	Experimental Curve Fit
	Watts $x10^{-6}$ (dB)	Watts $x10^{-6}$ (dB)	Watts $x10^{-6}$ (dB)	Watts $x10^{-6}$ (dB)
1	-312 (0.22)	NA (NA)	0.00 (-∞)	NA (NA)
2	-312 (0.22)	NA (NA)	0.00 (-∞)	NA (NA)
3	-312 (0.22)	-297 (0.0)	0.00 (-∞)	68.1 (-26.4)

reduction of flexural and extensional vibration. The filter schemes only require a small number of sensors, and are not computationally intensive. In the next section, the performance of only the wave vector filters will be examined at the 1120 Hz test case.

4.5.5.6 Wave Filter Performance Studies, Semi-infinite Beam, 1120 Hz

In the previous two sections, the wave vector filter proved to be an extremely useful element in the control flexural and extensional power flow in thin beams. In this section, using an identical approach as used in Section 4.5.5.3 for the 608 Hz test case, the experimental performance of the wave vector filtering portion of the control system will be examined in more detail for 1120 Hz. The

sensor/filter will be examined using three types of data. First, the wave vector filter amplitudes will be presented based on the actual PVDF sensors used in the experiment. This data corresponds to the actual PVDF signals which were used by the wave vector filters to estimate the traveling waves. Secondly, wave amplitudes will be examined based on the "curve fits" of the actual experimental data (velocity for flexural and strain for extension). The wave amplitudes obtained from the "curve fits" for the purpose of this study, will be considered the actual wave amplitudes present on the beam. Lastly, the response of the beam calculated using the "curve fit" wave amplitudes will be passed through wave vector filters equivalent to those used in this experiment. This portion of the study is included to show the slight modeling errors associated with the IIR filters used in the Cotangent Method of wave vector filtering. These model errors are evident in the comparison between the IIR filter and desired frequency response functions depicted in Figure 2.10.

Table 4.22 shows the performance of the flexural wave vector filtering scheme used during the experiment at 1120 Hz. These filters provided real time estimates of the traveling waves on a beam, and were the error signals for this portion of the active control experiments. The first three columns contain the wave estimates corresponding to the actual PVDF sensors used in the experiment. As discussed in the detail in Section 2.3.1, the wave vector filter

(the Cotangent Method in the case of flexure) provides an estimate proportional to the traveling waves but not there actual values. In order to make a direct comparison, the data taken from the PVDF sensors used in this experiment was multiplied by the proportionality constant given in Equation (2.38). The second set of three columns correspond to the experimental curve fit data which is to be considered the actual waves present on the beam, and was presented previously in Table 4.8 and Table 4.9. The last set of three columns corresponds to the experimental curve fit data that has been processed through ideal wave vector filters (in this case the filters corresponding to the Cotangent Method) to determine how the actual waves present on the beam would be estimated by the Cotangent Method for this particular test case. The flexural traveling wave amplitudes of the real time wave filters agree with those determined in the flexural velocity curve fit within 3%. The traveling wave reflection coefficient, R_{tf}, determined from the PVDF sensors was equal to 0.19 and agree quite well with the value of 0.18 found form the curve fit of the velocity data.

Table 4.23 shows the extensional wave vector filtering performance for the 1120 Hz case. Again the first three columns correspond to the wave estimates based on the actual PVDF sensors. As was shown in Section 2.3.3, the wave vector filter (the Time Delay Method in the case of extension) provides an

Table 4.22 Flexural Wave Vector Filtering, 1120 Hz

Test Case	Experimental Estimated Amplitudes			Curve Fit Amplitudes			Curve Fit Amplitudes acting through Ideal Filters		
	A	B	R_{tf}	A	B	R_{tf}	A	B	R_{tf}
	m x 10^{-9}	m x 10^{-9}	--	m x 10^{-9}	m x 10^{-9}	--	m x 10^{-9}	m x 10^{-9}	--
No Control	372	70.4	0.19	379	67.4	0.18	380	68.9	0.18
Control	1.08	8.56	7.95	1.13	8.52	7.51	1.10	8.55	7.75

estimate proportional to the traveling waves but not there actual values. In order to make a direct comparison, the data taken from the PVDF sensors used in this experiment was multiplied by the proportionality constant given in Equation (2.45). The second set of three columns correspond to the extensional waves based on the experimental curve fit strain gage data which is to be considered the actual waves present on the beam, and was presented previously in Table 4.11 and Table 4.12. The last set of three columns corresponds to the experimental curve fit data that has been processed through ideal wave vector filters (in this case the filters corresponding to the Time Delay Method) to determine how the actual waves present on the beam would be estimated by the Time Delay Method for this particular test case.

Table 4.23 Extensional Wave Vector Filtering, 1120 Hz

Test Case	Experimental Estimated Amplitudes			Curve Fit Amplitudes			Curve Fit Amplitudes acting through Ideal Filters		
	E	F	R_{te}	E	F	R_{te}	E	F	R_{te}
	m x 10^{-9}	m x 10^{-9}	--	m x 10^{-9}	m x 10^{-9}	--	m x 10^{-9}	m x 10^{-9}	--
No Control	41.9	53.9	1.29	39.0	58.4	1.50	39.0	58.4	1.50
Control	1.86	3.26	1.77	3.17	2.39	0.75	3.17	2.39	0.75

The wave vector filters show that there is a reflection coefficient of 1.29 which can only occur if wave energy is being converted by the termination from flexural to extensional. As stated before the LMS determined value of reflection coefficient. R_{te}, is 1.50. After control there is a larger discrepancy between the different estimated values which is attributed to the signals emitted by the PVDF sensors, laser vibrometer, and strain gages all being extremely small (only a few micro volts) in the region of the beam downstream of the control actuator with control applied and thus are difficult to measure accurately.

4.5.5.7 Finite Beam Flexural Response, 608 Hz

Control of flexural power flow has been demonstrated at 608 Hz and 1120 Hz

for the semi-infinite beam configuration. In the semi-infinite beam configuration, the traveling flexural wave reflection coefficients were 0.11 and 0.18. This corresponds to a reflected flexural wave which is less than twenty percent as large as the incident flexural wave. For the results presented in this section, the beam termination was modified as shown in Figure 4.33 by inserting aluminimum blocks at the entrance of the termination to provide a step discontinuity on the beam. The insertion of the blocks created a flexural traveling wave reflection coefficient (and thus reflected wave) much larger corresponding to a more resonant structure. This test case was developed to observe the wave vector filter and adaptive control systems performance for a more resonant structure, particularly in flexure. The sensor/controller concept can then be applied to any beam like structure or element of a structure. It is noted that for the two previous tests the beam was highly resonant in extension. In this test configuration the beam was also highly resonant in extension, but the experimental data was omitted from this dissertation for brevity.

In this section, the control of a finite beam with a much higher flexural traveling wave reflection coefficient will be presented. In terms of a typical feedback control system approach, a extremely lightly damped (resonant) structure tends to be more difficult to control (von Flotow and Vos, 1991). As will be

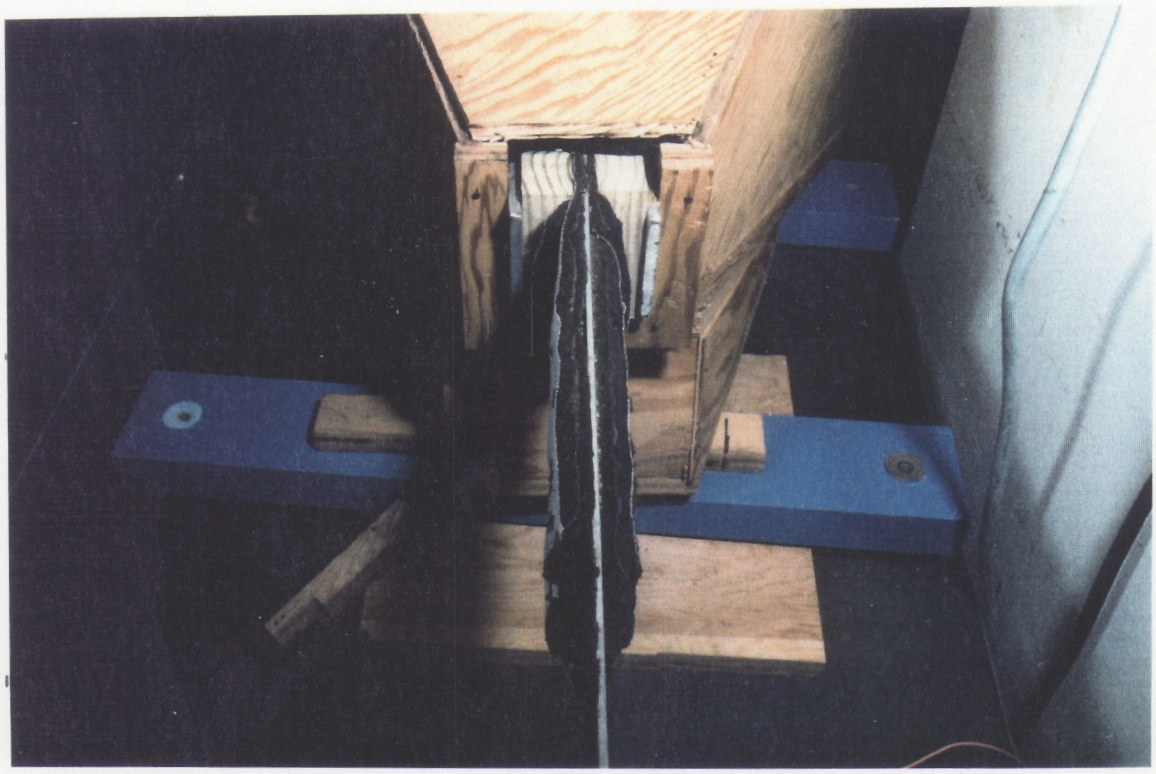

Figure 4.33 Photograph of the Modified Termination

demonstrated, feedforward control systems with wave vector sensors are a effective means of control for both infinite and resonant structures.

The out-of-plane velocity magnitude versus beam axial position for the no-control case is shown in Figure 4.34. The curve denoted as "Experimental" is the actual velocity magnitude determined in the experiment. A wave decomposition was performed on the experimental data as outline in Section 4.5.4. The resulting reconstruction of the velocity distribution based on these

wave amplitudes is shown as "Curve fit" in Figure 4.34. It is seen in Figure 4.34 that the two curves agree quite well suggesting an accurate wave decomposition.

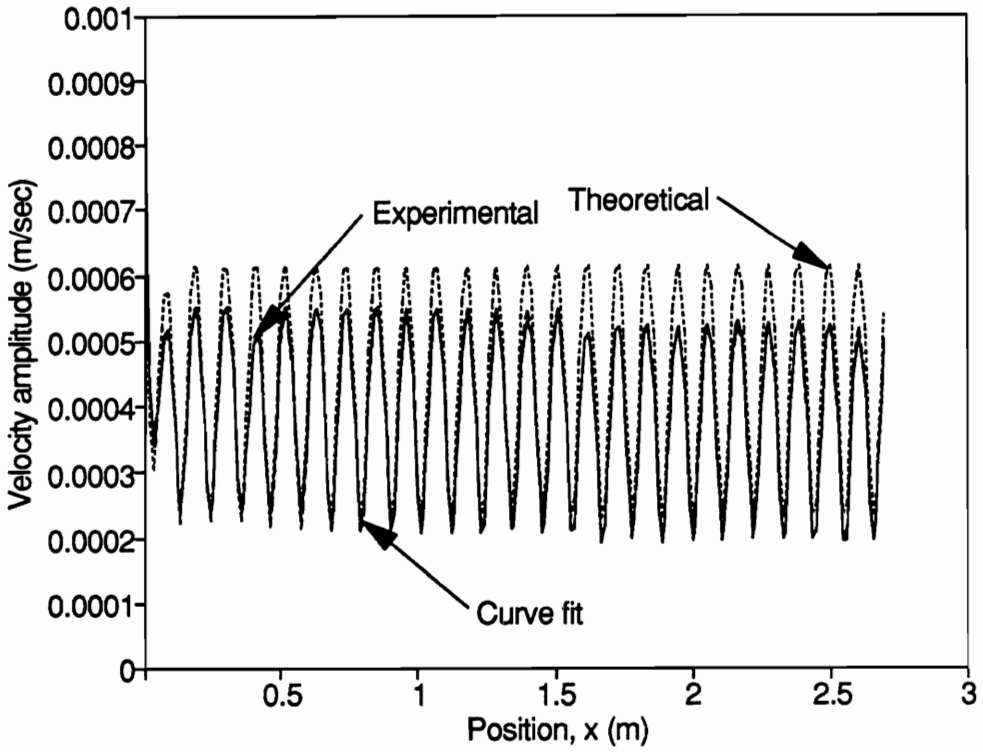

Figure 4.34 Flexural Velocity Distribution
No Control, 608 Hz, Finite Beam

The theoretical response of the beam to a point force excitation at the free end, and a variable termination at the other end is detailed in Chapter 2. The value of the primary force at the free end measured in the experiment was used as

the theoretical input force. The termination is described by its traveling wave reflection coefficient, R_{tf}, and its nearfield reflection coefficient, R_{nf}, as defined in Chapter 2. These values were set equal to the reflection coefficients determined from the aforementioned curve fit as outlined in Section 4.5.4. The resulting theoretical response is the curve labeled "Theoretical" in Figure 4.34.

The plot of the controlled velocity distribution is shown in Figure 4.35. The curve labeled "Experimental" is the actual measured velocity magnitude. The curve labeled "Curve fit" is a plot of the LMS wave deconvolution response. When control is applied to the beam the velocity distribution between the control point (0.4m) and the termination is reduced by the action of the controller on the order of 40 dB. The LMS fit of the flexural wave response as discussed in Section 4.5.4 is depicted as the "Curve fit" shown in Figure 4.35. The actual primary force as measured in the experiment as well as the flexural reflection coefficients determined from the wave decomposition as detailed in Section 4.5.4 were used to determine the theoretical response of the beam under control as described in Chapter 2. The theoretical response

corresponding to the optimal control case is given as the "Theoretical" curve of Figure 4.35.

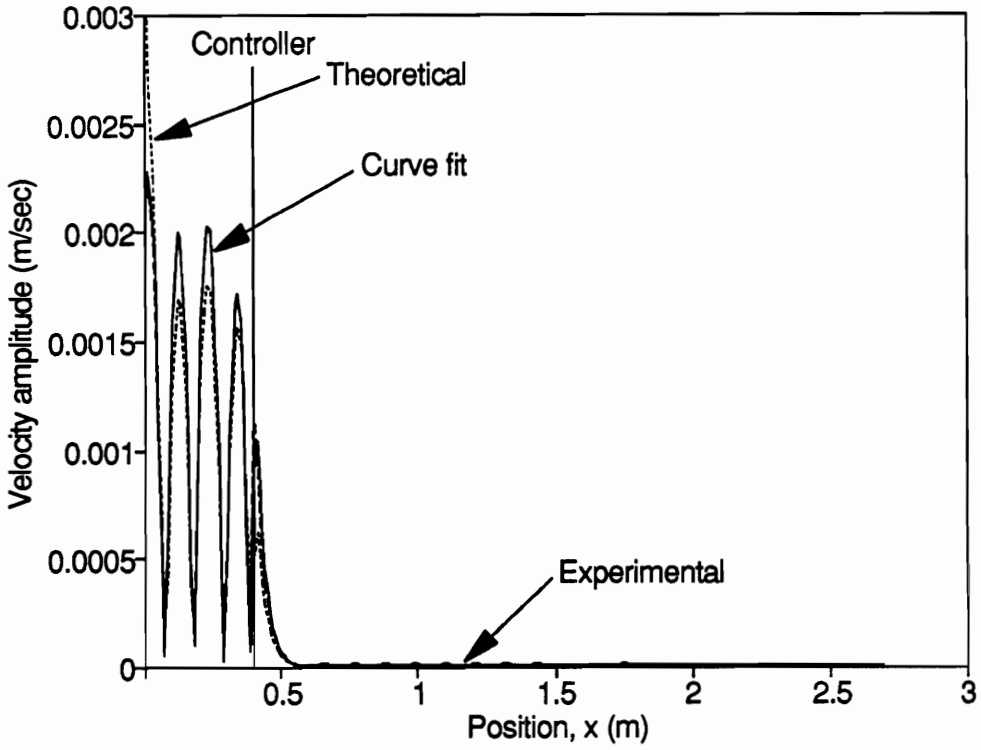

Figure 4.35 Flexural Velocity Distribution
Control, 608 Hz, Finite Beam

The flexural traveling wave amplitudes for the no control case corresponding to the velocity response plots shown in Figure 4.34 are shown in Table 4.24. The wave amplitudes are given in terms of displacement in meters. Again for the no control and control cases, the theoretical curves were determined based on the experimental traveling wave reflection coefficient of region 3b which equals 0.46. Note that before the termination was modified for this test as described at

the beginning of the section, the flexural traveling wave reflection coefficient was 0.11.

Table 4.24 Flexural Traveling Wave Amplitudes
No Control, 608 Hz, Finite Beam

Region	Theoretical			Experimental Curve Fit		
	A	B	R_{tf}	A	B	R_{tf}
	m x 10^{-9}	m x 10^{-9}	--	m x 10^{-9}	m x 10^{-9}	--
1	110	50.8	0.46	104	40.6	0.39
2	110	50.8	0.46	NA	NA	NA
3a	110	50.8	0.46	99.2	44.2	0.44
3b	110	50.8	0.46	93.7	43.2	0.46

The flexural traveling wave amplitudes for the control case corresponding to the velocity response plots shown in Figure 4.35 are shown in Table 4.25. The wave amplitudes are given in terms of displacement in meters. As seen previously, the theoretical optimal control solution provides zero traveling wave amplitudes at axial positions past the control point. Experimentally the traveling wave amplitudes in regions past the controller location were attenuated over 31 dB relative to the no control case, which for all practical purposes is equivalent to zero. The usable dynamic range of the DSP system, and the signal to noise ratio available at the error sensors limit control in this particular case to about a 40 dB reduction. Note that the boundary condition that the controller imparts on

the beam causes the traveling waves between the free end and the control point to rise by a factor of at least 2.5.

Table 4.25 Flexural Traveling Wave Amplitudes
Control, 608 Hz, Finite Beam

Region	Theoretical			Experimental Curve Fit		
	A	B	R_{tf}	A	B	R_{tf}
	m x 10^{-9}	m x 10^{-9}	--	m x 10^{-9}	m x 10^{-9}	--
1	229	229	1.0	266	263	0.98
2	222	222	1.0	NA	NA	NA
3a	0	0	0.46	1.76	1.21	0.69
3b	0	0	0.46	0.89	1.15	1.27

Table 4.26 details the flexural power flow corresponding to the velocity distributions shown in Figure 4.34 and Figure 4.35. In this case the power flow is given in both Watts and dB relative to the experimental no control case. As shown in Table 4.26 for the no control case, the power flow both experimentally and theoretically agree within 1.4 dB. As seen previously for the semi-infinite beam, the theoretical optimal control solution equates to zero flexural power flow throughout the entire beam. This is accomplished by totally reflecting the waves generated by the primary source and forcing a reactive input impedance at the primary source. Experimentally, the power flow downstream of the

controller location (regions 3a and 3b) is reduced by over 36 dB. The experimental case showed a reduction of 5.5 dB in region 1.

Table 4.26 Flexural Power Flow, 608 Hz, Finite

Region	No Control		Control	
	Theoretical	Experimental Curve Fit	Theoretical	Experimental Curve Fit
	Watts $x10^{-6}$ (dB)	Watts $x10^{-6}$ (dB)	Watts $x10^{-6}$ (dB)	Watts $x10^{-6}$ (dB)
1	12.2 (1.41)	11.8 (1.26)	0.00 (-∞)	3.35 (-4.2)
2	12.2 (1.41)	NA (NA)	0.00 (-∞)	NA (NA)
3a	12.2 (1.41)	10.1 (0.59)	0.00 (-∞)	0.0021 (-36.3)
3b	12.2 (1.41)	8.83 (0.00)	0.00 (-∞)	-0.0006 (-41.1)

The use of a feedforward adaptive control system in conjunction with a set of real time wave vector filters as error signals provides an effective means of controlling energy transmission in regions of both semi-infinite and finite beams with resonant behavior. The wave vector filtering scheme uses a relatively simple array of sensors and digital filters to accurately estimate the flexural and extensional traveling waves (and power flow) in beam like structures. This is in contrast to the modal approach were complex arrays of actuators and sensors are needed to observe and control the vibrating modes of the structure.

Since the motion of a beam like structure can be analyzed using either a wave or modal approach, it is important to distinguish their differences when applied to the wave vector filtering problem. The wave vector (for a single positive traveling wave for example) can be thought of as an infinite combination of beam normal modes. Each of these normal modes is represented by equal and opposite traveling waves of discrete wavenumbers which are related to the eigenvalues of the characteristic equation. If the power flow can be shown to be equivalent to the net traveling wave (the infinite combination of these modes) then it is not necessary to observe each mode and control each mode. What is important is that the combination of these modes which represents the traveling wave can be observed. Therefore, the positive traveling wave is a very important combination of normal modes which yields a single variable to exactly represent the total positive traveling flexural energy. This allows for the overall reduction of the sensor and actuator system when the proper variable is sensed.

Since, in extension, the wave field has been highly resonant for all the previously presented cases (the extensional traveling wave reflection coefficient, R_{te}, was greater than about 0.9) the extensional results for this case is omitted for brevity.

4.5.5.8 Simultaneous Control of a Finite Beam at 608 Hz and 1312 Hz

The purpose of this section is to demonstrate control of flexural and extensional power flow at multiple frequencies, namely 608 Hz and 1312 Hz. The section will present the results in terms of resultant flexural velocity distributions, and extensional strain distributions only. Multiple frequency control of linear systems can be separated, and analyzed in terms of the individual frequencies. The net displacement field can be considered the superposition of the fields generated by each component frequency. The remaining wave and power flow information is redundant, and omitted for brevity. Suffice it to say that the results for this particular case in terms of wave distributions and resulting power flow are similar to those previously presented. The control concepts can be extended in general to many frequencies, or even band limited excitation if the appropriate control scheme is used. As discussed in Chapter 2, the wave vector filtering scheme was developed for excitation by band limited spectra, and this experiment demonstrates the operation of the wave vector filter at multiple frequencies simultaneously.

For this test configuration the adaptive FIR filters used in the controller were expanded to four coefficients to accommodate the two frequencies as discussed in Chapter 3. In general these filters can be expanded further to accommodate

many frequencies, but this expansion is typically limited by the bandwidth of the digital signal processing board used to implement the control. Since the wave vector filters are designed to operate over band limited spectra, they did not require modification for this experiment. Again for this test case a sample rate of 5.3 kHz was used. The reference signal must, of course, contain both frequencies to be controlled, and in this case was obtained by analog summing two different signal generators.

The actual out-of-plane flexural velocity distribution for the uncontrolled excitation at frequencies of 608 Hz and 1312 Hz is the curve labeled "Experimental" in Figure 4.36, and was generated by adding the frequency domain laser measurement data (flexural velocity) taken from the B&K analyzer at the 608 Hz and 1312 Hz frequency bins. The velocity distribution for each separate frequency was used to determine the LMS flexural wave amplitudes as described in Section 4.5.4. The flexural wave amplitudes found in the wave decomposition for each frequency was used to create a velocity distribution as performed previously for the single frequency cases, and these distributions were superposed to create the net distribution. The net velocity distribution corresponding to the curve fit is the curve labeled "Curve fit" in Figure 4.36. In Figure 4.36, the axial velocity distribution contains an interference pattern corresponding to the two separate frequencies which have different

wavelengths. Note the extremely good agreement between the actual experimental data and the curve fit.

The theoretical response was determined as before for the single frequency cases for each frequency and combined by superposition to determine the net field. Note that the input force at the primary shaker was measured for each frequency and used in conjunction with the flexural wave reflection coefficients to determine the theoretical response. In this case the flexural traveling wave reflection coefficients, R_{tf}, were 0.49 and 0.24 in region 3b for frequencies of 608 Hz and 1312 Hz respectively.

When control is applied to the system, the resultant experimental out-of-plane velocity distribution is shown as the "Experimental" plot of Figure 4.37. The resultant power flow distribution between the controller location and the termination were calculated as previously for the single frequency cases, and showed a reduction by 30 dB at 608 Hz and 29 dB at 1312 Hz by the action of the controller. The tables are omitted for brevity. The LMS fit of the experimental velocity distribution is the plot labeled "Curve fit". The theoretical optimal control solution for the beam under the assumed conditions is again determined for each frequency independently and then superposed to provide the net field. This net field is the "Theoretical" curve of Figure 4.37. As seen

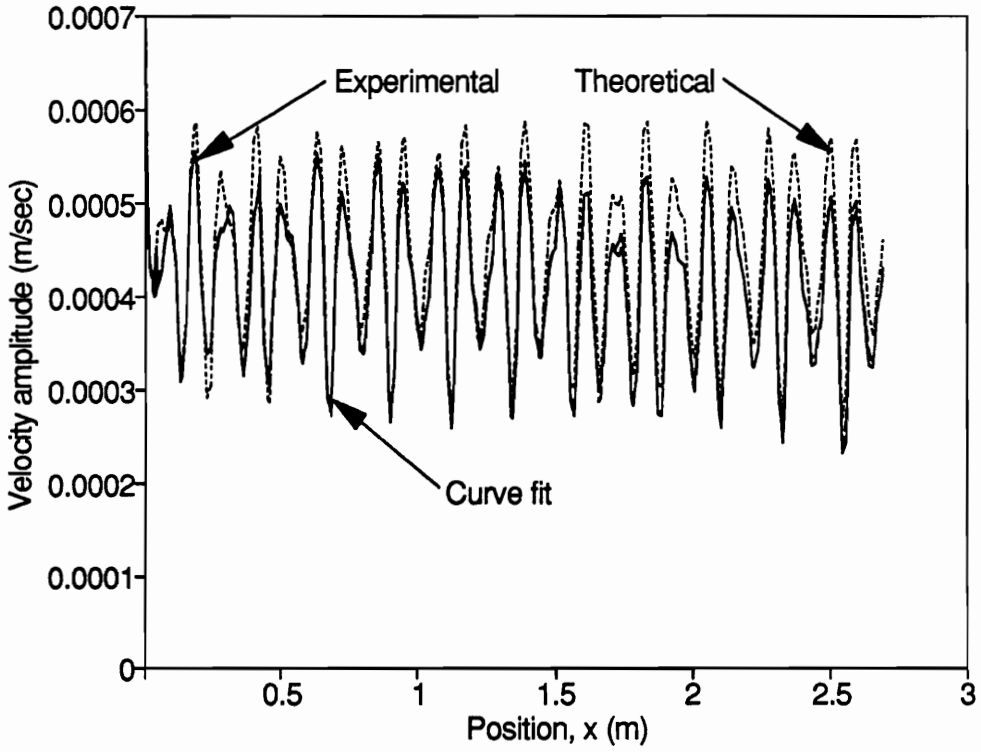

Figure 4.36 Flexural Velocity Distribution
No Control, 608 and 1312 Hz, Finite Beam

previously for the single frequency cases, the theoretical optimal solution produces net flexural traveling wave amplitudes of zero between the controller and the termination corresponding to the solid line at zero velocity in Figure 4.37. The tables of the corresponding wave amplitudes and power flow are similar to those previously presented for the single frequency cases, and are omitted for brevity.

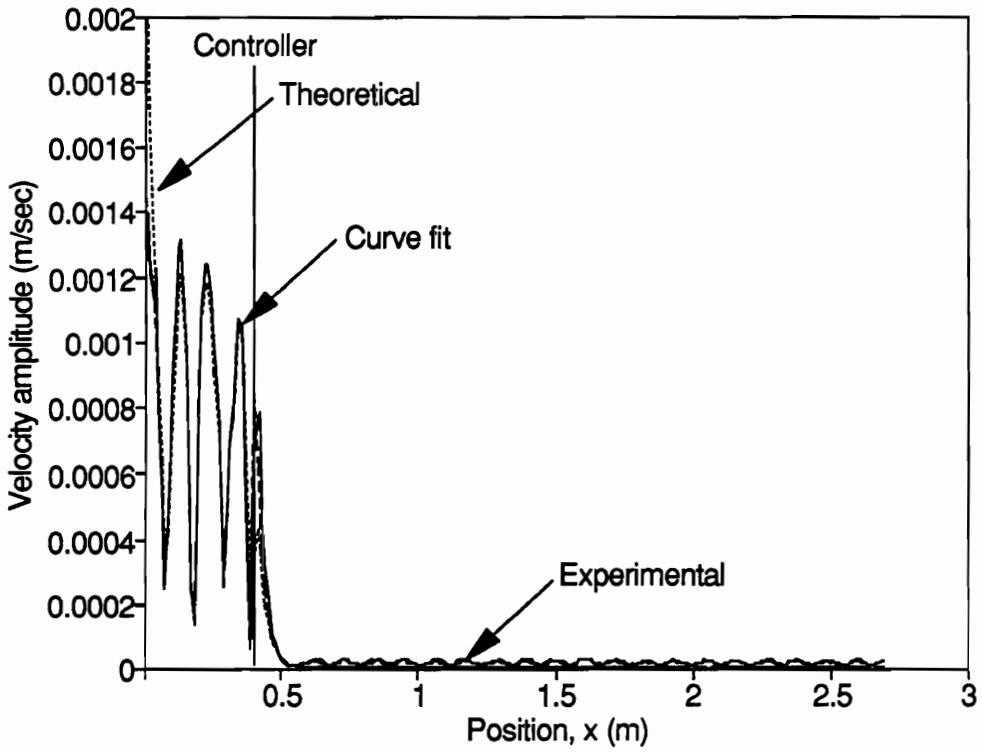

Figure 4.37 Flexural Velocity Distribution
Control, 608 and 1312 Hz, Finite Beam

The in-plane strain distribution for the test beam excited at frequencies of 608 Hz and 1312 Hz is shown as the plot labeled "Experimental" in Figure 4.38. These values again were taken at the four strain gage locations of 0.6m, 1.4m, 1.9m, and 2.7m from the free end. These values were used to determine the two LMS extensional traveling wave amplitudes as described in Section 4.5.4. The resultant wave amplitudes were used to reconstruct the strain field shown

as "Curve fit" of Figure 4.38. The theoretical strain distribution of a beam excited by a point force at the free end with a termination at the other end represented by a reflection coefficient determined from the LMS wave amplitude decomposition is shown as the "Theoretical" curve of Figure 4.38. The values of the extensional wave reflection coefficients were 0.90 and 1.8 for frequencies of 608 Hz and 1312 Hz, respectively.

When the controller is activated and reaches steady state, the strain distribution is found to be that represented by the plot labeled "Experimental" of Figure 4.39. The LMS curve fit of this extensional strain distribution is found in an identical fashion to the no control case, is shown as the "Curve fit" of

Figure 4.39. Lastly the theoretical optimal control solution produces the strain distribution labeled "Theoretical" in Figure 4.39. The maximum strain amplitude in the proximity of the actuator is 5.4E-6 which is much higher than that before control, and is necessary for the relatively short actuator to be able to control the long extensional waves. As discussed in Chapter 2, the piezoelectric actuator is modeled as equal and opposite in-plane forces acting at the ends of the actuator. When the actuator length is much shorter than a wavelength, the two sources tend to cancel out.

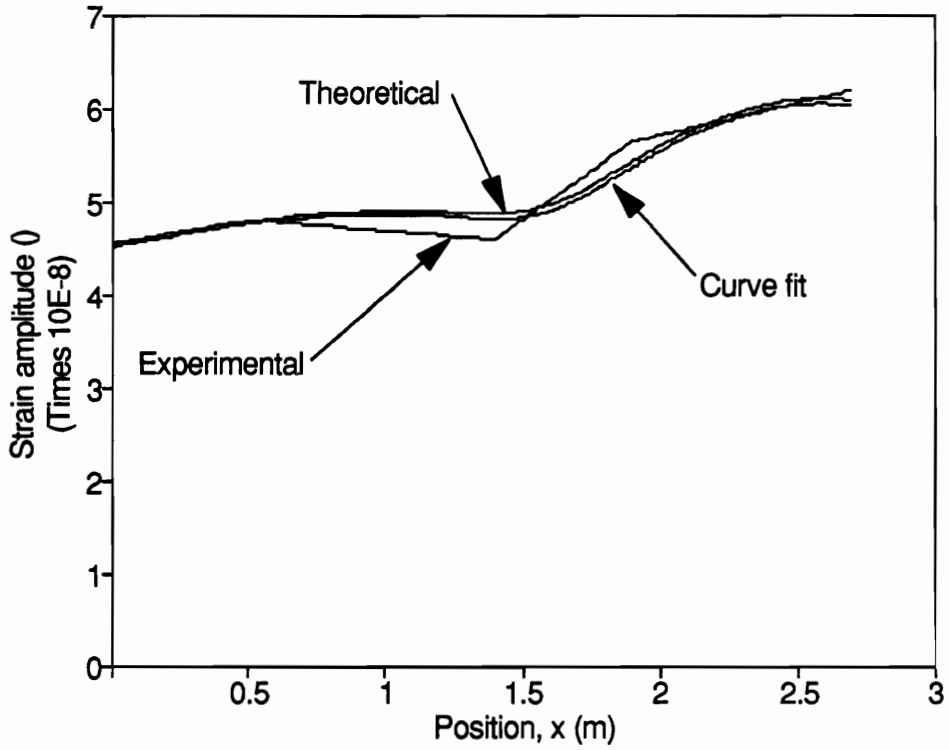

Figure 4.38 Extensional Strain Distribution
No Control, 608 and 1312 Hz

4.6 Discussion

In the beginning of the Chapter, control of flexural and extensional power flow was demonstrated for a semi-infinite beam case using sensors located downstream of the control point. This control is possible because the beam is

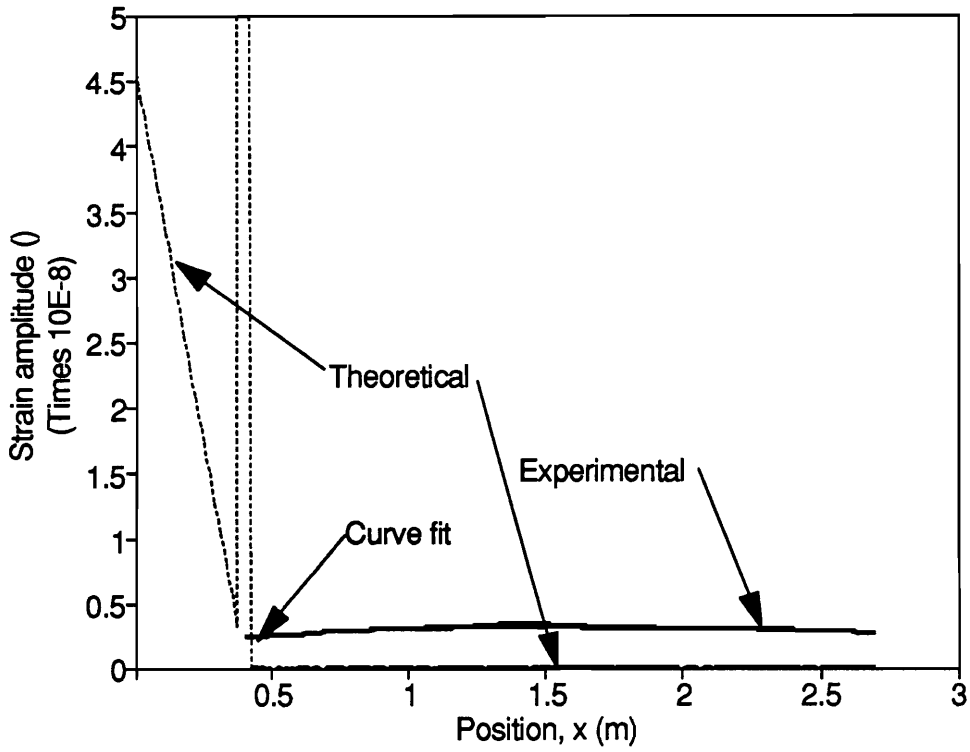

Figure 4.39 Extensional Strain Distribution
Control, 608 and 1312 Hz

semi-infinite, and thus is not characterized with nodal lines which, in the proximity of the error sensor, could adversely effect the control performance. Flexural control of a finite beam (with a blocking mass discontinuity) was demonstrated in the beginning of the chapter, but the error sensors were located in the semi-infinite portion of the beam.

For beam like structures, if the control actuator and primary disturbances are both located on the same end of the beam with respect to the error sensor location, and the beam does not have a traveling wave reflection coefficient near one at the boundary at the opposite end (see Figure 4.40, a)), then the total power flow can be estimated and controlled with one sensor for each type of vibration (i.e. flexural, extensional, etc.) located at any point downstream of the controller location. If the beam does have a reflection coefficient near one at the opposite end from the primary source (see Figure 4.40, b)), and the error sensor is placed away from the resultant nodal lines for the frequency range of interest, then the total power flow can also be estimated and controlled with one sensor for each type of vibration located at any point downstream of the controller location. However, if the beam has external sources (primary or control) on either side of the error sensor location (see Figure 4.40, c)), or if the nature of the boundary conditions (and subsequent nodal lines) are not known or are subject to change (see Figure 4.40, d)) then an alternate sensing technique called wave vector filtering must be used to estimate traveling waves and subsequent power flow. Experiments using this sensing technique were presented in the last part of this chapter.

In the last half of the Chapter, simultaneous control of flexural and extensional power flow in thin beams has been experimentally demonstrated for cases

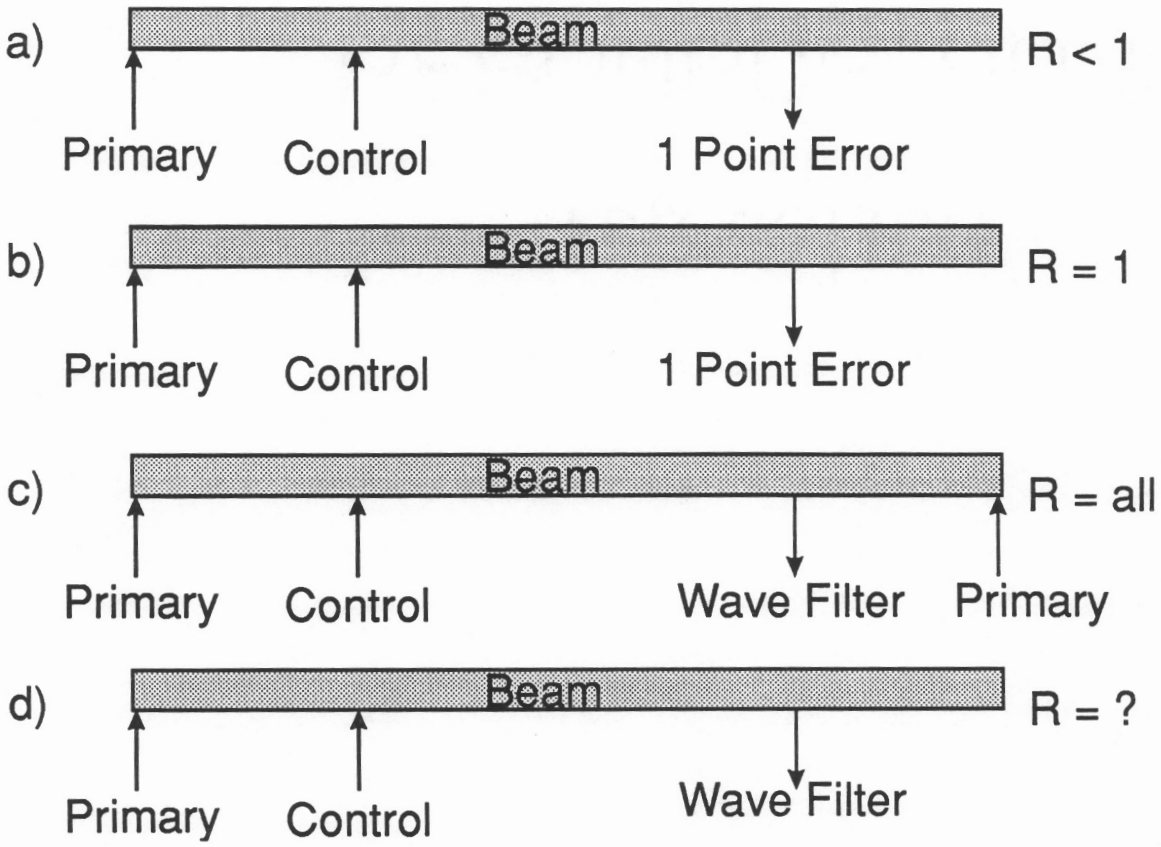

Figure 4.40 Required Sensor Configurations for Various Loading Conditions

where the error sensors are located in the finite section of the beam. This is possible because of the wave discrimination possible with the wave vector filtering scheme. The beauty of the aforementioned system of control is that it utilizes a real time wave vector filtering scheme to estimate traveling flexural and extensional waves, and uses these estimates as the error inputs to a filtered-x LMS adaptive controller. The control is demonstrated over a range of single or multiple frequencies for both non-resonant and resonant responding

beam systems because wave vector filters provide an estimate of the traveling waves and power flow under these general operating characteristics. The wave vector filtering scheme was found to provide extremely accurate wave estimation over a range of beam configurations and frequencies.

The sensors provided an estimate of the unidirectional wave amplitude and hence power transmitted in a beam responding in a number of modes, and thus have the ability to reduce the controller complexity by reducing the number of the sensors required compared to a typical modal sensing approach. The modal approach typically requires a large number of sensors (one per mode) that can only in the limit (as the number of sensors is increased) approximate what can be sensed directly with this new technique. It is noted however, that the modal approach can be used to observe and control the response over the entire beam, where the wave filtering approach observes and controls waves in a specific region of the beam (region between discontinuities where sensors are located). Both approaches require some type of beam modeling. In the modal approach, the normal modes (or admissible functions) must be known or assumed. In the wave sensing approach, the dispersive properties (i.e. wave number as a function of frequency) must be known or approximated.

In addition, the wave vector filtering technique will estimate the traveling waves for band limited spectra. The modal approach would require a different modal sensor for all modes that respond significantly in this same band of frequencies to perform the equivalent function. For certain systems using the modal approach, the number of sensors and resultant controller complexity required could be quite large.

The use of two independent actuators is experimentally shown to be able to excite both flexural and extensional motion simultaneously. In previous work by other researchers (Crawley and Anderson, 1990; Fanson and Chen, 1986; and Dimitriadis et al., 1991), the actuators were restricted to be wired in dedicated pairs. Two symmetrically mounted actuators wired in-phase to excite extensional motion, and two symmetrically mounted actuators wired out-of-phase to excite pure flexure. This would require a total of four actuators to perform the same function as that demonstrated here using only two. Hence the use of a coupled controller as in the work presented in this thesis allows a significant reduction in control order.

Chapter 5

Conclusions and Recommendations

The primary goal of this dissertation consisted of two related parts. The first was to develop an analytical basis for predicting the active control of flexural and extensional power flow in thin semi-infinite and finite beams (both independently and simultaneously) using piezoelectric actuators and sensors. The second part was to experimentally demonstrate these techniques applied to actual beam systems and validate the theory. In order to maintain total control authority over the system, the control actuators must be able to adequately excite both flexural and extensional motion in the beam. Accurate sensing or estimation of the actual power flow (or variables that can be related to the power flow) in the beam in real time is also a requirement. Here real time implies time domain error information. This dictated the development of advanced, new sensing techniques. In order that these overall goals were achieved several tasks and associated new research areas were carried out as discussed below.

A new analytical model for the excitation of thin beams by a single asymmetrically mounted piezoelectric element was presented in Chapter 2. The analysis shows that the single actuator is mathematically equivalent to equal and opposite moments (i.e. δ' functions in the out-of-plane force equation), and simultaneously, equal and opposite in-plane force (δ functions in the in-plane displacement equation) located at the ends of the actuator. The relative magnitudes of the forces/moments (and subsequent flexural and extensional wave motions) is shown to be dependent upon the actuator and beam configuration, and can be controlled by using a pair of collocated actuators with independent complex input voltages.

Two new techniques for the real time filtering of traveling waves in one a dimensional media using two axially spaced sensors were developed. These techniques filter and thus discriminate the separate positive and negative traveling flexural and extensional wave components over band limited spectra, for both dispersive and non-dispersive media. The techniques are termed wave vector filtering because they estimate the vector direction and complex amplitude of the traveling waves. The first technique is then applied to the sensing of positive and negative traveling flexural waves (Cotangent Method) and the second to extensional waves (Time delay Method) in thin beams of semi-infinite or finite length (i.e. with wave reflections). The Cotangent Method

is applicable to both dispersive and non-dispersive media, but tends to be accurate over a more limited frequency range because of approximations inherent in the IIR filter implementation. The Time Delay Method provides an extremely accurate wave vector filtering for only non-dispersive media, and is the method of choice for non-dispersive media (such as extensional waves in beams), or for frequency ranges over which the dispersion is negligible.

As was shown in Chapter 2, the power flow in a beam is proportional to the difference of the square of the traveling wave amplitudes. Thus, if the wave amplitudes can be sensed and subsequently attenuated in an active control approach then the power flow will accordingly be reduced. An important aspect is that the wave vector filter approach provides wave estimates in the time domain as opposed to previous methods which gave frequency domain information. The sensing technique is thus suitable for use with the time domain active LMS control approach.

The actuator and sensor models were used to show the theoretical optimal control of power flow in both a semi-infinite and a finite beam (with a variable termination impedance representative of a structural joint). When a semi-infinite or finite beam is subjected to a primary disturbance at the free end, then a single pair of piezoelectric actuators can produce a net power flow of zero

downstream of the actuators for both flexural and extensional vibration simultaneously. The controller generally forces a reactive boundary condition at the control location thus totally reflecting incoming waves back to the source forcing a reactive input impedance at the primary location.

Three sets of experiments were conducted to demonstrate the active control of flexural and extensional power flow in thin semi-infinite and finite beams containing a blocking mass using piezoelectric actuators and sensors. The first experiment controlled only the flexural power flow and used a pair of piezoceramic (PZT) actuators and another pair of piezoceramic sensors both pairs of which were hard wired 180 degrees out-of-phase to excite and sense, respectively, only flexural waves. The use of a Filtered-x LMS adaptive controller to optimize the signals to the actuators demonstrated attenuations in flexural power flow in both semi-infinite and finite beams on the order of 30 dB or more. The approach was also demonstrated over a range of frequencies for a semi-infinite beam case, and a finite beam with a blocking mass discontinuity. The results demonstrate that a single pair of piezoelectric actuators wired such that they produce pure flexure, and a single pair of sensors wired to sense pure flexure can be used to completely isolate (reductions of 30 dB or more) the beam downstream of the actuator location from unwanted flexural energy.

The second set of experiments demonstrated the simultaneous active control of flexural and extensional motion (and power flow) in semi-infinite (in terms of flexure) and finite (in terms of extension) thin beams. The results show that by using a single pair of symmetrically located piezoceramic actuators and another pair of sensors in conjunction with a multi-channel Filtered-x LMS controller, simultaneous attenuations of flexural and extensional power flow of 20 dB or greater is achievable. The piezoceramic actuator pair is thus capable of exciting both flexural and extensional motion in relative amplitudes dictated by the controller as discussed theoretically in Chapter 2, and the actuator pair is capable of isolating the beam downstream of the actuators from unwanted flexural and extensional power flow.

The final set of experiments demonstrated the use of the real time wave filtering scheme to the simultaneous control of flexural and extensional power flow in both finite and semi-infinite beams. The actuators consisted of two symmetrically mounted and independently driven piezoelectric elements. Three pairs of PVDF sensors in conjunction with a digital filter were used to provide a real time estimate of the positive and negative traveling flexural and extensional waves in the beam. These estimates were taken in a region of the beam were power flow was to be minimized, and therefore, these wave estimates provided a real time signal or the function to be minimized using the Filtered-x LMS

adaptive algorithm. Attenuations of greater than 26 dB of flexural and extensional power flow was observed over a range of frequencies and beam configurations. The wave vector filtering is capable of accurately observing and discriminating between the net positive and negative flexural and extensional waves in real time for both semi-infinite beams and resonant (finite) beams whose traveling wave reflection coefficients varied between 0.11 and 0.9. The outputs of the wave vector filters can be used as error functions of a time domain adaptive controller to isolate the region of a beam downstream of the control actuator location from unwanted flexural and extensional vibration and power flow.

For structures which are comprised of beam like elements, if the controller and primary (unwanted) disturbances are both located on the same end of the beam with respect to the error sensor location, and the beam does not have a traveling wave reflection coefficient near one at the boundary at the opposite end, then the total power flow can be estimated and controlled with one sensor for each type of vibration (i.e. flexural, extensional, etc.). If the beam does have a reflection coefficient near one at the opposite end from the primary source, and the sensor is not placed symmetrically over a resultant nodal lines, then the total power flow can also be estimated and controlled with one sensor for each type of vibration. It is noted that these nodal lines are a strong function of

frequency ,and thus control over a large bandwidth is not possible with using single sensor. If the beam has external sources (primary or control) on either side of the error sensor location, or if the nature of the boundary conditions (and subsequent nodal lines) are not known or are subject to change then an alternate sensing technique called wave vector filtering must be used to estimate traveling waves and subsequent power flow. Two piezoelectric actuators mounted symmetrically and driven independently can be used to control the total flexural and extensional power flow downstream of the actuators location for both finite and semi-infinite beams over frequency ranges where the actuators have sufficient control authority (i.e. do not produce a zero at the error sensor location). Optimal control over the primary field at frequencies where zeros are produced at the error sensor by excitation of only the control actuator would require theoretically infinite control actuator voltage and produce theoretically infinite upstream beam response (control voltage and upstream beam response "poles").

Future work should be devoted to the following topics:

1. To the development of sensing and actuation techniques for torsional vibration in beams.
2. To expand the wave vector filter scheme to include flexural nearfields and torsional waves.

3. To determine a means of making the wave filtering schemes adaptive (at least off line) using beam response data such as that produced by the laser vibrometer to determine the digital filter values. This will correct for discrepancies in the beam model if they exist.

List of References

Beyer, W. H., 1981. *CRC Standard Mathematical Tables*, CRC Press, Inc., Boca Raton, FL.

Burdisso, R. A., Fuller, C. R., 1992. "Theory of Feedforward Controlled System Eigenproperties," *The Journal of Sound and Vibration*, 153(3), pp. 437-451.

Burdisso, R. A., Fuller, C. R., 1993. Author's Reply to Comments on "Theory of Feedforward Controlled System Eigenproperties," To appear in *The Journal of Sound and Vibration.*

Clark, R.L and Fuller, C.R., 1990. "Experiments on Active Control of Structurally Radiated Sound Using Multiple Piezoelectric Actuators," Submitted to *The Journal of the Acoustical Society of America.*

Clark, R.L., Fuller, C.R. and Wicks, A.L., 1991. "Characterization of Multiple Piezoelectric Actuators for Structural Excitation," *The Journal of the Acoustical Society of America,* 90(1), pp. 346-357.

Collins, S.A., Miller, D.W. and von Flotow, A.H., 1991. "Piezopolymer Spatial Filters for Active Structural Control," Proceedings of the *Conference on Recent Advances in Active Control of Sound and Vibration,* Blacksburg, VA, April 15-17, pp. 219-234.

Collins, S.A., Miller, D.W. and von Flotow, A.H., 1990. "Sensors for Structural Control Applications Using Piezoelectric Polymer Film," MIT Report, pp. 1-83.

Crawley, E.F., and Anderson, E.H., 1990. "Detailed Models of Piezoceramic Actuation of Beams," *Journal of Intelligent Materials Systems and Structures*, Vol. 1, No. 2, pp. 235-247.

Crawley, E.F., and de Luis, J., 1987. "Use of Piezoelectric Actuators as Elements of Intelligent Structures," *AIAA Journal,* 25(10), pp. 1373-1385.

Cremer, L., Heckel, M. and Ungar, C.A., *Structure-Borne Sound*, Springer Verlag, Berlin, 1973.

Dantec Elektronik, 1984. *Instruction Manual*, 55N20 Doppler Frequency Tracker, published by Dantec Documentation Dept., Scientific Research Equipment Division, Dantec Elektronik, Mileparken 22, DK-2740 Skovlunde, Denmark.

Dimitriadis, E.K., Fuller, C.R. and Rogers, C.A., 1991. "Piezoelectric Actuators for Distributed Vibration Excitation of Thin Plates," *Journal of Vibration and Acoustics,* pp. 100-107.

Downing, J.M. and Shepard, K.P., 1988. "Power Flow in Beams Using a 5-Accelerometer Probe," *Proceedings* of Noise-Con 88, Noise Control Foundation, New York, pp. 335-340.

Downing, J.M., 1988. "Power Flow Intensity Measurement In a Beam Utilizing a Five Accelerometer Probe," Masters Thesis, The George Washington University, Washington, D.C.

Elliott, S.J., 1981. "A Simple Two Microphone Method of Measuring Absorption Coefficient," Acoustic Letters, 5(2).

Elliott, S.J., Strothers, I.M. and Nelson, P.A., 1987. "A Multiple Error LMS Algorithm and Its Application to the Active Control of Sound and Vibration," *IEEE Transaction on Acoustic Speech and Signal Processing*, ASSP-35, Vol. 1, pp. 1423-1434.

Fahy, F., 1985. *Sound and Structural Vibration,* Academic Press, Orlando Florida, pp. 60-72.

Fanson, J.L. and Chen, J.C., 1986. "Structural Control by the Use of Piezoelectric Active Members," *Proceedings of NASA-DOD Control-Structures Interaction Conference,* NASA CP-2447, Part II.

Fuller, C.R., Gibbs, G.P. and Silcox, R.J., 1990. "Simultaneous Active Control of Flexural and Extensional Power Flow in Beams," *Journal of Intelligent Materials Systems and Structures*," 1(2), pp. 235-247.

Gibbs, G.P. and Fuller, C.R., 1992(a). "Experiments on Active Control of Vibrational Power Flow Using Piezoceramic Actuators and Sensors," *AIAA Journal,* 30(2), pp. 457-463.

Gibbs, G.P. and Fuller, C.R., 1992(b). "Excitation of Thin Beams Using Asymmetric Piezoelectric Actuators," *The Journal of the Acoustical Society of America*, 92(6), pp. 3221-3227.

Gibbs, G.P., Fuller, C.R. and Silcox, R.J., 1992(a). "Method and Apparatus for Minimizing Multiple Degree of Freedom Vibration Transmission between two

Regions of a Structure," NASA Langley Research Center patent application LAR 14508-1-CU, U.S. Patent number 5156370, issued October 20,1992.

Gibbs, G.P., Fuller, C.R. and Silcox, R.J., 1992(b). "Real Time Wave Vector Filtering in One-Dimensional Media," Presented at the 123rd Meeting of the Acoustical Society of America, Salt Lake City, Utah, May 11-15.

Gibbs, G. P., Fuller, C. R., and Silcox, R. J., 1993. "Active Control of Flexural and Extensional Power Flow in Beams Using Real Time Wave Vector Sensors," Proceedings of the *Second Conference on Recent Advances in Active Control of Sound and Vibration*, Blacksburg, VA, April 28-30.

Golub, G. H., and Van Loan, C. S., 1989. *Matrix Computations*, Johns Hopkins University Press, Baltimore, MD.

Gonidou, L.O. and Fuller, C.R., 1989. "Further Research on Active Control of Flexural Power Flow in Elastic Thin Beams," *Journal of the Acoustical Society of America,* 85(S1), p. 573.

Jones, R.M., 1975. *Mechanics of Composite Materials,* Scripta Book Company, Washington, D.C., 1975.

Kinsler, L. E., Frey, A. R., Coppens, A. B., Sanders, J. V., 1982. *Fundamentals of Acoustics*, John Wiley & Sons, New York, NY.

KYNAR Piezo Film Technical Manual, 1987. Pennwalt Corp., Valley Forge, PA.

Lee, C.K. and Moon, F.C., 1990. "Modal Sensors/Actuators," *ASME JAM,* Vol. 57, pp. 434-441.

Liang, C., and Rogers, C. A., 1989. "Behavior of Shape Memory Alloy Actuators Embedded in Composites," Proceeding of the *1989 International Composites Conference*, Beijing, China.

Lindner, D. K., Baumann, W. T., Ho, F., Bielecki, E., 1991. "Modal Domain Optical Fiber Sensors for Control of Acoustic Radiation," Proceedings of the *Conference on Recent Advances in Active Control of Sound and Vibration,* Blacksburg, VA, April 15-17, pp. 839-850.

Math Works, 1987. *Matlab User's Guide*, The Math Works, South Natick, MA.

McGary, M.C., 1988. "Simulated Measurement of Power Flow in Structures Near to Simple Sources and Simple Boundaries," NASA TM-89124.

Meirovitch, L. and Norris, M. A., 1984. "Vibration Control," *Proceedings of Inter-Noise 84,* Noise Control Foundation, New York, New York, pp.477-482.

Miller, D. W., and von Flotow, A. H., 1989. "A Traveling Wave Approach to Power Flow in Structural Networks," *Journal of Sound and Vibration*, vol. 128, no. 1, pp. 145-162.

Miyoshi, M., Kaneda, Y., 1988. "Inverse Filtering of Room Acoustics," *IEEE Transactions on Acoustics, Speech, and Signal Processing*, Vol.36, No.2.

Miyoshi, M., Kaneda, Y., 1991. "Active Control of Broadband Random Noise in a Reverberant Three-Dimensional Space," *Noise Control Engineering Journal,* Vol. 36, No. 2.

Morgan, D. R., 1991. "An adaptive modal-based active control system," *Journal of the Acoustical Society of America*, 89(1), pp. 248-256.

Morse, P.M. and Ingard, K.U., 1968. *Theoretical Acoustics,* Princeton University Press, Princeton, NJ.

Noiseux, D.U., 1970. "Measurement of Power Flow in Uniform Beams and Plates," *The Journal of the Acoustical Society of America,* 47(1), Part 2.

Pan, J. and Hansen, C.H., 1990. "Active Control of Total Power Flow Along a Beam," *Proceedings from the International Congress on Recent Developments in Air and Structure-Borne Sound and Vibration,* Auburn University, AL, March 6-8.

Pavic, G., 1976. "Measurement of Structure Borne Wave Intensity, Part I: Formulation of the Method," *Journal of Sound and Vibration,* 49(2), pp. 221-230.

Piezo Systems, 1987. *Piezoelectric Motor/Actuator Kit Manual,* Piezoelectric Products Inc., Cambridge, MD.

Pines, D.J. and von Flotow, A.H., 1989. "Active Control of Flexural Wave Propagation at Acoustic Frequencies," *Proceedings of American Control Conference,* IEEE, pp. 221-229.

Pines, D.J. and von Flotow, A.H., 1990. "Development of Wave-Mode Observers for Active Control Wave Control of One-Dimensional Structures,"

Proceedings of The International Congress On Recent Developments in Air- And Structure-Borne Sound and Vibration, Auburn University, AL, March 6-8.

Post, J.T. and Silcox, R.J., 1990. "Active Control of the Forced Response of a Finite Beam," Proceedings of *Noise-Con 90*, University of Texas, Austin Texas, pp 197-202, October 15-17.

Redman-White, W., Nelson, P.A. and Curtis, A.R.D., 1987. "Experiments on Active Control of Flexural Wave Power," *Journal of Sound and Vibration,* 112(1), pp. 187-191.

Sundararajan, N., Williams, J. P., Montgomery, R. C., 1985. "Adaptive Modal Control of Structural Dynamic Systems using Recursive Lattice Filters," *Journal of Guidance, Control, and Dynamics,* Vol. 8, No. 2, pp.223-229.

Timoshenko, S., 1955. *Vibration Problems in Engineering*, Van Nostrand, Princeton, NJ.

von Flotow, A.H. and Schafer, B., 1986. "Wave Absorbing Controller for a Flexible System," *Journal of Guidance, Control, and Dynamics,* Vol. 9, pp.673-680.

von Flotow, A. H., and Vos, D. W., 1991. "The Need for Passive Damping in Feedback Controlled Flexible Structures," Proceedings of the *Conference on Recent Advances in Active Control of Sound and Vibration,* Blacksburg, VA, April 15-17, pp. 593-603.

Widrow, B. and Stearns, S.D., 1985. *Adaptive Signal Processing,* Prentice Hall Inc., Englewood Cliffs, NJ.

Appendix A

Beam Response Subjected to Various Loading Conditions

A.1 Point Force Excitation of Semi-infinite Beams

The flexural equation of motion of a semi-infinite beam subjected to a point force, F_f, at the free end and normal to the beams surface was previously presented as Equation (2.59) and is given as follows:

$$\frac{d^4w}{dx^4} - k_f^4 w = F_f \delta(x) \qquad \textbf{(A.1)}$$

The equation of motion will now be solved by using an assumed waves method. The response of the beam is assumed to be comprised of four waves: two traveling waves, and two decaying nearfields which can be mathematically written as follows:

$$w(x) = Ae^{jk_f x} + Be^{-jk_f x} + Ce^{k_f x} + De^{-k_f x} \qquad \textbf{(A.2)}$$

where A is the unknown positive traveling flexural wave coefficient, B is the unknown negative traveling flexural wave coefficient, C is the unknown negative

decaying flexural nearfield coefficient, and D is the unknown positive decaying nearfield coefficient, and k_f is the flexural wavenumber as defined by Equation (2.55). Since the beam is semi-infinite it is impossible for waves to arrive from infinity, and thus applying the Sommerfeld radiation condition results in wave coefficients B and C must be identically zero. Wave amplitudes A and D must be found by applying the boundary conditions at x = 0. The first boundary condition is that the moment must be zero which is found to be:

$$E_b I \frac{d^2 w(0)}{dx^2} = 0 = D - A \qquad \textbf{(A.3)}$$

The shear force must be equal to the externally applied force, F_f, which produces the following relation:

$$E_b I \frac{d^3 w(0)}{d} x^3 = F = E_b I k_f^3 (-jA - D) \qquad \textbf{(A.4)}$$

Combining Equations (A.3) and (A.4) and substituting back into the assumed solution of Equation (A.2) produces the following relation:

$$w(x) = \frac{jF_f}{2E_b I k_f^3} (e^{jk_f x} + e^{-k_f x}) \qquad \textbf{(A.5)}$$

Thus the total solution for all x and t is:

$$w(x,t) = \frac{jF_f}{2E_b I k_f^3} (e^{jk_f x} + e^{-k_f x}) e^{-j\omega t}. \qquad \textbf{(A.6)}$$

The extensional equation of motion of a semi-infinite beam subjected to an in-plane force, F_e, at the free end was presented as Equation (2.62) as the following:

$$\frac{d^2u}{dx^2} + k_e^2 u = \frac{F_e}{E_b(1 - \nu^2)a}\delta(x) \qquad \textbf{(A.7)}$$

The beam is assumed to have an in-plane motion of the form:

$$u(x) = Ee^{jk_e x} + Fe^{-jk_e x} \qquad \textbf{(A.8)}$$

where E is the unknown positive traveling extensional wave coefficient, F is the negative traveling extensional wave coefficient, and k_e is the extensional wavenumber. Since the beam is semi-infinite then no waves may arrive from infinity (Sommerfeld radiation condition) and thus the wave amplitude F must be identically zero. Next the boundary condition at x = 0 can be applied which states that the stress must be equal to the modulus of elasticity times the strain at x = 0 which is of the form:

$$\frac{F_e}{A} = E_b\frac{du(0)}{dx} = jk_e E_b E \qquad \textbf{(A.9)}$$

Solving Equation (A.9) for E and substituting into Equation (A.8) produces the following relation for the in-plane response:

$$u(x) = \frac{-jF_e}{E_b(1 - \nu^2)ak_e} e^{jk_e x} \quad \textbf{(A.10)}$$

The total in-plane response of a semi-infinite beam subjected to a point force, F_e, at the free end for all x and t is thus:

$$U(x,t) = \frac{-jF_e}{E_b(1 - \nu^2)ak_e} e^{jk_e x} e^{-j\omega t} \quad \textbf{(A.11)}$$

A.2 Excitation of a Semi-infinite Beam using a Single Piezoelectric Actuator

The flexural equation of motion, as previously presented in Equation (2.65), for the excitation of a semi-infinite thin beam by a single piezoelectric actuator located at a point x_a, and a length L_a is given by:

$$\frac{d^4w}{dx^4} - k_f^4 w = \frac{K^f d_{31} V}{T_a}[\delta'(x - (x_a - L_a/2)) - \delta'(x - (x_a + L_a/2))] \quad \textbf{(A.12)}$$

This relation can first be solved subjected to one moment (the one at $x = x_a - L_a/2$) and then the result can be superposed to form the flexural response of the beam due to both moments. When Equation (A.12) is modified such that the beam is only subjected to the moment at $x = x_a - L_a/2$ the following relation is produced:

$$\frac{d^4w}{dx^4} - k_f^4 w = \frac{K^f d_{31} V}{T_a}[\delta'(x - (x_a - L_a/2))] \qquad \textbf{(A.13)}$$

The Laplace transform is taken of both sides of Equation (A.13) and the result is:

$$s^4w(s) - s^3W(0) - s^2w'(o) - sw''(0) - w'''(o) - k_f^4 w(s) = s\frac{K^f d_{31} V}{T_a} e^{-s(x - \frac{L_a}{2})} \qquad \textbf{(A.14)}$$

The boundary conditions at x = 0 are that the moment and shear force are zero as presented in Equations (2.66) and (2.67) which requires that the w"(0) and the w'''(0) terms in Equation (A.14) be identically zero. Therefore Equation (A.14) can be solved for w(s) as

$$w(s) = s\frac{K^f d_{31} V}{T_a} e^{-s(x - \frac{L_a}{2})} + s^3\frac{w(o)}{s^4 - k_f^4} + s^2\frac{w'(o)}{s^4 - k_f^4} \qquad \textbf{(A.15)}$$

The inverse Laplace transform is found to be (Beyer, 1981):

$$w(x) = \frac{K^f d_{31} V}{4k_f^2} H\left(x - x_a + \frac{L_a}{2}\right)\left[e^{k_f\left(x - x_a + \frac{L_a}{2}\right)} + e^{-k_f\left(x - x_a + \frac{L_a}{2}\right)} - e^{jk_f\left(x - x_a + \frac{L_a}{2}\right)} - e^{-jk_f\left(x - x_a + \frac{L_a}{2}\right)}\right] +$$

$$\frac{w(0)}{4}\left[e^{k_f\left(x - x_a + \frac{L_a}{2}\right)} + e^{-k_f\left(x - x_a + \frac{L_a}{2}\right)} + e^{jk_f\left(x - x_a + \frac{L_a}{2}\right)} + e^{-jk_f\left(x - x_a + \frac{L_a}{2}\right)}\right] +$$

$$\frac{w'(0)}{4k_f}\left[e^{k_f\left(x - x_a + \frac{L_a}{2}\right)} - e^{-k_f\left(x - x_a + \frac{L_a}{2}\right)} - je^{jk_f\left(x - x_a + \frac{L_a}{2}\right)} + je^{-jk_f\left(x - x_a + \frac{L_a}{2}\right)}\right]$$

(A.16)

where H() is the unit step function. The Sommerfeld radiation condition states that waves cannot arrive from infinity, and thus, the coefficients for the negative traveling waves must be zero. These constraints are as follows:

$$\frac{K^f d_{31} V}{4T_a k_f^2} e^{-k_f\left(x_a - \frac{L_a}{2}\right)} + \frac{w(0)}{4} + \frac{w'(0)}{4k_f} = 0 \qquad \textbf{(A.17)}$$

$$-\frac{K^f d_{31} V}{4T_a k_f^2} e^{-k_f\left(x_a - \frac{L_a}{2}\right)} + \frac{w(0)}{4} + jk\frac{w'(0)}{4k_f} = 0 \qquad \textbf{(A.18)}$$

These two equations can be solved for w(0) and w'(0) producing

$$w(0) = \frac{K^f d_{31} V}{2k_f^2}\left[(-1 + i)e^{-k_f\left(x - x_a + \frac{L_a}{2}\right)} + (1 + i)e^{jk_f\left(x - x_a + \frac{L_a}{2}\right)}\right] \qquad \textbf{(A.19)}$$

$$w'(0) = -\frac{K^f d_{31} V(1+j)}{2k_f^2}\left[e^{-k_f(x-x_a+\frac{L_a}{2})} + e^{jk_f(x-x_a+\frac{L_a}{2})}\right] \qquad \textbf{(A.20)}$$

Substituting Equations (A.19) and (A.20) into Equation (A.16) produces the following relation for the excitation of a semi-infinite beam by a single moment:

For $x < x_a - L_a/2$:

$$w(x) = \frac{K^f d_{31} V}{4k_f^2}\left\{-e^{k_f(x-x_a+\frac{L_a}{2})} + (je^{-k_f(x_a-\frac{L_a}{2})} + (1+j)e^{jk_f(x_a-\frac{L_a}{2})})e^{-k_f x} + \right. \qquad \textbf{(A.21)}$$

$$\left. + ((-1+j)e^{-k_f(x_a-\frac{L_a}{2})} + je^{jk_f(x_a-\frac{L_a}{2})})e^{jk_f x} + e^{-jk_f(x-x_a+\frac{L_a}{2})}\right\}$$

For $x > x_a - L_a/2$:

$$w(x) = \frac{K^f d_{31} V}{8k_f^2}\left\{\left[2e^{k_f(x-x_a+\frac{L_a}{2})} + 2je^{-k_f(x_a-\frac{L_a}{2})} + (2+2j)e^{jk_f(x_a-\frac{L_a}{2})}\right]e^{-k_f x} + \right. \qquad \textbf{(A.22)}$$

$$\left. \left[-2e^{-jk_f(x_a-\frac{L_a}{2})} + (-2+2j)e^{-k_f(x_a-\frac{L_a}{2})} + 2je^{jk_f(x_a-\frac{L_a}{2})}\right]e^{jk_f(x-x_a+\frac{L_a}{2})}\right\}$$

The solution to the equation of motion excited with two equal and opposite moments, as was presented in Equation (A.12), can be solved by superposition using Equations (A.21) and (A.22). The resulting relation for the response of a

beam subjected to the excitation of a single piezoelectric actuator of length L_a at a distance x_a from the free end is presented as follows:

for $x < x_a - L_a/2$:

$$w(x) = \frac{K^f d_{31} V}{4T_a k_f^2}\left\{\left(e^{\frac{-k_f L_a}{2}} - e^{\frac{k_f L_a}{2}}\right)e^{-k_f x_a}e^{k_f x} + \left[j\left(e^{\frac{-k_f L_a}{2}} - e^{\frac{k_f L_a}{2}}\right) - (2j+2)\sin\left(\frac{k_f L_a}{2}\right)e^{jk_f x_a}\right]e^{-k_f x} + \left[(j-1)\left(e^{\frac{-k_f L_a}{2}} - e^{\frac{k_f L_a}{2}}\right) + 2\sin\left(\frac{k_f L_a}{2}\right)e^{jk_f x_a}\right]e^{jk_f x} + 2j\sin\left(\frac{k_f L_a}{2}\right)e^{jk_f x_a}e^{-jk_f x}\right\} \quad \textbf{(A.23)}$$

for $x_a - L_a/2 < x < x_a + L_a/2$:

$$w(x) = \frac{K^f d_{31} V}{4T_a k_f^2}\left\{ e^{k_f\left(x - x_a - \frac{L_a}{2}\right)} + \right.$$

$$\left[j\left(e^{\frac{k_f L_a}{2}} - e^{\frac{-k_f L_a}{2}}\right)e^{-k_f x_a} + (-2j + 2)\sin\left(\frac{k_f L_a}{2}\right)e^{jk_f x_a} + 2e^{k_f\left(x_a - \frac{L_a}{2}\right)} \right] e^{-k_f x} + \quad \textbf{(A.24)}$$

$$\left[(-1 + j)\left(e^{\frac{k_f L_a}{2}} - e^{\frac{-k_f L_a}{2}}\right)e^{-k_f x_a} + 2\sin\left(\frac{k_f L_a}{2}\right)e^{jk_f x_a} - 2e^{-jk_f\left(x_a - \frac{L_a}{2}\right)} \right] e^{jk_f x} +$$

$$\left. -2e^{-jk_f\left(x - x_a - \frac{L_a}{2}\right)} \right\}$$

for $x > x_a + L_a/2$:

$$w(x) = \frac{K^f d_{31} V}{4T_a k_f^2}\left\{ \left[\left(e^{k_f x_a} - je^{-k_f x_a}\right)\left(e^{\frac{-k_f l_a}{2}} - e^{\frac{k_f l_a}{2}}\right) + (2j+2)\sin\left(\frac{k_f l_a}{2}\right)e^{jk_f x_a} + 2e^{k_f\left(x_a - \frac{l_a}{2}\right)} \right] e^{-k_f x} + \right.$$

$$\left. \left[(-1 + j)\left(e^{\frac{k_f l_a}{2}} - e^{\frac{-k_f l_a}{2}}\right)e^{-k_f x_a} + 2\sin\left(\frac{k_f l_a}{2}\right)\left(e^{jk_f x_a} - je^{-jk_f x_a}\right) \right] e^{jk_f x} \right\} \quad \textbf{(A.25)}$$

The extensional equation of motion of a semi-infinite beam subjected to the excitation of a single piezoelectric actuator located at $x = x_a$ with a length L_a, as was previously presented in Equation (2.79), is presented as follows:

$$\frac{d^2 u}{dx^2} + k_e^2 u = \frac{K^e d_{31} V}{T_a}\left[\delta(x - (x_a - L_a/2)) - \delta(x - (x_a + L_a/2))\right] \quad \textbf{(A.26)}$$

The equation was solved by first determining the solution with only one of the two in-plane forces, then the total solution was found by superposition. The extensional equation of motion subjected to only one in-plane force at $x = x_a - L_a/2$ is :

$$\frac{d^2u}{dx^2} + k_e^2 u = \frac{K^e d_{31} V}{T_a}[\delta(x - (x_a - L_a/2)] \qquad \textbf{(A.27)}$$

The solution is found by assuming the in-plane displacement is comprised of two traveling waves of unknown amplitudes in the region of the beam between the free end and the point force, and by assuming there exists a single positive traveling wave in the region of the beam past the point force location. This can be written in equation form as follows:

For $0 < x < x_a - L_a/2$:

$$u_1(x) = E_1 e^{jk_e x} + F_1 e^{-jk_e x} \qquad \textbf{(A.28)}$$

For $x > x_a - L_a/2$:

$$u_2(x) = E_2 e^{jk_e x} \qquad \textbf{(A.29)}$$

The solution is found by applying boundary conditions, and solving for the unknown wave amplitudes. At $x = 0$ the in-plane force must be zero at the free boundary which is equivalent to

$$E_b a \frac{du(0)}{dx} = jk_e E_b a(E_1 - F_1) = 0 \qquad \textbf{(A.30)}$$

The displacement must be continuous, and the in-plane force must be discontinuous in a differential amount equal to the external applied force. These boundary conditions can be written in equation form as follows:

$$E_1 e^{jk_e(x-\frac{L_a}{2})} + F_1 e^{-jk_e(x-\frac{L_a}{2})} = E_2 e^{jk_e(x-\frac{L_a}{2})} \qquad \textbf{(A.31)}$$

and

$$jk_e E_b a\left(E_1 e^{jk_e(x_a-\frac{L_a}{2})} - F_1 e^{-jk_e(x_a-\frac{L_a}{2})}\right) + \frac{K^e d_{31} V}{T_a} = jk_e E_b a E_2 e^{jk_e(x_a-\frac{L_a}{2})} \qquad \textbf{(A.32)}$$

Equations (A.30), (A.31), and (A.32) can be solved for the unknown wave amplitudes E_1, E_2, and F_1. The resulting values for the unknown wave coefficients are presented as follows:

$$E_1 = F_1 = -\frac{jK^e d_{31} V}{2T_a k_e} e^{jk_e(x_a-\frac{L_a}{2})} \qquad \textbf{(A.33)}$$

and

$$E_2 = -j\frac{K^e d_{31} V}{k_e T_a} \cos\left(x_a - \frac{L_a}{2}\right) \qquad \textbf{(A.34)}$$

When (A.33) and (A.34) are substituted into the assumed response shown in Equations (A.28) and (A.29) the net extensional response to a single force is found to be

For $x < x_a - L_a/2$:

$$u(x) = -\frac{jK^e d_{31} V}{2T_a k_e} e^{jk_e\left(x_a - \frac{L_a}{2}\right)}\left[e^{jk_e x} + e^{-jk_e x}\right] \qquad \textbf{(A.35)}$$

for $x > x_a - L_a/2$:

$$u(x) = -j\frac{K^e d_{31} V}{k_e T_a}\cos\left(x_a - \frac{L_a}{2}\right)e^{jk_e x} \qquad \textbf{(A.36)}$$

The solution Equation (A.26) can be found by superposition using Equations (A.35) and (A.36). The resulting extensional response for a semi-infinite beam subjected to excitation by a single piezoelectric actuator of length L_a mounted on the upper surface a distance x_a from the free end is found to be

For $x < x_a - L_a/2$:

$$u(x) = -\frac{jK^e d_{31} V}{T_a k_e} e^{jk_e x_a}\sin\left(\frac{k_e L_a}{2}\right)\left[e^{jk_e x} + e^{-jk_e x}\right] \qquad \textbf{(A.37)}$$

For $x_a - L_a/2 > x > x_a + L_a/2$:

$$u(x) = -\frac{jK^e d_{31} V}{2T_a k_e}\left\{\left[-2e^{jk_e x_a}\sin\left(\frac{k_e L_a}{2}\right) - e^{-jk_e\left(x_a-\frac{L_a}{2}\right)}\right]e^{jk_e x} + e^{jk_e\left(x_a-\frac{L_a}{2}\right)}e^{-jk_e x}\right\} \quad \textbf{(A.38)}$$

For $x > x_a - L_a/2$:

$$u(x) = -j\frac{2K^e d_{31} V}{T_a k_e}\sin\left(\frac{k_e L_a}{2}\right)\sin(k_e x_a)e^{jk_e x} \quad \textbf{(A.39)}$$

A.3 Point Force Excitation of a Finite Beam

The flexural equation of motion of a finite beam subjected to a point force, F_f, at the free end and normal to the beams surface was previously presented as Equation (2.59) and is given as follows:

$$\frac{d^4 w}{dx^4} - k_f^4 w = F_f \delta(x) \quad \textbf{(A.40)}$$

In the finite beam case, the beam is free on one end and has a variable termination at the other that is described using two flexural reflection coefficients, R_{tf} and R_{nf}. and one extensional reflection coefficient, R_{te} as previously presented in Equation (2.96). Again an assumed waves solution was performed where the beam response is assumed to be of the form shown in Equation (A.2). In this particular case the boundary conditions at $x = 0$ are that the moment is zero, and the shear force is equal to the applied external force, F_f. The boundary conditions were applied to the assumed solution which produced the following set of equations:

$$E_b I \frac{d^2 w(0)}{dx^2} = E_b I k_f^3 (-A - B + C + D) = 0 \qquad \textbf{(A.41)}$$

and

$$E_b I \frac{d^3 w(0)}{dx^3} = E_b I k_f^3 (-jA + jB + C + D) = F_f. \qquad \textbf{(A.42)}$$

The boundary conditions at the variable termination were presented in Equation (2.96) are shown again for completeness as follows:

$$R_{tf} = \frac{B}{A} \qquad \textbf{(A.43)}$$

and

$$R_{nf} = \frac{C}{A} \qquad \textbf{(A.44)}$$

These flour equations were solved simultaneously for the unknown coefficients, A, B, C, and D and are presented as follows:

$$A = \frac{F_f}{E_b I k_f^3 [2R_{nf} - R_{tf} - 1 + j(R_{tf} - 1)]} \qquad \textbf{(A.45)}$$

$$B = \frac{F_f R_{tf}}{E_b I k_f^3 [2R_{nf} - R_{tf} - 1 + j(R_{tf} - 1)]} \quad \textbf{(A.46)}$$

$$C = \frac{F_f R_{nf}}{E_b I k_f^3 [2R_{nf} - R_{tf} - 1 + j(R_{tf} - 1)]} \quad \textbf{(A.47)}$$

and

$$D = \frac{F_f (1 + R_{tf} - R_{nf})}{E_b I k_f^3 [2R_{nf} - R_{tf} - 1 + j(R_{tf} - 1)]}. \quad \textbf{(A.48)}$$

Thus the flexural response of a finite beam subjected to a point force, F_f, at the free end is presented as:

$$w(x) = \frac{F_f \left[e^{jk_e x} + R_{tf} e^{-jk_e x} + R_{nf} e^{k_e x} + (1 + R_{tf} - R_{nf}) e^{-k_e x} \right]}{E_b I k_f^3 [2R_{nf} - R_{tf} - 1 + j(R_{tf} - 1)]} \quad \textbf{(A.49)}$$

The extensional equation of motion of a finite beam subjected to an in-plane force, F_e, at the free end was presented as Equation (2.62) as the following:

$$\frac{d^2u}{dx^2} + k_e^2 u = \frac{F_e}{E_b(1 - \nu^2)a} \delta(x) \quad \textbf{(A.50)}$$

The beam is assumed to have an in-plane motion of the form:

$$u(x) = Ee^{jk_e x} + Fe^{-jk_e x} \quad \textbf{(A.51)}$$

The boundary condition at x = 0 is identical to that presented for the semi-infinite beam case as shown in Equation (A.9). The boundary condition at the variable termination is dictated by the extensional traveling reflection coefficient presented again for completeness as

$$R_{te} = \frac{F}{E}. \tag{A.52}$$

Equation (A.9) and Equation (A.52) provide two equations to solve for the unknown extensional wave coefficients, E and F, and are presented as follows:

$$E = j\frac{F_e}{E_b a k_e (R_{te} - 1)} \tag{A.53}$$

and

$$F = j\frac{F_e R_{te}}{E_b a k_e (R_{te} - 1)} \tag{A.54}$$

Thus the extensional response of a finite beam subjected to an in-plane force, F_e, is

$$u(x) = j\frac{F_e\left[e^{jk_e x} + R_{te}e^{-jk_e x}\right]}{E_b a k_e (R_{te} - 1)} \tag{A.55}$$

A.4 Excitation of a Finite Beam Using a Single Piezoelectric Actuator

The extensional equation of motion a finite beam free at one end and subjected to excitation by a piezoelectric actuator of length L_a at a location x_a from the free end was previously presented by Equation (A.26). The equation was first solved by subjecting the beam to only one in-plane force as was shown in Equation (A.27). The solution is assumed to be of the form:

For $0 < x < x_a - L_a/2$:

$$u_1(x) = E_1 e^{jk_e x} + F_1 e^{-jk_e x} \tag{A.56}$$

For $x > x_a - L_a/2$:

$$u_2(x) = E_2 e^{jk_e x} + F_2 e^{-jk_e x}. \tag{A.57}$$

At $x = 0$ the in-plane force is zero which produces an identical relation as was shown in Equation (A.30). The displacement must be continuous, and the in-plane force must be discontinuous in a differential amount equal to the external applied force. These boundary conditions can be written in equation form as follows:

$$E_1 e^{jk_e(x-\frac{L_a}{2})} + F_1 e^{-jk_e(x-\frac{L_a}{2})} = E_2 e^{jk_e(x-\frac{L_a}{2})} + F_2 e^{-jk_e(x-\frac{L_a}{2})} \qquad \textbf{(A.58)}$$

and

$$jk_e E_b a\left(E_1 e^{jk_e(x_a-\frac{L_a}{2})} - F_1 e^{-jk_e(x_a-\frac{L_a}{2})}\right) + \frac{K^e d_{31} V}{T_a} = jk_e E_b a E_2\left(e^{jk_e(x_a-\frac{L_a}{2})} - F_1 e^{-jk_e(x_a-\frac{L_a}{2})}\right) \qquad \textbf{(A.59)}$$

At the variable termination the boundary condition is defined in terms of the extensional wave reflection coefficient as

$$R_{te} = \frac{F_2}{E_2} \qquad \textbf{(A.60)}$$

The Equations (A.30), (A.58), (A.59), and (A.60) provide 4 unique equations with four unknown amplitudes E_1, F_1, E_2, and F_2. After much algebra the resulting amplitudes were found to be:

$$E_1 = F_1 = -j\frac{K^e d_{31} V\left[R_{te} e^{-jk_e(x_a-\frac{L_a}{2})} + e^{jk_e(x_a-\frac{L_a}{2})}\right]}{2k_e T_a(1 - R_{te})} \qquad \textbf{(A.61)}$$

$$E_2 = -j\frac{K^e d_{31} V \cos\left(k_e(x_a-\frac{L_a}{2})\right)}{k_e T_a(1 - R_{te})} \qquad \textbf{(A.62)}$$

$$F_2 = -j\frac{K^e d_{31} V R_{te} \cos\left(k_e(x_a - \frac{L_a}{2})\right)}{k_e T_a(1 - R_{te})} \qquad \textbf{(A.63)}$$

Thus the total equation of motion was found by substituting Equations (A.61), (A.62), and (A.63) into the assumed solution of Equations (A.56) and (A.57), and is presented as follows

for $x < x_a - L_a/2$:

$$u(x) = -j\frac{K^e d_{31} V\left[R_{te} e^{-jk_e(x_a - \frac{L_a}{2})} + e^{jk_e(x_a - \frac{L_a}{2})}\right]}{2k_e T_a(1 - R_{te})}\left\{e^{jk_e x} + e^{-jk_e x}\right\} \qquad \textbf{(A.64)}$$

and for $x > x_a - L_a/2$:

$$u(x) = -j\frac{K^e d_{31} V \cos\left(k_e(x_a - \frac{L_a}{2})\right)}{k_e T_a(1 - R_{te})}\left\{e^{jk_e x} + R_{te} e^{-jk_e x}\right\} \qquad \textbf{(A.65)}$$

The solution to Equation (2.(A.26)) was found by superposition using the results of Equations (A.64) and (A.65) for a single in-plane force. The resulting extensional response of a finite beam due to excitation by a single piezoelectric actuator of length L_a mounted on the upper surface at a distance x_a from the free end is found to be:

for $x < x_a - L_a/2$:

$$u(x) = -\frac{K^e d_{31}(V_1 + V_2)}{k_e T_a(1 - R_{te})}\sin\left(\frac{k_e L_a}{2}\right)\left(e^{jk_e x_a} - R_{te}e^{-jk_e x_a}\right)\left(e^{jk_e x} + e^{-jk_e x}\right) \qquad \textbf{(A.66)}$$

for $x_a - L_a/2 < x < x_a + L_a/2$:

$$u(x) = -\frac{jK^e d_{31}(V_1 + V_2)}{2k_e T_a}\left\{\left[2\cos\left(\frac{k_e L_a}{2}\right)e^{jk_e x_a} + e^{-jk_e x_a}\left(e^{j\frac{k_e L_a}{2}} + R_{te}e^{-j\frac{k_e L_a}{2}}\right)\right]e^{jk_e x}\right.$$
$$\left. + \left[2R_{te}\cos\left(\frac{k_e L_a}{2}\right)e^{-jk_e x_a} + e^{jk_e x_a}\left(e^{j\frac{k_e L_a}{2}} + R_{te}e^{-j\frac{k_e L_a}{2}}\right)\right]e^{-jk_e x}\right\} \qquad \textbf{(A.67)}$$

for $x > x_a + L_a/2$:

$$u(x) = j\frac{2K^e d_{31}(V_1 + V_2)}{k_e T_a(1 - R_{te})}\sin\left(\frac{k_e L_a}{2}\right)\sin(k_e x_a)\left(e^{jk_e x} + R_{te}e^{-jk_e x}\right) \qquad \textbf{(2.68)}$$

APPENDIX B

Derivation of Far Field Power Flow for Flexural and Extensional Excitation

The total response of a thin beam can be described by four waves. Positive and negative traveling flexural waves of complex amplitudes, A and B, respectively, and positive and negative decaying nearfields of complex amplitudes, C and D respectively. This response can be written in complex form as

$$W(x,t) = \left(Ae^{jk_f x} + Be^{-jk_f x} + Ce^{k_f x} + De^{-k_f x}\right)e^{-j\omega t} \qquad \textbf{(B.1)}$$

The power flow due to the flexural excitation is found by the following relation (Cremer et al., 1973):

$$P_f(\omega) = \frac{1}{2}Re(F_w V_w^* + M\dot{\Theta}^*) \qquad \textbf{(B.2)}$$

Where F_w is the shear force, v_w is the out-of-plane velocity, M is the flexural moment, and Θ is the rotational velocity given by:

$$V_w(x,t) = \frac{\partial W}{\partial t} = -j\omega\left(Ae^{jk_f x} + Be^{-jk_f x} + Ce^{k_f x} + De^{-k_f x}\right)e^{-j\omega t} \qquad \textbf{(B.3)}$$

$$F_w(x,t) = E_b I \frac{\partial^3 W}{\partial x^3} = E_b I k_f^3 \left(-jAe^{jk_f x} + jBe^{-jk_f x} + Ce^{k_f x} - De^{-k_f x}\right) e^{-j\omega t} \quad \textbf{(B.4)}$$

$$\dot{\theta}(x,t) = \frac{\partial V_w}{\partial x} = \omega k_f \left(Ae^{jk_f x} - Be^{-jk_f x} - jCe^{k_f x} + jDe^{-k_f x}\right) e^{-j\omega t} \quad \textbf{(B.5)}$$

$$M(x,t) = -E_b I \frac{\partial^2 W}{\partial x^2} = E_b I k_f^2 \left(Ae^{jk_f x} + Be^{-jk_f x} - Ce^{k_f x} - De^{-k_f x}\right) e^{-j\omega t} \quad \textbf{(B.6)}$$

When Equations (B3) through (B6) are further reduced to the form of equation (B2) the resulting flexural power flow is:

$$P_f(\omega) = E_b I k_f^3 \omega \left(|A|^2 - |B|^2 - 2\,\mathrm{Imag}(CD^*)\right) \quad \textbf{(B.7)}$$

It is interesting to note that the power flow is consists of three main parts. The first part is associated with positive energy flow proportional to the magnitude of the A wave squared. The second part is associated with negative energy proportional to the magnitude of the B wave squared. The last portion is proportional to the imaginary portion of the complex product of the two nearfields (i.e. nearfield interaction). Thus if the nearfields of oppositely traveling motions are not totally in-phase or out-of-phase then there will exist a net flow of energy as shown in Equation (B.7). If the nearfields are totally in-phase, or out-of-phase then there will be no power flow associated with nearfield interaction. It is seen in Equation (B.7) that the nearfield contribution is independent of x. It could be argued that at locations where the nearfields

have decayed to be very small that the power flow must also be small. Equation (B.7) shows that the nearfield contribution is constant as a function of x. The understanding of this phenomena lies in the fact that all of the four wave are referenced to the same x origin. If the opposite decaying nearfields originate at discontinuities that are close together then there power flow will be large. If the opposite decaying nearfields originate at discontinuities that are far apart then the resultant power flow will be small. This occurs because a given nearfield may have a large amplitude coefficient when the origin is referenced to the discontinuity location which generated the nearfield but the identical nearfield will have a small amplitude coefficient when referenced to an origin far from the discontinutiy location. For most of the experimental and theoretical results presented in this dissertation the nearfield interaction was insignificantly small compared to the other terms.

The total response for the extensional excitation of a thin beam can be written as two traveling waves of amplitudes, E and F, as follows:

$$U(x,t) = \left(Ee^{jk_e x} + Fe^{-jk_e x}\right)e^{-j\omega t} \qquad \textbf{(B.8)}$$

The power flow due to extensional excitation is found by the following relation:

$$P_e(\omega) = \frac{1}{2}\mathrm{Re}(F_x v_x^*) \tag{B.9}$$

where F_x is the in-plane force and v_x is the in-plane velocity given by:

$$F_x(x,t) = -E_b a \frac{\partial U}{\partial x} = -jE_b a k_e \left(Ee^{jk_e x} - Fe^{-jk_e x}\right) e^{-j\omega t} \tag{B.10}$$

$$V_x(x,t) = \frac{\partial U}{\partial t} = -j\omega \left(Ee^{jk_e x} - Fe^{-jk_e x}\right) e^{-j\omega t} \tag{B.11}$$

When equations (B10) and (B11) are substituted into (B9) the resulting extensional power flow is:

$$P_e(\omega) = \frac{E_b a k_e \omega}{2}\left(|E|^2 - |F|^2\right) \tag{B.12}$$

Vita

Gary Parker Gibbs was born in Norfolk, Virginia on July 30, 1964 and was raised in Chesapeake, Virginia. He graduated from Indian River High School in 1982, and attended Virginia Polytechnic Institute and State University stating in the fall of that same year. Gary received a Bachelor of Science degree in Mechanical Engineering from Virginia Polytechnic Institute and State University in 1987 after completing a co-operative training program at Newport News Shipbuilding in the SSN688 Class Propulsion Plant Design Project. After graduation he was hired at Newport News Shipbuilding in the SSN21 Seawolf attack submarine project. Gary returned to Virginia Polytechnic Institute and State University in the fall of 1988 to pursue a Ph.D. degree in mechanical engineering in the area of active control of structures. In November of 1992 he successfully defended his Ph.D. dissertation and began working as a research associate at V. P. I. & S. U. under contract by the Office of Naval Research and Cessna Aircraft Company.